Turbulence Transition in Shear Flows and Dynamical Systems Theory

Dissertation

zur Erlangung des
Doktorgrades der Naturwissenschaften
(Dr. rer. nat.)

dem Fachbereich Physik
der Philipps-Universität Marburg
vorgelegt von

Tobias Kreilos
aus
Bonn

Marburg, 2014

Vom Fachbereich Physik der Philipps-Universität Marburg
(Hochschulkennziffer 1180) als Dissertation angenommen am: 3. Juni 2014

Autor: Diplom-Physiker Tobias Kreilos, geboren Madré

Erstgutachter: Prof. Dr. Bruno Eckhardt, Philipps-Universität Marburg
Zweitgutachter: Prof. Dr. Dan S. Henningson, KTH Stockholm

Tag der mündlichen Prüfung: 13. Juni 2014

Meinen Eltern

Abstract

Turbulence is allegedly "the most important unsolved problem of classical physics" (attributed to Richard Feynman). While the equations of motion are known since almost 150 years and despite the work of many physicists, in particular the transition to turbulence in linearly stable shear flows evades a satisfying description. In recent decades, the availability of more powerful computers and developments in chaos theory have provided the basis for considerable progress in our understanding of this issue. The successful work of many scientists proved dynamical systems theory to be a useful and important tool to analyze transitional turbulence in fluid mechanics, allowing to explain observed phenomena such as transition thresholds and transient lifetimes through bifurcation analyses and the identification of underlying state space structures. In this thesis we continue on that path with direct numerical simulations in plane Couette flow, the asymptotic suction boundary layer and Blasius boundary layers. We explore the state space structures and bifurcations in plane Couette flow, study the threshold dynamics in the ASBL and develop a model for the spatio-temporal dynamics in the boundary layers. The results show how the insights obtained for parallel, bounded shear flows can be transferred to spatially developing external flows.

Our simulations in plane Couette flow demonstrate the creation of the state space structures that support transient turbulence and the changes that lead to increasing transient lifetimes. The sequence of events which finally leads to a chaotic saddle starts with two fixed points. Those are created in a saddle node bifurcation and the upper branch is initially linearly stable. In a Hopf bifurcation, it gives rise to a stable periodic orbit, that subsequently undergoes a classical period doubling cascade leading to a chaotic attractor. This attractor is destroyed in a boundary crisis, where it becomes a chaotic saddle, supporting transient turbulent motion. The involved steps are well known in low-dimensional dynamical systems theory and our studies support the link to transitional turbulence. At higher Reynolds numbers, we demonstrate a similar sequence of events – creation of stable invariant solutions, bifurcations to a chaotic attractor followed by a boundary crisis – to be responsible for transient lifetimes increasing with Reynolds number.

Extending the known analysis and concepts from internal shear flows to a parallel boundary layer, we calculate and characterize edge states in the asymptotic suction boundary layer, investigating the stability boundary between laminar and turbulent motion. The states consist of long calm phases, where the flow is formed of a pair of downstream streaks and a pair of streamwise vortices, interrupted by violent bursts,

during which the structures break up and are reformed at a different spanwise location. In narrow domains the displacement is exactly half a wavelength and the state is a periodic orbit whose creation we relate to a saddle-node-infinite-period bifurcation. In wider domains the structures are localized and their displacement during the bursts can follow a regular pattern, making the state a relative periodic orbit, or be chaotic.

Recently a connection between the spatial spreading of turbulence in internal shear flows and directed percolation has been demonstrated. We extend this concept to the description of a boundary layer flow subject to turbulence in the free-stream. Here the transition to turbulence occurs through the generation of turbulent spots that are advected by the free-stream and at the same time grow in size. From numerical simulations of the flow we develop a probabilistic cellular automaton which describes the evolution of these turbulent spots. The model parameters turn out to be independent of the level of free-stream turbulence and Reynolds number so that the transition can be described as an activated process: once a turbulent spot is created, its time evolution is independent of the details of the surrounding flow. We propose a model describing the nucleation probability of turbulent spots which together with the spatial spreading according to the automaton model describes the spatio-temporal statistics of the transitional boundary layer extremely well.

Symmetries play an important role in many fields of physics and computational fluid dynamics is no exception; we develop a method to separate advection in directions of continuous symmetries from the dynamically relevant action of the Navier-Stokes equations. Applying this method to the asymptotic suction boundary layer we show that the edge state slows down during the burst and identify drifts in turbulent flow that persist for very long times.

As part of this work, the timestepper from the open source DNS code channelflow has been successfully parallelized; the parallel code has been made available to John F. Gibson, the author and maintainer of channelflow, and will be available publicly as part of the next major release at channelflow.org.

Zusammenfassung

Turbulenz gilt als „das wichtigste ungelöste Problem der klassischen Physik“ (Richard Feynman zugeschrieben). Obwohl die Bewegungsgleichung seit fast 150 Jahren bekannt sind und trotz der Arbeit zahlreicher Physiker ist insbesondere die Beschreibung des Turbulenzübergangs in linear stabilen Scherströmungen noch nicht zufriedenstellend möglich. In den letzten Jahrzehnten haben die Verfügbarkeit leistungsfähigerer Computer sowie Entwicklungen in der Chaosforschung die Grundlagen für erheblichen Fortschritt bei diesem Thema gelegt. Die erfolgreiche Arbeit zahlreicher Wissenschaftler hat gezeigt, dass die Theorie dynamischer Systeme ein hilfreiches und wichtiges Werkzeug in der Analyse transitionaler Turbulenz in der Fluidmechanik ist. Beobachtete Phänomene wie Transitionsschwellen und die Statistik transienter Lebenszeiten konnten durch Bifurkationsanalysen und die Identifizierung der zugrunde liegenden Phasenraumstrukturen erklärt werden. In dieser Dissertation setzen wir diesen Weg mittels numerischer Simulationen der ebenen Couette Strömung, der asymptotischen Abssauggrenzschicht sowie der Blasius Grenzschicht fort. Wir erforschen die Phasenraumstrukturen und Bifurkationen in der ebenen Couette Strömung, untersuchen die Dynamik in der laminar-turbulenten Grenze in der Abssauggrenzschicht und entwickeln ein Modell zur Beschreibung der raum-zeitlichen Dynamik in Grenzschichten. Die Ergebnisse zeigen wie die in parallelen, räumlich begrenzten Scherströmungen gewonnen Erkenntnisse auf räumlich entwickelnde Strömungen übertragen werden können.

Unsere Simulationen in der ebenen Couette-Strömung verfolgen die Entstehung der Phasenraumstrukturen welche transiente Turbulenz ermöglichen und zu ansteigenden turbulenten Lebenszeiten führen. Die Sequenz an Ereignissen, die schlussendlich auf einen chaotischen Sattel führt, beginnt mit zwei Fixpunkten. Diese entstehen in einer Sattel-Knoten Bifurkation und der obere Ast ist zu Beginn linear stabil. Bei wachsender Reynoldszahl entseht daraus in einer Hopf Bifurkation ein stabiler periodischer Orbit, welcher dann eine klassische Periodenverdopplungskaskade durchläuft und so zu einem chaotischen Attraktor führt. Dieser Attraktor wird in einer Krisen Bifurkation zerstört und durch einen chaotischen Sattel ersetzt, in welchem die chaotische Dynamik transient wird. Weiter zeigen wir, dass eine analoge Folge von Ereignissen – Entstehung stabiler invarianter Lösungen, eine Bifurkationskaskade, die zu einem chaotischen Attraktor führt, gefolgt von einer Krisen Bifurkation – für einen Anstieg der transienten Lebenszeit mit der Reynoldszahl verantwortlich ist.

Wir erweitern die bekannten Analysen und Konzepte von internen auf externe Scherströmungen und berechnen Grenz-Zustände in der asymptotischen Absauggrenz-

schicht, dynamische Attraktoren in der Grenze zwischen laminarer und turbulenter Strömung. Die Zustände durchlaufen lange, ruhige Phasen, während derer die Strömung aus einem Paar in Strömungsrichtung orientierter Wirbel besteht, unterbrochen von heftigen Ausbrüchen, während derer die Strukturen aufbrechen und an verschobener Stelle wieder neu entstehen. In engen Domänen entspricht die Verschiebung genau einer halben Wellenlänge und die Zustände sind periodische Orbits, deren Entstehung wir auf eine Sattel-Knoten-unendliche-Periode Bifurkation zurückführen konnten. In breiteren Domänen lokalisieren die Strukturen und ihre Verschiebung während der Ausbrüche kann entweder einem regulären Muster folgen, womit die Zustände relative periodische Orbits sind, oder chaotisch sein.

In letzter Zeit wurde eine enge Verbindung der räumlichen Ausbreitung von Turbulenz in internen Scherströmungen mit direkter Perkolation gezeigt. Wir erweitern dieses Konzept auf die Beschreibung einer Grenzschichtströmung unter dem Einfluss von Turbulenz in der äußeren Strömung. Hier erfolgt der Turbulenzübergang durch die Bildung von turbulenten Flecken, welche von der Grundströmung advektiert werden und gleichzeitig größer werden. Aus numerischen Simulationen der Strömung entwickeln wir einen probabilistischen zellulären Automaten, welcher die Entwicklung dieser turbulenten Flecken beschreibt. Die Modellparameter stellen sich als unabhängig von der Intensität der äußeren Turbulenz sowie der Reynoldszahl heraus, so dass die Transition durch einen aktivierten Prozess beschrieben wird: sobald ein turbulenter Flecken enstanden ist, ist seine Zeitentwicklung unabhängig von Details der umgebenden Strömung. Wir entwickeln ein Modell zur Beschreibung der Nukleationshäufigkeit von turbulenten Flecken, welches zusammen mit der räumlichen Ausbreitung anhand des Automatenmodells die raum-zeitlichen Statistiken der transitionalen Grenzschicht extrem gut beschreibt.

Symmetrien spielen in vielen Feldern der Physik eine wichtige Rolle und die Fluidmechanik ist keine Ausnahme. Wir entwickeln eine Methode mit der sich die Advektion in Richtungen kontinuierlicher Symmetrien vom dynamisch relevanten Teil der Navier-Stokes Gleichungen separieren lässt. Durch die Anwendung dieser Methode in der asymptotischen Absauggrenzschicht zeigen wir, dass die Grenz-Zustände während der Ausbrüche langsamer advektiert werden und dass in turbulenter Strömung extrem langlebiges Abdriften in Spannweitenrichtung vorkommt.

Als Teil dieser Arbeit wurde der Integrator des DNS codes channelflow parallelisiert. Der parallele Code wurde an John F. Gibson, den Autor von channelflow, weitergegeben und wird als Teil der nächsten Version auf channelflow.org allgemein verfügbar sein.

Preface

This thesis was written under the supervision of Bruno Eckhardt, with parts of the work done within the Max-Planck research group of Tobias M. Schneider and parts in collaboration with Taras Khapko, Philipp Schlatter, Yohann Duguet and Dan S. Henningson. This thesis is written in cumulative form, consisting of a first part with a summary of the results and a second part with the more detailed publications. The cumulative framework of this thesis comprises the six publications listed below.

1. **Tobias Kreilos** and Bruno Eckhardt
   Periodic orbits near onset of chaos in plane Couette flow
   Published in: Chaos, 22(4), 047505 (2012)

2. **Tobias Kreilos**, Bruno Eckhardt, and Tobias M. Schneider
   Increasing Lifetimes and the Growing Saddles of Shear Flow Turbulence
   Published in: Physical Review Letters 112, 044503 (2014)

3. **Tobias Kreilos**, Gregor Veble, Tobias M. Schneider and Bruno Eckhardt
   Edge states for the turbulence transition in the asymptotic suction boundary layer
   Published in: Journal of Fluid Mechanics 726, 100-122 (2013)

4. Taras Khapko, **Tobias Kreilos**, Philipp Schlatter, Yohann Duguet, Bruno Eckhardt and Dan S. Henningson
   Localized edge states in the asymptotic suction boundary layer
   Published in: Journal of Fluid Mechanics 717, R6 (2013)

5. **Tobias Kreilos**, Stefan Zammert and Bruno Eckhardt.
   Comoving frames and symmetry-related slow processes in parallel shear flows
   Accepted for publication in: Journal of Fluid Mechanics

6. **Tobias Kreilos**, Taras Khapko, Philipp Schlatter, Yohann Duguet, Dan S. Henningson and Bruno Eckhardt
   Bypass transition in boundary layers as an activated process
   Manuscript in preparation

In addition the author has contributed to the following articles that are not integrated into this cumulative thesis because the individual contribution was smaller or because they are contributions to special puclication formats.

7. Konstantin Melnikov, **Tobias Kreilos** and Bruno Eckhardt
   Long wavelength instability of coherent structures in plane Couette flow
   Published in: Physical Review E 89, 043008 (2014)

8. Taras Khapko, Yohann Duguet, **Tobias Kreilos**, Philipp Schlatter, Bruno Eckhardt and Dan S. Henningson
   Complexity of localised coherent structures in a boundary-layer flow
   Published in: European Physical Journal E, 37:32 (2014)

9. **Tobias Kreilos**, Taras Khapko, Tobias M. Schneider, Gregor Veble, Yohann Duguet, Philipp Schlatter, Dan S. Henningson and Bruno Eckhardt
   Turbulence Transition in the Asymptotic Suction Boundary Layer
   Accepted for publication in: Proceedings of the 8th International Symposium on Turbulence and Shear Flow Phenomena (TSFP 8)

10. Laurette S. Tuckerman, **Tobias Kreilos**, Hecke Schrobsdorff, Tobias M. Schneider and John F. Gibson
    Turbulent-laminar patterns in plane Poiseuille flow
    Under review

The outline of this work is as follows: in chapter 1 an introduction to the subject is given with an overview over the existing work and some methods and tools are introduced in chapter 2. In the following chapter 3 the results of the author's research are summarized, followed by a concluding discussion in chapter 4. The full results can be found in the authors publications, reproduced in chapter 5, with the author's contributions to each publication stated in section 5.7. Details on the parallelization of the channelflow DNS code are given in appendix A.

Contents

1. Introduction

1.1. Motivation

Under which conditions is the flow of a fluid smooth and laminar? When and why does it transit to turbulence? These questions, relating the two fundamentally different flow states of a fluid, either smooth and time-independent or rapidly and unpredictably varying, have puzzled physicists for centuries; they are fundamental in the research of fluid mechanics and key questions in numerous technological applications. In many cases an answer can however only be given through explicit studies of the system in question and theoretical predictions are unavailable as the processes that govern the transition are not fully understood.

Turbulence is intimately related to chaos theory, that some people say is the third grand physical theory of the twentieth century together with quantum mechanics and general relativity, having fundamentally altered the way we perceive our world (e.g. Emanuel, 2008). In this context chaos – in particular in the form of fluid turbulence – is special in the sense that it is a phenomenon that we can observe every day with the naked eye, not only appearing on scales that are so tiny that they evade direct observation or on scales as gigantic as stars and galaxies. Nevertheless, and despite having been investigated for several centuries, turbulence is way less understood than quantum mechanics or relativity and no complete description of turbulence from first principles is available.

The essence of chaos has been pointedly described by Edward Lorenz as "Chaos: When the present determines the future, but the approximate present does not approximately determine the future" (Danforth, 2013). This notion contradicts the traditional approach in mechanics, where it was assumed that small errors in the initial conditions will only lead to small changes in the long-term behavior. While the exact outcome at an exact time may be unpredictable, statistical predictions are possible. From the early days of chaos theory about fifty years ago, turbulence and fluid dynamics was one of the main focuses of interest and the development in nonlinear dynamical systems theory has greatly enhanced our understanding of turbulence.

A second development that led to great progress in the study of turbulence is the availability of powerful computers, giving rise to the field of computational fluid dynamics (CFD), often combined with dynamical systems analysis (e.g. Jiménez and Moser, 2007). If in simulations one really wants to understand the mechanisms at work, computations need to resolve all scales from the largest scales of the system

down to very small scales. These so called direct numerical simulations (DNS) require enormous computational power and the simulation of a full aircraft is out of reach by several orders of magnitude. But smaller systems are accessible to DNS studies and allow to perform "numerical experiments" from which information can be extracted which is inaccessible in laboratory experiments. Simulations of larger systems often make use of turbulence models, by which e.g. the small scales are represented by a sub-grid scale model and only the largest scales are directly simulated.

For many practical applications, the transition process from laminar to turbulent flow is relevant, as e.g. Moin and Kim (1997) state: "A great deal of the work of aerodynamicists involves understanding the mechanics of the generation and destruction of turbulence well enough to control it." A striking example is the design of aircrafts, where most fuel consumption is needed to overcome the drag. For a subsonic aircraft skin-friction drag is responsible for 50% of the total drag (Thibert et al., 1990), which is 90% lower for laminar than for turbulent flow (Joslin, 1998). Giving one example of the use of computational fluid dynamics in this context, the combination of simulations with wind tunnel experiments has shown that small riblets on the front of the wings may reduce viscous drag on the wings by 5-6% (see e.g. Viswanath, 2002). On the other hand, there also exist numerous cases where turbulence is desirable, e.g. in the mixing of fuel and oxygen in combustion chambers, where turbulent mixing is very efficient. And also for drag reduction, a controlled turbulence may be advantageous: the drag on a a golf ball is considerably smaller than on a smooth sphere because the boundary layer is turbulent almost everywhere, leading to a smaller pressure difference between the front and the end of the ball (Moin and Kim, 1997).

In this thesis, we numerically investigate the transition between laminar and turbulent motion in several simple flow situations, where a detailed study of the involved structures is possible. We identify topological structures and mechanisms that are known from simpler dynamical systems and show how they apply to turbulence transition. The systems studied here range from internal plane Couette flow via the parallel asymptotic suction boundary layer to spatially developing boundary layers. We hope that our work provides a useful step towards a better theory of turbulence transition in shear flows.

The outline for this introductory chapter is as follows: in the following section 1.2 we shortly discuss shear flows and observations therein that are relevant to our work. In section 1.3 the dynamical systems view on transitional shear flows and the knowledge about the state space is summarized. We finish the introduction with a discussion of turbulence transition in boundary layers and conceptual differences to internal flows in section 1.4.

1.2. Turbulence transition in shear flows

1.2.1. Equations of motion

Throughout this work, we numerically study incompressible Newtonian fluids. The equations of motion governing the evolution of a velocity field $\mathbf{v}(\mathbf{x}, t)$ are the famous Navier-Stokes-equations (Navier, 1823; Stokes, 1845)

$$\partial_t \mathbf{v} + (\mathbf{v} \cdot \nabla)\mathbf{v} = -\nabla P/\rho + \nu \Delta \mathbf{v} + \mathbf{F} \tag{1.2.1}$$

together with the continuity equation

$$\nabla \cdot \mathbf{v} = 0, \tag{1.2.2}$$

with P the pressure, ρ the (constant) density of the fluid, ν its dynamic viscosity and $\mathbf{F}$ a possible body force density. We use a typical size of the system, d, as length scale and a typical velocity, U, as velocity scale (measuring times in units of $t_0 = d/U$) and introduce the dimensionless combination

$$\mathrm{Re} = \frac{Ud}{\nu} \tag{1.2.3}$$

due to Reynolds (1883) that now carries his name. With this, we can rewrite the Navier-Stokes equations (1.2.1) for the dimensionless velocity $\mathbf{u} = \mathbf{v}/U$, the dimensionless pressure $p = P/(\rho U^2)$ and dimensionless forces $\mathbf{f}$

$$\partial_t \mathbf{u} + (\mathbf{u} \cdot \nabla)\mathbf{u} = -\nabla p + \frac{1}{\mathrm{Re}} \Delta \mathbf{u} + \mathbf{f}, \tag{1.2.4}$$

and the continuity equation,

$$\nabla \cdot \mathbf{u} = 0. \tag{1.2.5}$$

All system parameters are combined into the Reynolds number, which hence remains as the only control parameter of the flow if the boundary conditions and external forces remain constant.

1.2.2. Shear flows

At low Reynolds numbers, most flows are typically laminar, but if the Reynolds numbers are high enough, transition from laminar to turbulent flow is frequently observed, with the opposite transition also possible at moderate Re.

A first method to investigate the transition is linear stability theory. In many flows characterized by external body forces the laminar flow becomes unstable as the forces get stronger; the transition to turbulence is rather well understood in these cases. A typical example is Rayleigh-Bénard flow, the flow between two plates at fixed temperature of which the lower one is warmer than the upper one, where the

temperature changes the fluids density and gravitation acts as a body force. Taylor-Couette flow, the flow between two concentric cylinders, is another example e.g. if the outer cylinder is at rest and only the inner one rotates, in which case the instability is driven by centrifugal forces. As the forcing gets stronger, the laminar profile becomes linearly unstable and infinitesimal perturbations are exponentially amplified, driving the system away from the laminar flow into more complex motion and finally turbulence.

The situation is however different for many shear flows, as turbulent motion is observed while the laminar flow profile is still linearly stable and the transition to turbulence is subcritical. Typical examples include the flow through a cylindrical pipe under the action of a pressure gradient or between parallel plates, in the latter case either driven by a pressure gradient (so-called channel flow) or by the plates moving in opposite directions (called plane Couette flow). Taylor Couette flow in certain parameter regimes also shows a subcritical transition. While it has not been possible to exactly define a critical Re in linearly stable systems, turbulent motion is for example observed in plane Couette flow above $\mathrm{Re} \sim 300$, albeit the laminar flow is linearly stable for all Re (Romanov, 1973); here Re is defined by the half-gap between the plates and half their velocity difference. Pipe flow exhibits turbulence at $\mathrm{Re} \sim 2000$ (with Re defined by the pipe diameter and the mean velocity) while the laminar Hagen-Poiseuille profile is proven to be stable to axisymmetric disturbances for all Re (Salwen et al., 1980; Schmid and Henningson, 2001) and has been shown to be stable to asymmetric disturbances up to $\mathrm{Re} = 10^7$ (Meseguer and Trefethen, 2003); as stated for example by Kerswell (2005), there is a consensus that pipe flow is linearly stable for arbitrary Re. In channel flow, the laminar Poiseuille profile becomes linearly unstable at $\mathrm{Re} = 5772$ (Orszag, 1971) but turbulence is observed at $\mathrm{Re} \sim 1000$ (Orszag and Kells, 1980). Boundary layers develop when a solid object is in relative motion to a surrounding fluid, with commonly studied cases including the flow of air over a flat plate or over a plate with constant homogeneous suction into the plate. In these cases the turbulent dynamics extracts energy from the shear gradient due to the velocity difference between the free-stream and the wall. While many boundary layers develop a linear stability, turbulence can often be observed while the laminar profile is still linearly stable. Despite the practical relevance of these flows, the subcritical transition to turbulence is considerably less well understood.

As a consequence of the linear stability of the laminar flow infinitesimal perturbations to the laminar profile will always decay and perturbations of finite amplitude are needed in order to trigger a transition (Grossmann, 2000), where the critical amplitude depends on the shape of the perturbation. It has been found experimentally and numerically that the threshold in perturbation amplitude decreases with increasing Reynolds number, giving a double threshold for the transition: both the amplitude of the disturbance and the Reynolds number need to be large enough. The threshold scales as Re^{α} with α between one and two, depending on the shape of the perturbation (Darbyshire and Mullin, 1995; Hof et al., 2003; Peixinho and Mullin, 2007;

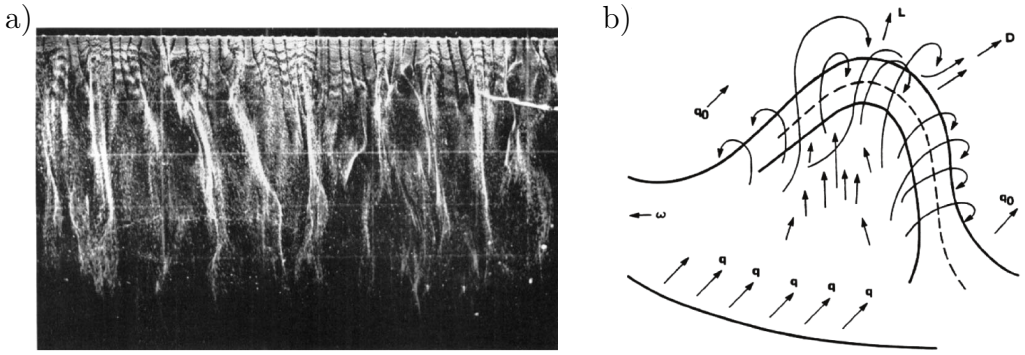

Figure 1.2.1.: Typical flow structures. (a) (From Kline et al., 1967) Visualization of streaks in a turbulent boundary layer. The flow is from top to bottom, at the top the flow is disturbed and downstream ordered streaks from with a typical spacing of $100x^+$. (b) (From Theodorsen 1952, reproduced after Adrian et al. 2000) Schematic illustration of a hairpin vortex, a flow structure typically observed in near-wall turbulence.

Mellibovsky and Meseguer, 2009).

While small disturbances will eventually decay, it should be noted that linear stability does not imply that they do so monotonically. Due to the non-normality of the linearized Navier-Stokes operator, a non-normal transient growth is possible (Grossmann, 2000). This linear transient growth, together with energy-conserving nonlinear mixing, can be strong enough to cause a transition to chaos (Gebhardt and Grossmann, 1994).

1.2.3. Typical flow structures in near-wall turbulence

In the vicinity of a wall, turbulent flow is often found to be highly organized as there exist regions, called coherent structures, where the fluid motion is more strongly correlated than in full turbulence. In figure 1.2.1(a) a flow visualization of a turbulent boundary layer is reproduced from Kline et al. (1967), showing alternating regions of low- and high-speed fluid, elongated in the streamwise direction. The spanwise spacing between these so-called streaks is best expressed in wall units, which are based on the wall shear stress $\tau_W = \mu \partial u/\partial y|_{y=0}$, with $\mu = \nu\rho$ the dynamic viscosity of the fluid. A length scale is defined by $l^+ = \nu/\sqrt{\tau_W/\rho}$ and the spacing is universally observed to be $\sim 100l^+$ (Klebanoff et al., 1962; Kline et al., 1967).

Further investigations (see e.g. Blackwelder and Eckelmann, 1979) reveal the existence of downstream vortices, occuring in counter-rotating pairs. Through linear advection, these vortices push fluid from the high-speed free stream towards the wall, thus creating and sustaining a high-speed streak. Vice versa, fluid is pulled from the wall into the free stream, resulting in a low-speed streak; this process of streak

creation through downstream vortices is termed lift-up effect. Vortices in near-wall turbulence are typically not exactly parallel to the downstream direction but aligend at a small angle. They are furthermore slightly inclined from the wall (Jeong et al., 1997; Schoppa and Hussain, 2002).

In open flows where no boundaries limit the flow in the wall-normal direction, horseshoe or hairpin shaped vortices are commonly observed (Head and Bandyopadhyay, 1981; Robinson, 1991; Adrian et al., 2000; Adrian, 2007). Close to the wall, these structures are similar to a counter-rotating vortex pair, but they are inclined and extend further into the free stream, where they are connected, forming a hairpin shaped structure. The concept goes back more than half a century to Theodorsen (1952), an illustration is reproduced in figure 1.2.1(b).

To better understand the dynamical properties of these typical flow structures, simulations are often performed in so-called minimal flow units defined by the fact that turbulence cannot be sustained if any of the dimensions is reduced (Jiménez and Moin, 1991), with some freedom in the definition of sustained turbulence and the ratio of the dimensions. The concept is useful because it allows to extract features of turbulence which are otherwise obfuscated by spatial processes and because a small periodic domain is cheaper in numerical simulations. In such a minimal flow unit, a self-sustaining cycle of near-wall turbulence has been identified (Hamilton et al., 1995; Waleffe, 1997, 2003), connecting the typical flow structures and their instabilities. The cycle starts with a pair of counter-rotating streamwise-aligned vortices, which create a pair of streaks through the lift-up effect. The streaks, initially straight, are linearly unstable to developing a wavy modulation, and the period in which the streaks are created is about as long as the subsequent period during which the instabilities grow. As the modulation becomes too strong, the structures break up, leaving behind a flow with strong downstream variations. The cycle is closed by nonlinear interactions recreating the downstream vortices. This so called self-sustaining process is found in many shear flows and was, for example, observed experimentally by Duriez et al. (2009). It also served as the stimulus for making an analogy between fluid mechanics and magnetohydrodynamic dynamos (Riols et al., 2013).

1.2.4. Transient turbulence

In linearly stable shear flows turbulence is not always sustained and transition from turbulent to laminar flow is frequently observed at moderate Re, with the transition happening suddenly in the sense that no precursor can be identified (Brosa, 1989). Using many initial conditions it has been found numerically and experimentally that the probability that the flow is still turbulent after a certain time decays exponentially with time,

$$P_{turb}(t) \propto \mathrm{e}^{-t/\tau}, \tag{1.2.6}$$

where the characteristic time scale τ is termed lifetime. Evidence that turbulence decays in pipe flow and that the survival times are exponentially distributed has been be found in many experiments (Darbyshire and Mullin, 1995; Hof et al., 2006; Peixinho and Mullin, 2007; Hof et al., 2008; Mullin, 2011) and numerical simulations (Faisst and Eckhardt, 2004; Schneider, 2007; Avila et al., 2010). Exponentially distributed lifetimes have also been found in plane Couette flow experiments and numerical simulations (Schmiegel and Eckhardt, 1997; Bottin and Chaté, 1998) and a nine-dimensional model shows similar properties (Moehlis et al., 2004a,b). See also the review articles by Kerswell (2005) and Eckhardt et al. (2007) for pipe flow and Eckhardt et al. (2008) for plane Couette flow.

There is compelling evidence that the lifetimes increase super-exponentially with Re and the exact functional form of the dependence of τ on Re has received much attention. In particular there was a heated debate whether at some point the lifetime diverges and becomes infinite (suggested by data from Faisst and Eckhardt, 2004; Peixinho and Mullin, 2006; Willis and Kerswell, 2007) or whether it does not diverge and turbulence in shear flows remains a transient phenomenon for all Re (Hof et al., 2006, 2008; Schneider and Eckhardt, 2008; Avila et al., 2010; Schneider et al., 2010a; Avila et al., 2011). Analogies to other physical processes with indefinitely growing time scales, like the glass transition (Dauchot and Bertin, 2014) where a possible divergence is discussed in view of super-exponentially growing relaxation times, have the potential to elucidate this issue.

1.2.5. Spatial spreading of localized turbulence

At transitional Re turbulence typically comes in localized patches, puffs and slugs in pipe flow (Wygnanski and Champagne, 1973) or tilted stripes in plane Couette flow (Prigent et al., 2002; Barkley and Tuckerman, 2005) and channel flow (Tsukahara et al., 2005; Tuckerman et al., 2014). The flow exhibits spatio-temporal intermittency as only a fraction of space is turbulent at a certain instant in time or, the other way round, a fixed point in space is only turbulent at some times. An intermittency factor γ is defined as the fraction of space that is covered by turbulence. While in a small computational domain turbulence may either be sustained or decay, meaning that γ can be either 0 or 1, localized structures also have the possibility to spread or split. And indeed, splitting events in which a turbulent puff creates another one downstream, or a turbulent stripe splits into two separated by a quasi-laminar region in between are observed with an increasing frequency at higher Re. At some critical Re the splitting rate may overcome the local decay of turbulence, thus leading to turbulence being sustained in a percolation-like phase transition (Moxey and Barkley, 2010; Avila et al., 2011). The intermittency factor γ becomes finite once the splitting and decaying processes equilibrate and typically increases with growing Re. At somewhat higher Re, localized turbulent patches expand in space, typically at rates that fill space so quickly that no further splitting events are observed.

Several simple models have been devised to explain the behavior. Barkley (2011a) introduced a one dimensional two-variable model, phenomenologically describing turbulence as an excitable and bistable medium, with the two variables representing turbulence intensity and mean shear. In the presence of noise the model is able to reproduce the puff and slug features of pipe flow, namely puff decay, puff splitting and the spreading of slugs. As a control parameter in the model is increased, the fraction of space that is turbulent increases from zero (everything is laminar) to one (everything is turbulent).

The spatio-temporal intermittency and the competition between decay and spreading is reminiscent of directed percolation (Pomeau and Manneville, 1980; Chaté and Manneville, 1987, 1988a; Manneville, 2009). In these models space and time are discretized and every point is assigned a binary value of laminar or turbulent. At every time step, turbulence may spread to neighboring cells or decay with prescribed probabilities. Such models have been discussed in the context of pipe flow by Sipos and Goldenfeld (2011), Barkley (2011a,b), Allhoff and Eckhardt (2012), and in the context of boundary layers by Vinod and Govindarajan (2004, 2007).

1.3. The state space of transitional shear flows

1.3.1. Dynamical systems

In the last decades, a lot of progress on understanding transition to turbulence has been achieved by considering fluid mechanics as a dynamical system,

$$\partial_t \mathbf{u} = f(\mathbf{u}, S), \tag{1.3.1}$$

where the right-hand side gives the time evolution of $\mathbf{u}$ by the Navier-Stokes equations together with external parameters S and the boundary conditions.[1] The parameters S latter usually comprise the Reynolds number and possibly changes to the boundary conditions.

The state space of the system is the space of all velocity fields that fulfill the boundary conditions and the incompressibility condition, equation (1.2.5).[2] While in principal infinite dimensional, viscous dissipation introduces a cutoff at small scales and the state space can be regarded as finite dimensional for most practical considerations. In particular in numerical implementations the state space is finite dimensional, a velocity field is represented by its independent coefficients and the right hand side of equation (1.3.1) represents the discretized Navier-Stokes equations, i.e. the numerical integrator.

[1] The pressure is a priori a fourth state variable in addition to the three components of the velocity. As it is determined by the velocity field through the incompressibility condition, it does not show up in the equation as an independent variable.

[2] In the following, we imply these conditions in using the term velocity field.

1.3.2. Turbulence, chaotic attractors and chaotic saddles

In systems with a linear instability of the laminar flow the transition to turbulence is rather well understood in terms of dynamical systems theory. Amongst others, Ruelle and Takens (1971) have proposed the use of chaotic attractors to model the onset of turbulence, which has later been verified in several linearly stable systems by following the bifurcations leading from the stable laminar attractor to chaos. The first observation of a route to chaos (Eckmann, 1981) in fluid dynamics was documented by Gollub and Swinney (1975) in experiments of Taylor-Couette flow with the outer cylinder at rest. As the rotation of the inner cylinder increases, a linear instability of the laminar flow leads to the creation of Taylor-vortices, angle-independent vortical structures aligned in the angular direction. They subsequently develop oscillations, visible as transverse waves, first with only one but later with three distinct frequencies, before giving way to a chaotic attractor – a sequence of changes corresponding to the Ruelle-Takens-Newhouse route to chaos (Newhouse et al., 1978). The connection between chaotic attractors and fluid mechanics was irrevocably established in a Rayleigh-Bénard experiment with liquid Helium by Maurer and Libchaber (1979). Time independent straight convection rolls develop as the Rayleigh number is increased, subsequently developing oscillations. They subsequently develop oscillations. The final step before the motion becomes chaotic is the observation of oscillations whose frequency continuously doubles, in very good quantitative agreement with the theory of Feigenbaum (1979) and thus demonstrating the existence of the period-doubling route to chaos.

The situation is however more complicated in linearly stable shear flows, where the laminar profile remains an attractor for all Re. Since at least at moderate Re turbulence is transient in these systems, it is evident that turbulence can not be modeled by a turbulent attractor. But motion that is only transiently chaotic before reaching a simpler attractor is well known in low-dimensional dynamical systems, where the supporting structure in state space is termed chaotic saddle, also known as strange saddle or strange repeller. Early work on using chaotic saddles for describing transient turbulence in shear flows goes back to Brosa (1989).

Strange repellers feature exponential escape rates as shown by Kadanoff and Tang (1984), thus the results on transient lifetimes discussed in section 1.2.4 obtained in linearly stable shear flows are in very good agreement with the hypothesis that chaotic saddles exist in the state space of fluid mechanical systems. Further support comes from the fact that transient chaos involves positive Lyapunov exponents, i.e. sensitive dependence on initial conditions (Faisst and Eckhardt, 2004) and the identification of invariant solutions as discussed in section 1.3.3. While these observations are strong indications of the existence of a chaotic saddle, details of its formation as Re increases have not been studied.

The question of whether the lifetimes diverge at some point (see section 1.2.4) becomes the question if at some point the saddle undergoes some sort of inverse

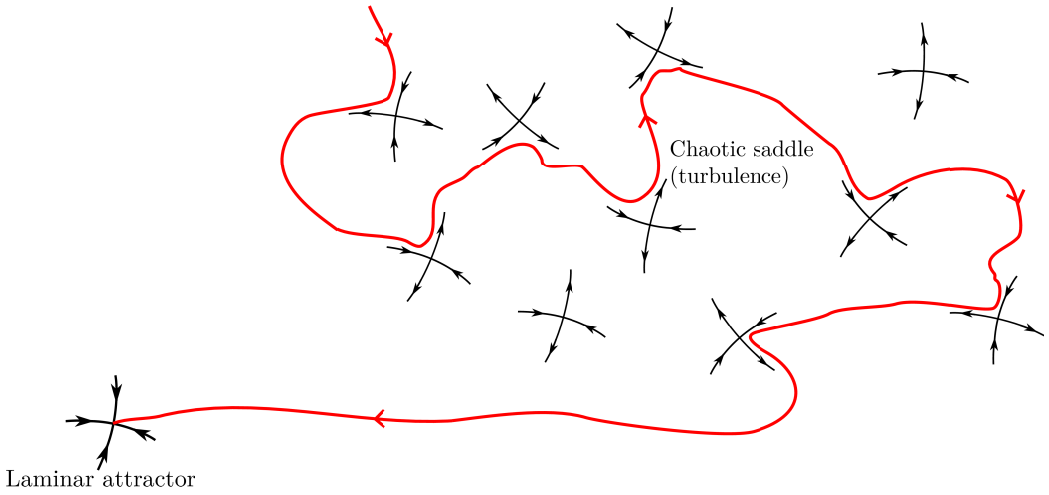

Figure 1.3.1.: A simplified sketch of a transient turbulent trajectory in state space. The trajectory approaches unstable solutions along their stable eigendirections, and lingers in their neighborhood for a while, before being pushed away in the unstable directions. At some point, the trajectory leaves the chaotic saddle and decays to the laminar fixed point.

boundary crisis, in which it becomes an attractor.

1.3.3. The role of invariant solutions

The notion of chaos is invariably connected to the notion of periodic orbits or, more generally, invariant solutions, as already noted in Poincarés seminal work on chaotic motion in the solar system (Poincaré, 1892). A periodic orbit is a state that returns after a finite time. In a chaotic attractor, periodic orbits are dense in the sense that every point on the attractor is approached arbitrarily close by a periodic orbit (Ott, 1993) and, conversely, the existence of a periodic orbit with period three implies chaos (Li and Yorke, 1975). Hopf (1948) formulated the vision that also Navier-Stokes turbulence can finally be expressed in terms of invariant solutions.

In this framework the turbulent region of state space consists of numerous invariant solutions, connected by a web of homoclinic and heteroclinic connections. A chaotic trajectory performs a walk through this forest, where it transiently approaches an invariant solution, stays in its neighborhood for some time before being pushed away in an unstable direction an approaching another solution, as schematically illustrated in figure 1.3.1.

The advancement of the possibilities offered by numerical simulations led to the discovery of exact invariant solutions in fluid mechanical systems, first as infinitely extended ones but later also localized ones. In linearly stable flows, they are usually unstable and their calculation requires robust Newton algorithms and good initial guesses. Nagata (1990) was the first to discover a fixed point in plane Couette flow,

exploiting a homotopy to Taylor-Couette, where the solutions show up as bifurcations of the laminar profile. The state was further analyzed by Clever and Busse (1997) and Waleffe (1998). This NBC state is a fixed point which consists of a pair of streaks, one with lower and one with higher velocity than the laminar flow, accompanied by a pair of counter-rotating vortices, and this composition of the invariant solution by coherent structures has been coined in the terminology *exact coherent structures* (Waleffe, 2001).

Nowadays, numerous solutions of different types are known, all of them with one or more positive eigenvalues, which means that they are unstable and any slight perturbation will lead the time evolution away from them. In spatially periodic plane Couette flow, they include not only fixed points but also traveling waves, which are fixed points in a comoving frame of reference (Viswanath, 2007; Gibson et al., 2008) and (relative) periodic orbits (Cvitanović and Gibson, 2010). Heteroclinic connections between the solutions have been demonstrated (Gibson et al., 2008; Halcrow et al., 2009) and even a homoclinic tangle has been explicitly calculated (van Veen and Kawahara, 2011). In pipe flow fixed points cannot exist, the first traveling waves in small periodic domains were found by Faisst and Eckhardt (2003) and Wedin and Kerswell (2004), followed by the identification of more traveling waves and relative periodic orbits in their neighborhood (Pringle and Kerswell, 2007; Pringle et al., 2009; Duguet et al., 2008; Mellibovsky and Eckhardt, 2011). More relative periodic orbits have recently been discovered by Willis et al. (2013) using symmetry reduction by the method of slices. Close approaches to traveling wave solutions have been observed in experiments by Hof et al. (2004) and simulations by Kerswell and Tutty (2007). See Kawahara et al. (2012) for a recent review of known invariant solutions in many different geometries.

In view of the localized nature of turbulence at transient Re (see section 1.2.5) it is to be expected that localized exact coherent structures exist in extended domains. A glimpse of the periodic solutions was the observation of structures that look similar to traveling waves in less energetic regions of localized puffs in pipe flow (Willis and Kerswell, 2008). Localized invariant solutions have been found in spanwise extended plane Couette flow (Schneider et al., 2010c; Duguet et al., 2009), downstream extended plane Couette flow (Marinc, 2008) and pipe flow (Avila et al., 2013). Most of them have been realized from spatially periodic solutions, either through homoclinic snaking (Schneider et al., 2010b), windowing functions (Gibson and Brand, 2013) or instabilities of periodically continued solutions (Melnikov et al., 2014; Chantry et al., 2013). A doubly localized solution, where both the streamwise and spanwise direction are extended, was found in plane Couette flow by Brand and Gibson (2014) and a doubly localized periodic orbit in channel flow by Zammert and Eckhardt (2014).

This description of chaos (or turbulence) as a walk through a forest of invariant solutions works equally well for a chaotic attractor, where it was first developed, as for a chaotic saddle. In a chaotic attractor, the solutions together with their heteroclinic connections form an attractive invariant set, which is not the case in a chaotic saddle.

Here, the laminar fixed point remains an attractor and a trajectory will eventually leave the part of state space dominated by the invariant solutions, decaying towards the laminar state as illustrated in figure 1.3.1.

The picture envisioned by Hopf (1948) is corroborated by the identification of the great number of invariant solutions, but it is not complete. Single invariant solutions describe several features of near-wall turbulence quite well (van Veen and Kawahara, 2011; Jiménez et al., 2005). There even exists a periodic orbit in plane Couette flow that undergoes all three parts of the self-sustaining process (Kawahara and Kida, 2001). Another solution shows an algebraic decay in amplitude with Re and hence comes infinitely close to the laminar state as Re goes to infinity (Itano et al., 2014). While this agreement between properties of single invariant solutions and turbulence emphasizes the importance of the invariant solutions in transitional flows, it is rather a coincidence and does not allow to make any predictions.

But if enough relevant solutions are known, one can predict all statistical quantities of a chaotic system by calculating weighted sums over the solutions (Cvitanović, 2013). Periodic orbit theory shows that averages over the invariant measure can be obtained as averages over all periodic orbits, of which there is an infinite number in a chaotic system (Ott, 1993). The cycle expansion then shows how these averages can be calculated in a systematic expansion by adding contributions from longer and longer orbits (Gutzwiller, 1971; Cvitanović and Eckhardt, 1991; Eckhardt, 1991; Cvitanović et al., 2012a).

The applicability of the cycle expansion to describe statistical properties of a chaotic system was first shown by Cvitanović and Eckhardt (1989) for the three-disk system, where a symbolic dynamics is introduced by numbering the disks and classifying orbits by the sequence of the disks visited. As a first approach to fluid mechanics the Lorenz system (Lorenz, 1963), a simplified model for the description of atmospheric convection, was described in terms of periodic orbit theory by Eckhardt and Ott (1994), where a symbolic dynamics is based on loops on the left or right branch of the attractor in an appropriate projection. As a further step towards fluid mechanics, the Kuramoto-Sivashinsky system was successfully analyzed (Christiansen et al., 1997; Lan and Cvitanović, 2008; Froehlich and Cvitanović, 2012), a partial differential equation in one spatial dimension that arises in several physical systems far from equilibrium, including the fluid mechanical description of the dynamics of flame fronts (Sivashinsky, 1977). A binary symbolic dynamics was introduced by Christiansen et al. (1997), allowing to label periodic orbits as a sequence of two symbols, and a systematic way to find longer cycles based on shorter ones could be established.

But in a fully three-dimensional fluid mechanical system it has up to now not been possible to find enough periodic orbits or a systematic way to order and calculate them so that a description of Navier-Stokes turbulence, even in a confined geometry, has not been possible in terms of periodic orbit theory.

A different question arises regarding the onset of turbulence, as the first coherent structures are are created at smaller Re than those where turbulent motion can be

observed in simulations or experiments. For example in plane Couette flow, the saddle-node bifurcation creating the NBC solutions can be as low as Re = 127.7 (Waleffe, 2003) where almost all initial conditions decay directly, but turbulence is only observed above Re $\sim$ 300; the situation is similar in pipe flow. What happens in state space in the Re range between the creation of the first coherent structures and the onset of turbulence, remains an open question, as for example stated by Eckhardt (2008).

1.3.4. The edge of chaos

Since turbulence in shear flows occurs while the laminar profile is linearly stable, two regions coexist in state space: the laminar region where initial conditions directly decay and the turbulent region, formed by the invariant solutions and their connections. To which of the two regions an initial condition belongs is not only defined by the amplitude of the perturbation but also by its shape. This can be seen in the pipe flow experiments of Darbyshire and Mullin (1995), where in a Re-amplitude plane no clear border separating transition from decay can be identified, see figure 1.3.2(a), and experiments by Tasaka et al. (2010). A better control of the initial perturbation is possible in numerical simulations, where the stability border was found to be fractal in plane Couette flow (Schmiegel and Eckhardt, 1997), see also figure 1.3.2(b).

Skufca et al. (2006) studied in detail the boundary in a 9D model (Schmiegel, 1999) and came up with two interesting findings: first, the boundary is indeed a (hyper-) surface in state space and second, it is the stable manifold of an invariant object; they termed the boundary *edge of chaos* and the attracting invariant object inside it *edge state*. The edge state is, in the model, a periodic orbit with a single unstable eigenvalue, its unstable direction points perpendicular to the edge, towards laminar or turbulent flow, all stable eigendirections lie within the edge of chaos, which itself is an invariant set of codimension one. The situation is illustrated in figure 1.3.3.

A numerical method to find the edge state is based on repeated bisection and has first been used in channel flow by Itano and Toh (2001). With the help of this edge tracking algorithm many systems have been investigated; the edge state can be a fixed point like in spatially periodic plane Couette flow where it is the NBC state (Schneider et al., 2008), a travelling wave in spanwise extended plane Couette (Duguet et al., 2009; Schneider et al., 2010c) and axisymmetric pipe flow (Schneider and Eckhardt, 2009) or it can be more complex and even chaotic like in full pipe flow (Schneider et al., 2007b; Mellibovsky et al., 2009). While edge tracking requires rescaling of initial conditions, which is only possible in numerical studies, de Lozar et al. (2012) observed close approaches to the edge state during turbulence decay in pipe flow experiments. They used the measured velocity field as an initital guess in a Newton search, which then converged to the edge state, thus corroborating that they had indeed observed close approaches to the edge state.

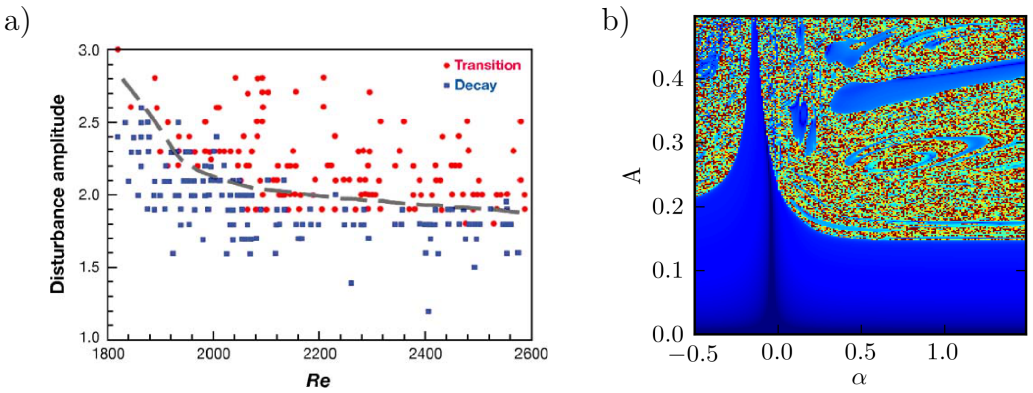

Figure 1.3.2.: Dependence on initial conditions (a) (From Darbyshire and Mullin, 1995), reproduced after Eckhardt et al. (2007). In experiments in pipe flow, no clear boundary between initial conditions that give rise to a transition to turbulence or decay can be found. (b) (From Kreilos et al., 2014a). A two-dimensional section through state-space, where A is the perturbation amplitude and α a vector of initial conditions in state space. Color-coding indicates the time it takes an initial condition to reach the laminar state, blue corresponding to fast decay and red to no decay within the time of the simulation. There exist regions of rapidly varying lifetimes, corresponding to the turbulent saddle, and blue bubbles and islands, with no clear dependence on amplitude.

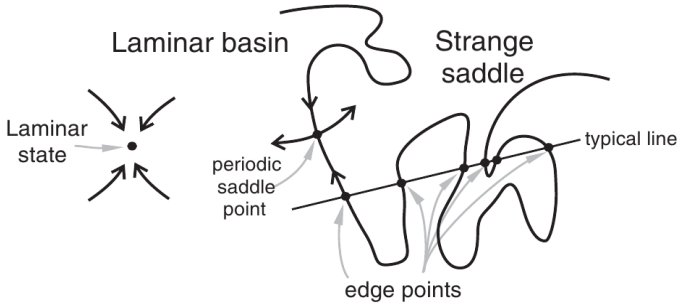

Figure 1.3.3.: (From Skufca et al., 2006) A sketch of the edge of chaos and the edge state in state space. The edge state, labeled periodic saddle point, has a single unstable direction, in which trajectories either escape to the laminar state or to turbulence. Its stable manifold, the edge of chaos, separates the laminar basin from the strange saddle associated with turbulence. It is a highly convoluted, fractal surface and a typical line in state space will cut it numerous times.

The edge state is usually created as the lower branch solution of a saddle-node bifurcation (Nagata, 1990; Clever and Busse, 1997). The findings from Skufca et al. (2006) have thus been validated in the high-dimensional fluid mechanical systems: the laminar-turbulent boundary is the stable manifold of an invariant object. The edge state has a single unstable direction, its stable manifold is of codimension one, i.e. it is able to separate state space into two regions, with all initial conditions that decay on one side of the edge and all that become turbulent on the other side, as depicted in figure 1.3.3. This simple picture however precludes transient turbulence as the time evolution of an initial condition may never cross a manifold of codimension one (Guckenheimer and Holmes, 1983).

Edge states in minimal flow units are typically built of streamwise streaks and vortices, hence featuring the predominant structures of near wall turbulence. Their ability to extract energy from the shear gradient is so strong that they do not decay, but not strong enough to trigger a transition, making them intrinsically relevant to the transition process. Indeed, many edge states are similar to linear optimal perturbations which show maximum amplification through transient growth (Levin et al., 2005), although non-linear optimals have a much lower amplitude; the transition to turbulence from non-linear optimals passes by the edge state (Duguet et al., 2013) if the perturbation energy is extremely close to the minimum; with slightly higher amplitudes different routes lead to faster transition. The stable manifold of the edge state organizes turbulence and the edge state is transiently approached by turbulent trajectories, so that the knowledge of the edge state permits elaborated control strategies for forced relaminarization, at least in numerical simulations (Kawahara, 2005).

1.4. Boundary layers

1.4.1. Turbulence transition in boundary layers

Boundary layers develop when a solid object is moving through a fluid and both accelerating or delaying the transition to turbulence in boundary layers is of interest in numerous technological applications.

The prototypical example of a boundary layer flow is the Blasius boundary layer (BBL), the flow of fluid over a flat plat. As scaling arguments show, the thickness of the boundary layer δ grows with increasing distance from the leading edge x as $\delta \sim \sqrt{\nu x/U_\infty}$, where U_∞ is the free-stream velocity and ν the fluids viscosity. To obtain a laminar solution for the flow over a flat plate, Prandtl's boundary layer approximation to the Navier-Stokes equations were solved by Blasius (1907). The solution is self similar in the dimensionless coordinate $\eta = y\sqrt{\frac{U_\infty}{\nu x}}$, where y is the distance to the wall. The height above the wall where the fluids velocity reaches 99% of the free-stream velocity is $\delta_{99} \approx 5.0\sqrt{\nu x/U_\infty}$ and the displacement thickness is

(Schlichting, 2004)

$$\delta^* = \int_{y=0}^{\infty} \left(1 - \frac{u}{U_\infty}\right) \mathrm{d}y \approx 1.72\sqrt{\frac{\nu x}{U_\infty}}. \tag{1.4.1}$$

The Reynolds number is usually based on either the distance to the leading edge or the displacement thickness and accordingly not constant throughout the boundary layer but increases with distance to the leading edge. In the following, we adopt the definition based on the displacement thickness,

$$\mathrm{Re}_\delta = \frac{U_\infty \delta^*}{\nu}. \tag{1.4.2}$$

The laminar profile of the BBL is linearly unstable above a critical Reynolds number of $\mathrm{Re}_\delta = 520$, where Tollmien-Schlichting waves appear (Schlichting, 2004). These waves are initially parallel to the spanwise direction and grow slowly but exponentially, finally developing spanwise modulations and leading to turbulence. In the presence of disturbances, e.g. noise in the free-stream or roughness on the plate, this classical route to turbulence can by bypassed as finite-amplitude perturbations develop and trigger a faster transition to turbulence, in analogy to the subcritical transition in internal shear flows. Figure 1.4.1 shows a snapshot of boundary layer transition under the effect of free-stream turbulence. The flow is from left to right and the free-stream turbulence is clearly visible near the inflow, quickly decaying further downstream. As disturbances from the free-stream penetrate into the boundary layer, they give rise to perturbations in the form of elongated downstream streaks, which grow in amplitude as they are advected downstream and finally break down into localized turbulent spots. The occurrence of these localized turbulent spots is a common phenomenon in studies of boundary layer transition, irrespective of the origin of the perturbations. As they travel downstream, the spots spread and merge with neighboring spots, so that turbulence eventually extends over the whole width of the domain (Emmons, 1951; Narasimha, 1957).

As a consequence of the localized nature of transitional turbulence, an intermittency factor defined as the fraction of space that is turbulent, rises from zero to one as a function of downstream position. Dhawan and Narasimha (1957) showed that the curves become universal when rescaled with the width of the transition region. Assuming that all spots get created at the exact same downstream position, termed concentrated breakdown hypothesis, he was able to derive a simple formula which reproduced the intermittency curves qualitatively.

Measurements of transitional boundary layers subject to various levels of free-stream turbulence show that the energy of the streaks, measured by u_{rms}^2, is during the earlier stages given by

$$u_{rms}^2 \propto x\ \mathrm{Tu}^2, \tag{1.4.3}$$

where Tu is the free-stream turbulence intensity and x the distance from the leading edge (Alfredsson and Matsubara, 2000; Brandt et al., 2004; Fransson et al., 2005).

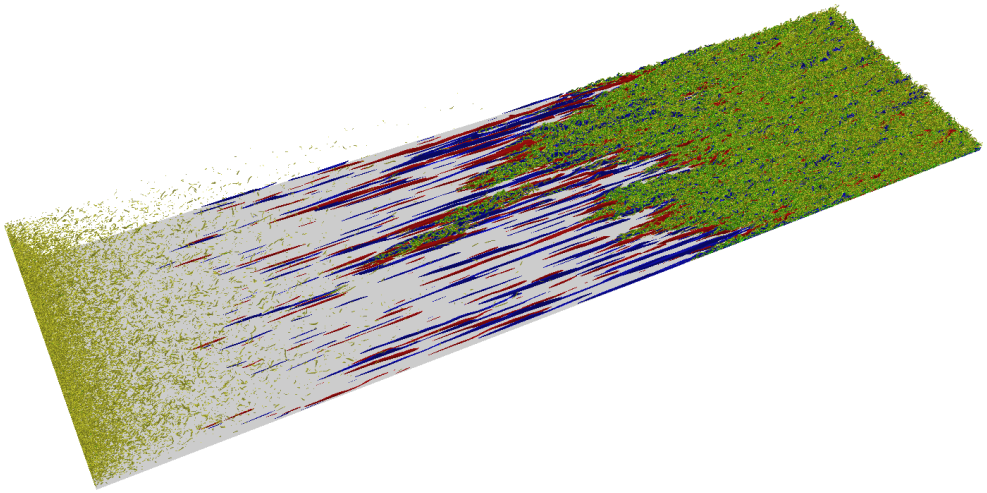

Figure 1.4.1.: A numerical simulation of transition in the Blasius boundary layer subject to free-stream turbulence. The flow goes from left to right, the color-coding green indicates vortices by isocontours of λ_2, red and blue are high- and low-speed streaks, respectively, by isocontours of positive and negative velocity. Near the inflow, the free-stream turbulence can be seen, which decays further downstream. Near the wall, a background of alternating streaks develops, which later shows transition to turbulence by creating localized patches that spread before filling the whole domain.

This relation was proposed by Andersson et al. (1999) based on transient growth theory under the assumption that the energy of the disturbances in the boundary layer is proportional to the free-stream turbulence (FST) energy.

The transition Reynolds number is by the intermittency being exactly one half, $\gamma(\mathrm{Re}_{x,tr}) = 0.5$. It is widely observed (e.g. Brandt et al., 2004; Fransson et al., 2005) that $\mathrm{Re}_{x,tr}$ scales with FST intensity as

$$\mathrm{Re}_{\delta,tr} = C\ \mathrm{Tu}^{-1}. \tag{1.4.4}$$

1.4.2. The asymptotic suction boundary layer

The spatial growth of the flat-plate boundary layer requires large simulations and prohibits access to the asymptotic dynamics at a fixed Re. As a numerically more convenient case in this work also the asymptotic suction boundary layer (ASBL) is studied, a flow that develops if fluid is streaming over a flat plate through which homogeneous suction is applied (Schlichting, 2004). The ASBL combines several desirable aspects which make it a good candidate to study turbulence transition in boundary layers: it is translationally invariant, which makes it easily usable in existing numerical codes using Fourier-decomposition, and on the other hand it is a true boundary layer flow that has also been realized experimentally (Fransson, 2001;

Fransson and Alfredsson, 2003). With the suction velocity V_S, the laminar velocity profile is

$$(U_\infty(1 - \mathrm{e}^{-y/\delta}), -V_S, 0), \tag{1.4.5}$$

where $\delta = \nu/V_S$ is the laminar displacement thickness. Based on δ as a length scale the Reynolds number is defined as

$$\mathrm{Re} = \frac{U_\infty \delta}{\nu} = \frac{U_\infty}{V_S}. \tag{1.4.6}$$

Turbulent motion in the ASBL can be sustained at Re on the order of 270 (Khapko, 2014), while it is linearly stable up to Re = 54370 (Hocking, 1975). This delay of the linear instability by two orders of magnitude compared to the Blasius boundary layer makes suction a promising approach in laminar flow control (see e.g. Joslin, 1998).

1.4.3. Extension of concepts from internal shear flows

All concepts discussed in section 1.3 considered internal flows and it is an open question to which extent they are applicable to external flows. In their review article Saric et al. (2002) stated "It is well known that the stability, transition, and turbulent characteristics of bounded shear layers are fundamentally different from those of free shear layers (Morkovin, 1969; Reshotko, 1976; Bayly et al., 1988). Likewise, open systems are fundamentally different from closed systems. The distinctions are trenchant and thus form separate areas of study."

But from the perspective of dynamical systems, there are some indications that it is not that hopeless to make analogies. Boundary layers show turbulent motion while being linearly stable, so the existence of a separating boundary is assured and Duguet et al. (2012) and Cherubini et al. (2011) have calculated a critical trajectory on this boundary in the Blasius boundary layer. Furthermore, turbulence in bypass transition arises in localized patches, which spatially spread before filling the whole domain, in analogy to puffs and slugs in pipe flow. The notion of invariant solutions is however not that easily transferred due to the spatial growth and the associated advection of the structures to higher Re.

The ASBL is a parallel boundary layer and the conceptual analogy to internal flows is more evident. Subcritical transition to turbulence is observed while the laminar profile is linearly stable, suggesting the existence of a separating boundary in state space. Furthermore, invariant solutions can arise in the form of relative fixed points, i.e. traveling waves, and (relative) periodic orbits. The invariant states will probably differ in shape and dynamics from the solutions that form the backbone of turbulence in internal flows, but the conceptual view of turbulence as a walk through a forest of invariant solutions remains intact.

2. Methods and tools

2.1. Numerical simulations

Most parts of this work contain direct numerical simulations of parallel shear flows, namely plane Couette flow and the ASBL. Plane Couette flow is the flow between two infinitely extended parallel plates, where no-slip boundary conditions are enforced at the plates, i.e. the fluid at the plates moves exactly with the velocity of the plates and the wall-normal velocity must vanish. For simulations of the ASBL, no-slip boundary conditions combined with homogeneous suction are employed at the wall, resulting in the condition $(u, v, w)_{y=0} = (0, -V_S, 0)$. The free-stream velocity is enforced at a height h above the wall by setting boundary conditions $(u, v, w)_{y=h} = (U_\infty, -V_S, 0)$, where the blowing boundary condition in the wall-normal direction ensures continuity. In all simulations we ensure that h is large enough to not influence the flow. In the wall-parallel directions we employ periodic boundary conditions in both flow cases and we use Cartesian coordinates, denoting the downstream direction as x, the wall-normal direction as y and the spanwise direction as z.

Most numerical simulations of shear flows in this work are done with the DNS (direct numerical simulations) code channelflow (Gibson, 2012), which is written in `C++` and available as open source software at channelflow.org. The code uses a spectral expansion of velocity fields in space, with Fourier modes in the periodic directions and Chebyshev polynomials in the wall-normal one. For time integration several algorithms are available, we mostly used a semi-implicit backwards-differentiation method of order three. Some of results were cross-validated by comparing to the SIMSON-code from KTH (Chevalier et al., 2007), which was also used in the final runs for the data presented in Khapko et al. (2013), section 5.4 and for the LES simulations of spatially developing boundary layers in Kreilos et al. (2014b), section 5.6.

Part of the channelflow library is a powerful Newton-Krylov algorithm, implemented by John F. Gibson based on Viswanath (2007), with which fixed points, traveling waves, periodic orbits and relative periodic orbits can be efficiently calculated. The package contains further tools that are useful in the context of dynamical systems theory, like calculation of eigenvalues and Floquet multipliers with Arnoldi iterations and pseudo-arclength continuation of solutions in parameter space. All fixed points, eigenvalues and paramter continuations that are presented in the following are based on these tools from the channelflow library.

We have parallelized the timestepping algorithm of channelflow with MPI, details thereof are given in appendix A. The parallel code has been successfully used for calculations in Khapko et al. (2013), Kreilos et al. (2014c) and Tuckerman et al. (2014) and we have shown it to scale almost linearly up to 768 processors, the largest number of processors available to us at the cluster at the MPI-DS in Göttingen we used for the benchmark.

2.2. Discrete and continuous symmetries

2.2.1. Symmetries of parallel shear flows

Symmetries, or more precisely invariance under symmetries, play an important role in studying fluid mechanics and in particular in simulations of flows in periodic domains.

When talking about invariance under symmetries, we need to discern two fundamentally different notions: invariance of the system, i.e. of the equations of motion together with the boundary conditions, and invariance of particluar solutions. The system is said to be invariant under a given symmetry[1] σ if the condition

$$\mathbf{f}(\sigma(\mathbf{u})) = \sigma(\mathbf{f}(\mathbf{u})) \tag{2.2.1}$$

is fulfilled, where $\mathbf{f}(\mathbf{u})$ denotes the time evolution of the velocity field $\mathbf{u}$. On the other hand, a velocity field is invariant under a given symmetry σ if it is unchanged under the action of the symmetry operator,

$$\sigma\mathbf{u} = \mathbf{u}. \tag{2.2.2}$$

For example, in plane Couette flow and the ASBL, the equations of motion and boundary conditions are invariant under a reflection in the spanwise direction followed by a translation in the downstream direction of half a box width, called shift-and-reflect symmetry s_1. A generic turbulent velocity field is however different when this operation is applied, i.e.

$$s_1[u, v, w](x, y, z) = [u, v, -w](x + L_x/2, y, -z) \neq [u, v, w](x, y, z), \tag{2.2.3}$$

while for example the NBC-states are invariant under this transformation.

If a given velocity field is invariant under a symmetry, its time evolution will also be invariant

$$\sigma\mathbf{u} = \mathbf{u} \Rightarrow f(\mathbf{u}) = f(\sigma\mathbf{u}) = \sigma f(\mathbf{u}) \tag{2.2.4}$$

and the symmetry operator σ defines a symmetry invariant subspace; the time evolution of a velocity field will never leave this subspace.

[1] In the notation of the symmetry operations we follow Gibson et al. (2008).

Both plane Couette flow and the ASBL are invariant under arbitrary translations along the periodic directions,

$$\tau(l_x, l_z)[u, v, w](x, y, z) = [u, v, w](x + l_x, y, z + l_z) \tag{2.2.5}$$

and reflections in the spanwise direction,

$$\sigma_1[u, v, w](x, y, z) = [u, v, -w](x, y, -z). \tag{2.2.6}$$

In addition, plane Couette flow is invariant under reflection in the downstream direction combined with reflection in the wall-normal direction,

$$\sigma_2[u, v, w](x, y, z) = [-u, -v, w](-x, -y, z), \tag{2.2.7}$$

which is not the case for the ASBL. These operators form a group and can be combined to obtain all symmetries of the system.

In our work, a couple of discrete symmetries appear several times, starting with the shift-and-reflect symmetry introduced above in equation (2.2.3), which is for example satisfied by the NBC states. These states are furthermore invariant under the shift-rotate symmetry

$$s_2[u, v, w](x, y, z) = [-u, -v, w](-x + L_x/2, -y, z + L_z/2), \tag{2.2.8}$$

and the combination $s_3 = s_1 s_2$

$$s_3[u, v, w](x, y, z) = [-u, -v, -w](-x, -y, -z + L_z/2). \tag{2.2.9}$$

Restriction of the dynamics to symmetry invariant subspaces can greatly simplify the analysis in many cases, since e.g. enforcing the symmetry s_1 fixes the spanwise phase of velocity fields up to a discrete translation of $L_z/2$. One precludes, however, motion outside that symmetry subspace, which might heavily alter the results depending on the question of interest. For example, restriction to the s_1-symmetry subspace in plane Couette delays the onset of the superexponential increase of lifetimes to Re $\gtrsim 300$.

2.2.2. The method of comoving frames

If one does not want to fix the phase of the fields by imposing discrete symmetries, translations in the directions of continuous symmetries are possible and the question arises how to deal with them (Cvitanović et al., 2012a). In Kreilos et al. (2014c) we develop a way to separate the purely advective action of the Navier-Stokes equations from the dynamically relevant part. Writing $\mathbf{f} = \mathbf{f}_\parallel + \mathbf{f}_\perp$, where $\mathbf{f}_\parallel$ denotes advection parallel to the symmetry, e.g. the x direction, and noting that translations in the x direction are generated by $\partial_x \mathbf{u}$, we project

$$\mathbf{f}_\parallel = \frac{\langle f(\mathbf{u}) | \partial_x \mathbf{u} \rangle}{\|\partial_x \mathbf{u}\|^2} \partial_x \mathbf{u}, \tag{2.2.10}$$

where $\langle\cdot|\cdot\rangle$ denotes an appropriately chosen scalar product in state space and $\|\cdot\|$ the norm defined by that scalar product. In an infinitesimal time interval δt, the velocity field will hence be advected by

$$\delta x = \frac{\langle \mathbf{f} | \partial_x \mathbf{u} \rangle}{\|\partial_x \mathbf{u}\|^2} \delta t \equiv c_x \delta t, \tag{2.2.11}$$

where

$$c_x = \frac{\langle \mathbf{f} | \partial_x \mathbf{u} \rangle}{\|\partial_x \mathbf{u}\|^2} \tag{2.2.12}$$

defines the instantaneous advection speed. By choosing a frame of reference that moves with this speed c_x compared to the laboratory frame of reference, the advective action of the time evolution is removed and only the dynamically active part is kept. This method is introduced as *method of comoving frames* in Kreilos et al. (2014c), since it is a generalization of the frame of reference that is moving with a traveling wave to arbitrary velocity fields.

3. Summary of the results

3.1. The onset of turbulence in plane Couette flow

Our studies in plane Couette flow, published in Kreilos and Eckhardt (2012) and Kreilos et al. (2014a), cover the gap between the appearance of the first coherent structures and the onset of sustained turbulence. We follow the bifurcations leading from the NBC state to the creation of the chaotic saddle that supports turbulence and its growing complexity in plane Couette flow.

3.1.1. A chaotic attractor

In the numerical domain studied, with a size of $L_x \times L_y \times L_z = 2\pi \times 2 \times \pi$ and an imposed shift-and-reflect symmetry,[1] the NBC solutions are created in a saddle-node bifurcation at Re = 163.8, differing from Nagata (1990) and the lowest possible one at Re = 127.7 (Waleffe, 2003) due to the different domain size. As also noted by Clever and Busse (1997) in their computational domain, the upper branch state is linearly stable. As Re increases it undergoes a Hopf bifurcation, creating a stable periodic orbit which then undergoes a period doubling bifurcation. In contrast to the previous studies, in our domain this period doubling bifurcation is the first step in a period doubling cascade in which a chaotic attractor is created. The cascade is illustrated in the bifurcation diagram in figure 3.1.1, where the attractor is visualized by plotting the maxima of the cross flow energy E_{cf} along a trajectory. In state space, the stable manifold of the lower-branch NBC state is the separatrix between the basin of attraction of the laminar state and the one of the chaotic attractor.

The motion on the chaotic attractor is rather gentle as regards the velocity fields, consisting merely of wiggles of the two streamwise streaks and vortices that never break up. Nevertheless, the dynamics is chaotic in the sense that it is unpredictable where the next wiggle will be.

3.1.2. Periodic orbits

The identification of the period doubling cascade relates the flow to low-dimensional dynamical systems and even unimodal maps. In pursuing the analysis, we use the

[1] While only the shift-and-reflect symmetry s_1 is imposed, all states are attracted towards a symmetry subspace satisfying the additional symmetries s_2 and s_3.

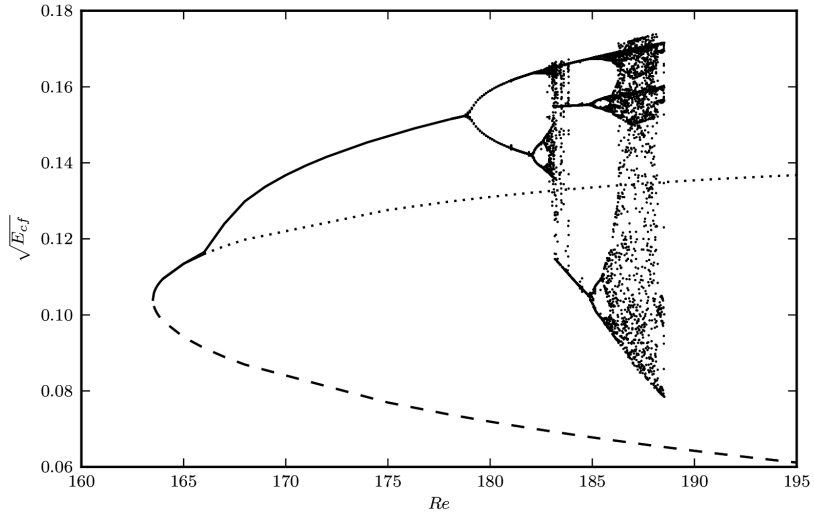

Figure 3.1.1.: The bifurcation diagram of the NBC states in plane Couette flow in a domain of size $L_x \times h \times L_z = 2\pi \times 2 \times \pi$, taken from Kreilos and Eckhardt (2012). The NBC states are fixed points that are created in a saddle-node bifurcation at Re = 163.8. The square root of the cross-flow energy E_{cf} of the lower branch, which has one unstable direction, is plotted as a dashed line, the upper branch is solid as long as it is stable and dotted afterwards. At Re = 166.05 the upper branch undergoes a Hopf-bifurcation in which a periodic orbit is created; from now on the attractor is visualized by plotting every maximum of the cross-flow energy along a long trajectory. The periodic orbit undergoes a classical period doubling cascade, eventually leading to a chaotic attractor. At Re = 188.51 the attractor is destroyed in a crisis bifurcation, explaining its sudden disappearing in the diagram.

bifurcation diagram (figure 3.1.1) to introduce a binary symbolic dynamics on the attractor in the following way: for a fixed Re, the ith maximum of E_{cf} on a trajectory is labeled x_i and we visualize the attractor by plotting x_{i+1} vs x_i, shown in figure 3.1.2. In this representation the attractor is very thin and, albeit having several branches, this looks quite similar to the attractors known from unimodal maps and in particular the Hénon map. Assigning a binary symbolic dynamics in the standard way, with 0 for every point left of the maximum and 1 for every point right of it, we can organize the family of periodic orbits. We find 6 periodic orbits with a length shorter than 6. Every one of them has only a single unstable eigenvalue (see table 5.1.1, Kreilos and Eckhardt (2012)) and we conclude that the dynamics on the attractor in the high-dimensional state space is basically one dimensional.

In the symbolic dynamics, the orbits with consecutive sequences of 0s are pruned, i.e. they do not exist, similar to phenomenology in the logistic map $x_{i+1} = \lambda x_i(1-x_i)$ for values of $\lambda < 4$. The equation for the logistic map describes a full parabola, but for $\lambda < 4$ the attractor only traces out parts thereof, with a notable left-right

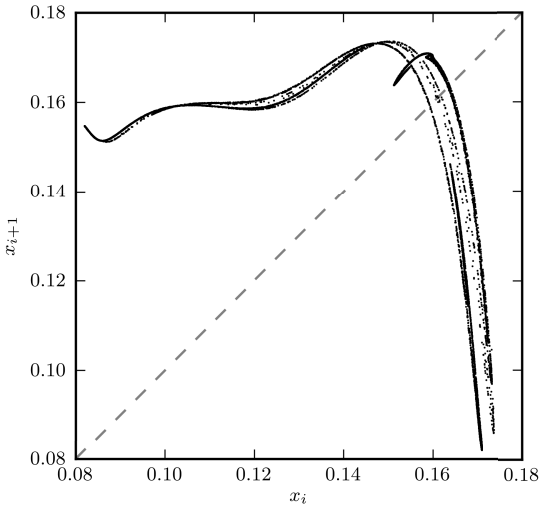

Figure 3.1.2.: Visualization of the chaotic attractor at Re = 187.8, from Kreilos and Eckhardt (2012). As in figure 3.1.1 we use maxima of E_{cf} to visualize the attractor, plotting the i-th maximum versus the (i+1)-th. In this representation, the attractor is very thin, albeit having multiple branches, very similar to e.g. the Hénon map. Identifying the applicable branch, we assign a binary value of 0 (1) to every point left (right) of the maximum and with that introduce a symbolic dynamics on the attractor. In this symbolic dynamics, we are able to classify periodic orbits, analogous to unimodal maps.

asymmetry: the right leg of the parabola extends to lower values of x_{i+1} than the left one. As λ approaches 4, the left leg extends further and further down until at $\lambda = 4$ it touches the unstable fixed point at $x = 0$. Comparing this behavior to the visualization of the attractor in plane Couette flow in figure 3.1.2, we also see that the right leg of it extends considerably further down than the left one, indicating why so many orbits are pruned.

3.1.3. A crisis bifurcation

The bifurcation cascade in the plane Couette system does not continue to the creation of all periodic orbits as the attractor is destroyed at Re = 188.51. At this Re, the chaotic attractor touches its own boundary and a crisis bifurcation occurs (Grebogi et al., 1983). In this bifurcation, discussed very descriptively for a model in Vollmer et al. (2009), the chaotic attractor is transformed into a chaotic saddle, it becomes "leaky" in the sense that trajectories are chaotic for a certain time but may suddenly escape and decay to the laminar state. At this crisis, the attractor and its boundary are identical, making the boundary inherently fractal and rendering the notion of

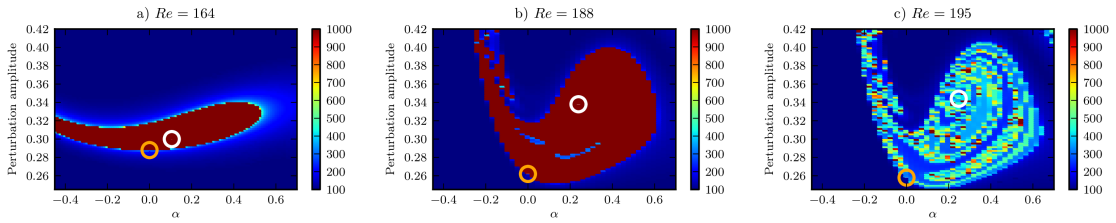

Figure 3.1.3.: Visualization of the boundary crisis in a two-dimensional projection of state space, from Kreilos and Eckhardt (2012). The color coding shows the lifetime of initial conditions, i.e. the time it takes for an initial condition to come into a neighborhood of the laminar state. On the x-axis a state space vector interpolates between the lower- and upper-branch NBC states and the initial condition is rescaled in amplitude along the y-axis. The x-axis has been rescaled such that the geometrical distance between the lower- (orange circle) and upper-branch (white circle) NBC states is proportional to their distance in state space. (a) At Re = 164, just after the creation of the fixed points, the upper-branch is an attractor, its basin of attraction is visible as the red bubble-shaped region of initial conditions that never decay. The stable manifold of the lower-branch is the separatrix of the two basins of attraction. (b) Just before the boundary crisis, at Re = 188, the attractor is chaotic and its basin of attraction has grown. (c) After the boundary crisis, at Re = 195, almost all initial conditions decay. The chaotic saddle is visible as the colorful region of sensitive dependence of the lifetime on initial condition.

"inside" and "outside" meaningless. The effect of the crisis is visualized in a two-dimensional projection of state space in figure 3.1.3.

Since by construction the boundary of the chaotic attractor is the stable manifold of the lower branch, i.e. the edge of chaos, this also explains why transition from turbulence to laminar is possible despite the edge being locally of codimension one. This explanation is in agreement with results from Lebovitz (2009, 2012), investigating scenarios of transient turbulence in low dimensional models.

3.1.4. Non-monotonic variation of turbulent lifetimes with Re

Before the crisis bifurcation, initial conditions from the basin of attraction of the chaotic attractor will never decay to the laminar state and the turbulent lifetime τ is infinite. After the crisis, τ becomes the escape time from the chaotic saddle and drops quickly with increasing Re, the expected behavior from low-dimensional systems (Grebogi et al., 1983). However, it does not drop to zero but increases again not too far beyond the crisis point; the variation of τ with Re is non-monotonic and shows strong peaks at various Re, as shown in figure 3.1.4.

Each of the peaks corresponds to a Re range where a stable attractor exists and where the lifetimes formally diverge, which is not always visible in figure 3.1.4 due to the small fraction of the sampled initial conditions that converge to the attractor

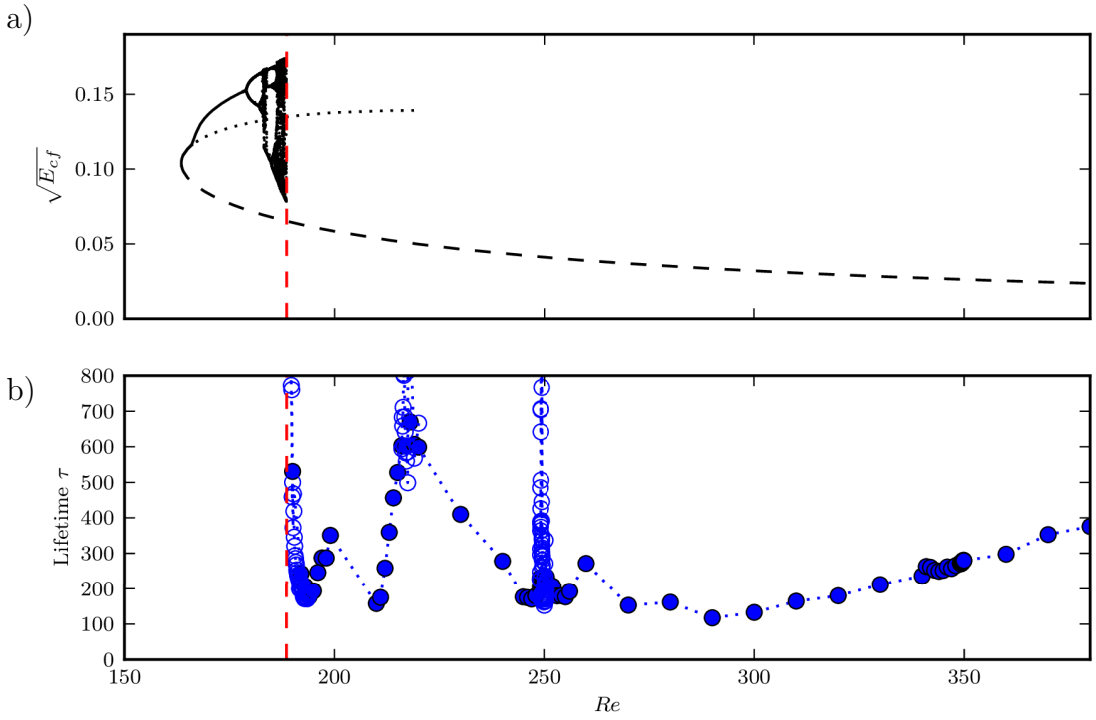

Figure 3.1.4.: (a) The bifurcation diagram of the NBC states. The stability properties of the lower branch do not change. The crisis bifurcation at Re = 188.51 is visible as the sudden disappearance of the chaotic attractor. The upper branch survives, albeit unstable, and is part of the chaotic saddle. (b) The variation of τ as a function of Re. Beyond the crisis bifurcation, marked by the red dashed line, lifetimes drop quickly from infinity. They do, however, not reach zero. Instead, a non-monotonic variation with strong peaks is visible. At each of the peaks, the lifetimes actually diverge, as stable "chaotic bubbles" are formed within the turbulent saddle, see section 3.1.5. Closed and open symbols indicate Re where τ is determined from 50,000 and 5,000 initial conditions, respectively.

and the range in Re being very short. Such an event is detailed in the following section 3.1.5.

For Re $\gtrsim$ 300 the lifetimes start to increase more monotonically – this is the onset of the super-exponential increase observed at higher Re, in our system delayed due to the small domain size and the imposed shift-and-reflect symmetry.

3.1.5. The growing complexity of the chaotic saddle

We investigate one of the peaks seen in the lower panel of figure 3.1.4 in greater detail. At Re = 249.01 a pair of periodic orbits is created in a saddle node bifurcation, of which the upper branch is stable. It undergoes a bifurcation cascade, in which a

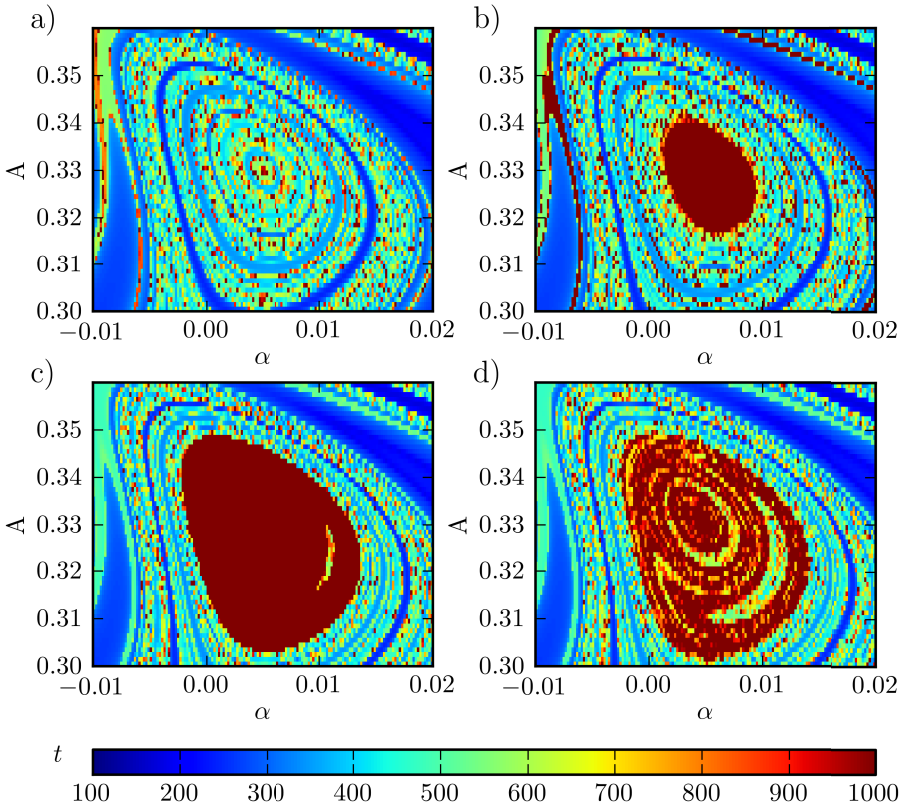

Figure 3.1.5.: The creation and destruction of the embedded attractor in a two-dimensional visualization of state space, from Kreilos et al. (2014a), corresponding to the peak around Re = 250 in figure 3.1.4. Visualized are lifetimes of initial conditions in an appropriately chosen section. (a) At Re = 248.5, we only see the turbulent saddle with its characteristic sensitive dependence of τ on the initial condition. At Re = 249.01 two periodic orbits are created in a saddle-node bifurcation, of which the upper branch one is stable. It's basin of attraction is visible at Re = 249.1 (b) as a region of infinite lifetimes, separated from the surrounding saddle by the stable manifold of the lower branch periodic orbit. As Re increases, the upper branch undergoes a bifurcation cascade leading to a chaotic attractor (c, Re = 250.1). At Re = 250.13 a boundary crisis occurs as the chaotic attractor touches its boundary, the stable manifold of the lower branch, leaving behind a chaotic saddle embedded in the outer one. Slightly beyond the crisis, the remnant of the former attractor is still visible as a region of higher lifetimes (d, Re = 250.25).

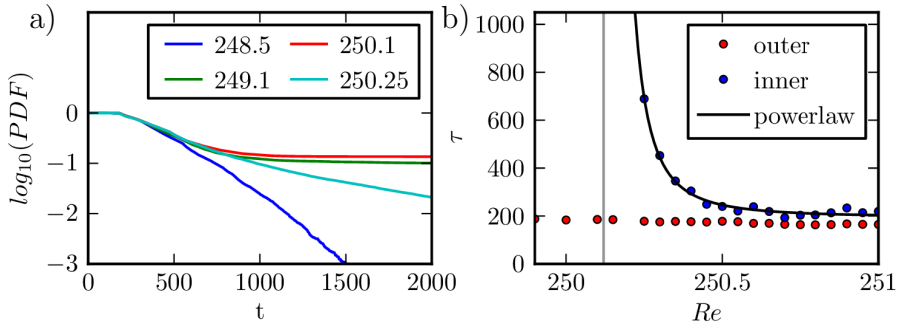

Figure 3.1.6.: Lifetime distributions during creation and destruction of the "turbulent bubble", from Kreilos et al. (2014a). (a) Before the creation of the attractor, the lifetimes are distributed exponentially. While the attractor exists, initial conditions from its basin of attraction never decay, leading to diverging lifetimes (red and green line). After the boundary crisis of the embedded attractor (light blue line), the distribution of lifetimes is a superposition of two exponentials. (b) Characteristic lifetimes measured separately for initial conditions from the inner and outer saddle. The lifetimes of the outer saddle remain almost constant, while the lifetimes from the inner saddle drop from infinity and settle slightly *above* the values of the outer one, leading to an increase.

chaotic attractor is created; a stable "turbulent bubble" is formed inside the turbulent saddle. The lower branch has a single unstable direction for the whole range of Re considered so that its stable manifold forms the separatrix between the newly formed chaotic attractor and the surrounding turbulent saddle. At Re = 150.13 the chaotic attractor touches the lower branch and a boundary crisis occurs in which the chaotic attractor is replaced by a chaotic saddle and becomes part of the turbulence supporting saddle. Figure 3.1.5 shows a visualization of the sequence of events in state space.

During the process, the lifetimes diverge and their distribution is non-exponential, as the distributions from the inner and outer saddle overlap, figure 3.1.6(a). Calculating lifetimes independently for initial conditions from the inner and outer saddle, figure 3.1.6(b), we see that the escape rate of the outer saddle remains almost constant, while the lifetimes of the inner saddle drop after the boundary crisis, settling slightly *above* the value of the outer saddle. The entanglement of the inner saddle with the outer one hence gives rise to an increase of τ.

We have observed this sequence of events – formation of a stable invariant solution, a bifurcation cascade leading to a chaotic attractor and its subsequent destruction in a boundary crisis – for several of the peaks in figure 3.1.4, suggesting it to be a generic route to increasing the complexity of the chaotic saddle and with it the lifetimes. The gap in Re between several events can be extremely small, with the events even overlapping each other. Our method of detection relies on the attractor being stable.

The same bifurcation scenario can also take place in an unstable subspace, making it more generic but harder to detect. In figure 3.1.4 no strong peaks, indicating a divergence of τ, are visible anymore for Re $\gtrsim 300$ – it remains unclear whether this is due to either the sampling distance in Re being too coarse, or the events happening in unstable subspaces, or the mechanism of increasing τ changing completely.

3.2. The state space of the asymptotic suction boundary layer

In this section, we investigate whether the concepts developed for internal shear flows as described in section 1.3 are applicable to an external flow, namely the asymptotic suction boundary layer (ASBL). The ASBL is not only similar to internal shear flows in that turbulence occurs while the laminar flow profile is linearly stable but also in that turbulence at moderate Re is transient, see e.g. figure B.1 in Madré (2011) and the recent work of Khapko (2014). Inspired by the success in internal shear flows, we investigate the edge of chaos in the ASBL and study the relative attractor in it, the edge state. The relevant publications are Kreilos et al. (2013) and Khapko et al. (2013), where the edge state is studied in small periodic domains in spanwise extended ones, as well as the first part of Kreilos et al. (2014c), where the downstream advection of the edge state is analyzed. In Khapko et al. (2014), the analysis of the edge of chaos is pursued further and bifurcations depending on the domain size are investigated.

3.2.1. The edge of chaos in a small periodic domain

The edge tracking algorithm converges in a small periodic domain of size $L_x \times L_z = 4\pi\delta \times 2\pi\delta$ at Re $= 400$ to a state that is independent of the initial condition used for the algorithm (modulo translations in the directions of continuous symmetries). Figure 3.2.1(a) shows the cross flow energy E_{cf} of the edge state as a function of time. It displays violent bursts at constant intervals, interspersed by long times of small and steady variations. In figure 3.2.1(b) the x-averaged velocity field is shown in the z-y-plane at two successive minima of E_{cf}. We see that the state is the same except for a shift in the spanwise direction by $L_z/2$, suggesting that the edge state is a (relative) periodic orbit with period twice the burst interval, which is confirmed by further analysis (Kreilos et al., 2013).

During the long, calm phases the state consists of a pair of downstream streaks, one high- and one low-speed, accompanied by a pair of counter-rotating streamwise-oriented vortices. The vortices sustain the streaks through linear advection (lift-up effect); as time progresses, the streaks develop a sinuous instability and the vortices get more tilted, before they finally cross the low-speed streak, tearing it apart in an event corresponding to the burst in cross-flow energy. Afterwards, the vortices switch

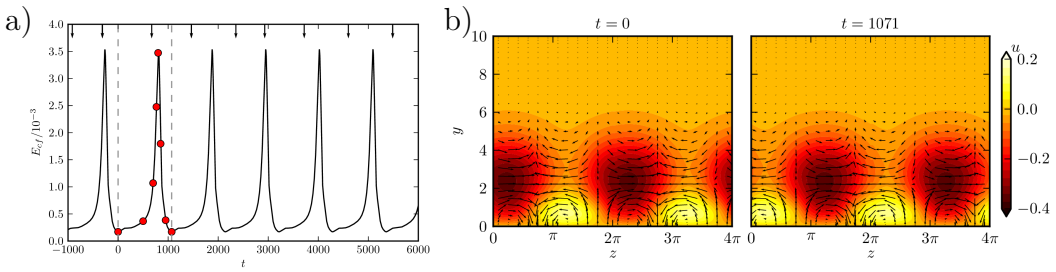

Figure 3.2.1.: The edge state in the ASBL, from Kreilos et al. (2013). (a) The cross-flow energy E_{cf} of the edge state as a function of time shows periodic bursts with a period of $T = 1072$. In between two bursts, the variation of E_{cf} is small. (b) Snapshot of the x-averaged velocity field at two consecutive bursts in a y-z plane, where the domain is shown twice in the spanwise direction. The averaged downstream velocity is shown with colors, the spanwise and wall-normal velocity is depicted with arrows. We see that the velocity field consists of two alternating streaks and two counter-rotating vortices. After a burst, the field is exactly the same, only displaced by half a domain width in the spanwise direction, indicating that the edge state is a periodic orbit whose period is twice the burst interval.

their positions and recreate the streaks, shifted by half a domain width compared to their original location. This is reminiscent of the self-sustaining cycle of near wall turbulence (see section 1.2.3), albeit we show in Kreilos et al. (2013) that the mechanisms at work are somewhat different than those described by Hamilton et al. (1995). While the edge state itself does not contain any hairpin vortices, they are typically observed in transition to turbulence from the edge state.

The dynamics of the edge state is structurally stable under variations of Re and domain size, as shown for $320 < \mathrm{Re} < 750$ in Kreilos et al. (2013) and domain sizes from $L_x \times L_z = 3.2\pi\delta \times 1.6\pi\delta$ to $7\pi\delta \times 4\pi\delta$ in Madré (2011).

Although not imposed, the edge tracking algorithm converges to a symmetry-subspace that is invariant under reflection in z followed by a downstream translation of $L_x/2$. The edge state does hence not drift in the spanwise direction and the distance in the jumps must be exactly $L_z/2$, the only distance that does not leave the symmetry-subspace.[2]

3.2.2. Explaining the spatial dynamics: a SNIPER bifurcation

The short-term dynamics of the edge state are similar to the traveling waves found in other shear flows. Embedding the flow in a family which interpolates between plane Couette flow and the ASBL by gradually increasing the suction boundary condition from $V_S = 0$ to $V_S = U_\infty/\mathrm{Re}$, we are able to explain the spatial, long-term dynamics.

[2]The results described in this section 3.2.1 were part of the authors diploma thesis (Madré, 2011).

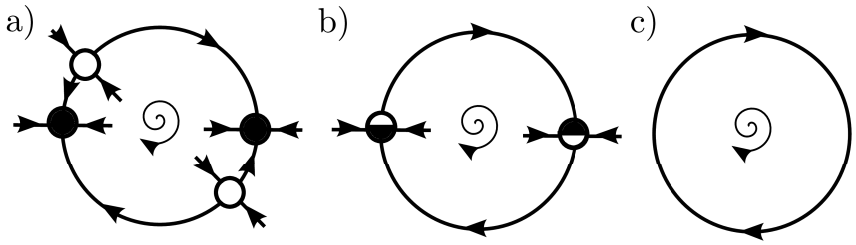

Figure 3.2.2.: An illustration of the SNIPER bifurcation, from Kreilos et al. (2013). (a) Two symmetry-related pairs of fixed points exist on a limit cycle. Both pairs consist of a stable one and one with a single unstable direction. (b) As V_S increases, the fixed points belonging to one pair collide and annihilate in a local saddle-node bifurcation. (c) Afterwards, no fixed points are left and the dynamics explores the limit cycle.

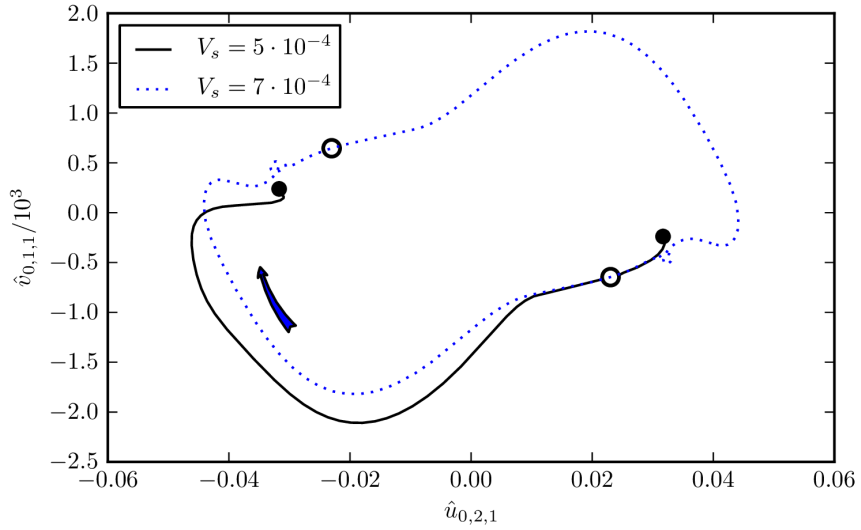

Figure 3.2.3.: (From Kreilos et al., 2013) Illustration of the SNIPER bifurcation in a two-dimensional projection of the dynamics, plotting two expansion coefficients of the velocity field. At $V_S = 5{\cdot}10^{-4}$ (black line), before the saddle node bifurcation, two symmetry-related pairs of fixed points exist, which are heteroclinically connected. Restricted to the edge, one of the fixed points is an attractor, while the other one has a single unstable direction and the heteroclinic connections have been explicitly calculated with the edge tracking algorithm. At $V_S = 7 \cdot 10^{-4}$ (dotted blue line) the fixed points have annihilated removed in a saddle-node bifurcation and the edge tracking algorithm converges to a limit cycle, corresponding to the edge state in the ASBL.

Starting with the edge state in plane Couette flow, which is a simple fixed point, and increasing the suction, the state becomes a traveling wave that subsequently is destroyed in a saddle-node bifurcation. Restricted to the edge of chaos the edge state is an attractor and hence the node, with the saddle state having one unstable direction inside the edge. The pair of fixed points is heteroclinically connected to a symmetry-related pair, obtained by shifting the states by $L_z/2$ in the spanwise direction, as illustrated in figure 3.2.2(a) in a projection inside the edge. The long heteroclinic connection, connecting the unstable state on the left to the stable one on the right, has been explicitly calculated, see figure 3.2.3. As V_s increases, the two states annihilate in a local saddle-node bifurcation, leaving behind a stable (within the edge) limit cycle that becomes the new attractor in the laminar-turbulent boundary. This so-called SNIPER (saddle-node-infinite-period or saddle-node in periodic orbit) bifurcation is illustrated in figure 3.2.2.

The energetic bursts associated with the destruction and reformation of the coherent structures are associated with motion on the limit cycle. If V_S is not too far away from the value of the SNIPER bifurcation, the trajectory stays close to the ghost of the saddle-node bifurcation for a long while, with this time getting shorter as V_S increases. The expected scaling is $T \propto \sqrt{V_S - V_{S,c}}$, which we verified for the bifurcation.

3.2.3. Downstream advection of the edge state

In Kreilos et al. (2014c) the downstream advection of the edge state, calculated with equation (2.2.12), is studied.[3] Note that while domain size and Re differ from Kreilos et al. (2013), the dynamical structure of the edge state does not change, while the time between two bursts is increased to about 1500, as shown in figure 3.2.4(a). The advection velocity, shown in figure 3.2.4(b), is almost constant during the calm phase of the edge state, where it is around 66% of U_∞, which is close to the mean convection speed of spots in turbulent boundary layers (Wygnanski et al., 1976) and of coherent structures in boundary layers (Duguet et al., 2012). However, during the bursts the speed is significantly reduced as energy is taken from the mean flow and non-linearly distributed into spanwise motion.

A movie of the periodic orbit, available online with Kreilos et al. (2014c), clearly demonstrates the effect of removing the advection. In the laboratory frame of reference, the vortices and streaks fly by the observer, concealing the dynamics. On the other hand, in the comoving frame of reference the structures are stationary and the observation of the dynamics is possible in much greater detail.

[3] As noted in section 3.2.1 a drift in the spanwise direction is not possible because the state is attracted to a symmetry-invariant subspace.

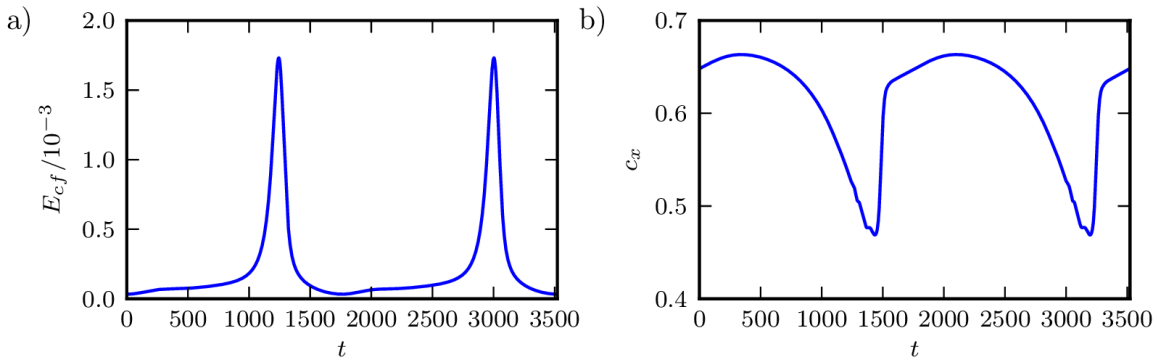

Figure 3.2.4.: (From Kreilos et al., 2014c) Downstream advection of the edge state in a domain of size $L_x \times L_z = 6\pi \times 3\pi$ at $\mathrm{Re} = 500$. (a) The dynamics is qualitatively the same as in the smaller domain discussed in the previous sections, the cross-flow energy shows periodic bursts with a period of about 1500 time units. (b) The downstream advection velocity drops significantly during the bursts, as energy is nonlinearly distributed from the streaks to stronger fluctuating vortical motion.

3.2.4. Spanwise localization in extended domains

Since the edge state in a small domain shows interesting dynamics associated with the spanwise direction, the question arises what happens to the dynamics once the constraints of spanwise periodicity are removed, i.e. how the dynamics changes in a wide domain.

The edge tracking algorithm in a wide domain of length $L_x = 6\pi\delta$ (see Khapko et al., 2013) converges to three qualitatively different states. All three states are similar to the edge state in a small periodic domain in their local dynamics and show periodic bursts in energy, at which the structures break up and are reformed at a different spanwise location. The three distinct states that we identified can be classified according to the relative position of the structures after a burst, which can be always translated to the left (in which case we denote the state as L), always to the right (R), or alternatingly left and right (LR). A space-time diagram in figure 3.2.5 shows streamwise velocity fluctuations averaged over x at $y = \delta$ as a function of z (x-axis) and t (y-axis), with the states L, R and LR in panels (a), (b) and (c), respectively. Blue corresponds to the position of a low-speed streak, red to a high-speed streak. In figure 3.2.5 we see that at every burst, the low-speed streak splits into two, translated symmetrically left and right, of which only one survives.

The local dynamics of the three states is very similar to the state in a small periodic domain (section 3.2.1). A pair of alternating streaks is accompanied by a pair of counter-rotating downstream vortices. As the streaks develop a sinuous instability, the vortices start to tilt and lean over the low-speed streak, before eventually crossing each other and tearing the streak apart in an event associated to a maximum in the

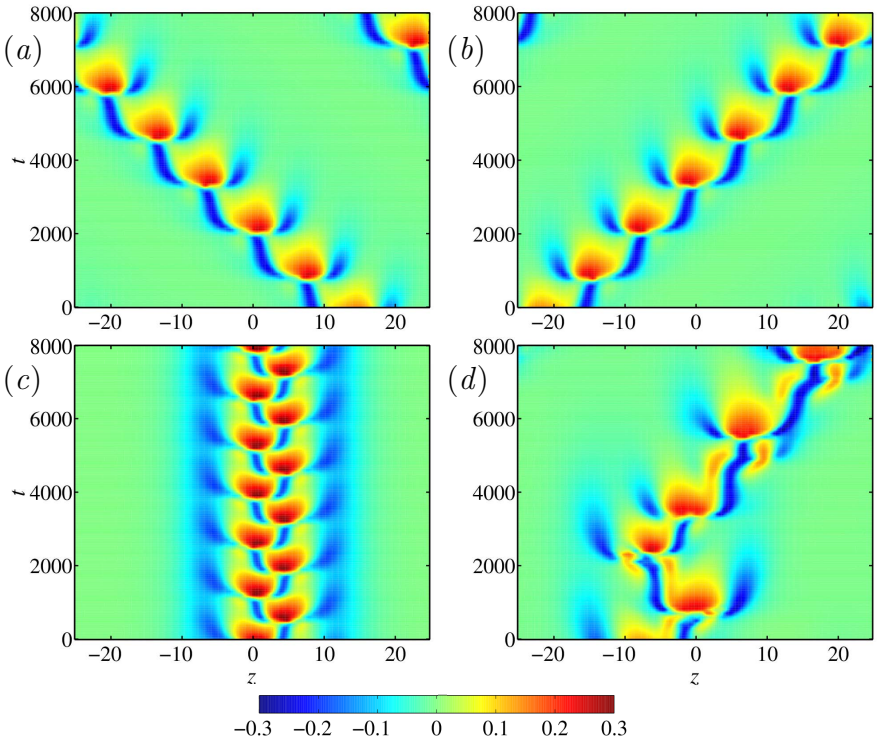

Figure 3.2.5.: (From Khapko et al., 2013) Space time diagrams of the edge state in a spanwise extended domain, showing the streamwise velocity fluctuations averaged over x at $y = \delta$. The dynamics of the edge states is always similar to the narrow domains, with calm phases interrupted by violent bursts at which the flow structures are displaced in the spanwise direction. In a domain of length $L_x = 6\pi$ (a-c), three qualitatively different periodic orbits are approached by the edge tracking algorithm, characterized by the direction in which the structures move after a burst, either always left (a), always right (b) or alternatingly left and right (c). If the length is only $L_x = 4\pi$ (d), no periodic state is found, though the qualitative dynamics remains the same.

cross-flow energy. The structures are reformed from a strongly fluctuating flow at a shifted spanwise position, as one of the streaks survives and serves as the nucleus of a new more ordered set of structures. In contrast to the smaller domains, where the two splitted parts of the low-speed streak rejoin over the periodic boundary conditions, in the wide domains of the two streaks formed only one survives.

Figure 3.2.5(d) shows the space-time representation of a typical edge tracking in a somewhat shorter domain with $L_x = 4\pi\delta$. Here, the edge tracking does not converge to a periodic orbit. While the short-term dynamics – streak formation, linear instability, vortices crossing, streak breakup and reformation at a shifted position – remain intact, there is no continuity in the directions in which the structures are translated after a burst, the pattern of shifts is chaotic. The transition from the pe-

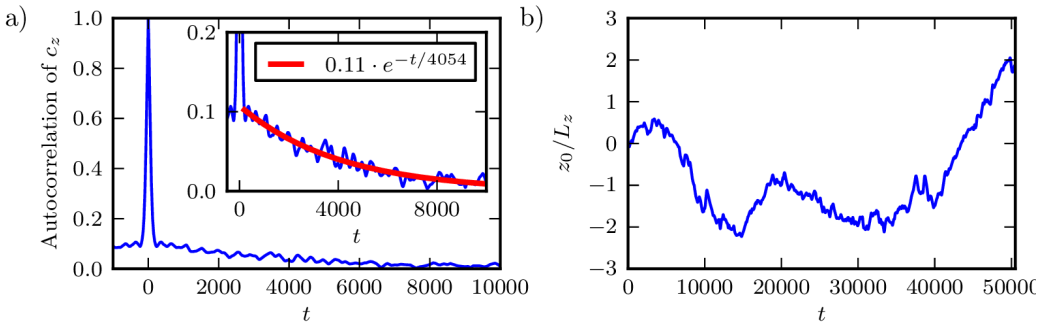

Figure 3.3.1.: (From Kreilos et al., 2014c) Spanwise advection in turbulent ASBL in a domain of size $L_x \times L_z = 6\pi \times 3\pi$ at $\mathrm{Re} = 500$. (a) The autocorrelation function of the spanwise advection velocity shows a sharp peak around zero, corresponding to short-term fluctuations. But there is a long tail, approximated by an exponential with a characteristic time of approximately 4000 time units. (b) The integrated advection velocity, i.e. the spanwise displacement, reveals drifts that prevail for tens of thousands of time units.

riodic edge states to erratically jumping ones as the length of the domain is reduced is investigated in Khapko et al. (2014). The bifurcation sequence involves states with several jumps into one direction before the direction is reversed (e.g. $LLLRRR$) and Pomeau-Manneville intermittency (Pomeau and Manneville, 1980). This behavior has been identified in simple non-linear maps and its identification on the laminar-turbulent boundary in a boundary layer flow is another example of the relevance of concepts from low dimensional dynamical systems theory for fluid turbulence.

3.3. Slow processes in turbulent ASBL

Having studied the role of downstream advection of the edge state (see section 3.2.3), in the second part of Kreilos et al. (2014c) we focus on fully turbulent ASBL. While the edge state is attracted to a symmetry-invariant subspace which prohibits advection in the spanwise direction, this constraint does not exist in fully turbulent flow and equation (2.2.12) can not only be used to extract advection in the downstream advection but also in the spanwise one. We study a computational domain of size $L_x \times h \times L_z = 6\pi \times 25 \times 3\pi$, where the great height is necessary due to plumes from the turbulent BL reaching far into the free-stream (Schlatter and Örlü, 2011).

On short timescales the spanwise advection velocity c_z, as calculated from equation (2.2.12), fluctuates heavily and the fluctuations are approximately Gaussian. But on longer timescales, the integrated advection velocity, i.e. the total spanwise displacement, shows continuous drifts over extremely long times on the order of thousands and tens of thousands time units (figure 3.3.1b).

To better understand those drifts we calculate the time autocorrelation function

$$R(t) = \int_0^\infty c_z(t + dt)c_z(t)\ \mathrm{d}t \tag{3.3.1}$$

averaged over 14 trajectories each integrated for 200,000 time units, shown in figure 3.3.1(a). It exhibits a sharp peak around 0, corresponding to the short-term correlations. But then it does not drop to zero directly but slowly with an exponential behaviour with a characteristic time scale of ~ 4000 time units. In addition to the example of the edge state, where turbulent bursts occur with a period on the order of 1000 time units, this is the second instant where the system shows extremely long time scales associated with motion in the spanwise direction.

The long-term spanwise drifts in the system can also be visualized. Since the main driving force in near wall turbulence is vortical motion close to the wall where the strongest shear gradients are present (Robinson, 1991), we define a quantity

$$A(z, t) = \langle v(x, y = \delta, z, t)\rangle_x \tag{3.3.2}$$

measuring the downstream averaged wall-normal velocity component at a y coordinate that is the laminar displacement thickness, where streamwise vortices are expected to show a strong contribution. Figure 3.3.2(a) shows a space-time plot of $A(z, t)$ over 3000 time units, the domain is shown twice in the spanwise direction. For most times, we see one positive and one negative region, a pattern corresponding to a pair of downstream vortices where one is rotating clockwise and one counterclockwise. This pattern is drifting to the right. The thick black line on top is the integrated spanwise advection velocity c_z – it falls along a prominent rift in the plot. In panel (b), the integrated drift has been subtracted from $A(z, t)$. The pattern is now aligned mostly downstream, confirming that indeed the near-wall vortices are advected by the mean flow and the advection is accounted for by equation (2.2.12).

We furthermore show in Kreilos et al. (2014c) that similar phenomena are found in turbulent channel flow, with long drifts in the spanwise direction and no long correlations in the downstream advection velocity.

3.4. A probabilistic cellular automaton model for bypass transition in boundary layers

We study the transition to turbulence in the Blasius boundary layer (BBL) subject to free-stream turbulence (FST). As discussed in section 1.4.1 the transition occurs through the creation of isolated turbulent spots, which grow in both the downstream and spanwise direction, merge with other spots and eventually lead to a fully turbulent boundary layer.

We model the evolution of turbulent spots by a probabilistic cellular automaton, inspired by the percolation type models describing the evolution of puffs in pipe flow

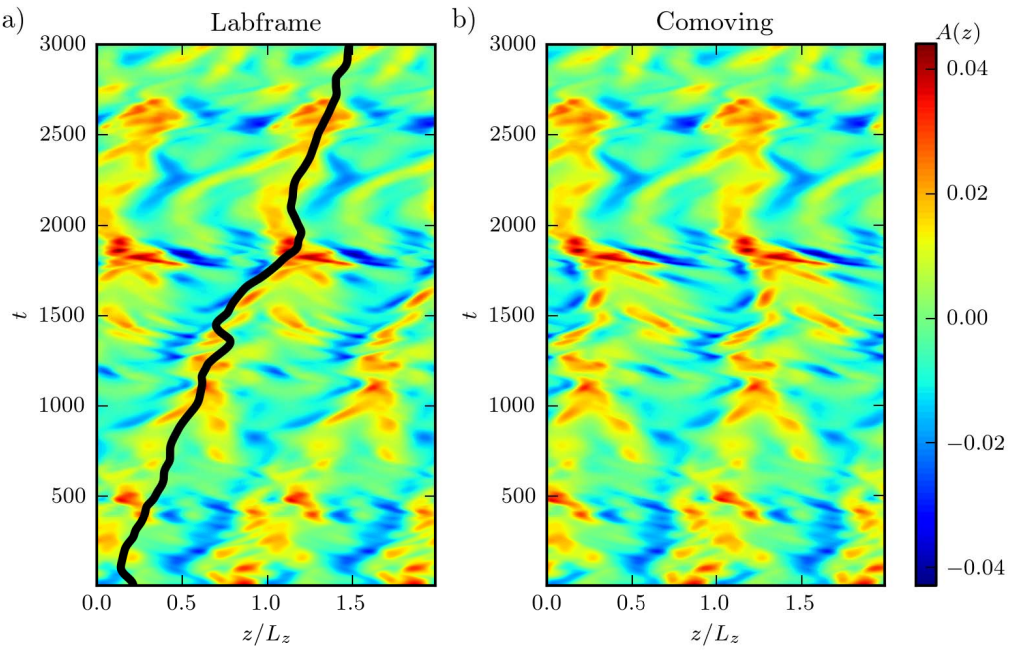

Figure 3.3.2.: (From Kreilos et al., 2014c). Space-time diagram showing the quantity $A(z,t)$, equation (3.3.2). For most times, one blue and one red region are visible, revealing the existence of a pair of counter-rotating vortices. (a) In the laboratory frame of reference, the structures display an angle with the z-direction, indicating a drift in the spanwise direction. The black line on top is the integrated spanwise advection as calculate from equation (2.2.12), it falls along a prominent rift in the figure. (b) In the comoving frame of reference, where the advection has been subtracted, the spanwise drift is gone and the structures are mostly aligned downstream.

and the deterministic models of Vinod and Govindarajan (2004, 2007). Space and time are discretized and each cell at each instant in time is assigned a binary value of laminar or turbulent. The boundary layer is modeled as two-dimensional, thus eliminating any dependency on the wall-normal coordinate. At each timestep turbulence is advected downstream by one cell and spreads with prescribed probabilities into its four neighboring cells as illustrated in figure 3.4.1. The model governing the evolution of spots has hence four parameters, the probabilities that turbulence persists (p_p) or spreads forward (p_f), sideways (p_s) or backwards (p_b).

We obtain the parameters from LES simulations of a flat-plate boundary layer subject to free-stream turbulence, with a numerical setup similar to Brandt et al. (2004). We base the identification of turbulence on the spanwise wall shear stress, $\tau_s = \partial w/\partial y|_{y=0}$, which is very low in the streaky flow before transition and high in the presence of strong vortical motions characteristic of turbulence. A good cell size for the PCA is deduced from the autocorrelation functions of τ_s and the data from the

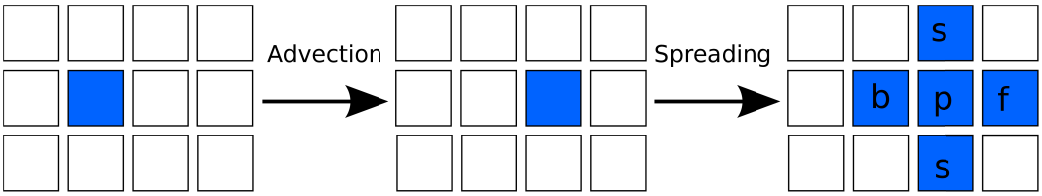

Figure 3.4.1.: (From Kreilos et al., 2014b). Sketch of the probabilistic cellular automaton describing the evolution of turbulent spots. The model works on a 2D grid. At each timestep, a turbulent cell (indicated in blue) is advected one cell in the streamwise direction. It then spreads turbulence into neighboring cells with prescribed probabilities.

LES simulations is reduced to these cells with a spatial filter, followed by a Gaussian filter with kernel size 0.5 cells that removes flickering and finally a threshold in τ_s to discriminate laminar from turbulent cells.

From the binary data we directly deduce the spreading parameters of the PCA in the following way: the state of each cell is only laminar if turbulence did not persist and if none of the surrounding turbulent cells spread turbulence into it. The probability for a cell to be laminar is hence given by a product of up to five factors, involving one term of the form $(1-p)$ for each surrounding turbulent cell. Identifying the corresponding configuration in the LES data, we count how often it is encountered and how often it leads to the cell being laminar, thus obtaining a measured value of the probability that the cell is laminar. There are $2^5 = 32$ possible configurations (symmetries are not implemented in the optimization) and we determine the 5 parameters of the model through a least squares fit.

In our simulations the intensity of the FST ranges from Tu = 3% to Tu = 4% of the free-stream velocity U_∞. It turns out that the probability to persist is one in all our simulations, i.e. decay of turbulence is almost never observed. Furthermore, the spreading probabilities are constant and do not vary with Reynolds number or the FST level. This independence of the probabilities on any external quantity shows that the transition is an *activated process*: once a turbulent spot is initiated, its future fate is entirely determined by processes that are internal to the turbulent boundary layer and do not depend on either the free-stream turbulence outside the boundary layer or the laminar Reynolds number.

In order to use the PCA for simulations of the boundary layer, we need an expression for the probability $p_c(x)$ with which turbulent spots are nucleated. We derive an analytical expression for the spot nucleation rate and validate its applicability with simulations of the PCA using the nucleation rate as the probability to create a spot. In the derivation of p_c we follow the process discussed for example by Brandt et al. (2004) and Fransson et al. (2005): disturbances in the free-stream induce perturbations in the boundary layer, which then exhibit non-normal linear growth until crossing a threshold in amplitude, at which the streaks break down and a turbulent

spot is nucleated. More quantitatively a perturbation with an initial amplitude A_0 becomes amplified to $A_0(\mathrm{Re} - k/\mathrm{Tu})$ at a higher Re, the offset of k/Tu being motivated by the observed u_{rms} dependence on Re in the pre-transitional boundary layer, see figure 5.6.13 below. If the threshold function is assumed as $a/(\mathrm{Re} - \mathrm{Re}_c)$, we obtain a relation between the initial amplitude of a perturbation and the Reynolds number where it will nucleate a spot

$$A_0 = \frac{a}{\mathrm{Re} - \mathrm{Re}_c} \frac{1}{\mathrm{Re} - k/\mathrm{Tu}}.$$

It is known that u_{rms} scales linearly with Tu, indicating a linear receptivity mechanism, and we make an ansatz for the distribution of initial amplitudes as

$$p_{A_0}(A_0)\mathrm{d}A_0 = \frac{c}{\mathrm{Tu}} \mathrm{e}^{-(A/\mathrm{Tu})^2} \cdot \mathrm{e}^{-b/\mathrm{Tu}} \mathrm{d}A_0,$$

where amplitudes are distributed Gaussian and the factor $\mathrm{e}^{-b/\mathrm{Tu}}$ captures the observation that at higher Tu more spots are nucleated (Fransson et al., 2005). Combining the two relations we obtain a distribution of Reynolds numbers where spots are created,

$$p_{\mathrm{Re}}(\mathrm{Re})\mathrm{dRe} = p_{A_0}(A_0(\mathrm{Re})) \left| \frac{\mathrm{d}A_0}{\mathrm{dRe}} \right| \mathrm{dRe},$$

which is mapped to a distribution of positions and used as p_c in the simulations. The missing parameters in the expression for the nucleation rate are obtained by running the PCA with a given p_c, demanding that the resulting intermittency curves resemble those of the numerical data and performing a least squares fit on the free parameters. The resulting nucleation rates are shown in figure 3.4.2.

The comparison of the results obtained by simulating the model with the numerical data is shown in figure 3.4.3 for three quantities, the intermittency γ, the average width of turbulent spots $w(x)$ and the average number of turbulent spots $n(x)$. The panels show the value obtained from the LES data in black and the result of the model in color, the shaded area indicates a one σ interval around the mean. The agreement between the model and the data is excellent and shows that our model does not only reproduce intermittency very accurately but also other spatio-temporal properties of turbulent spots.

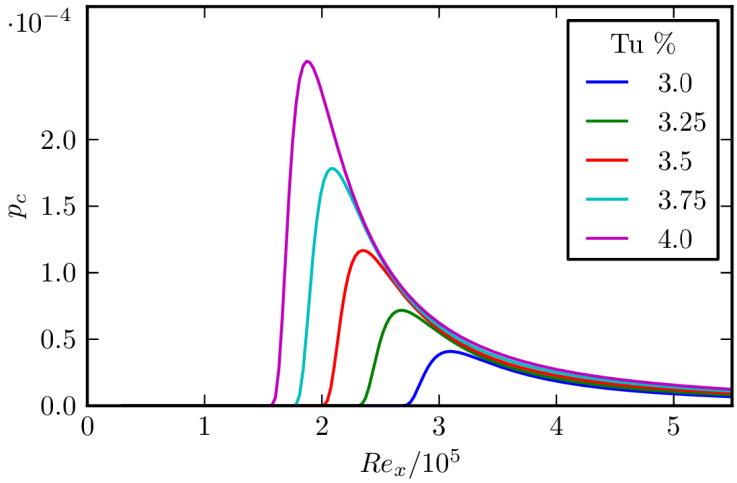

Figure 3.4.2.: The nucleation rate obtained for the five different levels of Tu. The shape is similar for all cases, with a sharp increase and a slower decay after a maximum.

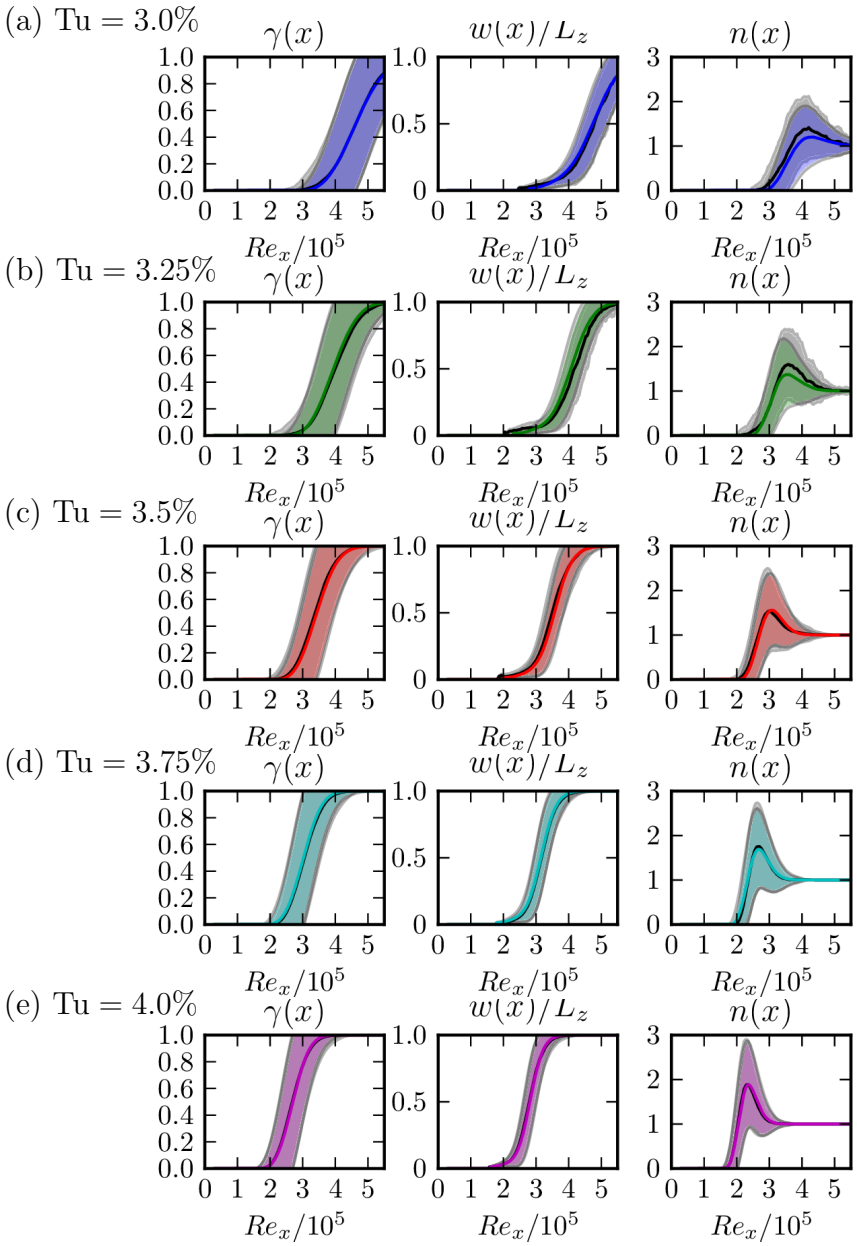

Figure 3.4.3.: Comparison of spot statistics between the numerical data and the PCA for all five values of Tu, with color coding the same as in other figures. For each quantity, the value from the LES simulations is shown in black with the gray shaded area indicating a one σ interval around the mean. The value obtained from the PCA is plotted in color. In most cases, the agreement is so good in all quantities, intermittency, spot width and number of independent spots, that no difference between the two curves is visible. Only for the smallest two values of Tu, there is a very small deviation in the number of spots, which upon inspection of videos is due to flickering in the binary LES data.

4. Concluding discussion

In the attempt to understand the onset of turbulence in linearly stable shear flows with dynamical systems theory a coherent picture starts to emerge, describing the creation of structures in state space that support the (transient) turbulent dynamics. In plane Couette flow at Reynolds numbers well below those where turbulence is typically observed, a pair of invariant solutions is created in a saddle-node bifurcation, of which the upper branch solution is stable and the lower branch one has a single unstable eigenvalue. As Re increases the upper branch undergoes a bifurcation cascade, leading to a chaotic attractor, separated from the laminar state by the stable manifold of the lower branch, i.e. the lower branch becomes the edge state and its stable manifold is the edge of chaos. At a somewhat higher Re, the chaotic attractor touches the lower branch solution and is subsequently destroyed in a boundary crisis, leaving behind a chaotic saddle. This saddle grows in complexity and forms the backbone of transient turbulence, where trajectories may meander in the saddle for arbitrarily long times, but may suddenly escape and be attracted to the laminar state. While the existence of a chaotic saddle in transitional shear flows has up to now only been rationalized based on features of the transient dynamics, positive Lyapunov exponents and exponentially distributed escape times, we have proven its existence by following the process of its creation.

While our own results only demonstrate this bifurcation scenario in plane Couette flow, the same sequence of events has been found subsequently in pipe flow (Avila et al., 2013) and in plane channel flow (Stefan Zammert, private communication), validating that it is a generic way to generate state space structures that support transient turbulence. Furthermore, we identified the same sequence of events to be responsible for the growing complexity of the turbulent saddle and increasing turbulent lifetimes, as stable chaotic bubbles form within the turbulent saddle that break up in further boundary crises and entangle with the surrounding saddle. The collective effect of a great number of such bifurcation sequences, possibly in unstable subspaces and hence more difficult to detect, will finally lead to globally growing lifetimes. While this is a first mechanism that leads to an increase in transient lifetimes, it remains an open question whether this is the root of the ubiquitously observed superexponential scaling of lifetimes with Re.

The boundary crisis in which the chaotic saddle is created happens as a chaotic attractor collides with the stable manifold of the edge state, the attractor becomes leaky and the notion of "inside" and "outside" is lost. Our observation of this crisis bifurcation hence explains the coexistence of the edge of chaos, which is of codimen-

sion one, and transient turbulence, answering one of the long outstanding questions that arise from the identification of the edge (see e.g. Eckhardt, 2008). Our results, which are obtained in fully three-dimensional plane Couette flow, support the picture developed in simplified models by Vollmer et al. (2009) and Lebovitz (2009, 2012), specifically designed to understand the coexistence of the edge of chaos with transient turbulence.

Most of the advancements in nonlinear dynamical systems theory come from the study of low-dimensional maps and differential equations, while on the other hand turbulence is an intrinsically extremely high dimensional phenomenon. Nevertheless, great progress has been made as it was possible to apply concepts from low-dimensional dynamical systems theory to turbulence. Our results from transitional plane Couette flow and from Khapko et al. (2014), studying the edge of chaos in spanwise extendend ASBL, add two cases in which the dynamics in transitional shear flows is extremely similar to low dimensional chaos.

While the analogy to unimodal maps made it possible to establish a systematic way of obtaining periodic orbits in plane Couette flow, too many orbits were pruned in order to calculate statistics with periodic orbit theory. So the task to describe a three-dimensional fluid mechanical system completely in terms of periodic orbits and thus to get closer to Hopf's vision (Hopf, 1948) remains open for the future.

Transferring results from internal to external shear flows, we studied the edge of chaos in the ASBL. The successful identification of edge states in the ASBL shows that the general structure of state space is the same as for internal shear flows: there is a region in state space, surrounding the laminar state, of initial conditions that directly decay, and a region where initial conditions undergo (transient) turbulent motion. The two regions are separated by the stable manifold of an invariant object, which is of codimension one and fractal. While it has not been possible to follow the edge state to the saddle-node bifurcation in which it is created due to the long time scales, there is no reason to assume that the creation of the chaotic saddle would fundamentally differ from the process in internal shear flows.

Edge states in the ASBL have been characterized in small periodic computational domains as well in spanwise extended ones; in the latter case, the states localize in the spanwise direction. They are periodic orbits (for suitable downstream wavelengths) and their dynamics is amazingly similar regardless of whether they are spanwisely localized or not. The dynamics consist of long calm phases in which the states are similar to traveling wave solutions known from other shear flows, followed by violent bursts in which the structures break up and reform at a different spanwise location. We have related the bursts to a SNIPER bifurcation occurring on a homotopy connection to plane Couette flow.

Biau (2012) investigated edge states in a different boundary layer, in which the spatial growth is artificially compensated by a temporally varying body force. The edge states in this boundary layer flow are very similar to the ones in the ASBL, showing calm phases interrupted by strong bursts in which the structures are displaced

by half a wavelength. Together with the similarity to the edge states in plane channel flow, which are localized near one wall and exhibit hence a base flow comparable to boundary layer situations (Toh and Itano, 2003; Zammert and Eckhardt, 2013), this suggests the spatio-temporal dynamics to be universal for boundary layer flows.

The conceptual extension to the technologically more relevant flat plate boundary layer without suction remains difficult, though, due to the spatial growth of the boundary layer with increasing distance from the leading edge. A critical trajectory on the laminar-turbulent boundary has been calculated by Duguet et al. (2012), suggesting that the general notion of an edge of chaos separating laminar from turbulent dynamics is applicable, but due to the spatial growth no access to the asymptotic dynamics is possible. The identification of a cyclic process on the edge, as described in Duguet et al. (2012), has hence to be treated with caution, while being in nice agreement with the cyclic motion on the edge in the ASBL and other parallel boundary layers.

The probabilistic cellular automaton that was derived from numerical simulations of transitional boundary layer subject to free-stream turbulence shows that the transition in this flow is an activated process, with only the spot nucleation depending on details of the environment. We propose a new model that gives a quantitative description of the spot nucleation rate in the flow. This model, together with the probabilistic cellular automaton describing the evolution of turbulent spots, allows to accurately reproduce spatio-temporal properties of turbulent spots in transitional boundary layers.

Symmetries, continuous or discrete, play an important role in almost all fields of physics. The method of comoving frames deals with one aspect of systems with continuous symmetries in allowing to separate the advection in the direction of a symmetry from the active dynamics. We detected drifts in those directions in the ASBL that survive for thousands of advective time units and similar phenomena are found in plane channel flow. Applications in experimental data from pipe flow or Rayleigh-Bénard convection, where the angular advection can be removed, are straightforward and might help to elucidate the role of drifts in those systems.

We have presented several new links between low-dimensional dynamical systems theory and turbulence, describing the onset of turbulence in plane Couette flow and a conceptual extension to boundary layers. The results presented in this work provide a further building block for describing Navier-Stokes turbulence in terms of dynamical systems theory.

5. Publications

In this chapter the six publications containing the detailed results of the author's work are reproduced. The revised submitted version of the manuscripts is used, with two semantical changes: the numbering of figures and other references is adapted to integrate with the other chapters and the list of references is removed from the end of a publication and integrated into the bibliography at the end of this work; for publications where the journals citation style is numeric, we have adapted it to author-year citations to conform with the rest of this work.

Publication 5 is accepted for publication and will appear soon, the manuscript present in section 5.5 is available on the arXiv. The manuscript for publication 6 is still in preparation and section 5.6 contains the current draft.

5.1. Periodic orbits near onset of chaos in plane Couette flow

Tobias Kreilos[1] **and Bruno Eckhardt**[1,2]
[1]Fachbereich Physik, Philipps-Universität Marburg, D-35032 Marburg, Germany
[2]J.M. Burgerscentrum, Delft University of Technology, Mekelweg 2, 2628 CD Delft, The Netherlands

Published in Chaos 22(4), 047505 (2012)

We track the secondary bifurcations of coherent states in plane Couette flow and show that they undergo a periodic doubling cascade that ends with a crisis bifurcation. We introduce a symbolic dynamics for the orbits and show that the ones that exist fall into the universal sequence described by Metropolis, Stein and Stein for unimodal maps. The periodic orbits cover much of the turbulent dynamics in that their temporal evolution overlaps with turbulent motions when projected onto a plane spanned by energy production and dissipation.

The identification of the different 'routes to chaos' (Eckmann, 1981; Ott, 1981) has suggested ways in which they can also be 'routes to turbulence' that lead from a laminar flow state through various bifurcations to a turbulent attractor. Studies of the turbulence transition in plane Couette flow and pipe flow, which do not have a linear instability of the laminar profile, have revealed a route to turbulence that passes through the formation of a chaotic saddle (Eckhardt et al., 2007; Eckhardt, 2008). The saddle develops around a scaffold of coherent structures that appear in saddle-node type bifurcations, with the notable difference to the standard scenario that also the 'node'-states typically become unstable very quickly. In this transitional region the turbulence is not persistent but transient, and can hence be associated with a transient chaotic saddle rather than an attractor. In the spirit of a dynamical systems approach to characterizing these features (Gutzwiller, 1971, 1990; Cvitanović and Eckhardt, 1991), we here present an analysis of the state space structures near transition in plane Couette flow and study the various bifurcations and periodic orbits that appear.

5.1.1. Introduction

The application of dynamical systems ideas to fluid mechanical problems has provided much insight into the ways fluids transit from a laminar state to a turbulent one. The various bifurcations that appear in the case of fluids heated from below (Rayleigh-Benard) or fluids driven by centrifugal instabilities (Taylor-Couette) have

been studied experimentally and theoretically in considerable detail (Andereck et al., 1986; Koschmieder, 1993). Studies of turbulence in liquid helium have shown the period doubling cascade (Maurer and Libchaber, 1979) and the quasi-periodic routes to chaos (Stavans et al., 1985), and the rich structures of secondary bifurcations and flow states in RB and TC have been explored (Busse, 1978; Andereck et al., 1986; Koschmieder, 1993). The approach has been so successful that flows without linear stability of the linear profile, like plane Couette flow and pipe flow, have been suspected to belong to the class of subcritical bifurcations (Cross and Hohenberg, 1993), perhaps with the bifurcation point at infinity (as reflected, e.g., in the title of Nagata's first papers on coherent structures in plane Couette flow (Nagata, 1990)). However, the first structures that are observed near the transition point are not steady or simple flows, but they are fluctuating spatially and temporally, indicating that these states undergo many further bifurcations as the Reynolds number is lowered.

A more promising approach starts with the turning points of the subcritical bifurcations, the saddle-node bifurcations in which these structures appear. The possibility to approach flows from this point of view is suggested by the remarkable persistence of key features of these structures (Eckhardt et al., 2007): they are all dominated by downstream vortices which modify the base profile to generate streaks. This by itself is not enough, as flows that are translationally invariant in the downstream direction cannot be sustained (Moffatt, 1990). So three-dimensionality is another key element, and also the reason for the absence of analytical studies of this transition scenario.

The importance of vortices and streaks has been deduced from numerical studies of plane Couette flow in small domains, where a recurrent pattern of vortices and streaks could be identified (Jiménez and Moin, 1991; Hamilton et al., 1995). The interactions between vortices and streaks and the instabilities that streaks can undergo has been studied by Waleffe (Waleffe, 1995), who proposed a self-sustaining process (analyzed also in (Schoppa and Hussain, 2002; Lagha and Manneville, 2007; Aubry et al., 1988; Smith et al., 2005)). This process is usually explained by starting with the vortices, which then drive streaks, and the streaks then undergo an instability in which normal vorticity is created. The cycle is closed by nonlinear interactions that lead to the recreation of streamwise vortices.

An example where the transitions between the different states and their symmetry can he analyzed directly, and in a physically meaningful setting, is Taylor-Couette flow in the limit in which it approaches plane Couette flow (Faisst and Eckhardt, 2000). In the curved case, say with the inner cylinder rotating and the outer one at rest, the flow undergoes a first bifurcation to Taylor-vortex flow, in which vortices with an azimuthal symmetry appear. As the rotation rate is increased, the vortices undergo a secondary bifurcation, in which an azimuthal modulation is added and the rotational symmetry is broken. Increasing the radii while keeping the distance between the cylinders fixed, the influence of the curvature becomes smaller and the flow approaches plane Couette flow. Along the way, the bifurcation structure changes: the transition point to the formation of azimuthally symmetric vortices moves out infinity, so that the linear

stability of plane Couette flow is recovered (Faisst and Eckhardt, 2000). The three-dimensional wave structures, arising in secondary bifurcations of the Taylor vortex flow, can be traced over to plane Couette flow, where they now appear in a saddle node bifurcation (Faisst and Eckhardt, 2000). In going from the Taylor-Couette to plane-Couette flow the transition can be studied within realistic models. In the case of pipe flow no physical family of flows could be identified, so a body force was introduced to embed the system into one where the bifurcations can be realized. Despite this artificial setting, the coherent structures thus found are similar to the ones in plane Couette flow and share many properties (Faisst and Eckhardt, 2003).

The coherent structures just described are usually unstable, and can appear only transiently in the flow (Hof et al., 2004; Schneider et al., 2007a; Lai and Tél, 2011). Moreover, it was found that they are not sufficiently entangled to close off the state space around them to form an attractor: thus it is not only the coherent structures that are visited transiently, but the entire turbulent dynamics becomes a transient phenomenon, characterized by an exponential distribution of lifetimes, as can be expected for a chaotic saddle (Hof et al., 2006; Schneider and Eckhardt, 2008). While this sets the stage from the dynamical systems point of view, several questions remain to be addressed (Eckhardt, 2008). We will address two of them, related to the secondary bifurcations of coherent structures, in the following.

It was noticed long ago in (Clever and Busse, 1997), that the coherent structures that appear in plane Couette flow at Re= 125 are stable very close to the bifurcation point and become unstable via Hopf bifurcations. This would suggest that the transition creates an attractor rather than a transient saddle. However, at higher Re the flowed evidently is transient: so how does the state space near these coherent states change as one increases the Reynolds number and how does the flow change from chaotic but persistent to transient? The analysis of these properties in pipe flow shows that the sequence of bifurcations that lead from a (small) chaotic attractor to transient dynamics can be rather intricate (Mellibovsky and Eckhardt, 2011, 2012).

A second item concerns the possibility to describe the flows using periodic orbits, as is possible in other dynamical systems (Cvitanović, 1988; Cvitanović and Eckhardt, 1991; Eckhardt and Ott, 1994; Christiansen et al., 1997). Identifying periodic orbits in high-dimensional systems is a major technical challenge, which has been overcome in a few cases only. Most notably, for the cases studied here, a number of isolated periodic orbits have been found in (Kawahara and Kida, 2001; Viswanath, 2007; Cvitanović and Gibson, 2010). In the present case their identification is considerably simplified by the presence of a period doubling cascade, that arranges them in families.

The outline of the paper is as follows: in section 5.1.2 we discuss the organization of the state space near the lowest saddle-node bifurcation in plane Couette flow in our domain. In section 5.1.3 we discuss the characterization of the internal dynamics and bifurcations in terms of a discrete map. We follow this in section 5.1.4 with a discussion of the periodic orbits and their properties.

5.1.2. Bifurcations

We study an incompressible Newtonian fluid between two infinitely extended plates in the x-z plane located at $y = \pm h$ that move with speed $\pm U_0$ along the x-axis. A length-, velocity and time-scale are given by h, U_0 and $t = h/U_0$. The control parameter is the Reynolds number $\mathrm{Re} = U_0 d/\nu$, where ν is the viscosity of the fluid. We use periodic boundary conditions in the spatially extended directions and no-slip boundary conditions at the walls, with a box size of $2\pi \times 2 \times \pi$ in the downstream, wall-normal and spanwise directions, respectively. We use channelflow (Gibson, 2011) to integrate this system with a Fourier-Chebyshev-Fourier scheme and a numerical resolution of $32 \times 33 \times 32$ modes; some key results, like the stability properties of our solutions, have been verified at a doubled resolution of $64 \times 65 \times 64$ modes. The main quantity we use in this study is the cross-flow energy, i.e. the amount of energy in the flow components transverse to the laminar base flow,

$$E_{cf} = \frac{1}{V} \int_V \left(v^2 + w^2 \right) \mathrm{d}V, \tag{5.1.1}$$

or the square root of E_{cf} so as to reduce the range of it.

The box size in this study is just slightly longer and narrower than the cell studied in Ref. (Waleffe, 1995). In this and other smaller boxes the typical flow consists of a pair of counter-rotating streamwise vortices and a pair of alternating streaks. This limitation in the number of possible flow structures greatly simplifies the sequence of bifurcations. To simplify the analysis even further we enforce a shift-and-reflect symmetry

$$s_1[u, v, w](x, y, z) = [u, v, -w](x + L_x/2, y, -z), \tag{5.1.2}$$

which, up to a discrete displacement by $L_z/2$, fixes the spanwise location of the flow structures. While we have not imposed further symmetries, all our solutions satisfy the additional symmetries

$$s_2[uvw](x, y, z) = [-u, -v, w](-x + L_x/2, -y, z + L_z/2) \tag{5.1.3}$$

and

$$s_3[uvw](x, y, z) = [-u, -v, -w](-x, -y, -z + L_z/2). \tag{5.1.4}$$

These are the symmetries of the Nagata-Busse-Clever equilibrium, see e.g. (Schmiegel and Eckhardt, 1997; Gibson et al., 2008) for a discussion.

The different box size compared to the calculations by Nagata (Nagata, 1990) and Clever and Busse (Clever and Busse, 1997) has the effect of moving the first bifurcation to a higher Reynolds number, namely $\mathrm{Re} = 163.8$, where a pair of fixed points appears in a saddle-node bifurcation. The lower branch equilibrium (LB) has one unstable direction, the upper branch equilibrium (UB) is linearly stable in the symmetry-reduced subspace. Since the laminar profile is linearly stable for all Reynolds numbers (Drazin and Reid, 2004), there now coexist two different kinds of

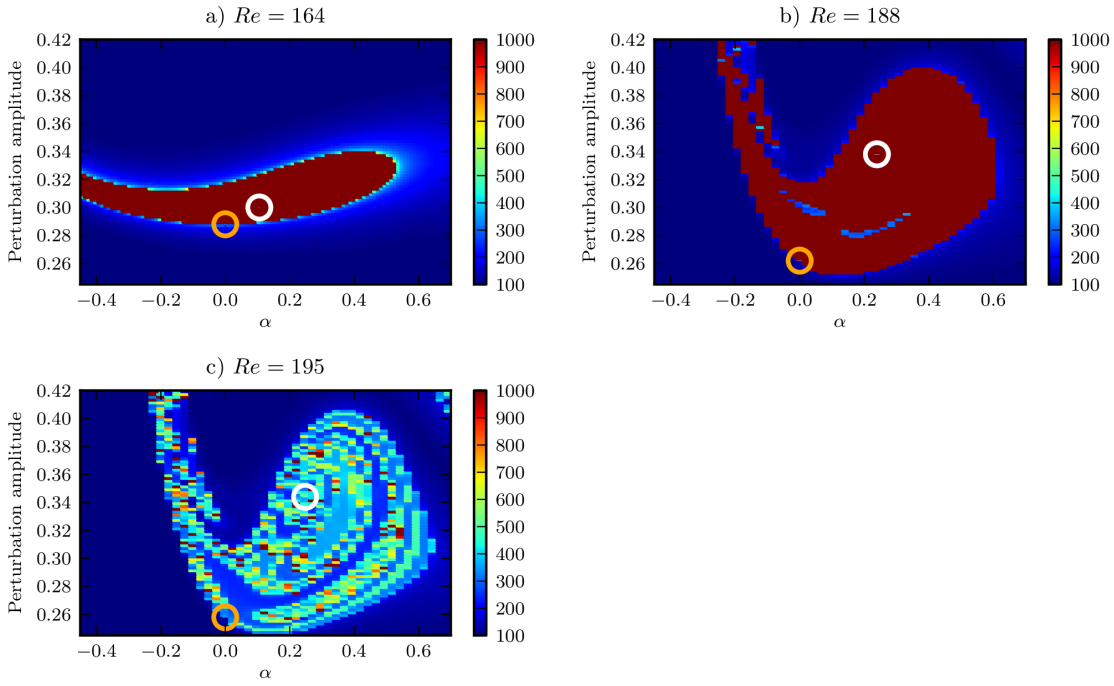

Figure 5.1.1.: The basins of attraction of the attractors in plane Couette flow for three Reynolds numbers near the bifurcation point of the Nagata-Clever-Busse state. Basins are depicted by the lifetime of initial conditions in advective timeunits, i.e. the time it takes for an initial condition to come into a distance $E_{cf}(u(t) - u_{lam}) < \epsilon$ of the laminar state. States on the x-axis are obtained by interpolating between the lower- and the upper-branch solution, rescaled by a factor that ensures that the distance between the two solutions in the plot is equal to the L_2-norm of their difference, see equation (5.1.6). These states are then scaled in amplitude along the y-axis. The lower branch equilibrium is marked with an orange circle, the upper one with a white circle. (a) For Re just slightly above the bifurcation point, the basin of attraction of the upper branch is a small region with a bubble-like shape. Its boundary is formed by the stable manifold of the lower branch. (b) For Re = 188, the overall structure has not changed a lot, though the attractor is no longer a fixed point but a chaotic orbit. (c) At Re = 188.51 a boundary crisis occurs – the chaotic attractor becomes "leaky" and all trajectories eventually relaminarize. This bubble-like shape remains visible as an envelope of the initial conditions for longer living states, though.

attractors, the laminar flow and a set of attractors related to UB by symmetry. The separatrix of their basins of attraction is formed by the stable manifold of LB.

The situation is illustrated in figure 5.1.1(a). The initial conditions that correspond to the points in the plane of the figures are spanned by the laminar profile, and the upper and lower branch states. The x-axis is a linear interpolation between LB and UB and the y-axis gives the perturbation amplitude with which the state is scaled.

Formally, the initial conditions are given by

$$u(\alpha, A) = A \cdot u_\alpha / \|u_\alpha\| \tag{5.1.5}$$

with

$$u_\alpha = u_{LB} + \frac{\alpha \cdot (u_{UB} - u_{LB})}{\sqrt{\|u_{UB} - u_{LB}\|^2 - (\|u_{UB}\| - \|u_{LB}\|)^2}}. \tag{5.1.6}$$

The division by the root scales the x-axis in a way that the distance between LB and UB in the plot corresponds to the L_2-norm of the difference between the two fixed points.

The basins of attraction are obtained by studying the lifetimes, defined as the time it takes for the flow to satisfy for the first time the condition $E_{cf}(u(t) - u_{lam}) < \epsilon = 10^{-8}$. Initially, when the basin of attraction is closed and trajectories are attracted to a stable fixed point that is not the laminar profile, there is a solid block of long, actually infinite, lifetimes. The stable fixed point lies somewhere in the center of the blob and the unstable saddle lies on its boundary.

A notable feature of these plots is the bubble shape of the basins of attraction of the stable fixed points. The unstable manifold of the unstable fixed point that loops around the stable fixed point folds back to approach the other branch of the stable manifold. This behaviour was identified by Lebovitz (Lebovitz, 2009, 2012) in a model flow, and as the present figures shows it also is relevant to full representations of the flow. In view of the bifurcation structures described in (Mellibovsky and Eckhardt, 2011) one can expect that this bubble shape is rather generic.

As Reynolds number increases, the stability properties of LB do not change up to at least $\mathrm{Re} = O(10^4$ (Wang et al., 2007). On the other side, UB is only an attractor for a very short range and undergoes a Hopf bifurcation at $\mathrm{Re}_H = 166.05$, which has already been noted by Clever and Busse (Clever and Busse, 1997). The bifurcation is supercritical, as is revealed by the emergence of a limit cycle whose amplitude grows as $\sqrt{\mathrm{Re} - \mathrm{Re}_H}$. The emerging stable periodic orbit undergoes a period doubling at $\mathrm{Re} = 178.9$ which, for this domain size, results in a period doubling cascade.

While the way to represent fixed points in a bifurcation diagram is straightforward, it is less so for periodic orbits or chaotic trajectories. To visualize the attracting state once it gets more complicated we introduce a reduced representation of the flow by focussing on the maxima in energy: we calculate a typical trajectory originating near UB (and hence not lying in the immediate basin of attraction of the laminar state), omit an initial transient and all intermediate times except for the maxima. We then keep values of the maxima in $\sqrt{E_{cf}}$ to represent the flow. The method is illustrated in figure 5.1.2, where a short section of a typical chaotic trajectory for $\mathrm{Re} = 187.8$ is shown. The maxima are marked with symbols corresponding to the symbolic dynamics that will be introduced in section 5.1.3.

The bifurcation cascade is summarized in figure 5.1.3, where the square root of the cross-flow energy E_{cf} is plotted. The attractor is plotted with a dot for every

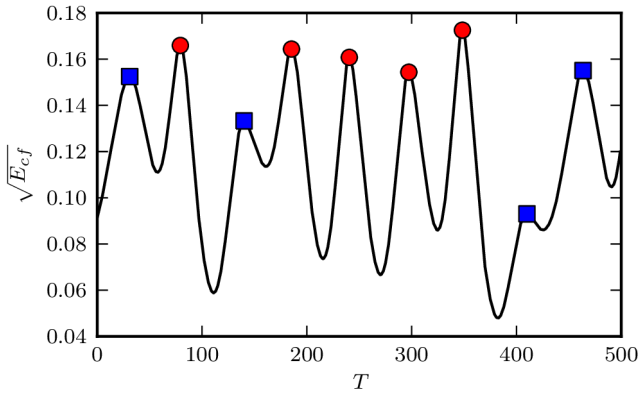

Figure 5.1.2.: Example of a typical chaotic trajectory at Re = 187.8. For the reduction to a map, we only keep the energies at the maxima. The different symbols assigned to the maxima follow from the symbolic dynamics that will be introduced in section 5.1.3: squares represent the symbol 0 and circles the symbol 1.

maximum of E_{cf}, LB is a dashed line and UB is a dotted line once it becomes unstable. In this representation the emergence of a limit cycle at Re_H with an amplitude that grows as $\sqrt{\mathrm{Re} - \mathrm{Re}_H}$ is clearly visible. It is followed by a period doubling cascade resulting in a chaotic attractor. We find a stable period three window from Re = 183.8 to Re = 185.0, followed by a new period doubling cascade of the period three orbit. The basin of attraction is still confined to a small region in state space, as is evident from figure 5.1.1(b), which shows the basin for Re = 188. Compared to the above picture at Re = 164, the general shape of the basin has not changed. Near the crisis bifurcation perhaps also the homoclinic tangles described in (van Veen and Kawahara, 2011) form. The transition in the lifetimes is in agreement with the phenomenology observed also in the two-dimensional map described in (Vollmer et al., 2009).

For $\mathrm{Re} > \mathrm{Re}_c = 188.51$, there are no more dots in figure 5.1.3: all trajectories eventually relaminarize. Our interpretation is that at Re_c the chaotic attractor touches the fixed point LB (or, equivalently, its stable manifold) and a boundary crisis (Grebogi et al., 1983) occurs and the attractor becomes "leaky". Even though the crisis is not visible in figure 5.1.3 due to the chosen representation, it will become visible later in another view of state space, see figures 5.1.11 below. We show a state space plot of Re = 195 in figure 5.1.1(c). The bubble shape that formed the basin of attraction of the chaotic attractor before the crisis is still visible. But the lifetimes of the initial conditions from that region now are no longer infinite but vary drastically between almost direct decay and very long survival. The distribution of the lifetimes (not shown here) turns out to be exponential – a signature of a chaotic saddle left behind by the boundary crisis (Lai and Tél, 2011).

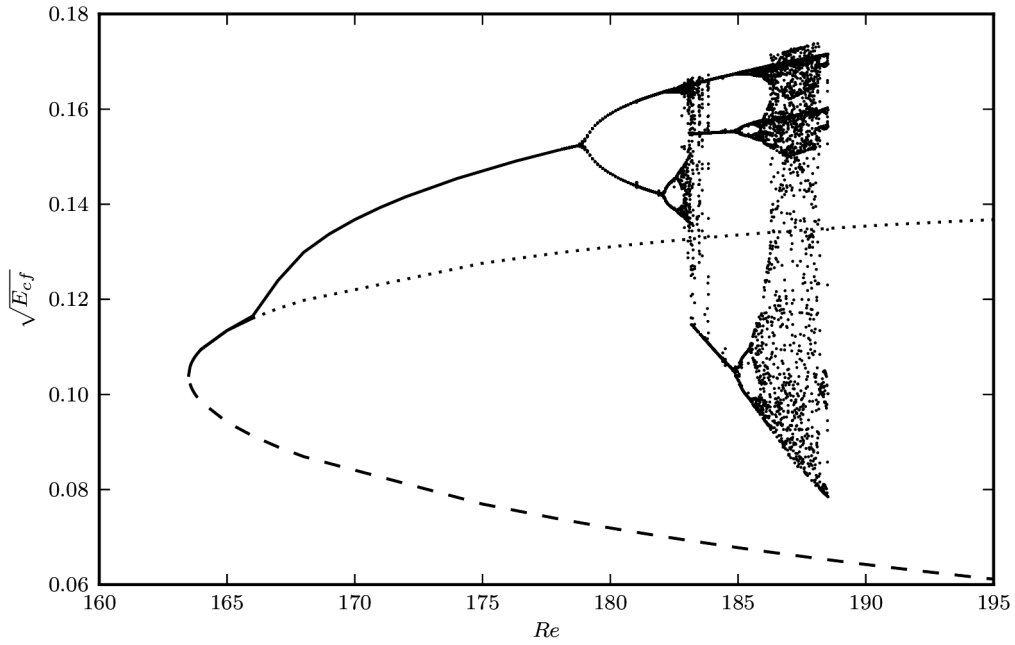

Figure 5.1.3.: The square root of the cross-flow energy $\sqrt{E_{cf}}$ for the upper- and lower-branch solutions and the attractor coexisting with the laminar state. To visualize periodic orbits and chaotic attractors, we plot every maximum of E_{cf} with a dot. The Nagata-Busse-Clever state is born in a saddle-node bifurcation at Re = 163.8, we plot the lower branch with a dashed line and the upper branch with a line as long as it is stable, and with a dotted line afterwards. The upper branch loses stability in a Hopf bifurcation at Re = 166.05, the emergence of a limit cycle is nicely visible. It undergoes a period doubling cascade. After the boundary crisis at Re = 188.51, the laminar state is the only attractor.

5.1.3. Symbolic dynamics

In this and the next section we focus on the situation just before the crisis, namely at Re = 187.8, where the attractor appears chaotic. We now use the reduction of the flow to the location of its maxima to introduce an approximately one-dimensional map of the flow. We denote the value of the i-th maximum of $\sqrt{E_{cf}}$ along this trajectory by x_i and plot x_{i+1} vs. x_i. This then gives a 1-dimensional projection of the Poincaré return map, $x_i \to x_{i+1} = f(x_i)$. Figure 5.1.4 shows a plot of the map obtained from a trajectory with 10798 maxima.

In this representation, the attractor looks very thin and almost one-dimensional, though a fractal structure can be seen perpendicular to it. In this sense it is qualitatively similar to fractal attractors in well-known low-dimensional systems like the Hénon map with standard parameters. The attractor consists of several branches, all of which show a distinctive maximum between $x_i = 0.14$ and $x_i = 0.16$, but the

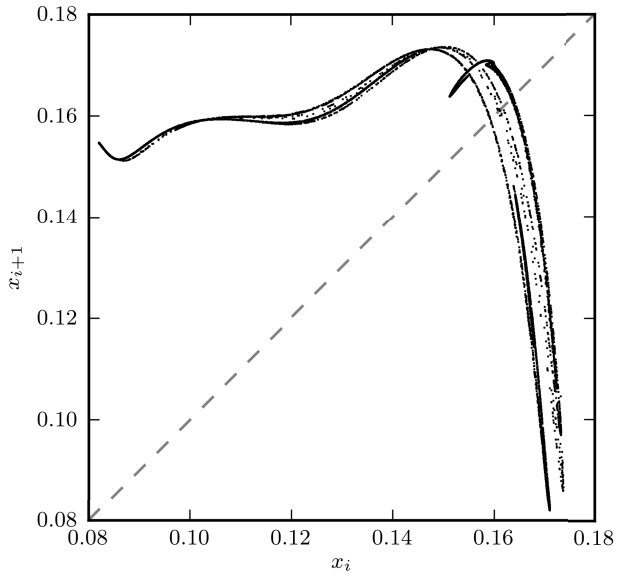

Figure 5.1.4.: The chaotic attractor at Re = 187.8. It is obtained by calculating for a trajectory that contains 10799 maxima of E_{cf}. The values of the maxima of $\sqrt{E_{cf}}$ are denoted x_i for the i-th maximum and the map is obtained by plotting x_{i+1} vs. x_i. It consists of several branches that lie close to each other and, for the purposes of labelling trajectories, can be collapsed into a one-dimensional uni-modal map. A binary symbolic dynamics can be introduced according to the relative location of the points: points that lie on a branch left or right of the maximum are labeled 0 or 1, respectively.

location of the maxima do not coincide.

Given this representation of the attractor, we introduce a binary symbolic dynamics in the usual way: on each branch, a point is labeled as 0 or 1 if it lies to the left or right of the maximum, respectively. The symbolic dynamics is shown in figure 5.1.5 for the same snapshot of the trajectory as in figure 5.1.2. We find that a partition cannot be based on a single value of x_i and that the branch on which it comes to lie also has to be taken into account: x_6 is a little lower than x_9 but assigned the symbol 1 while x_9 is assigned 0 because of its different location relative to the maximum of the corresponding branch. The two rightmost squares in figure 5.1.5(b) lie on the branch of the rightmost maximum while the circle just above them lies on the branch of a maximum further left.

5.1.4. Periodic orbits

In this section, we will describe the periodic orbits we found at Re = 187.8. We obtain initial guesses by scanning the map f (figure 5.1.4) for close returns along a trajectory

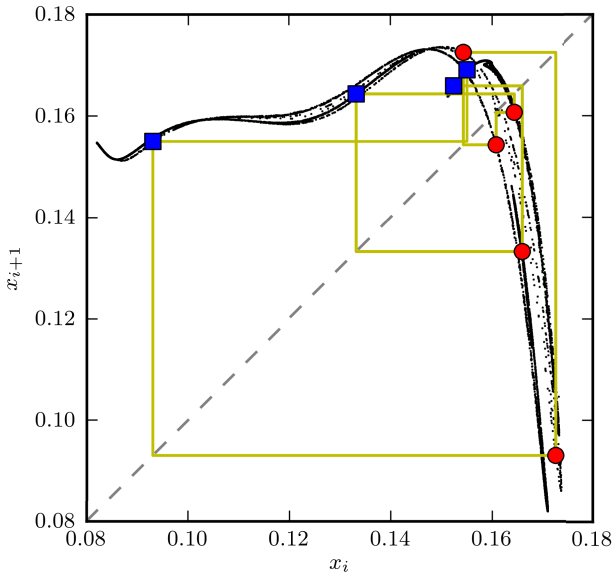

Figure 5.1.5.: Symbolic dynamics for the same trajectory as in figure 5.1.2, squares are 0 and circles 1. The rightmost square is left of the maximum and has to be labeled as 0 despite the fact that it is further right than the leftmost circle.

Table 5.1.1.: Properties of the periodic orbits. The first column contains the symbolic sequence of the orbit, the second column the period in advective time-units of Navier-Stokes. The third column gives the Reynolds numbers where the orbits are created. The remaining columns give the eigenvalues with the largest magnitudes. where Λ_i denotes the eigenvalues of the monodromy matrix and $\lambda_i = \ln|\Lambda_i|/T$ the Lyapunov exponents. The eigenvalues Λ_2 and Λ_3 correspond to streamwise and spanwise translations and are mathematically equal to one, the difference $\Lambda - 1$ serves as a measure for the accuracy of the numerics. All orbits have one and only one unstable eigenvalue.

Orbit	T	Re_{Bif}	Λ_1	λ_1	$\Lambda_2 - 1$	$\Lambda_3 - 1$	Λ_4	λ_4
$\overline{1}$	55.22	166.0	-2.64	0.0176	$9.83 \cdot 10^{-7}$	$-5.65 \cdot 10^{-7}$	0.4	-0.0166
$\overline{01}$	106.95	179.3	-4.79	0.0146	$2.11 \cdot 10^{-6}$	$-5.33 \cdot 10^{-7}$	0.13	-0.0191
$\overline{001}$	162.1	181.9	-4.6	0.0094	$1.95 \cdot 10^{-5}$	$2.76 \cdot 10^{-6}$	0.05	-0.0185
$\overline{011}$	159.21	181.9	9.43	0.0141	$1.37 \cdot 10^{-7}$	$-4.33 \cdot 10^{-6}$	0.048	-0.0191
$\overline{0111}$	215.84	182.1	-27.73	0.0154	$3.56 \cdot 10^{-4}$	$-8.81 \cdot 10^{-7}$	0.017	-0.0189
$\overline{01101}$	266.87	182.2	-50.67	0.0147	$4.21 \cdot 10^{-3}$	$-1.70 \cdot 10^{-5}$	0.0063	-0.0190
$\overline{01111}$	270.65	182.2	76.63	0.0160	$4.87 \cdot 10^{-6}$	$4.87 \cdot 10^{-6}$	0.0061	-0.0188

and then use channelflows excellent Newton-Krylov-Hookstep algorithm, based on (Viswanath, 2007) and implemented by John F Gibson in channelflow (Gibson, 2011), for finding periodic orbits. Since the attractor for this Reynolds number is chaotic, we expect all orbits to be linearly unstable. For reasons of computational stability we restrict the search to orbits of symbolic period not exceeding five.

With this method we found seven different orbits – they are listed, along with their properties in table 5.1.1. The first column contains the symbolic name of the orbit, the second one the period of the orbit in time-units of Navier-Stokes. The Reynolds number where the orbits bifurcate, either pitchfork or saddle node bifurcations, are given in the fourth column. The orbit $\overline{1}$ is created in a Hopf-bifurcation of UB, the orbits $\overline{01}$ and $\overline{0111}$ result from period-doublings of the former one. The pairs of the two period-3 and period-5 orbits are the result of saddle-node bifurcations. To better illustrate the bifurcation sequence, we show the bifurcation diagram again in figure 5.1.6 with the bifurcation points indicated by dashed lines. The solid line at Re = 187.8 indicates the Reynolds number where the analysis of the symbolic dynamics takes place.

The bifurcation sequence of the orbits is almost the same as the universal sequence described by Metropolis, Stein and Stein (Metropolis et al., 1973), with the only exception being that the period-doubling of $\overline{01}$ that creates $\overline{0111}$ takes place slightly after the saddle-node bifurcations in which the orbits $\overline{001}$ and $\overline{011}$ appear. We have not found the orbits $\overline{0011}$, $\overline{0001}$, $\overline{00111}$, $\overline{00011}$, $\overline{00001}$ and $\overline{00101}$ – which is in accordance with the universal sequence and also found in the the logistic map for $R < 4$.

The eigenvalues Λ_i of the monodromy matrix of the periodic orbits are calculated using channelflow's Arnoldi iteration (Viswanath, 2007). From the eigenvalues Λ_i one can extract Lyapunov exponents $\lambda_i = \ln|\Lambda_i|/T$. The four eigenvalues of largest magnitude and the corresponding nontrivial Lyapunov exponents are given in the last six columns of table 5.1.1. All of the periodic orbits have exactly one unstable eigenvalue Λ_1 and two eigenvalues $\Lambda_{2,3}$ that correspond to translation along x and time that are theoretically strictly equal to 1 (translations along z are excluded by the enforced shift-and-reflect symmetry). The deviation of $\Lambda_{2,3}$ from 1 can be used as a measure of the accuracy of our numerics. If the calculations are restricted to the full symmetry-subspace of the Nagata state, the marginal eigenvalues corresponding to shifts in the downstream direction disappear. Λ_4 is the least stable eigenvalue of the orbit and measures the contraction in the directions perpendicular to the attractor. The positive first Lyapunov exponent varies between 0.0094 and 0.176, where the largest value comes from the shortest orbit $\overline{1}$. All orbits have exactly one unstable direction and their weakest contracting Lyapunov exponent λ_4 is of the same order, this supports the conjecture that the system can be approximated by a one dimensional map.

The upper branch becomes unstable via a Hopf bifurcation and at Re = 187.8 the complex conjugate pair of eigenvalues is still the only unstable ones. The values

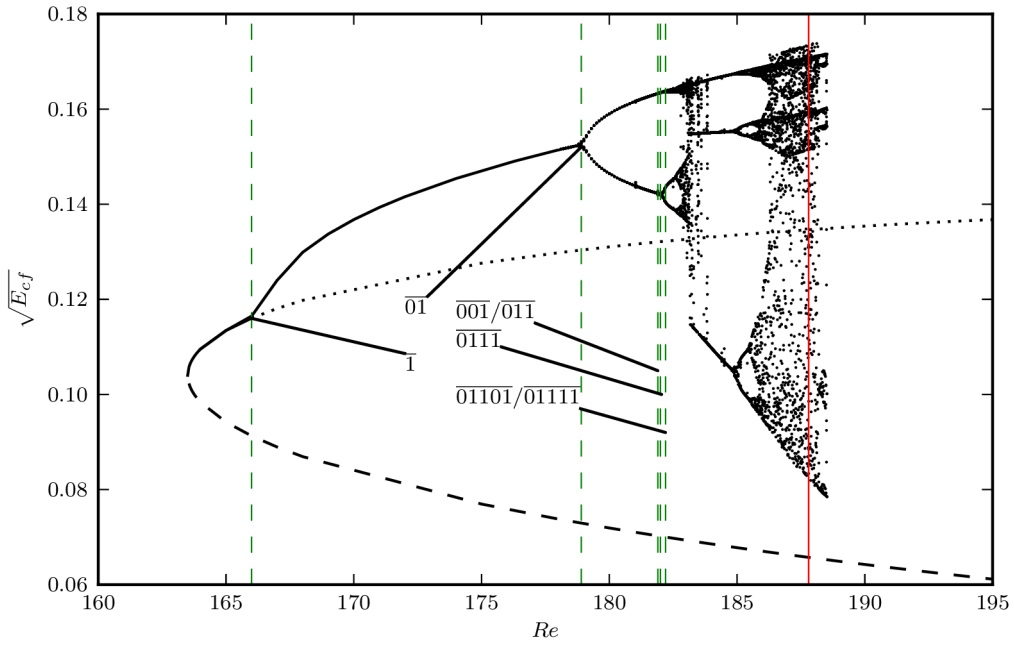

Figure 5.1.6.: Critical Reynolds numbers for the periodic orbit bifurcations, indicated with dashed lines. The straight line at Re = 187.8 corresponds to the Reynolds number where the analysis takes place.

are $\lambda_{1,2} = 0.023 \pm i0.128$ and the imaginary part corresponds to a period of $T = 2\pi/\mathrm{Im}(\lambda) = 48.93$ which is not too far from the period of the orbit $\overline{1}$.

We have not been able to determine the orbit $\overline{0}$.

Cobweb-plots of all orbits are presented in figure 5.1.7. While most of the orbits concentrate in the upper right corner of the map, only $\overline{001}$ stretches out to the lowest and highest values. Since $\overline{001}$ is the only orbit with a sequence 00, this suggests that longer orbits containing 00 would also stretch out to those more extreme regions of the attractor.

In figures 5.1.8 and 5.1.9 we present orbits in a plane spanned by the cross-flow energy E_{cf} and the wall shear rate $u^* = \sqrt{\partial/\partial y U|_{y=\pm 1}}$, respectively. Figure 5.1.8 shows nicely the composition of the longer orbits as repetitions of the shorter ones. For example, the orbit $\overline{011}$ is very similar to $\overline{0111}$ and $\overline{01111}$, except that the latter ones have one (two) additional peak(s) that looks quite similar to $\overline{1}$. Note also how the orbits explore the ranges covered by a turbulent trajectory, lending support to the idea that periodic orbits can be used to represent all possible motions and that averages could be calculated from the periodic orbits.

We show some averaged quantities of the orbits in figure 5.1.10. We use small letters for the fluctuating components and U_0 for the base flow. The left plot shows

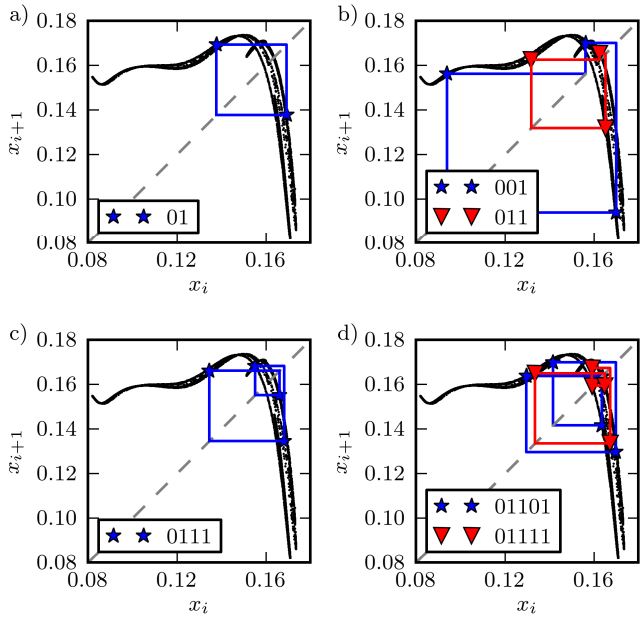

Figure 5.1.7.: The periodic orbits, presented in cobweb-plots. Only the orbit $\overline{001}$ visits the extremer position on the attractor.

$\langle u \rangle + U_0$, the middle one $\langle uu \rangle$ and the right one $\langle vv \rangle$. In all three plots, the mean profiles for nearly all orbits are impossible to distinguish among each other. Within the group of orbits of period less than six, the exception is $\overline{001}$, which is marginally offset to the right in (b) and (c). We indicate the averages obtained from a chaotic trajectory with 5000 time units by crosses – they can hardly be distinguished from the averages of the periodic orbits.

The motion of the walls injects energy into the fluid motion which in turn is dissipated by viscosity. The energy balance can be written as (Gibson et al., 2008)

$$\dot{E} = I - D,$$

where the change of the kinetic energy density E is from the bulk viscous dissipation rate D and the wall-shear power input I,

$$E = \frac{1}{V} \int_V \frac{1}{2} \left(\mathbf{u} + \mathbf{U}_0 \right)^2 \mathrm{d}V,$$

$$D = \frac{1}{V} \int_V \left(\nabla \times \left(\mathbf{u} + \mathbf{U}_0 \right) \right)^2 \mathrm{d}V,$$

$$I = 1 + \frac{1}{2A} \int_A \left(\left. \frac{\partial u}{\partial y} \right|_{y=1} + \left. \frac{\partial u}{\partial y} \right|_{y=-1} \right) \mathrm{d}x \mathrm{d}z.$$

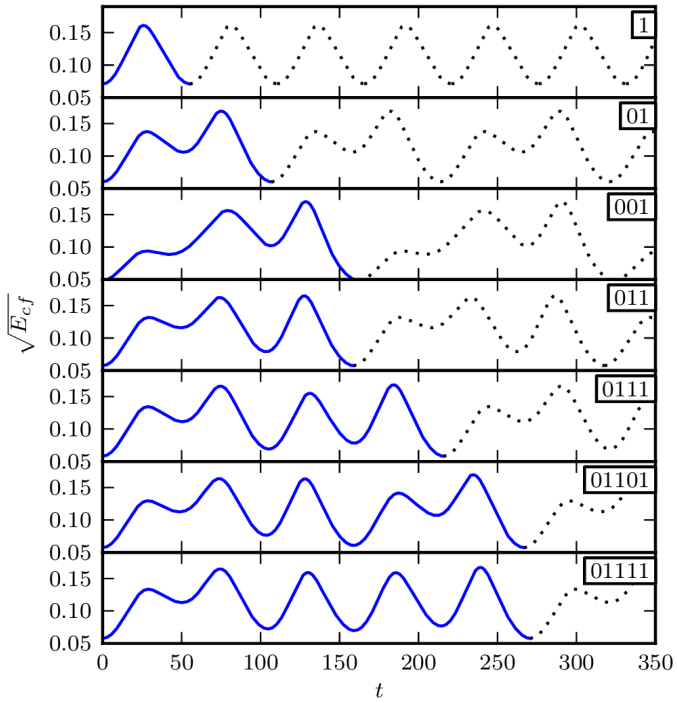

Figure 5.1.8.: The root of the cross-flow energy $\sqrt{E_{cf}}$ for all periodic orbits. One cycle of each periodic orbit is shown solid, with continuation dotted. The composition of the longer orbits from parts of the shorter ones is nicely visible.

Here $V = 2L_xL_z$ and $A = L_xL_z$. The normalizations are chosen so that $D = I = 1$ for laminar flow and $\dot{E} = I - D$.

In a plot of I vs. D, fixed points must lie on the diagonal $I = D$. For periodic orbits and also for the non-periodic chaotic motions, the center, defined as time-averages of I and D, will also lie on the diagonal. In figure 5.1.11 we present all periodic orbits and a chaotic trajectory. The points corresponding to the maxima of E_{cf} are marked with circles for symbol 0 and squares for 1, the diamond shaped symbol in the lower left corner marks LB. There are three points noteworthy in this figure: First, the symbols are clearly separated and a partition could be based on the location of a maximum in that representation. Second, the periodic orbits capture all of the qualitative features and loops of the chaotic trajectory. And third, one sees that the chaotic trajectory in the background is about to touch LB, the event that will trigger the crisis.

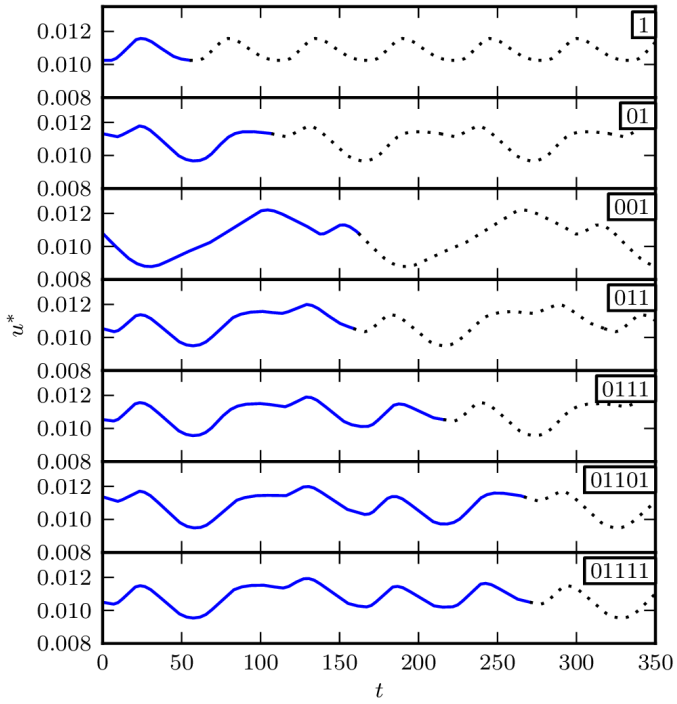

Figure 5.1.9.: The wall shear rate for all periodic orbits. One cycle of each periodic orbit is shown solid, with continuation dotted. While u^* has maxima at roughly the same points as E_{cf}, the symbolic dynamics can not be recognized.

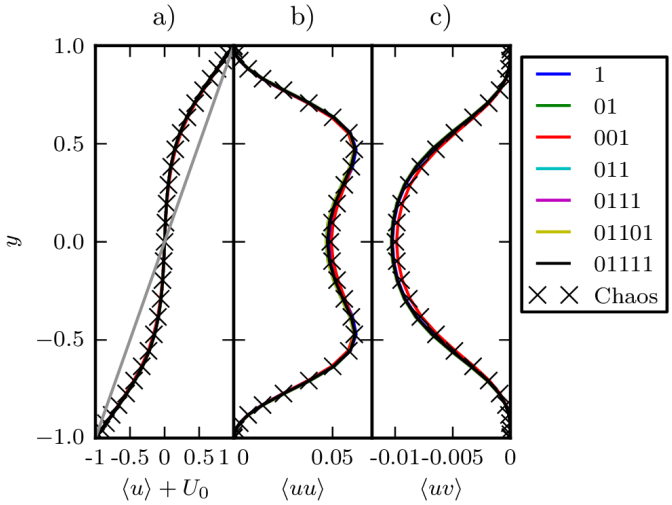

Figure 5.1.10.: Averaged quantities of the periodic orbits (lines) and a chaotic trajectory (crosses) as a function of y. (a) Averaged downstream velocity u.(b) Fluctuations in the downstream component $\langle uu \rangle$. (c) Average of $\langle uv \rangle$.

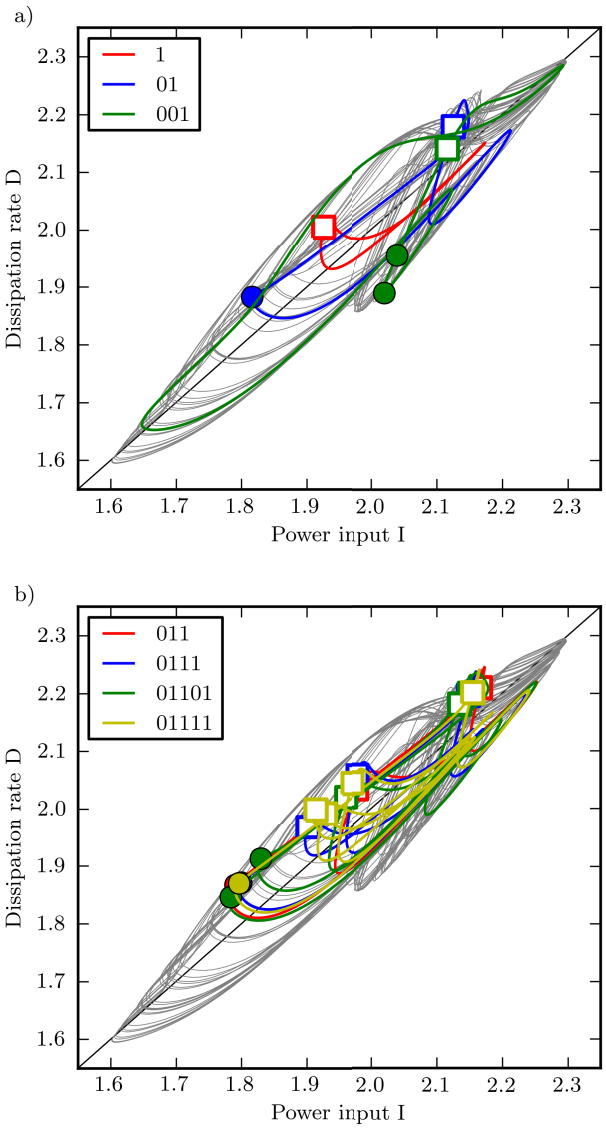

Figure 5.1.11.: The periodic orbits in the input-dissipation plane. In the background a chaotic trajectory is plotted in gray. The maxima of E_{cf} along the orbits are indicated with circles for symbol 0 and open squares for 1. In this plots, the regions of the different symbols do not overlap. It is interesting to notice that the only two symbols below the diagonal belong to the orbit $\overline{001}$.

5.1.5. Final remarks

The detection of periodic orbits in this system was certainly assisted by the fact that the flows studied here were confined to a small domain, restricted by a discrete shift and reflect symmetry, and also analyzed at a low Reynolds number. In this sense, it is similar to the study of fluctuations in the Kuramoto-Shivashinsky equation (Christiansen et al., 1997). Nevertheless, the reduction to a symbolic dynamics compatible with a unimodal one-dimensional map and the association of the orbits to the universal Metropolis-Stein-Stein sequence shows that also this high-dimensional system follows the universal dynamics identified in low-dimensional systems. This raises the hope that bifurcation analyses and periodic orbits can also be identified and used in other systems, such as pipe flows or plane Poiseuille flow. The ultimate goal, however, is to analyze not only chaotic but also some turbulent flows in terms of periodic orbits, as suggested e.g. in (van Veen et al., 2006).

Acknowledgements

We would like to thank John F Gibson for developing and providing access to his open source Channelflow.org code, on which the calculations presented here are based, and Norman Lebovitz and Tobias M Schneider for helpful discussions. We thank Predrag Cvitanović for maintaining a continously updated source on periodic orbit theory at chaosbook.org. This work was supported in part by the German Research Foundation within Forschergruppe 1182.

5.2. Increasing Lifetimes and the Growing Saddles of Shear Flow Turbulence

Tobias Kreilos,[1,2] **Bruno Eckhardt,**[2,3] **and Tobias M. Schneider**[1,4]

[1]Max Planck Institute for Dynamics and Self-Organization, Am Fassberg 17, 37077 Göttingen, Germany
[2]Fachbereich Physik, Philipps-Universität Marburg, 35032 Marburg, Germany
[3]J.M. Burgerscentrum, Delft University of Technology, Mekelweg 2, 2628 CD Delft, The Netherlands
[4]Institute of Mechanical Engineering, École Polytechnique Fédérale de Lausanne, 1006 Lausanne, Switzerland

Published in Physical Review Letters 112, 044503 (2014)

In linearly stable shear flows turbulence spontaneously decays with a characteristic lifetime that varies with Reynolds number. The lifetime sharply increases with Reynolds number so that a possible divergence marking the transition to sustained turbulence at a critical point has been discussed. We present a mechanism by which the lifetimes increase: in the system's state space, turbulent motion is supported by a chaotic saddle. Inside this saddle a locally attracting periodic orbit is created and undergoes a traditional bifurcation sequence generating chaos. The formed new 'turbulent bubble' is initially an attractor supporting persistent chaotic dynamics. Soon after its creation it collides with its own boundary, by which it becomes leaky and dynamically connected with the surrounding structures. The complexity of the chaotic saddle that supports transient turbulence hence increases by incorporating the remnant of a new bubble. As a a result, the time it takes for a trajectory to leave the saddle and decay to the laminar state is increased. We demonstrate this phenomenon in plane Couette flow and show that characteristic lifetimes vary non-smoothly and non-monotonically with Reynolds number.

The emergence of turbulence in shear flows such as pipe or Couette flow has puzzled scientists for more than a century, because the transition is not associated with a linear instability of the laminar base flow (Grossmann, 2000) and requires perturbations of finite amplitude (Darbyshire and Mullin, 1995; Schmiegel and Eckhardt, 1997). Once triggered, turbulence in these flows is not persistent but can spontaneously decay (Eckhardt et al., 2007). This phenomenology can be understood in the context of dynamical systems, where the structure of the state space - the space of all instantaneous velocity fields - is investigated. The state space is filled with a multitude of unstable invariant solutions and a turbulent trajectory transiently visits those solutions before it eventually escapes their neighborhood and decays to the laminar state. This picture of a *chaotic saddle* that supports transient turbulence has been corroborated by the direct identification of numerous invariant solutions and some dynamical connections between them both in plane Couette and pipe flow (Eckhardt,

2008; Kreilos and Eckhardt, 2012; Kawahara et al., 2012). Further support comes from the distribution of transient lifetimes, which is found to be an exponential and thus of the form expected for chaotic saddles. The characteristic time of the exponential distribution increases sufficiently rapidly with Reynolds number Re to explain why decays are rarely observed at high Re. How exactly the characteristic lifetime τ increases has attracted much recent attention, specifically the question whether there is a critical Re at which lifetimes diverge and turbulence becomes sustained (Grebogi et al., 1986; Bottin and Chaté, 1998; Hof et al., 2006; Peixinho and Mullin, 2006; Willis and Kerswell, 2007; Hof et al., 2008; Schneider and Eckhardt, 2008; Schneider et al., 2010a; Eckhardt et al., 2007; Kerswell, 2005; Crutchfield and Kaneko, 1988; Kadanoff and Tang, 1984; Duguet et al., 2008; Gibson et al., 2008; Vollmer et al., 2009; van Veen and Kawahara, 2011).

While previous studies have characterized a functional form of the dependence of τ on Re, we here present a mechanism that leads to increasing lifetimes. Within the picture of a turbulent trajectory meandering between invariant solutions before eventually escaping the chaotic saddle and decaying to laminar flow, increasing turbulent lifetimes are directly linked to changes of the chaotic saddle structure. We describe a sequence of events within a small range of Re that add an infinite number of invariant solutions to the chaotic saddle. Thereby the complexity of the chaotic saddle grows and lifetimes increase. During the process the lifetimes diverge for some Reynolds numbers, leading to a non-monotonic and non-smooth variation of τ with Re.

In extended flow systems, the local relaminarization of turbulence can be overcome by spatial spreading so that turbulence may become sustained in a percolation-like phase transition despite its local decay (Allhoff and Eckhardt, 2012; Avila et al., 2011). To separate the strongly increasing variations of τ in a confined domain from the spatial spreading of turbulence, we consider plane Couette flow in a small periodic box. The box is chosen such that the flow is described by a comparably low number of degrees of freedom ($\mathcal{O}(10^5)$). This allows for a detailed analysis of the high-dimensional state-space, which remains computationally challenging; specifically we consider the system studied previously in (Kreilos and Eckhardt, 2012), which is a bit longer and narrower than the minimal flow unit studied for example in (Waleffe, 1998). Plane Couette flow is the flow of a fluid between two parallel plates moving at constant speed in opposite direction governed by the incompressible Navier Stokes equations $\partial_t \mathbf{u} + (\cdot\mathbf{u}\nabla)\mathbf{u} = -\nabla p + \mathrm{Re}^{-1}\Delta\mathbf{u}$ together with the continuity equation $\nabla \cdot \mathbf{u} = 0$ and boundary conditions $\mathbf{u} = \pm\mathbf{e}_x$ at $y \pm 1$, where p is the pressure and y the wall-normal coordinate. The Reynolds number is defined by $Re = U_0 h/\nu$ with U_0 half the relative plate velocity, h half the plate separation and ν the viscosity of the fluid and using U_0 and h as velocity- and length-scale, respectively. Direct numerical simulations are performed using the pseudo-spectral solver channelflow (Gibson et al., 2008; Gibson, 2012) developed by John F. Gibson. The computational domain is of size $L_x \times 2h \times L_z = 2\pi \times 2 \times \pi$ with a resolution of $48 \times 33 \times 48$ modes subject to periodic boundary conditions in the homogeneous directions and enforced shift-and-

reflect symmetry $(u, v, w)[x, y, z] \equiv \sigma_{SR}(u, v, w)[x, y, z] = (u, v, -w)[x + L_x/2, y, -z]$.

Plane Couette flow is linearly stable for all Re and the first (known) non-trivial invariant solutions are the Nagata-Busse-Clever (NBC) states (Nagata, 1990; Clever and Busse, 1997; Waleffe, 1998), a pair of fixed points that are created in a saddle-node bifurcation. In our domain the bifurcation takes place at $Re = 163.8$ and the upper-branch solution (with higher energy) is attracting while the lower branch has a single unstable direction. As a consequence, the lower branch's stable manifold forms the separating boundary between trajectories approaching the upper branch and the laminar state (Skufca et al., 2006; Schneider et al., 2008). Increasing Re, the upper branch undergoes a period doubling cascade, generating chaos. At $Re = 188.51$ the chaotic attractor formed around the upper branch subsequently collides with the lower branch. In this boundary crisis (Kreilos and Eckhardt, 2012), the chaotic attractor becomes "leaky" and turns into a chaotic saddle, from which trajectories eventually escape. Similar scenarios have been found for periodic (Mellibovsky and Eckhardt, 2012) and localized (Avila et al., 2013) structures in pipe flow as well as in magnetohydrodynamics (Riols et al., 2013), indicating a generic mechanism by which the saddle that supports first short-lived turbulent transients in shear flows is created. Similar scenarios are well-known in low-dimensional dynamical systems (Grebogi et al., 1983; Lai and Grebogi, 1994; Lai and Tél, 2011).

As Re increases, the chaotic saddle grows to fill a larger part of state space. In Fig. 5.2.1 this is visualized for three successively increasing Re by plotting the lifetimes of initial conditions, see figure caption for details. Blue regions correspond to initial conditions that directly laminarize while the chaotic saddle appears as colorful fractal regions of rapidly varying lifetimes indicative of the sensitive dependence on initial condition. Since the lower branch solution has a single unstable direction, its stable manifold is of co-dimension one and the general topology of state space can be understood in a two-dimensional section. For Re=210 (panel *a*), the saddle only occupies a small area. As Re increases (panels *b* and *c*), the colorful fractal regions marking the saddle both grow and the variations inside become denser. As expected, the survival probabilities, shown in panel *d*, show exponential tails indicating a constant escape probability from the saddle. Their slope, the characteristic lifetime τ, increases with Re as the saddle structure fills the domain.

How does the complexity of the saddle increase? We explore one mechanism and specifically demonstrate a sequence of bifurcation events, in which an infinite number of invariant solutions is added to the saddle, leading to an increase in lifetimes; the mechanism bears a strong resemblance with the events at the creation of the saddle as summarized above. At $Re = 249.01$ a local saddle-node bifurcation creates a pair of new solutions which are not fixed points as the NBC-states but periodic orbits of period $T \simeq 60$. Of those, as for the NBC-states, the lower branch has a single unstable direction and the upper branch solution is an attractor. The stable periodic orbit is surrounded by its basin of attraction, visible in Fig. 5.2.2b) at $Re = 249.1$. As Re increases, the orbit undergoes a bifurcation cascade, creating infinitely many invariant

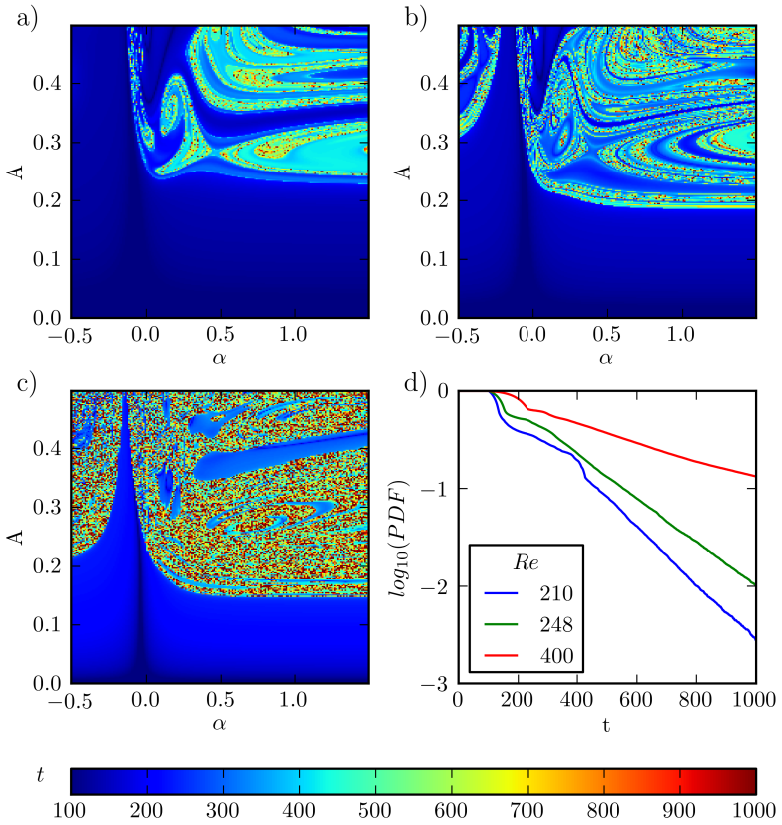

Figure 5.2.1.: (color online) (a) - (c): The growing turbulent saddle in state space for different Reynolds numbers, visualized by the lifetime of initial conditions in a 2D section. The 50,000 initial conditions in each panel are chosen by interpolating between lower- and upper-branch NBC-solutions on the x-axis and rescaling the perturbation amplitude A on the y-axis. The x-axis is rescaled such that the L_2-distance of the NBC-states is proportional to their distance in the projection, giving a physical meaning to the scales in the figure: $u = Au_\alpha/\|u_\alpha\|, u_\alpha = u_{LB} + \alpha(u_{UB} - u_{LB})/\sqrt{\|u_{UB} - u_{LB}\|^2 - (\|u_{UB}\| - \|u_{LB}\|)^2}$; In the sequence a) $Re = 210$. b) $Re = 248$. c) $Re = 400$, the saddle grows while it develops ever finer striations, indicating the structures supporting the saddle to get denser. d) Survival probabilities for the presented Reynolds numbers show clear exponential tails with increasing slope, indicating a characteristic lifetime which increases with Re.

states and generating a local chaotic attractor (panel c). On further increasing Re, the chaotic attractor grows until at $Re_c = 250.13$ it collides with its own basin boundary in a crisis bifurcation. While the signature of the basin of attraction of the former attractor is still visible for $Re > Re_c$ (panel d), trajectories may now escape from the newly created "inner" saddle into the already existing "outer" one. Thus at the crisis bifurcation the infinitely many invariant solutions from the former chaotic attractor are added to the turbulent saddle. As before, the two-dimensional visualization captures the essential features of the process since the lower-branch orbit has only a single unstable direction and hence a stable manifold of co-dimension one.

Over the sequence of these bifurcations, the decay rate from the turbulent saddle to the laminar state varies non-monotonically. Before the saddle-node bifurcation at $Re = 249.01$, the survival probabilities are distributed exponentially (Fig. 5.2.3a). Beyond $Re = 249.01$, there are initial conditions that are trapped inside the stable region and never decay. Thus, the overall distribution is a linear superposition of an exponential and a constant. The contribution of the non-decaying trajectories increases with higher Reynolds numbers as the attractor grows to fill more of the projection plane. After the boundary crisis at $Re = 250.13$, the new bubble becomes a part of the turbulent saddle. Initially the escape rate from the newly created embedded part of the saddle differs substantially from the outer saddle's escape rate. Thus, for short observation times the distribution is a linear superposition of two different exponentials resulting in a non-exponential variation.

To quantify the variation of lifetimes due to both parts of the saddle, we separate initial conditions into two groups corresponding to the location of the former attractor in the discussed projection plane and compute lifetimes for both parts of the saddle independently. This is detailed for $Re = 250.25$ in Fig. 5.2.3c, where instead of a *normalized* survival probability we plot the absolute number of initial conditions that survive for a given time. Since the initial conditions are uniformly distributed over the area shown in Fig. 5.2.2 the absolute numbers are a measure of the state space area that contributes to a given lifetime. The total number of data points is separated into those initial conditions from the inner and outer saddle. In Fig. 5.2.3 both individual distributions show clear exponential tails with characteristic lifetimes of 700 and 180, respectively. The sum of the two exponentials, weighted by the number of initial conditions in the two regions, (thick black line) almost perfectly recovers the total distribution. Similar non-exponential distributions due to several weakly connected saddle structures have also been studied in Hamiltonian systems, where nested saddles are shown to generate algebraic lifetime distributions (Hanson et al., 1985).

The variation of τ with Re for both the inner and outer saddle region is shown in Fig. 5.2.3(b). While it remains almost constant for the outer region, in the inner region the lifetime diverges while the attractor exists and drops after the boundary crisis, well approximated by a power law with exponent -2.1. The characteristic lifetime levels off slightly above the value of the outer saddle, indicating that trajectories

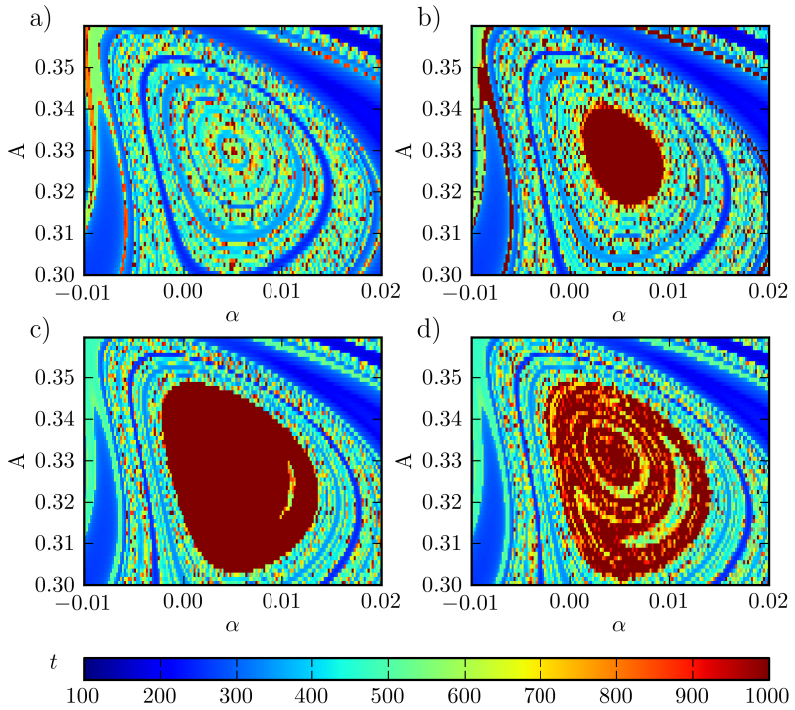

Figure 5.2.2.: (color online) Growth of the turbulent saddle via the emergence of a chaotic attractor followed by its destruction in a boundary crisis. Visualized is a small region of the saddle in a projection similar to Fig. 5.2.1 but spanned by the new pair of periodic orbits at $Re = 250$ (with the phase such that energy is maximal). Within the pre-existing chaotic saddle at $Re = 248.5$ (a) the saddle-node bifurcation creates the new pair of two periodic orbits, of which one is stable. Its basin of attraction at $Re = 249.1$ (b) just after the bifurcation is visible as the red region of initial conditions that never reach the laminar state. On further increasing Re, the orbit undergoes a bifurcation cascade generating a chaotic attractor, shown at $Re = 250.1$ (c), whose basin of attraction has grown. At $Re_c = 250.13$ the attractor collides with its boundary in a crisis bifurcation. Beyond the crisis bifurcation, the attractor has turned into a repellor and it is now a part of the turbulent saddle. The remnant of the attractor's basin of attraction remains visible at $Re = 250.25$ (d), where now the new "inner" saddle is immersed in the "outer" one.

that leave the inner saddle have to first pass through the outer one before decaying. Consequently, those trajectories have longer lifetimes. At higher Re, additional heteroclinic bifurcations will enhance the dynamical connectivity between the inner and outer saddle region which finally translates the higher lifetimes from the inner region to the whole saddle. Thereby, the characteristic lifetime of the saddle increases when it expands due to the incorporation of the newly created turbulent bubble.

We have found sudden expansions of the structure of the chaotic saddle at discrete Reynolds numbers as discussed for $Re \simeq 250$ at various Re, indicating that the

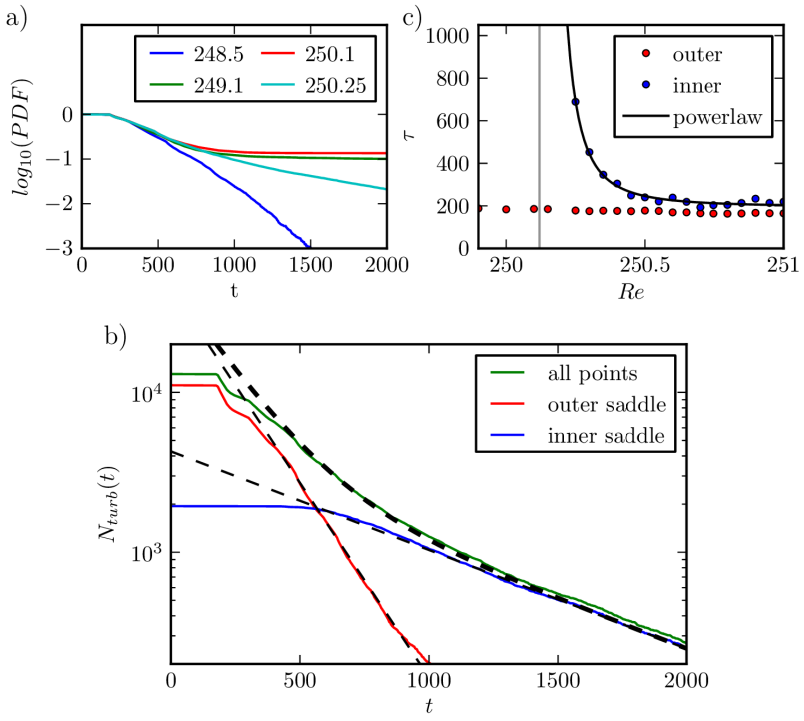

Figure 5.2.3.: (color online) Variations of lifetimes with Reynolds number. (a) Survival probability calculated from the data in Fig. 5.2.2 for all four Re. Before the saddle-node bifurcation ($Re = 248.5$), survival probabilities are exponentially distributed. After the bifurcation, the attractor causes an offset corresponding to the initial conditions that never decay. After the boundary crisis (Re=250.25), the distribution is non-exponential. b) Detailed analysis of the lifetime statistics at $Re = 250.25$, with the total number of trajectories that have not decayed up to a given time t as a function of time. In Fig. 5.2.2d the shape of the former attractor is still visible and allows to calculate the characteristic lifetime separately for initial conditions from the new, inner saddle and the outer saddle. Both show exponential tails with a characteristic lifetime of 700 and 180, respectively. The thick dashed line on top shows the weighted average of the two exponentials – it very well fits the observed distribution (green) apart from the trajectories that decay immediately. c) Reynolds number vs. characteristic lifetime τ as a function of Re, calculated separately for initial conditions from the inner and outer saddle. Lifetimes for the outer saddle are almost constant. The lifetime corresponding to the inner saddle diverges up to the crisis bifurcation, after which it drops drastically with a power-law behavior and levels slightly above the value of the outer saddle, showing that lifetimes have increased.

mechanism is a generic way to increase the complexity of the state space. While the presented example of a *stable* periodic orbit emerging in a saddle-node bifurcation followed by a chaotic cascade and a boundary crisis of a transiently existing attractor is observed for many parameters in our system, a more general variant of the discussed mechanism starts with *unstable* states. The sequence of events described above then appears in a weakly unstable subspace of the full system. This does not involve a global attractor for intermediate Re and is hence more difficult to detect as the lifetimes do not diverge. Yet, the same scenario still increases the complexity of the saddle, leading to growing lifetimes.

The formation of turbulent bubbles and their destruction at discrete Re values constitutes abrupt changes in the state space of shear flows. The described mechanism naturally leads to non-smooth and non-monotonic variations of τ as well as non-exponential lifetime statistics. While we have found these features for intermediate Re in the considered system they have not been reported yet for experimental lifetime studies. Apart from the symmetry restriction, which is only possible in numerics, one challenge is that the bifurcations become dense in Re and begin to overlap. To resolve this, very fine steps in Re are needed, as well as a very exact control of the applied perturbation. In a sufficiently coarse grained analysis, an apparent smooth variation emerges due to the collective effect of many bifurcations.

The mechanism we explored in this letter allows to directly relate state-space structures and their variation to statistical properties of transitional flows. While our analysis is focused on plane Couette flow, recent investigations of pipe flow and even mangnetohydrodynamic systems suggest that the described mechanism by which turbulent saddles grow in complexity are very generic. This emphasizes the significance of low-dimensional dynamical systems theory for understanding the physics of fluid mechanical systems with a subcritical transition to turbulence.

The authors acknowledge financial support by the *Niedersächsisches Ministerium für Wissenschaft und Kultur* and the *Deutsche Forschungsgemeinschaft*. We thank Hendrik Degering and Denny Fliegner for computing support.

5.3. Edge states for the turbulence transition in the asymptotic suction boundary layer

Tobias Kreilos[1,2], Gregor Veble[3,4], Tobias M. Schneider[2,5] and Bruno Eckhardt[1,6]

[1]Fachbereich Physik, Philipps-Universität Marburg, Renthof 6, D-35032 Marburg, Germany
[2] Max Planck Institute for Dynamics and Self-Organization, Am Fassberg 17, D-37077 Göttingen, Germany
[3] Pipistrel d.o.o. Ajdovščina, Goriška c. 50a, SI-5270 Ajdovščina, Slovenia
[4] University of Nova Gorica, Vipavska 13, SI-5000 Nova Gorica, Slovenia
[5] School of Engineering and Applied Sciences, Harvard University, 29 Oxford Street, Cambridge MA 02138, USA
[6]J.M. Burgerscentrum, Delft University of Technology, Mekelweg 2, 2628 CD Delft, The Netherlands

Published in Journal of Fluid Mechanics 726, pp. 100-122 (2013)

We demonstrate the existence of an exact invariant solution to the Navier-Stokes equations for the asymptotic suction boundary layer. The identified periodic orbit with a very long period of several thousand advective time units is found as a local dynamical attractor embedded in the stability boundary between laminar and turbulent dynamics. Its dynamics captures both the interplay of downstream oriented vortex pairs and streaks observed in numerous shear flows as well as the energetic bursting that is characteristic for boundary layers. By embedding the flow into a family of flows that interpolates between plane Couette flow and the boundary layer we demonstrate that the periodic orbit emerges in a saddle-node infinite-period (SNIPER) bifurcation of two symmetry-related travelling wave solutions of plane Couette flow. Physically, the long period is due to a slow streak instability which leads to a violent breakup of a streak associated with the bursting and the reformation of the streak at a different spanwise location. We show that the orbit is structurally stable when varying both the Reynolds number and the domain size.

5.3.1. Introduction

Recent progress in understanding transitional turbulence and the transition itself is based on the application of concepts from dynamical systems theory. The picture that emerges builds on invariant solutions of the underlying Navier-Stokes equations such as fixed points, travelling waves and periodic orbits. Together with their entangled stable and unstable manifolds these solutions form the backbone of a chaotic saddle that supports the observed turbulent chaotic dynamics: a trajectory approaches the invariant solutions along their stable manifolds and leaves again along the unstable ones; it consists of a chaotic sequence of close visits to the invariant solutions. Support

for this concept comes in particular from numerical observations in confined geometries, including plane Couette flow (Nagata, 1990; Schmiegel and Eckhardt, 1997; Kawahara and Kida, 2001; Viswanath, 2007; Gibson et al., 2009; Halcrow et al., 2009), Taylor Couette flow (Faisst and Eckhardt, 2000) and most prominently pipe flow (Faisst and Eckhardt, 2003; Wedin and Kerswell, 2004; Eckhardt et al., 2008; Willis et al., 2013), where flow structures very similar to the numerically calculated ones have been observed experimentally by Hof et al. (2004); see also Schneider et al. (2007a).

These flows are known to show a transition to turbulence for flow rates where the laminar profile is stable against infinitesimal perturbations (Grossmann, 2000); finite amplitude perturbations are required to trigger the transition. In these systems, the study of dynamically attracting objects within the boundary that separates laminar from turbulent dynamics – the so called edge states – has proven very fruitful as these states seem to guide the transition to turbulence (Toh and Itano, 2003; Skufca et al., 2006; Schneider et al., 2007b, 2008; Duguet et al., 2008; Mellibovsky et al., 2009; Duguet et al., 2010a; Kreilos and Eckhardt, 2012). In some confined flow geometries, edge states haven been very well characterized; they can be invariant solutions like fixed points in plane Couette flow, travelling waves in symmetry reduced pipe flow or extended plane Couette flow (Duguet et al., 2009; Schneider et al., 2010c) or be more complex and even chaotic in full pipe-flow (Schneider et al., 2007b).

The transition to turbulence in boundary layers that form around bodies in open flows shares with the internal flows just described the fact that turbulence is observed in parameter ranges where the laminar flow is still stable. Techniques of edge state tracking, initially developed for internal flows, have been adapted and applied to the Blasius boundary layer by Cherubini et al. (2011) and Duguet et al. (2012). However, limitations on the domain size prevented a full characterization of the invariant solutions. More generally, the extension of the concepts developed for internal flows to external flows is interesting because of the rich phenomenology seen in external flows. For instance, in addition to the near-wall downstream vortices and streaks, which seem similar to the structures found in internal flows, energetic bursting events occur where low-speed fluid is ejected from the wall into the free-stream. These bursts are responsible for the majority of turbulence production in the boundary layer (Kline et al., 1967; Robinson, 1991). The extent to which the invariant solutions can capture both the near-wall vortex structures and the bursting in boundary layers remains open; see (Kawahara et al., 2012) for a recent review.

As a step towards open flows, we here investigate the turbulence transition in the asymptotic suction boundary layer (ASBL), a boundary layer with a mean normal flow (Fransson, 2001; Schlichting, 2004) that shows many features of both internal and external flows. It is ideally suited for an investigation of invariant solutions and edge states in boundary layers, as it has a translationally invariant base flow. Furthermore, we gain the possibility to connect the system to plane Couette flow by tracking a homotopy parameter, which will allow us to fully characterize and explain

the dynamics of the edge state. Finally, the flow connects to engineering applications in which suction is a well studied concept for turbulence control, see for example Joslin (1998).

This paper is organized as follows: In §5.3.2 we describe the flow, its numerical implementation and the algorithms used to find edge states. In §5.3.3 we discuss the flow fields for $Re = 400$, followed by a discussion of the Reynolds number and aspect ratio variations in §5.3.4. Concluding remarks are given in §5.3.5.

5.3.2. System, numerical scheme and algorithms

The asymptotic suction boundary layer

The asymptotic suction boundary layer (see figure 5.3.1) describes a situation where fluid flows with velocity U_∞ over a flat plate into which it is sucked with a perpendicular velocity V_S. We work in a Cartesian coordinate system, with x the downstream direction; y and z are the wall-normal and spanwise directions, respectively. The equations of motion for an incompressible fluid are the Navier–Stokes equation

$$(\partial_t + \mathbf{u}\cdot\nabla)\mathbf{u} = -\nabla p + \nu\Delta\mathbf{u} \tag{5.3.1}$$

together with the continuity equation

$$\nabla\cdot\mathbf{u} = 0. \tag{5.3.2}$$

The no-slip boundary conditions at the wall, the downstream flow and a constant, homogeneous suction V_S give for the stationary laminar solution to the full Navier–Stokes equation an exponential profile,

$$\mathbf{u}_0 = \left(U_\infty(1-\mathrm{e}^{-y/\delta}),\quad -V_S,\quad 0\right). \tag{5.3.3}$$

The length $\delta = \nu/V_S$ equals the displacement thickness, defined by $\int_0^\infty (1-u(y)/U_\infty)\mathrm{d}y$, and is used as length-scale. Velocities are measured in units of U_∞ and time in units of $t_u = \delta/U_\infty$. The Reynolds number for the ASBL is defined as

$$\mathrm{Re} = \frac{U_\infty\delta}{\nu} = \frac{U_\infty}{V_S}. \tag{5.3.4}$$

The laminar profile (equation 5.3.5) is linearly stable for Reynolds numbers up to a critical value of $\mathrm{Re}_c = 54382$ (Hocking, 1975). This is a factor of about 100 more than for a boundary layer without suction Schlichting (2004). As calculations in this work do not exceed Reynolds numbers beyond 750, the laminar flow is stable for all our considerations.

For the numerical treatment, the unbounded wall-normal direction is cut off at a height h, where a second porous plate that moves with constant velocity U_∞ is

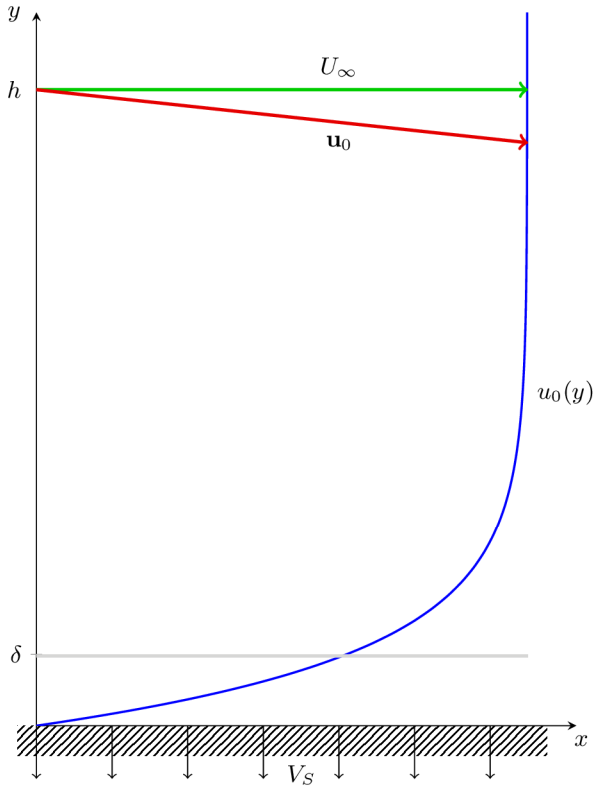

Figure 5.3.1.: Laminar velocity profile $u_0(y)$ for a boundary layer with homogeneous suction V_S and for $h = 10\delta$.

introduced. At both walls we enforce no-slip boundary conditions for the x- and z-components of the velocity and homogeneous suction for the y-component. In the spanwise and streamwise directions we employ periodic boundary conditions with periods L_x and L_z, respectively. The upper wall modifies the downstream velocity in the profile slightly. It now is

$$\mathbf{u}_0 = \left(U_\infty^*(1 - \mathrm{e}^{-y/\delta}), \quad -V_S, \quad 0\right), \tag{5.3.5}$$

where $U_\infty^* = U_\infty/(1 - \mathrm{e}^{-h/\delta})$. For $h \to \infty$ the denominator is 1 and $U_\infty^* = U_\infty$. The 99% boundary layer thickness slightly depends on h; it is $\delta_{99\%} = 4.605\delta$ for $h \to \infty$ and $\delta_{99\%} = 4.601\delta$ for $h = 10$, the box height used in most of this work. The laminar velocity profile $u_0(y)$ for this height is shown in figure 5.3.1.

Numerical aspects

For all DNS (Direct Numerical Simulation) in this work we use the open source channelflow library (Gibson, 2012), developed and maintained by John F. Gibson. The code solves the full incompressible Navier–Stokes equations in channel geometries with

periodic boundary conditions in the streamwise and spanwise directions and no-slip boundary conditions at the walls. It uses spectral discretization with Fourier×Chebyshev×Fourier modes in the x, y and z directions and finite differencing in time. The code has been modified to allow for the blowing/suction boundary conditions. As suggested by the channelflow manual, computations in this work use 2/3-dealiasing in the x, z transforms and calculation of the nonlinear term in the rotational form $(\mathbf{u}\cdot\nabla)\mathbf{u} = (\nabla \times \mathbf{u}) \times \mathbf{u} + \nabla(\mathbf{u}\cdot\mathbf{u})/2$. For time-stepping a third-order semi-implicit backwards-differentiation method is used.

The resolution necessary to resolve all relevant flow structures has been carefully investigated. In a box of size $L_x \times h \times L_z = 4\pi \times 10 \times 2\pi$ at Reynolds number 400 we increased the number of modes until all parameters of two edge states found at two different resolutions were identical to within 1%. A resolution of $48 \times 129 \times 48$ modes was found to be sufficient. The high number of required Chebyshev modes is caused by the need to resolve small fluctuations near the lower wall. For wider and longer boxes the resolution was chosen such that the number of modes per unit length is at least the resolution demanded by the above analysis, i.e. $M_x/L_x \geq 48/4\pi$ and $M_z/L_z \geq 48/2\pi$. We have examined the influence of the box height on the flow with a similar method and found that a height of $h = 10$ is sufficient to calculate edge states. It is not sufficient, though, for simulating fully turbulent flows, which need a much higher domain.

We also found good agreement between our results and independent simulations by Schlatter and Duguet (2010, private communication), see also Khapko et al. (2013). This way we could verify our implementation of both the ASBL modifications in channelflow and the edge state tracking algorithm.

The edge of chaos and the edge state

In the asymptotic suction boundary layer turbulent motion is observed while the laminar profile is still linearly stable. It is in that sense similar to other parallel shear flows like plane Couette flow (Grossmann, 2000) or pipe flow (Eckhardt et al., 2007) and ideas about the state space structure can be carried over from these systems. There is a basin of attraction around the stable laminar profile in which all initial conditions evolve towards the laminar flow. For sufficiently high Reynolds numbers and sufficiently large perturbations a second region appears in which the flow evolves towards a turbulent state (for our purposes here it does not matter whether this turbulent state is transient or persistent). In between those two regions is a laminar-turbulent boundary, the edge of chaos (Skufca et al., 2006), which is characterized by initial conditions that neither decay nor become turbulent. The edge of chaos forms an invariant manifold of codimension one that separates the basin of attraction of the laminar state from the turbulent region of state-space.

States within the edge of chaos evolve towards a relative attractor, the so-called edge state. This may be a fixed point as in plane Couette flow for low Reynolds

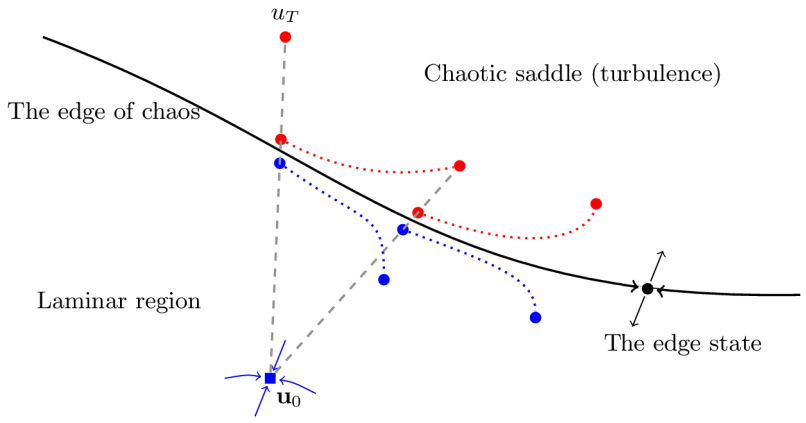

Figure 5.3.2.: Schematic representation of the edge tracking algorithm. The black line represents the edge of chaos, the laminar fixed point $\mathbf{u}_0$ is at the bottom. A bisection is performed on the line between the laminar and a known turbulent state. The states that bracket the edge are then propagated in time until their separation exceeds a threshold. Then, a refining bisection along the line connecting the new turbulent state and the laminar fixed point is carried out.

numbers (Schneider et al., 2008), a periodic orbit as in some parameter regions of plane Poisseuille flow (Toh and Itano, 2003) and some low dimensional models (Skufca et al., 2006) or a relative chaotic attractor as in pipe flow (Schneider, 2007; Schneider et al., 2007b), see also Vollmer et al. (2009); Mellibovsky et al. (2009); Duguet et al. (2009, 2010a). Its unstable manifold has codimension one, so that the edge of chaos is the stable manifold of the edge state.

In order to find the edge of chaos and the edge state we use the technique described in Schneider et al. (2007b), see also Toh and Itano (2003); Skufca et al. (2006). For this edge tracking, we classify states that directly decay to the laminar state as lying on the *"low side"* of the edge and states that become turbulent as lying on the *"high side"*. Starting with a turbulent state u_T (on the high side) and the laminar fixed point u_0, we use a bisection method to determine two states u_L and u_H on either side of the edge of chaos which are arbitrarily close to it. We can then propagate these states in time, always knowing that the edge lies between them. The two states quickly separate in the edge's unstable direction; after some time, we need a refining bisection to find a new pair of states that are closer together. The edge state tracking algorithm consists of a constant repetition of bisection and time integration, see figure 5.3.2 for a schematic representation.

As indicated in figure 5.3.2, refining bisections are performed along the line connecting u_H and u_0 rather than between u_H and u_L, because this method leads to better convergence. The reason for this improved performance seems to be connected

with the folds in the edge, see Moehlis et al. (2004a); Schneider et al. (2007b); Vollmer et al. (2009): Bisecting between u_H and the laminar fixed point seems to increase the probability of avoiding these folds and of staying near the edge. In our simulations we bring the relative L_2-distance of u_L and u_H down to 10^{-6} and perform a refining bisection once it is larger than 10^{-4}.

We classify flow states as lying on the low or high side of the edge by thresholds of the cross-flow energy, i.e. the energy in the in-plane velocity components,

$$E_{cf} = \frac{1}{L_x L_z \delta} \int_{box} \left(v^2 + w^2\right) \mathrm{d}V, \tag{5.3.6}$$

as a measure of the fluctuations perpendicular to the mainly downstream laminar flow. E_{cf} should be a better indicator for the presence turbulence than just taking the L_2-norm of the velocity field since it avoids the dominant contribution from the downstream component and focuses on the perpendicular parts that are necessary to sustain the three-dimensional turbulence. States with E_{cf} greater than an appropriately chosen threshold become turbulent, while states with E_{cf} smaller than another threshold decay directly. The use of E_{cf} as a classification for states proved reliable and well-defined in our simulations, justifying the choice a posteriori.

5.3.3. The edge state

In this section, we discuss the results of edge state tracking at $\mathrm{Re} = 400$ in a box of size $L_x \times h \times L_z = 4\pi \times 10 \times 2\pi$ and report the properties of the edge state. The resolution for this simulation was $48 \times 129 \times 48$. A large number of edge state trackings for different initial conditions in this box have been performed. All initial conditions that converged to some state with regular structure converged to the same state, up to trivial translations, which we hence call the edge state. For infinite integration times, we expect all initial conditions to finally approach that state.

Description of the dynamics

Figure 5.3.3 shows the energy in the in-plane velocity components, E_{cf}, as a function of time. Only the trajectory eventually becoming turbulent is shown, the laminarizing one being visually indistinguishable. An outstanding feature of this plot are the periodic strong bursts during which the cross-flow energy E_{cf} increases almost tenfold. These bursts provide the main starting point for understanding the edge state dynamics. The time interval between bursts is $T = 1071$ time units δ/U_∞. While the figure only shows six bursts in approximately 6000 time units, we follow the dynamics for more than 80000 time units to confirm the strict periodicity of the bursts.

Figure 5.3.4 shows the deviation of the flow from the laminar profile averaged over x at the minimum of E_{cf} and exactly one burst later. To help visualizing structures across the periodic boundaries in z we show the box twice. This representation

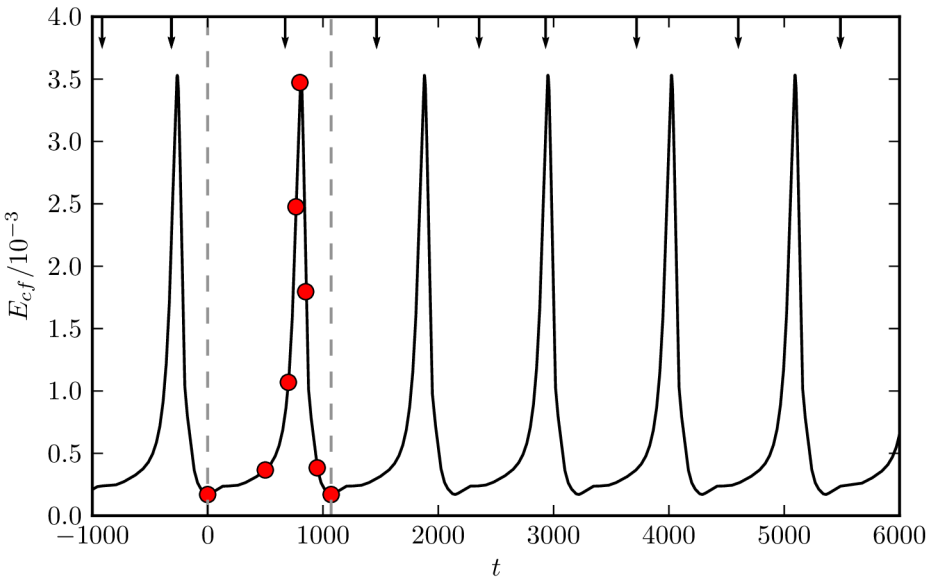

Figure 5.3.3.: Time evolution of the cross-flow energy of the edge state. The initial transient behaviour is not shown. The arrows at the top indicate the times when a refining bisection was performed, the circles indicate the times where the snapshots in the following figures have been taken. The locations of two minima are indicated with dashed lines; their distance is 1071 time units.

suggests that after $T = 1071$ the flow is the same except for a shift by π, corresponding to half a box width. After a second burst, the structures are hence back to their original location. Taking the changes in velocity into account, the full period is thus twice the time interval between bursts in E_{cf}. To verify that we have an exact invariant solution, we calculate the L_2-distances between three fields: the field at t=0, 40 bursts later and 80 bursts later, i.e. after more than 80000 time units. The relative distances, $L_2(u_0 - u_{40})/L_2(u_0) = 7.86 \cdot 10^{-6}$, $L_2(u_0 - u_{80})/L_2(u_0) = 7.94 \cdot 10^{-6}$ and $L_2(u_{40} - u_{80})/L_2(u_{40}) = 5.01 \cdot 10^{-6}$, are very small; the state is indeed an invariant solution to the Naviers-Stokes equations.

In order to study the dynamics of the edge state further, we present it in different representations at times corresponding to the circles in figure 5.3.3. Figure 5.3.5 shows snapshots of the fluctuating velocity field in a slice in the yz-plane. The plots are cut off at $y = 2\pi$ since in the upper part of the box no deviations from the laminar flow are visible. It becomes clear that the regions of high- and low-speed fluid already visible in the x-averaged plots are in fact streamwise high- and low-speed streaks. The snapshots hint at some internal dynamics, which below will be associated with a travelling-wave-like behaviour.

The in-plane components in figure 5.3.4 suggest that vortices play an important role in the edge state's dynamics; we visualize them using the λ_2 vortex detection criterion

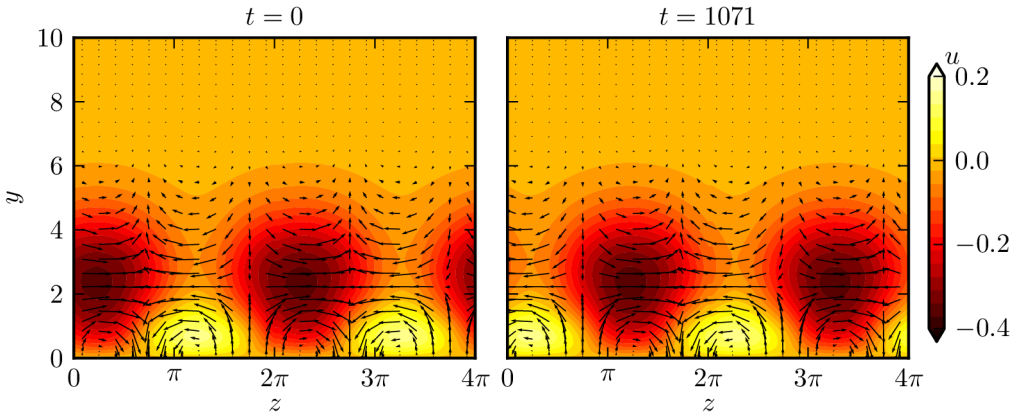

Figure 5.3.4.: Fluctuating velocity field of the edge state at two successive minima of E_{cf}. The velocity field is averaged in the downstream direction, the downstream component is colour coded, in-plane components are indicated with arrows with length proportional to the in-plane vector amplitude. The two images coincide when shifted by $\pi = L_z/2$, indicating a periodic orbit with period 2142 time units.

(Jeong and Hussain, 1995). Figure 5.3.6 shows the position of vortices by isocontours of λ_2 and their interaction with the low-speed streak (isocontour $u = -0.33$, light gray) in a parallel projection, seen from the top of the box. Since the strength of the vortices varies considerably, we have normalized λ_2 at every time slice such that $min(\lambda_2) = -1$ and plot the isocontour $\lambda_2 = -0.6$. It is coloured according to the sign of the downstream vorticity ω_x in order to distinguish vortices that rotate left and right.

We start describing the sequence of events at time $t = 0$ where E_{cf} is minimal. The flow consists of two streamwise streaks: one low-speed streak that reaches out to approximately $\delta_{99\%}$ into the flow, and beneath it one smaller high-speed streak closer to the wall. They are mostly aligned in the downstream direction, but the downstream modulation in figure 5.3.6 shows that it corresponds to a travelling-wave-like structure. The two streaks are accompanied by two streamwise elongated counter-rotating vortices, located at both sides of the low-speed streak and at different streamwise positions, just like the typical flow structures identified in Jeong et al. (1997). The vortices create and sustain the streaks by linear advection of the laminar base flow. On one side a vortex lifts low-speed fluid from near the wall upwards and supports the low-speed streak. On the other side, fast moving fluid from the upper flow regions is pushed towards the wall where the base flow is slower, thereby creating a streak of high-speed fluid. Since the two vortices are counter-rotating, they both act to feed both streaks. For a long time the streaks persist without much change in shape while the energy in the in-plane velocity components E_{cf} remains small. The

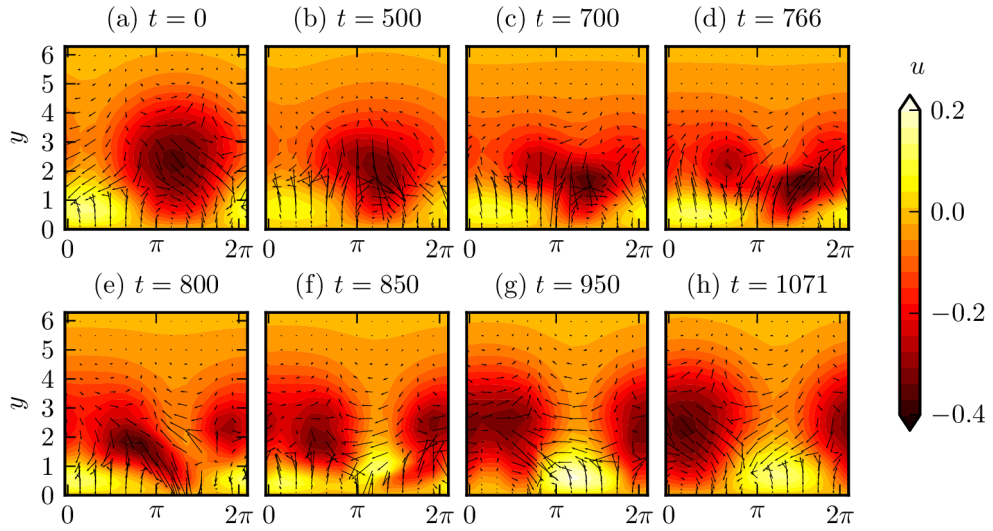

Figure 5.3.5.: The fluctuating velocity field in a slice in the yz-plane at $x = 0$ at different times. Downstream velocity is colour coded, in-plane velocity is shown by arrows. The length of the arrows is proportional to the in-plane component of the velocity vector. The box has been cut off at $y = 2\pi$. The times correspond to the dots in figure 5.3.3.

vortices slowly grow in strength and start to "lean" over the low-speed streak, which in turn becomes wavier and the oscillations increase considerably. Approximately 700 time units after the burst the vortices lie on top of the now very contorted low-speed streak. A little later the oscillations become too strong and the streaks break up – the event corresponding to the strong burst in E_{cf}. Figure 5.3.6(d) suggests that the vortices actually switch places. The low-speed streak does not vanish in the process, but rather is torn apart into two smaller streaks, which then reunite across the periodic boundary conditions. After the break-up, the pairs of streaks and vortices are located at a spanwise location that is shifted by exactly $L_z/2$ or half a box width. Comparing figures 5.3.6(a) and (h) one finds that there is no shift in the downstream position of the structures.

Another representation of the periodic orbit is presented in figure 5.3.7. The reduced state-space plot of two expansion coefficients in figure 5.3.7(a) shows that the trajectory is a closed orbit in this representation. The circle in the figure indicates the point of lowest E_{cf}. The spacing between the crosses that are drawn at equidistant time intervals of 20 units shows that the trajectory moves rather slowly near the points, before rapidly going over to the other side in an event corresponding to the burst. In figure 5.3.7(b) we show the time evolution of a single in-plane velocity component at a fixed position in the box, namely $v(0, 1.46, 0)$. The bursts show up as a slow drift from positive to negative values and back. An interesting feature are the short period oscillations. By averaging over 20 maxima of $v(0, 1.46, 0)$ we

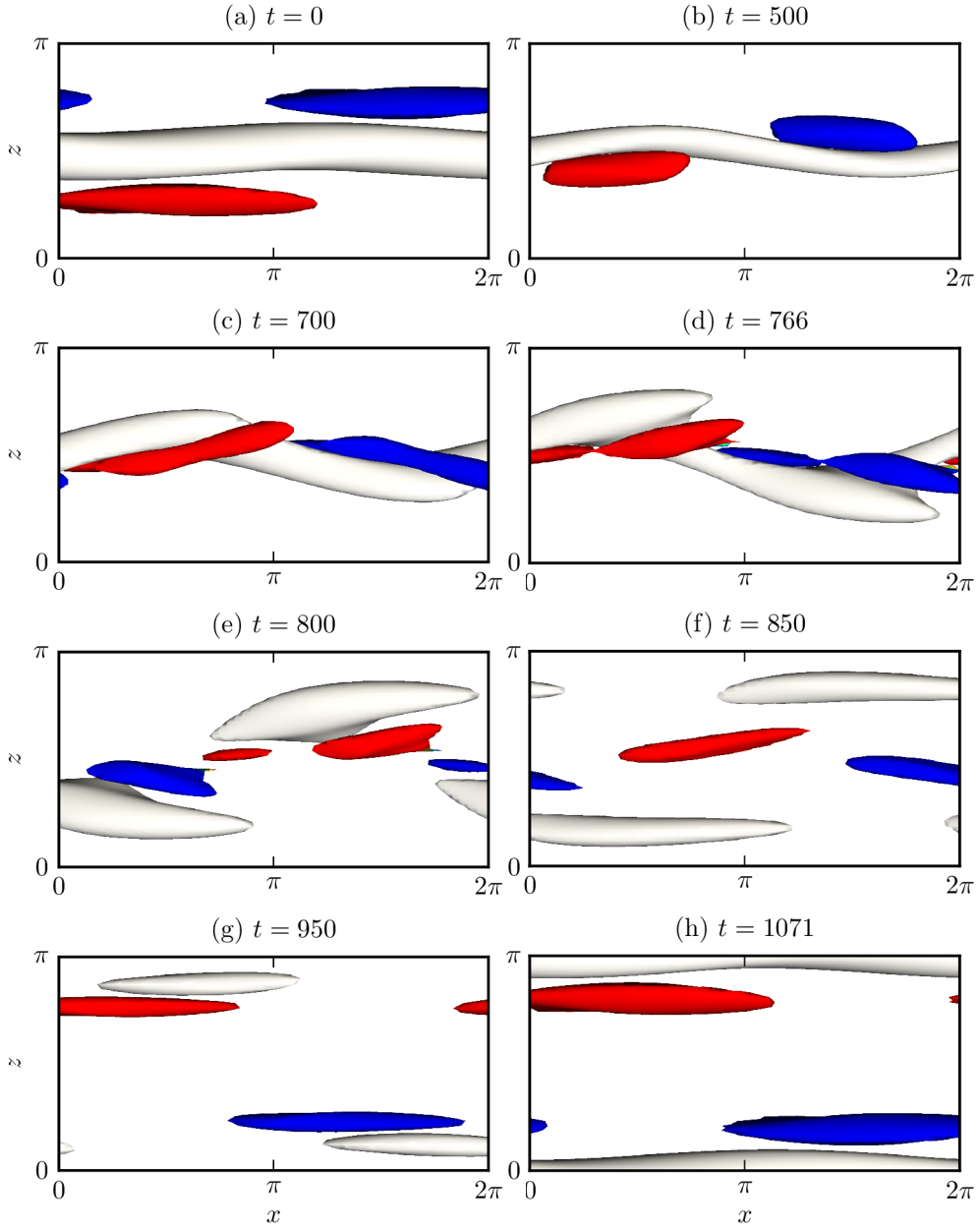

Figure 5.3.6.: Snapshots of vortex-streak-interactions in a view from the top. We show the isocontour $u = -0.33$ of the deviation from the laminar profile in light gray together with isocontours of $\lambda_2 = -0.6$ (Jeong and Hussain, 1995), where we have normalized λ_2 such that $min(\lambda_2) = -1$. The λ_2 isocontours are coloured red and blue for positive and negative downstream vorticity, respectively, with red indicating a vortex that rotates clockwise. Between $t = 766$ and $t = 800$ the vortices switch places, thereafter new streaks are created.

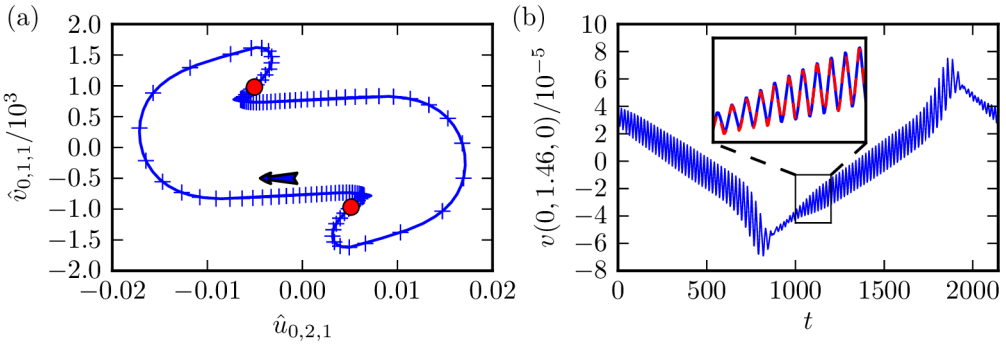

Figure 5.3.7.: Time traces of the edge state. (a) A plot of the edge state trajectory in a projection of state space. The circles correspond to the minima of E_{cf}, crosses are drawn every 20 time units. The trajectory is a closed orbit passing through two minima. After a minimum of E_{cf} the dynamics is rather slow, followed by a rapid motion as the next minimum is approached. (b) Time evolution of v at $(0, 1.46, 0)$. The curve shows that two timescales are involved in the process. The inlet shows the same velocity component at time t and $t + 2142$ and reveals that the orbit is a periodic orbit without shift in the downstream direction.

find that the period is not constant during a cycle: directly after the burst, it is 18.4, corresponding to a phase-speed of approximately $2/3U_\infty$. The period increases slightly and just before the burst it is 20.6. The inset in figure 5.3.7(b) contains a magnification of the indicated black rectangle. In addition to the original curve, the dashed line shows the component at time $t + 2142$: that it lies exactly on top of the first curve demonstrates that the edge state is a periodic orbit and that there is no phase-shift – the high frequency oscillations are perfectly aligned so that the fast and slow dynamics are phase-locked. The velocity field during one of the short periods is reminiscent of the travelling waves found also in other systems.

A space-time plot of the streak positions shows that the shift distance is always exactly $L_z/2$. To determine the instantaneous position of the streaks, we average the fluctuating downstream velocity component u over x and y and take extrema as points of reference for the location of the streak. The velocities are fitted with a parabola to locate the minima with higher precision. Two examples of the averaged profiles are shown in figure 5.3.8(a); the circles show the profile at $t = 0$, the triangles at $t = 850$ during the burst. While in the former curve, only one low speed streak is present, the latter one shows two low speed regions. In figure 5.3.8(b) we show the positions of the low-speed streaks as a function of time. That provides a reliable method to determine the shift distance of the structures at a burst and confirms that this distance is exactly $\pi = L_z/2$. Moreover, the plot shows that the streak does not shift to one side at a burst but that two streaks form to the left and right of it which then reconnect to form a single one at the new position.

The edge state obeys a shift-and-reflect symmetry, that is it is unchanged by a

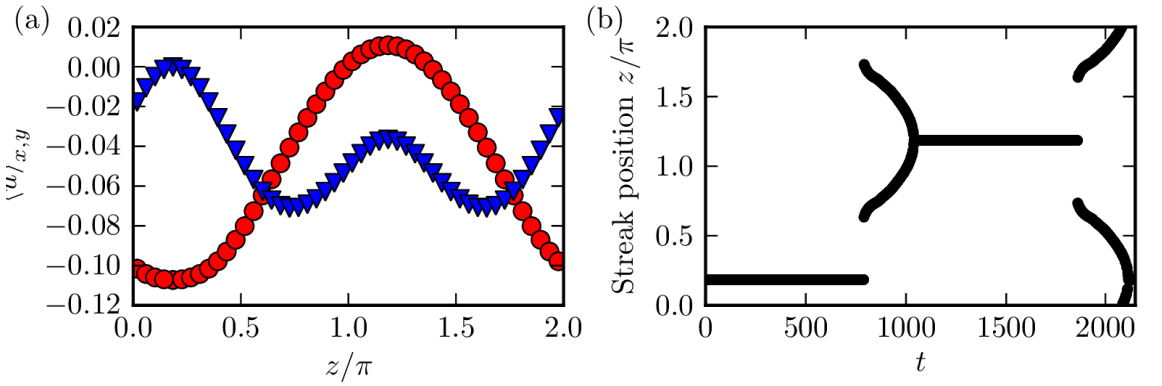

Figure 5.3.8.: Localization and dynamics of low speed streaks. (a) The velocity profile of the edge state averaged over x and y at time $t = 0$ (circles) and $t = 850$ (triangles). The position of the streaks is determined by fitting a parabola through the minima of those curves. (b) The z-position of the low speed streaks as a function of time. During a burst, the low speed streak splits into two streaks on either side, which then reconnect to form a new one.

downstream shift of $L_x/2$ combined with spanwise reflection at an appropriately chosen plane. Formally, it is invariant under the operation $\sigma[u, v, w](x, y, z) = [u, v, -w](x + L_z/2, y, -z)$. We emphasize that no symmetry has been enforced in the calculations, but that edge trajectories are drawn to this apparently attracting invariant subspace. It is actually this symmetry that fixes the distance of the shifts: the only other possible location for the structures in the same invariant subspace is the one related by a shift of $L_z/2$. This symmetry of the state also explains why the state does not drift in the spanwise direction – a drift would require that it leaves the symmetry-invariant subspace.

A regenerating cycle?

Hamilton et al. (1995) and Waleffe (1995) discuss a three step regeneration cycle for near wall turbulence. This quasi-cyclic process is based on the interaction between two alternating streaks and two streamwise elongated vortices. The streamwise vortices create the streaks by linear advection of the laminar base flow. But the streaks are linearly unstable to wavy modulations, that eventually lead to their break-up, causing a peak in the turbulent energy production. The resulting flow has a strong x-dependence and nonlinear interactions lead to the recreation of streamwise vortices. Moehlis et al. (2004a) were able to capture the essential features of the process with a nine-dimensional model. A similar mechanism has also been used to describe a self-sustaining process for coherent structures such as travelling waves (Waleffe, 1997).

In the edge state in the asymptotic suction boundary layer, we see structures that closely resemble the travelling waves found in pipe flow (Faisst and Eckhardt, 2003;

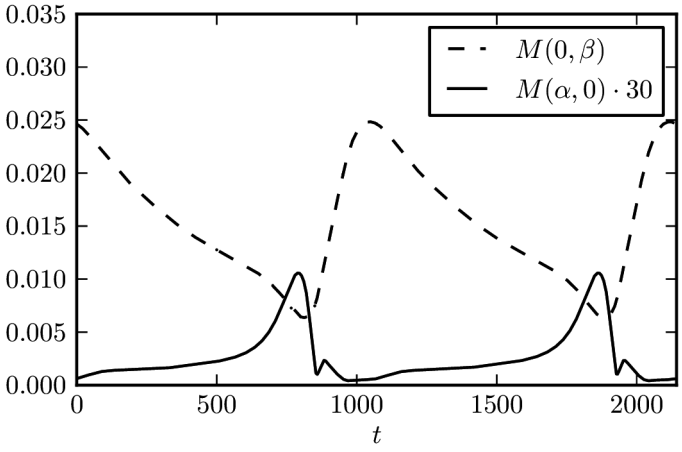

Figure 5.3.9.: Modal energies $M(0,\beta)$ and $M(\alpha,0)$ as a function of time for a full cycle of the edge state. The changes in the two quantities are anticorrelated during most of the process, except for a small time interval $t = 850$ to 880. There are two phases, a long one during which $M(0,\beta)$ decreases and a short one where it increases.

Wedin and Kerswell, 2004; Hof et al., 2004) or plane Couette flow (Nagata, 1997; Clever and Busse, 1997; Wang et al., 2007). They have rather high-frequency oscillations, see figure 5.3.7(b). Such coherent structures have often been explained with the self-sustaining process (Waleffe, 1997), but in the edge state there is a second time scale from the bursts. We find that the qualitative description of the low-frequency process of the bursts is more reminiscent of the process described in Hamilton et al. (1995) than the high-frequency travelling wave part. Important quantities for identifying the cycle are the modal energies

$$M(k_x = m\alpha, k_z = n\beta) = \left\{ \int_{-1}^{1} \left[\hat{u}^2(m\alpha, y, n\beta) + \hat{v}^2(m\alpha, y, n\beta) + \hat{w}^2(m\alpha, y, n\beta) \right] \mathrm{d}y \right\}^{1/2} \tag{5.3.7}$$

The general interpretation is that $M(0,\beta)$ corresponds to the streaks and $M(\alpha,0)$ to the waviness of the streaks. Hamilton et al. (1995) found that during the cycle $M(\alpha,0)$ and $M(0,\beta)$ are strictly anticorrelated. In their regeneration cycle two phases of approximately the same duration are clearly distinguishable, one where the streaks grow, $\mathrm{d}M(0,\beta)/\mathrm{d}t > 0$, and one where streaks break down, $\mathrm{d}M(0,\beta)/\mathrm{d}t < 0$. We present the corresponding plot of the two quantities in figure 5.3.9. $M(0,\beta)$ and $M(\alpha,0)$ are anticorrelated for most of the time, with the exception of a very small time interval during bursts – possibly indicating that the mechanism that leads to the recreation of the streamwise vortices is a different one. The streak formation phase after a burst takes only 200 time units, their slow breakdown lasts for more than 800 time units. In the discussion of figure 5.3.6 in the previous section, we argued that streak formation is due to linear advection by the streamwise vortices.

A sinuous streak instability that leads to a waviness of initially straight streaks has often been observed, see for example Andersson et al. (2001) and there is little doubt that this linear instability is present in our case. Finally, the interactions leading to the recreation of the streamwise vortices are unquestionable nonlinear – which means that all ingredients of the regeneration mechanism described by Hamilton et al. (1995) are present.

The edge state in state space

The dominance of the streaks, the long period and the dramatic bursts are reminiscent of behaviour seen in other boundary layers (Kline et al., 1967)

In a low dimensional model obtained by proper orthogonal decomposition, Aubry et al. (1988) identified an attracting heteroclinic cycle which connects two fixed points, that are related by a discrete symmetry. The fixed points have exactly one unstable eigenvalue whose real part is smaller than the modulus of the real part of the least stable eigenvalue. Trajectories spend a long time near the fixed points, before following the heteroclinic connection to the other fixed point in a wild burst. Motivated by these studies, Armbruster et al. (1988) undertook further analysis of the phenomenon and concluded "that the heteroclinic cycles present in this model arise as a natural feature in the context of evolution equations which are translation and reflection invariant with respect to a spatial direction." (Armbruster et al., 1988, p. 257) Since the required $O(2)$ symmetry is also present in our system due to the periodic boundary conditions in the spanwise direction, we tried to connect our observations to their mechanisms. But despite considerable effort to locate the fixed points visited transiently by the trajectory, we have not been able to find them with a Newton search (Viswanath, 2007). It eventually turned out that the mechanism responsible for the bursts is different, as we now explain.

The origin of the slow oscillations was found by embedding the flow in a family of flows, obtained by keeping U_∞ fixed and varying V_S, thus exploiting the connection from ASBL to plane Couette flow (pCf). We work in a box of size $4\pi \times 8 \times 2\pi$ at a resolution of $32 \times 65 \times 32$ in order to reduce the computational effort. This resolution is a little lower than for the calculations above, but the edge state dynamics is still reproduced, though the values of some variables may vary slightly; for example the bursting period T increases by less than 1%. Since the edge states in both the ASBL as well as in pCf have a shift-and-reflect symmetry, we enforce this symmetry for all calculations in this section.

We start in a plane Couette system with the lower plate at rest and the upper plate moving with velocity U_∞, where the Reynolds number based on half the velocity difference and half the gap width is $\mathrm{Re}_{pCf} = U_\infty H/4\nu = 800$. The edge state is a fixed point in an appropriately chosen frame of reference and hence a travelling wave in the lab frame. The eigenvalues of the equilibrium state are calculated by means of

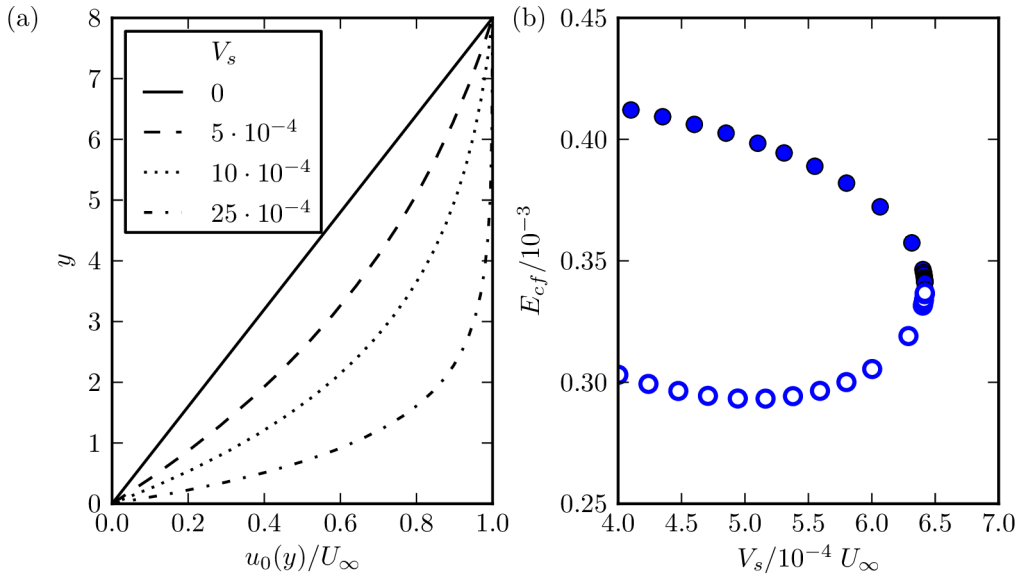

Figure 5.3.10.: Connecting the asymptotic suction boundary layer to plane Couette flow. (a) The laminar velocity profile $u_0(y)$ for different values of V_S as indicated in the legend in a box of height 8. For plane Couette flow ($V_S = 0$) the laminar profile is a straight line. It is smoothly transformed into the exponential profile of the ASBL as V_S increases. (b) Bifurcation diagram of the edge state (full circles). At $V_S = 6.418 \cdot 10^{-4}$, corresponding to $\delta = 3.89$, it collides with a lower branch equilibrium (open circles) in what looks locally like a saddle-node bifurcation. Restricted to the edge, the upper branch equilibrium is stable while the lower branch has one unstable eigenvalue.

Arnoldi iteration (implemented in channelflow by John F. Gibson, see Gibson (2012)); it has exactly one unstable direction, i.e. it is an attractor for edge trajectories.

The suction velocity V_S serves as a homotopy parameter between pCf and the ASBL. As V_S increases from 0, the laminar profile gradually transforms from a straight line to an exponential, figure 5.3.10(a), while the boundary layer thickness $\delta = \nu/V_S$ decreases from ∞ to 1. Starting with the relative equilibrium that is the edge state in the plane Couette system, we continue the solution in V_S; it vanishes in a saddle-node bifurcation at $V_S/U_\infty = 6.418 \cdot 10^{-4}$. Restricted to the edge the edge state is a node and it corresponds to the upper branch of the saddle-node bifurcation. We were able to continue it to the lower branch which has two unstable eigenvalues. The bifurcation diagram E_{cf} versus V_S is shown in figure 5.3.10(b). Very close to the bifurcation, the leading eigenvalues, without the neutral one, of the node and the saddle are 0.0051, $-3.76 \cdot 10^{-5}$, $-0.0022 \pm 0.0136i$ and 0.0053, $2.36 \cdot 10^{-5}$, $-0.0026 \pm 0.0137i$, respectively. The difference occurs in the next to leading eigenvalue, which is real, indicating a standard saddle-node bifurcation.

In figure 5.3.11 we present the results of edge state tracking for four values of V_S

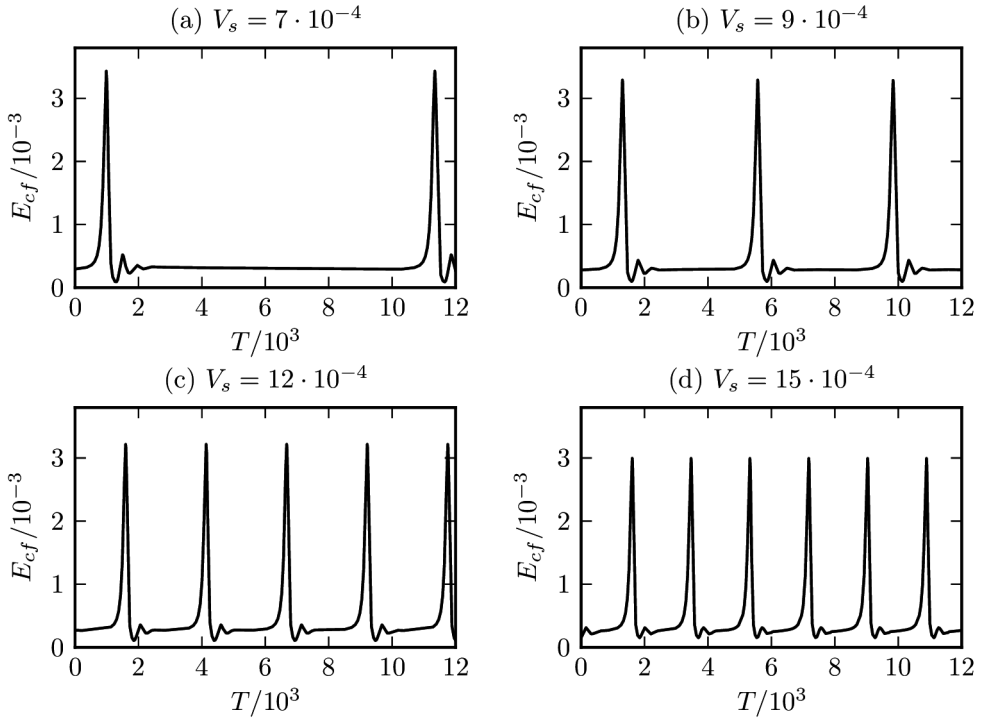

Figure 5.3.11.: Cross-flow energy of edge states for several values V_S. After the bifurcation point, periodic bursts set in with an extremely long period. The period decreases rapidly as the distance from the bifurcation point increases.

after the critical value. Directly after the bifurcation, periodic bursts set in with an extremely long period. The period rapidly decreases with increasing distance from the critical suction value, as can be seen in figure 5.3.11(b-d). At every burst, the state shifts by $L_z/2$.

This behavior can be explained if the edge state is heteroclinically connected with a copy of it that is obtained by shifting it by $L_z/2$ in the spanwise direction. Such heteroclinic connections between symmetry related fixed points have been found in several studies with $O(2)$-symmetry, see Aubry et al. (1988); Armbruster et al. (1988); Tuckerman and Barkley (1988); Halcrow (2008); Gibson et al. (2008) Since both states are attractors (in the same symmetry-subspace inside the edge), they have to be separated by a saddle. For symmetry reasons, the heteroclinic connection exists as well in the other direction, making it an attracting invariant cycle. The resulting state-space structure is shown in figure 5.3.12(a); the unstable direction of the edge points perpendicular to the plane. The global bifurcation is hence a saddle-node infinite-period (SNIPER) bifurcation (Strogatz, 1994; Tuckerman and Barkley, 1988; Abshagen et al., 2005), also known as saddle-node-on-invariant-cycle (SNIC). One indicator of a SNIPER bifurcation is a divergence of the period (figure 5.3.12 b,c),

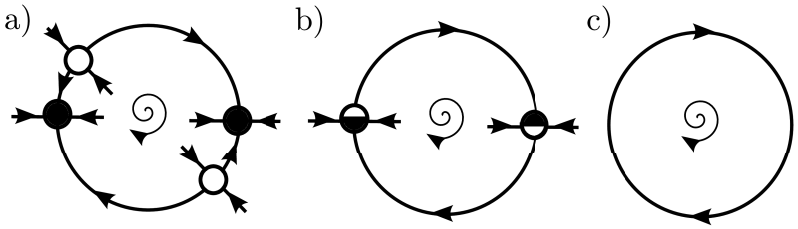

Figure 5.3.12.: Schematic representation of the bifurcation in state-space. a) for small V_S two pairs of fixed points, one stable (full circles), one unstable (open circles), exist which are related by a discrete symmetry, namely shifting by $L_z/2$; they are heteroclinically connected as indicated. b) as V_S increases, the fixed points annihilate in a saddle-node infinite-period (SNIPER) bifurcation c) The fixed points are gone for larger V_S, the edge state now goes around the cycle. For V_S near the bifurcation value, the period of the cycle diverges due to the ghost left behind by the saddle-node bifurcation. The stable directions shared by the fixed points and the periodic orbit contain both real and complex stable eigenvalues.

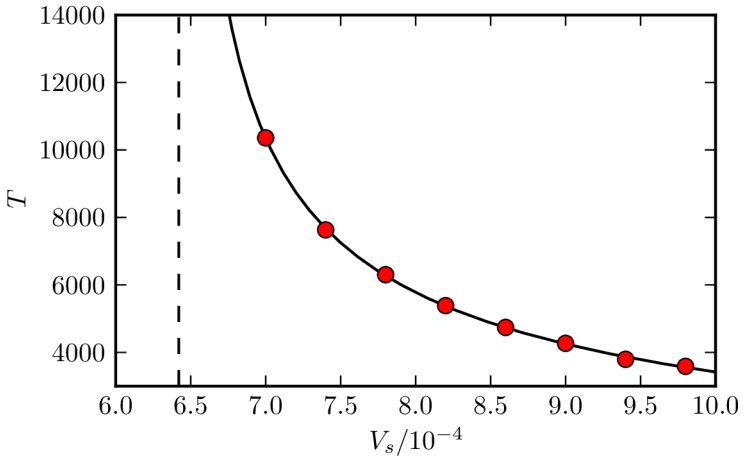

Figure 5.3.13.: Divergence of the bursting period close to the bifurcation point. The fit (solid line) to the expected theoretical scaling of a SNIPER bifurcation, $T \propto 1/\sqrt{V_S - V_{Sc}}$, agrees very well with the measured data (circles). Moreover, the critical value for V_S in the fit is $6.42 \cdot 10^{-4}$ (indicated by a dashed line) in very good agreement with the value obtained from the saddle-node bifurcation in figure 5.3.10(b).

which can already be read off from figure 5.3.11. More quantitatively, one expects the period to diverge like $1/\sqrt{V_s - V_{Sc}}$ at the bifurcation point. The data shown in figure 5.3.13 together with the fit, $T = 88.30/\sqrt{V_s - 6.42 \cdot 10^{-4}} - 1249$, is in very good agreement with this expectation. Also the critical value for V_S obtained from the fit is $6.42 \cdot 10^{-4}$, in excellent agreement with the value obtained from the saddle-node bifurcation in figure 5.3.10(b).

Further evidence for this scenario comes from a study of the explicit identification

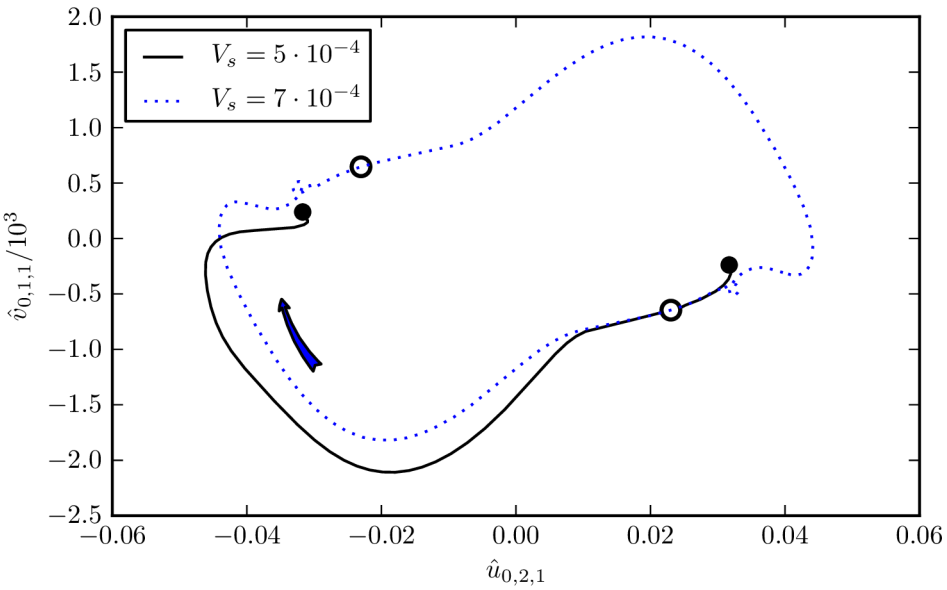

Figure 5.3.14.: The heteroclinic connection in state-space at $V_S = 5 \cdot 10^{-4}$ in a two dimensional projection. We show the node (full circle) and the saddle (open circle) together with the pair of fixed points obtained by a shift of $L_z/2$ (the projection is independent of x). The black lines are obtained by edge tracking from initial conditions which are slight perturbations of the saddle point; they reveal the heteroclinic connections from the saddle to both stable fixed points. The dotted line is the (bursting) edge state at $V_S = 7 \cdot 10^{-4}$, slightly above the bifurcation.

of the heteroclinic connection. The procedure we used to identify the connection is as follows: restricted to the edge of chaos, the node is an attractor while the saddle has one unstable direction. According to figure 5.3.12, an edge-trajectory that starts near the saddle will follow the heteroclinic connection either to the node or the shifted node. Using the edge state tracking algorithm to restrict the trajectories to the edge, we start from initial conditions near the saddle. A projection of state-space in figure 5.3.14 shows the two pairs of node and saddle, the heteroclinic connection to both sides as well as an edge state after the bifurcation.

The long phase between two bursts of the edge state in the ASBL does hence not correspond to the transient visit of a weakly unstable fixed point but rather to the ghost left behind by a saddle-node bifurcation on an invariant cycle.

5.3.4. Variation of flow parameters

We now turn to a study of the properties of the edge state at different Reynolds numbers and in different domains. Roughly 200 edge states have been calculated for different parameter values. While there are some changes in detail, the edge states'

structure is preserved in all cases. It consists of two streamwise streaks and two streamwise elongated counter-rotating vortices and there are periodic bursts where the state is shifted by half a box width.

The criterion for the convergence of a calculation is based on the cross-flow energy. We only consider states where the evolution of E_{cf} settles to a clearly identifiable asymptotic state, either constant or periodic. We found that all states falling into this category display periodic bursts. Convergence is assumed if E_{cf} has at least three peaks where their height and the time between the peaks agree within a relative tolerance of 2%.

Reynolds number

In this section the Reynolds numbers is varied while the box size is kept fixed at $4\pi \times 2\pi$. Calculations still take place in the transitional regime, with Reynolds numbers between 320 and 750. Below $\mathrm{Re} = 320$ the cross-flow energy at bursts is of the same order as the cross-flow energy of fully turbulent states and the distinction between the edge state and turbulent motion becomes difficult as in pipe flow (Schneider and Eckhardt, 2009). The highest Reynolds number we calculated is 750. There is, however, no indication that the structure of edge states would change for slightly higher Reynolds numbers.

Figure 5.3.15 shows the cross-flow energy E_{cf} as a function of Reynolds number. The maximum value of E_{cf} at a burst is plotted with triangles. This value may be taken as a measure for the burst intensity, it decreases monotonically with Reynolds number. A potential explanation comes from the observation, that at higher Reynolds numbers the critical amplitude for triggering transition to turbulence is lower (Levin et al., 2005) and that the edge state's energy reflects this descending threshold. The circles show the time averaged cross-flow energy. It decreases monotonically and smoothly with Re for the same reasons as the maximum energy. A power law gives the best fit with $\langle E_{cf} \rangle_T \sim \mathrm{Re}^{-3}$, plotted as a dashed line in the same figure.

Streamwise and spanwise domain-size

In this section, we study edge states at Reynolds number 400 but in boxes of different size. L_x varies from 3.2π to 7π in steps of 0.2π, with L_z ranging from $L_x/2 - 0.5\pi$ to $L_x/2 + 0.4\pi$ in steps of 0.1π. In smaller boxes it was difficult to find sustained turbulent states.

In figure 5.3.16 the cross-flow energy is plotted as a function of the boundary layer volume $L_x \cdot L_z$. We distinguish two qualitatively different regions: small boxes with $L_x L_z \lesssim 10\pi^2$ and larger boxes with $L_x L_z \gtrsim 10\pi^2$. In larger boxes, the variation of the cross-flow energy is rather smooth. $E_{cf_{max}}$ is roughly constant in those boxes: the burst intensity does not depend on the box size if the box is large enough. Both $E_{cf_{min}}$ and $\langle E_{cf} \rangle_T$ decrease for increasing box size, but the variation is very small

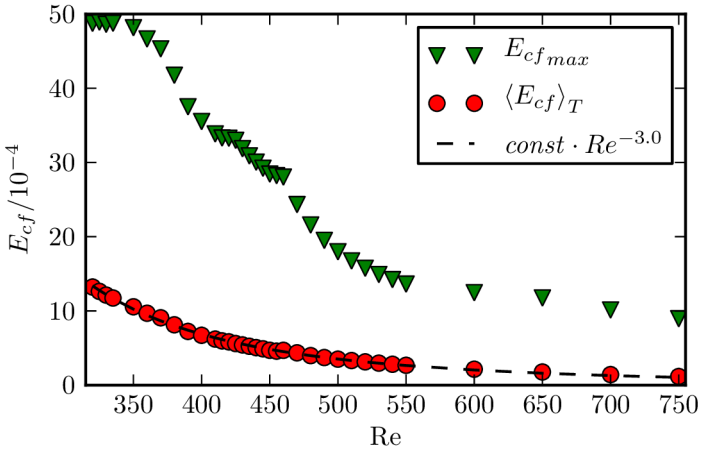

Figure 5.3.15.: The energy of the cross-flow E_{cf} as a function of Re. Green triangles: maximum of E_{cf} at bursts; red circles: E_{cf} averaged over one period. The dashed line is a fit to a power law, $E_{cf} \sim \mathrm{Re}^{-3}$. The energy generally decreases with increasing Re.

for the largest boxes. In the small boxes, the minimum and time-averaged cross-flow energy are not constant as a function of box size. States in these boxes seem to depend heavily on the available space and the greatest possible wavelength. Many states in these boxes have a comparable value of $E_{cf\,max}$ which is roughly 50% higher than in larger boxes.

There are some states, mainly from boxes around $5.4\pi \times 2.5\pi$, where the edge trajectory seems to converge to one state, before switching over to another one, with less amplitude in the bursts. As an example, in figure 5.3.17 we present an edge state tracking in the box $4.2\pi \times 2\pi$ where that happens. We first see five peaks of the same height and at equal distance, where the edge state tracking seems to be converged. But then the curve changes and another state is approached, where $E_{cf\,max}$ and $E_{cf\,min}$ are lower and higher, respectively. We explain this behavior as follows: there exist two periodic orbits in these boxes, one of which is stable inside the edge and the other one is weakly unstable. The edge trajectory approaches the unstable one first and lingers so close to it that it seems to be converged. But if the integration is carried on long enough, it leaves this unstable state and finally converges to the edge state. Figure 5.3.17 shows that sometimes edge tracking has to be continued for very long times before converged results are obtained. It would be possible to distinguish transient states from true periodic states if they could be identified numerically exactly, say using Newtons method. Then the differences in the number of unstable eigenvalues would show up. However, it has not been possible to achieve this because of the long periods. Given the large number of calculated states we feel that the overall trends discussed in this section are reliable.

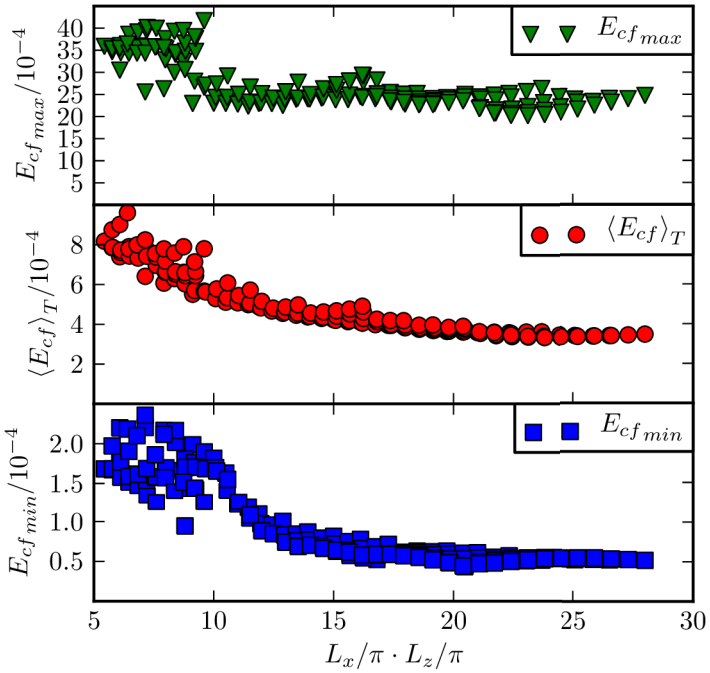

Figure 5.3.16.: The cross flow energy E_{cf} as a function of the boundary layer volume. Two qualitatively different regions can be distinguished: states with $L_x \cdot L_z < 10$ are somewhat higher in energy and show wide variations. For larger values the maximum of E_{cf} seems to prefer a value near 25 and the variations in all energies are reduced.

Burst period

The trend in the bursting period T is inverse to that in cross-flow energy. The period is small for low Reynolds numbers and grows with increasing Re. Similarly, it is small for small boxes and larger in larger boxes.

A breaking of the space-symmetry

Figure 5.3.18 shows the cross-flow energy of the edge state in the box $5.6\pi \times 3\pi$. The burst intensity, measured by the maximum of E_{cf}, is no longer the same for every burst, it alternates between a lower and a higher value. The periodicity of E_{cf} is not completely lost, but the time interval after which it repeats has doubled. Still, at every burst the position of the streaks is shifted by half a box width, but the symmetry between the two positions is broken.

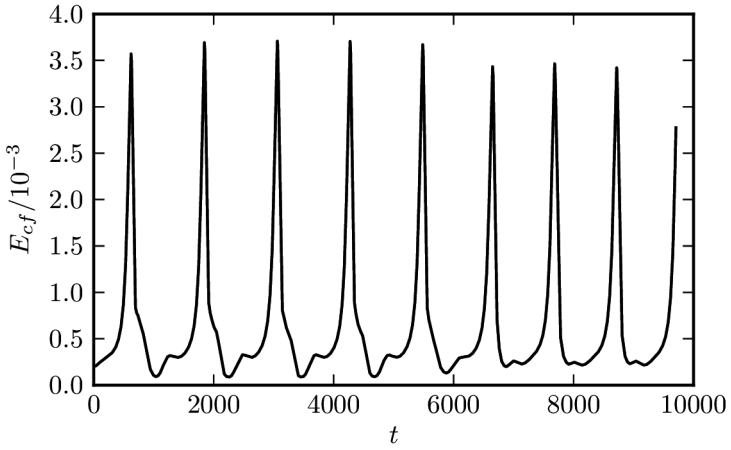

Figure 5.3.17.: Non-converged edgetracking evidenced by the cross-flow energy in a box of size $4.2\pi \times 2\pi$. Up to a time of about 6000 the tracking seems to converge rapidly. However, beyond that the curve changes: the bursts are less intense, the bursting period is a little lower – the edge state tracking has converged to another state, even though the first one would have been considered as converged by the criterion described at the beginning of this section.

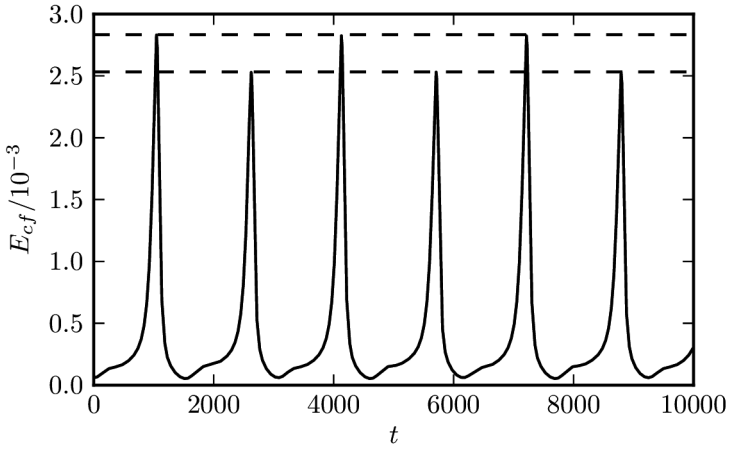

Figure 5.3.18.: Cross-flow energy of the edge state in the box $5.6\pi \times 3\pi$. The burst intensity is no longer the same for every burst, but alternates between a lower and a higher value. The dashed lines correspond to the two maxima and confirm the periodicity of the state.

5.3.5. Conclusions

The periodic orbit in the asymptotic suction boundary layer which we have characterized here shows dynamics on two different time scales: similar to invariant states in plane Couette and pipe flow, it shows the typical advection of downstream vortices on a fast time scale. Regular energetic burst events, not unlike those that have been reported as a key feature of boundary layer flows, occur on a much slower time scale. Although the flow can be turbulent and the dynamics is characterized by positive Lyapunov exponents, the two time scales remain phase-locked over the whole period of several thousand advective time units. In view of the translational symmetry of the asymptotic suction boundary layer these phenomena could well be the periodically continued version of the evolving boundary layer edge state described by Duguet et al. (2012).

For the bursting dynamics, an explanation from two different view points is given. Physically, the bursting is the result of vortex-streak interactions. A pair of downstream vortices creates and sustains the streaks by linear advection. The low-speed streaks are linearly unstable and develop a waviness, which in turn causes the vortices to become tilted with respect to the x-axis. The two counter-rotating vortices "lean" over the low-speed streak, tearing it apart, and eventually switch sides. Afterwards, the streaks are recreated by the vortices and the process begins anew, only shifted by half a box width. From a dynamical systems point of view, we are able to associate the bursting with a SNIPER-bifurcation: in plane Couette flow, two symmetry-related pairs of saddle and node are heteroclinically connected. As the homotopy parameter, the suction velocity, is increased, each of the pairs collides in a local saddle-node bifurcation, leaving behind a periodic orbit along the former heteroclinic connections.

The orbits discussed here are linearly unstable. They have a single unstable direction and are part of the edge that controls the transition to turbulence. Typically, they are lower branch states in a saddle-node bifurcation where the upper branch state becomes part of the turbulent dynamics. One can then expect, though this deserves further study, that the upper branch state shows a similar dynamics. Solutions like the one discussed here, even when they are unstable, form a backbone for the turbulent dynamics, as they are transiently visited by a turbulent trajectory. Then the long periodic dynamics provides a mechanism for energetic bursts and adds one more possibility to the list of bursting phenomena discussed by Robinson (1991).

The obvious spatial localization in the edge calculations in the Blasius boundary layer (Cherubini et al., 2011; Duguet et al., 2012), as well as similar structures in confined flows, suggests the existence of spatially localized counterparts of the periodic orbit discussed here, as indeed found for spanwise localization in Khapko et al. (2013). We expect that further comparisons between these and other features found in the asymptotic suction boundary layer and the full Blasius boundary layer will help to identify and characterize shared generic features and to separate them from suction related influences.

Acknowledgements

We thank John F Gibson for providing and maintaining the open source Channelflow.org code. We thank Taras Khapko, Yohann Duguet, Philipp Schlatter and Dan S Henningson for discussions and the exchange of results and Stefan Zammert and Fernando Mellibovsky for discussions.

5.4. Localized edge states in the asymptotic suction boundary layer

Taras Khapko[1], Tobias Kreilos[2,3], Philipp Schlatter[1], Yohann Duguet[4], Bruno Eckhardt[2,5] and Dan S. Henningson[1]

[1]Linné FLOW Centre, KTH Mechanics, Royal Institute of Technology, SE-100 44 Stockholm, Sweden
[2]Fachbereich Physik, Philipps-Universität Marburg, D-35032 Marburg, Germany
[3]Max Planck Institute for Dynamics and Self-Organization, D-37077 Göttingen, Germany
[4]LIMSI-CNRS, UPR 3251, Université Paris-Sud, F-91403, Orsay, France
[5]J.M. Burgerscentrum, Delft University of Technology, NL-2628 CD Delft, The Netherlands

Published in Journal of Fluid Mechanics 717, R6 (2013)

The dynamics on the laminar-turbulent separatrix is investigated numerically for bound-ary-layer flows in the subcritical regime. Constant homogeneous suction is applied at the wall, resulting in the parallel Asymptotic Suction Boundary Layer (ASBL). When the numerical domain is sufficiently extended in the spanwise direction, the coherent structures found by edge tracking are invariably localised and their dynamics shows bursts that drive a remarkable regular or irregular spanwise dynamics. Depending on the parameters, the asymptotic dynamics on the edge can be either periodic in time or chaotic. A clear mechanism for the regeneration of streaks and streamwise vortices emerges in all cases and is investigated in detail.

5.4.1. Introduction

Near-wall coherent structures such as streaks and quasi-streamwise vortices are an ubiquitous feature of transitional and turbulent wall-bounded shear flows. Their regeneration process is intimately connected with the occurrence of *bursting* events, *i.e.* strong intermittent ejections of low-speed fluid from the wall (for a review see *e.g* Robinson, 1991). Classical linear stability theory applied to the base profiles of the various canonical wall-bounded flows predicts spanwise independent modes, so-called Tollmien–Schlichting waves, as the most unstable disturbances (see *e.g.* Schmid and Henningson, 2001). As evidenced by numerous experiments and simulations, these waves are not relevant in the context of sustaining near-wall turbulence. In the case of a spatially developing Blasius boundary layer, the laminar base flow is linearly stable up to a finite value of the Reynolds number Re, where $Re_c \approx 520$ based on the displacement thickness (see *e.g.* Schlichting, 2004). However, in the presence of strong noise, subcritical transition may as well occur further upstream via the formation of streamwise streaks, bypassing the classical transition scenario(see *e.g.* Brandt et al., 2004). These elongated structures appear as a result of the large sensitivity to

forcing and large transient energy growth of these structures in shear flows (Schmid and Henningson, 2001). Thus streamwise streaks and streamwise vortices can also be observed for boundary-layer flows in the absence of any linear instability of the base flow. Such coherent structures seem closely connected with the finite-amplitude solutions encountered in studies of subcritical transition in channels (Itano and Toh, 2001; Jiménez et al., 2005). We will hence focus here on coherent structures as well as bursting events in the framework of subcritical transition only. A recent idea specific to subcritical instabilities is to analyse the laminar-turbulent separatrix, the invariant phase-space region separating trajectories that relaminarise from those experiencing turbulent dynamics (Itano and Toh, 2001). Relative attractors on this separatrix are called edge states (Skufca et al., 2006). They correspond to an (unstable) equilibrium regime and are thus crucial for i) understanding the structure of the phase space and ii) identifying the physical mechanisms by which the flow can sustain non-trivial dynamics. The concept of edge states has been developed in studies of cylindrical Poiseuille flow and plane Couette flow, that both admit simple laminar solutions that are linearly stable for all Reynolds numbers Re. However, in practice another concurrent flow regime, namely turbulence, can be observed for moderate values of the Re, depending on the shape and amplitude of the initial perturbation to the laminar base flow. There is compelling evidence that trajectories restricted to the laminar-turbulent separatrix are attracted towards the edge state (see figure 5.4.1(a)), which can be either a fixed point (Schneider et al., 2008), a travelling wave (Duguet et al., 2008), a relative periodic orbit (Toh and Itano, 2003) or even a chaotic object (Schneider et al., 2007b). These pioneering investigations of edge states were performed numerically in the context of minimal flow units (Jiménez and Moin, 1991; Hamilton et al., 1995). Later investigations in extended computational domains (Duguet et al., 2009; Mellibovsky et al., 2009; Schneider et al., 2010c) revealed robust spatial localisation for the edge state, indicating a connection to incipient turbulent spots (Henningson et al., 1987; Lundbladh and Johansson, 1991), puffs and slugs (Duguet et al., 2010b).

The concept of edge states was recently carried over to the Blasius boundary-layer flow over a flat plate (Cherubini et al., 2011; Duguet et al., 2012), where an additional complication is the spatial development of the boundary layer. Duguet et al. (2012) have identified almost-cyclic dynamics on the edge in terms of rescaled variables, where the rescaling is done with respect to the local boundary-layer thickness. Edge tracking in a spatially inhomogeneous context is however computationally demanding as the proper asymptotic dynamics remains currently out of reach in a numerical domain of finite streamwise extent. Parallel flows are much better suited to asymptotical edge tracking since periodic boundary conditions both allow for streamwise periodic structures, and a constant layer thickness (*i.e.* Reynolds number) in the domain. We are hence focusing here on a parallel model for boundary layers, for which a number of variants have been discussed in the literature. Spalart and Yang (1987) proposed a model for a temporal boundary layer in a moving frame of refer-

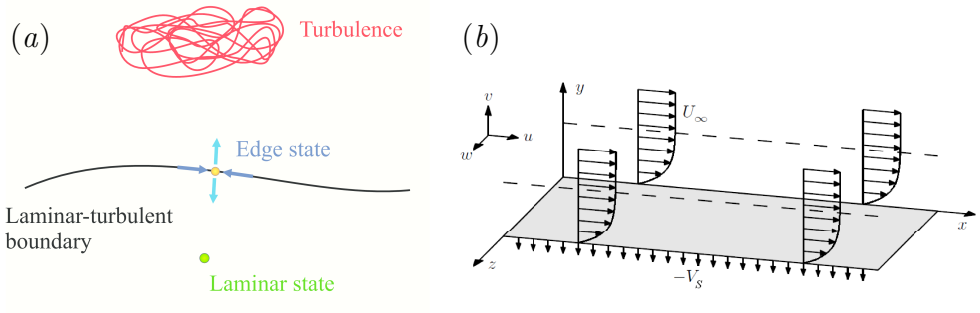

Figure 5.4.1.: (*a*) Conceptual two-dimensional sketch of the state space. The turbulent and laminar states are shown in red and green, respectively. The separatrix (black line) supports the edge state (yellow circle), which is attracting within the boundary and repelling in a direction transverse to it. (*b*) Sketch of the asymptotic suction boundary layer (ASBL), where constant homogeneous suction is applied at the wall. Figure adapted from Levin and Henningson (2007).

ence, which implies a homogeneous boundary-layer thickness throughout the domain which slowly grows in time. Another approach was developed by Spalart (1988) and recently used with some modification in an edge tracking study (Biau, 2012). In their model a multi-scale approximation of the flow was used to simulate the temporal evolution of a fixed short streamwise portion of the boundary layer. In this paper we will focus on a third alternative: suction is applied at the lower wall to compensate for the spatial growth of the laminar profile. In the case when the suction is constant and homogeneous the boundary-layer thickness rapidly saturates and the associated flow is termed Asymptotic Suction Boundary Layer (ASBL). Studying transition to turbulence in ASBL bears considerable advantages: i) its laminar solution is independent of the streamwise position, ii) it is one of the canonical solutions of the incompressible Navier–Stokes equations (Schlichting, 2004), iii) the laminar solution is linearly stable for a wide range of values of Re, and iv) it is realisable in wind-tunnel experiments using a porous plate with well-controlled suction. Applying suction is a powerful technique for flow control, hence ASBL has been the subject of a number of numerical (Mariani et al., 1993; Levin and Henningson, 2007; Schlatter and Örlü, 2011) and experimental studies (Antonia et al., 1988; Fransson and Alfredsson, 2003).

A numerical characterisation of the edge states in ASBL is the main focus of this paper. The structure of the paper is as follows. Parameters and numerical technique are described in § 5.4.2. The results of edge tracking are presented in § 5.4.3 both for a minimal flow unit and a spanwisely extended domain, where the spatial localisation and dynamics will be scrutinised. The main conclusions are given in the final section.

5.4.2. Problem setup and numerical methodology

ASBL is the flow above a permeable flat plate subject to constant homogeneous suction (see figure 5.4.1(b)). The incompressible Navier–Stokes equations admit in this case a laminar solution where the velocity field is independent of the streamwise position x,

$$U = U_\infty(1 - e^{-yV_S/\nu}) \ , \qquad V = -V_S \ . \tag{5.4.1}$$

Here y is the wall-normal distance from the plate, $\mathbf{U} = (U, V)$ is the velocity field of the base flow in the streamwise and wall-normal (x, y) directions, U_∞ and V_S are the imposed free-stream and suction velocities, respectively and ν is the fluid kinematic viscosity. An expression for the laminar displacement thickness δ^* can be found analytically,

$$\delta^* = \int_0^\infty (1 - u(y)/U_\infty) \ \mathrm{d}y = \frac{\nu}{V_S} \ . \tag{5.4.2}$$

The Reynolds number based on δ^* is defined by $Re = U_\infty\delta^*/\nu = U_\infty/V_S$. The laminar solution is linearly stable for Reynolds numbers up to $Re_c = 54370$ (Hocking, 1975), however transition to turbulence can be observed already above $Re \approx 300$ (Schlatter and Örlü, 2011).

Numerical simulations of the ASBL are performed here with a fully spectral method which solves the unsteady incompressible Navier–Stokes equations in a domain $\Omega = [-L_x/2, L_x/2] \times [0, L_y] \times [-L_z/2, L_z/2]$. The velocity field $\mathbf{u} = (u, v, w)$ is expanded using N_x and N_z Fourier modes in the streamwise x and spanwise z directions, respectively, and N_y Chebyshev polynomials in the wall-normal y direction. Hence, periodicity is imposed in both x and z. In the wall-normal direction, Dirichlet boundary conditions are used at both ends of the domain,

$$(u, v, w)_{y=0} = (0, -V_S, 0) \ , \tag{5.4.3a}$$

$$(u, v, w)_{y=L_y} = (U_\infty, -V_S, 0) \ . \tag{5.4.3b}$$

Dealiasing with the 3/2 rule is performed in the x and z directions. The results were validated by comparison between two codes – SIMSON (Chevalier et al., 2007) and ChannelFlow (Gibson, 2012). For time advancement a third-order Runge–Kutta and a second-order Crank–Nicolson methods are used for nonlinear and linear terms respectively with SIMSON, and a third-order semi-implicit backward differentiation scheme with ChannelFlow. We have verified that both codes lead to the same results and the same edge states both qualitatively and quantitatively. We therefore only present results obtained with SIMSON in this paper. Non-dimensionalisation with U_∞ and δ^* is used throughout the paper. One has to be careful when choosing the height L_y of the numerical domain, since the boundary layer tends to become very thick for turbulent ASBL (Schlatter and Örlü, 2011), saturating at very high values of 99% velocity thickness δ_{99} compared to the laminar case. However, δ_{99} for edge states is much lower, and $L_y = 15$ proved sufficient for the present investigation.

Edge tracking was performed in two different distinct setups. In the first case, which we refer to as a minimal flow unit, the domain has size $(L_x, L_y, L_z) = (10, 15, 6)$, with a numerical resolution of $N_x \times N_y \times N_z = 32 \times 129 \times 32$ spectral modes. In the second case the numerical domain is extended in the spanwise direction to a size of $(L_x, L_y, L_z) = (6\pi, 15, 50)$ with the corresponding resolution $N_x \times N_y \times N_z = 48 \times 129 \times 192$. The results presented here were obtained for $Re = 500$. Lowering Re to 400 did not show any significant changes in the dynamics. Resolution checks were performed for the key simulations by doubling the number of spectral modes in each direction. It turns out that the chosen resolution is fully adequate for edge states and the early transitional stages, while higher resolution and larger values for L_y are needed for the turbulent state to be accurately captured.

The dynamics on the separatrix is tracked using the bisection technique described by Skufca et al. (2006). A set of initial conditions $\mathbf{u}_\lambda = \mathbf{U} + \lambda(\mathbf{u}_0 - \mathbf{U})$ is considered, where $\mathbf{u}_0$ is an arbitrary non-trivial flow state. Initial conditions corresponding to various values of λ are evolved in time until they approach either the laminar or the turbulent state, according to the pre-defined thresholds for the rms (root-mean-square) of the wall-normal velocity fluctuations v_{rms}. By iteratively bisecting the value of λ we bracket the laminar-turbulent boundary and obtain a trajectory that evolves for a sufficiently long time without becoming neither laminar nor turbulent. Because of the exponential separation of initially nearby trajectories and the limited numerical accuracy of the bisection, the resulting trajectory visits the boundary for a finite time only. However, by restarting the bisection from the last state closest to the edge often enough it is possible to stay on the edge for an infinite time and to reach a relative attractor.

5.4.3. Edge states

Minimal flow unit

The edge state in small computational domains close to a minimal flow unit has been discussed by Kreilos et al. (2013). We briefly summarise the key features of the edge state in a box of size $(L_x, L_y, L_z) = (10, 15, 6)$.

The time evolution of the cross-flow energy based on the wall-normal $v' = v - V$ and spanwise $w' = w$ velocity fluctuations of this state,

$$E_{\mathrm{cf}} = \frac{1}{L_x L_z \delta^*} \int_\Omega (v'^2 + w'^2)\, \mathrm{d}x\, \mathrm{d}y\, \mathrm{d}z \ , \tag{5.4.4}$$

is shown in figure 5.4.2(a). This quantity measures the energy in the components transverse to the downstream flow and captures the intensity of the vortices. We see that there are long phases in which E_{cf} changes only slowly, followed by strong bursts at regular time intervals. Figure 5.4.2(b) shows the downstream velocity fluctuations $u' = u - U$ averaged in x at $y = 1$. We see that during the calm phase, the state

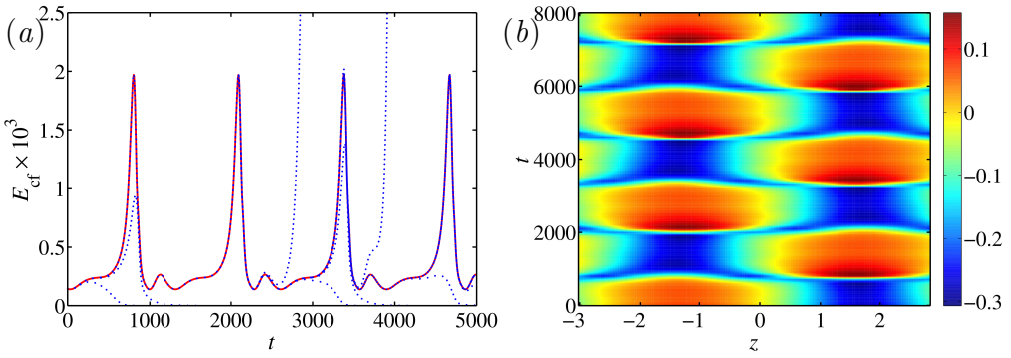

Figure 5.4.2.: (*a*) Evolution of the cross-flow energy E_{cf} with time t for the edge state in a minimal flow unit. The solid red line corresponds to the converged edge trajectory, whereas dotted blue lines correspond to trajectories diverging from the edge. (*b*) Space-time diagram for the streamwise velocity fluctuations u' averaged in x at $y = 1$ corresponding to the edge state in the minimal flow unit.

consists of a low- and a high-speed streak. At each burst, the low-speed streak is broken up into two parts, which reconnect across the periodic boundaries to form a new low-speed streak at a position that is shifted by half the box width. The edge state is hence a periodic orbit with a period that is twice the interval between bursts, *i.e.* 2×1290. A homotopy between plane Couette flow and ASBL was suggested by Kreilos et al. (2013) to explain the bifurcation underlying the bursts and the shifts: on the path from plane Couette flow to ASBL, the periodic orbit emerges from a saddle-node infinite-period (SNIPER) bifurcation undergone by two symmetry-related pairs of travelling waves.

Spanwise localised edge states

The dynamics described above relies heavily on the spanwise periodicity imposed by the value of L_z which is comparable to the streak spacing. In this work, we want to investigate the dynamics of the edge state in the absence of interaction with its periodic copies. We thus extend the spanwise width of the computational box to $L_z = 50$ while keeping L_x relatively low at 6π. As in the minimal flow unit, the cross-flow energy of the edge state is found to be periodic in time. By varying the initial perturbation $\mathbf{u}_0$ used for edge tracking, we obtain not one, but three states. Two of them are actually related by $z \leftarrow z_0 - z$ transformations, under which the system with boundary conditions (5.4.3) is invariant (z_0 is arbitrary). The time evolution of the cross-flow energy for all these states is shown in figure 5.4.3. Despite the difference in the periods, the edge trajectories all show similar characteristics to the small box case, *i.e.* a periodic alternation of calm phases and bursts. Space-time diagrams for $\langle u \rangle_x (y = 1)$ shown in figure 5.4.4(*a*)–(*c*) reveal a clear spanwise localisation of

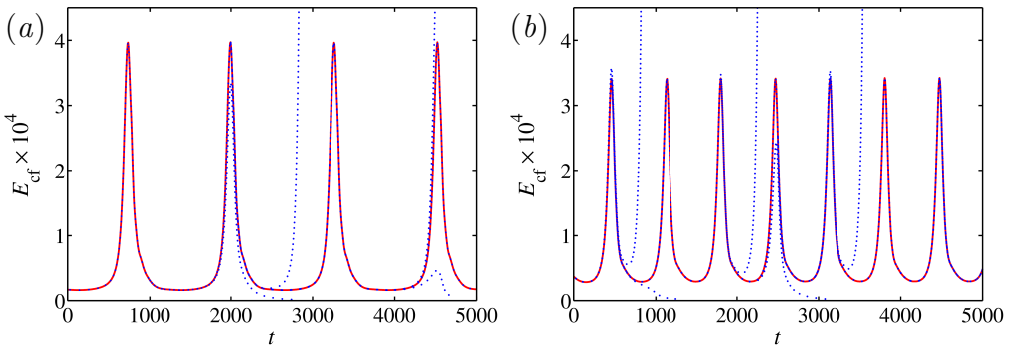

Figure 5.4.3.: Time evolution of the cross-flow energy E_{cf} for the three edge states obtained in the wide domain. (a) L edge state (indiscernible from R state). (b) LR state. The colour coding is the same as in figure 5.4.2(a). See the text for the definition of L, R and LR states.

the kinetic energy, as in former studies of edge states in other systems (Schneider et al., 2010c). This localisation property is robust to variations in L_z, as attested by figure 5.4.5(a).

The structure and dynamics of the three edge states can be understood from the space-time diagrams in figure 5.4.4(a)–(c). The velocity fields are dominated by a pair of high- and low-speed streaks which undergo a burst in cross-flow energy before being shifted in the spanwise direction. Depending on the direction of the shift we distinguish between the two symmetry-related states that repeatedly hop towards the right (R) or towards the left (L), and the state that alternates regularly between hopping left and right (LR). As already mentioned the L and R states differ in the direction of the shifts but otherwise have the exact same characteristics since they are related by a reflection symmetry. The period between two bursts of the LR state is approximately 1263, while that for both L and R states is 668, hence a bit longer than half the LR period.

Though we distinguish between two fundamental states based on the different motion in the spanwise direction z, the qualitative dynamics between two consecutive bursts appears to be similar in all three cases. Therefore our analysis of the detailed sequence of events during one period can be limited to one of these states only. In the following, we focus on the left-hopping state (L). Key snapshots of the cycle are shown in figure 5.4.6; supplementary movies are available at journals.cambridge.org/flm. Starting from the calm phase, the state consists of one high-speed streak with two low-speed streaks on each side. One of the low-speed streaks is moderately bent and is flanked by counter-rotating quasi-streamwise vortices. These vortices induce upward motion that advects slow fluid away from the wall, explaining the presence of the low-speed streak (lift-up effect). Conversely, the second streak is less bent and is slowly decaying. As the vortices grow in strength they wrap around the streak, tilting

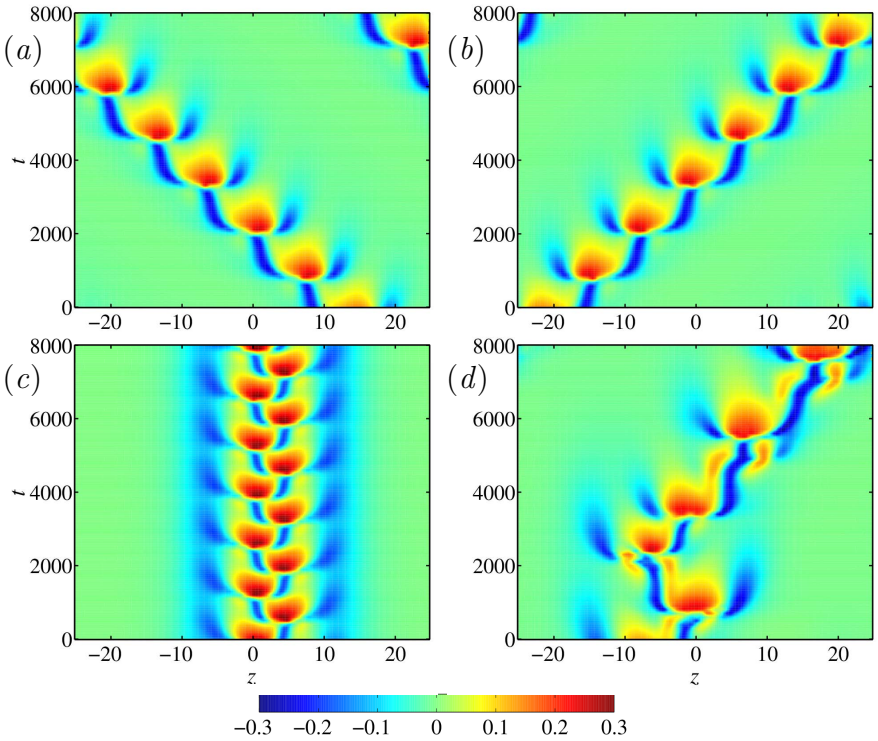

Figure 5.4.4.: Space-time diagrams for streamwise velocity fluctuations u' averaged in x at $y = 1$. (a) Left going state (L). (b) Right going state (R). (c) Left-right going state (LR). (d) Chaotic edge state for $L_x = 4\pi$.

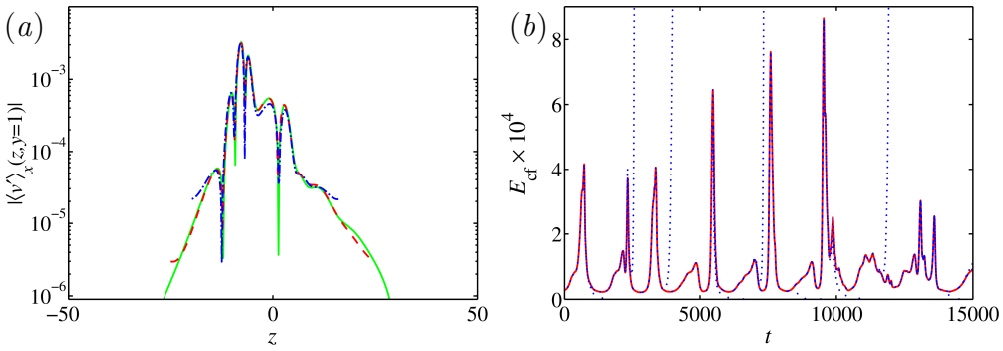

Figure 5.4.5.: (a) Absolute value of the wall-normal velocity fluctuations averaged in x at $y = 1$ evaluated at the time between two bursts for the L state with various spanwise widths of the domain: solid $L_z = 100$, dashed $L_z = 50$, dotdashed $L_z = 36$. (b) Time evolution of the cross-flow energy E_{cf} for one of the edge trajectories in the shorter domain $L_x = 4\pi$.The colour coding is the same as in figure 5.4.2(a) .

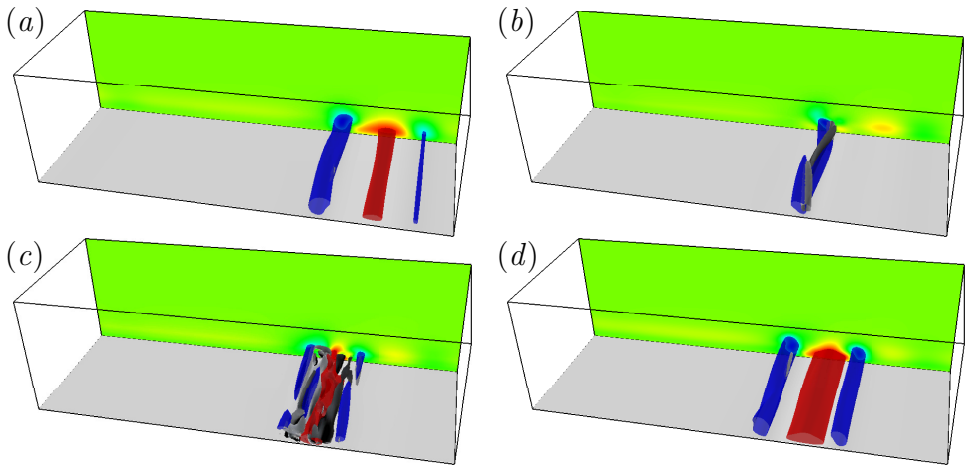

Figure 5.4.6.: Three-dimensional visualisation during one period of the L state. Isosurfaces of streamwise velocity fluctuations $u' = \pm 0.15$ are coloured in blue (low-speed streak) and red (high-speed streak), respectively. Vortices are visualised using the λ_2 criterion (Jeong and Hussain, 1995) with the isosurface $\lambda_2 = -0.001$ coloured by the streamwise vorticity (grey-scale). The whole computational domain is shown. (a) High-speed streak with two low-speed streaks on the side during the calm phase at $t = 2500$. (b) Strong quasi-streamwise vortices which lean over the active low-speed streak at $t = 3100$. (c) Breakdown at $t = 3300$. (d) Initial structures regenerated with a shift in the spanwise direction at $t = 3470$. Supplementary movies for the L state as well as the LR state are available at journals.cambridge.org/flm.

in the streamwise direction and causing the streak to bend even further. At some point the tips of the vortices cross the bent streak, each of them dividing the streak into two regions with respect to its streamwise extent. In the first region the vortex is still sustaining the streak, while in the second one it pushes fluid down instead of lifting it up. As the vortices cross the streak, they also cross each other, enhancing the push-down effect and ultimately leading to the breakdown of the low-speed streak and creation of a high-speed streak at the same location. During the same time the other low-speed and high-speed streaks decay. Those events correspond to the burst in the cross-flow energy. In the streak breakdown process the initial streamwise vortices are destroyed and new vortices are recreated in the area around the newly created high-speed streak. The vortices on both sides of the high-speed streak create two low-speed streaks and the loop is closed. The low-speed streak on the left is the active one that will develop instabilities and break down during the next burst, while the right one will slowly decay, resulting in a leftwards shift of the whole structure.

This self-sustaining process resembles the regeneration cycle of the near-wall turbulent structures discussed by Hamilton et al. (1995). We also start with streaks, one of which develops an instability leading to its streamwise modulation (x-dependent flow in the work by Hamilton et al. (1995)). In the process of streak breakdown, new

vortices are created, which corresponds to the vortex regeneration phase. Finally the streamwise vortices recreate the streaks by linear advection and return to the beginning of the cycle. A distinct feature of the process in ASBL is the spanwise shift of the regenerated streaks, which was not an intrinsic part of the self-sustaining process by Hamilton et al. (1995).

One of the most important parts of the dynamics – vortices crossing the streak, was also suggested in near-wall turbulence in minimal units (Jiménez and Moin, 1991) and later confirmed using feature eduction in extended domains (Jeong et al., 1997). Similar structures are also observed in boundary layers during bypass transition (Schlatter et al., 2008). The same mechanism can also be identified in the small box ASBL (Kreilos et al., 2013), albeit the two low-speed streaks created after the burst correspond to the same streak in this case due to the small box periodicity.

Chaotic behaviour of the localised edge state

As the domain length is decreased to 4π, the periodicity of all three edge states is lost. The resulting dynamics on the edge is chaotic, though also consisting of calm and bursting regions (see figure 5.4.5(b)). In figure 5.4.4(d) we present the space-time diagram corresponding to one of the edge trajectories in this case. We see that the structures remain localised and that the bursts in the cross-flow energy still correspond to hops in the spanwise direction. However, the direction and the distance of those shifts is no longer fixed but varies in an unpredictable fashion.

Insights into the transition from the periodic to the aperiodic behaviour can be obtained by slowly lowering the parameter L_x from 6π towards 4π. We find that the periodic behaviour is sustained at least down to $L_x = 5\pi$, below which new states – with longer periods and more complex sequences of spanwise shifts – emerge as attractors. These bifurcations indicate that the periodic solutions discussed above acquire at least one more unstable direction, hence can not serve as relative attractors any longer and can only be visited transiently by the edge trajectories (Duguet et al., 2008). Nevertheless, they may still constitute the beginning of a symbolic dynamics for the chaotic regime. The complete cascade of bifurcations leading from periodic towards chaotic edge states is currently under investigation.

5.4.4. Conclusions

To summarise, we have tracked the dynamics on the laminar-turbulent separatrix in the asymptotic suction boundary layer, which turns out to always be localised in wide enough domains. We were able to identify a robust cycle encompassing a calm phase with slow growth of a sinuous-type instability on a low-speed streak, and a violent burst of the streak due to vortex interaction once they are crossing the streak. Regeneration of new quasi-streamwise vortices and low-speed streaks accompanied by a spanwise shift is closing the cycle. This mechanism bears many similarities to pro-

cesses previously discussed in the context of minimal channel flow and the near-wall regeneration cycle in wall-bounded turbulence (Jiménez and Moin, 1991; Hamilton et al., 1995; Jiménez et al., 2005). Depending on the streamwise length of the domain used in simulations, imposing the wave length of the instability, the edge dynamics can be regular or erratic. This suggests existence of periodic orbits on the edge which behave as attractors or saddle points. A more detailed study of the effects of the streamwise localisation and the relevance of the identified bursting dynamics for both laminar-turbulent transition and fully developed near-wall turbulence are currently under investigation.

Computer time provided by SNIC (Swedish National Infrastructure for Computing) is gratefully acknowledged.

5.5. Comoving frames and symmetry-related slow processes in the asymptotic suction boundary layer

Tobias Kreilos[1,2], Stefan Zammert[1] and Bruno Eckhardt[1,3]
[1]Fachbereich Physik, Philipps-Universität Marburg, 35032 Marburg, Germany
[2]Max Planck Institute for Dynamics and Self-Organization, Am Fassberg 17, 37077 Göttingen, Germany
[3]J.M. Burgerscentrum, Delft University of Technology, Mekelweg 2, 2628 CD Delft, The Netherlands

Accepted for publication in Journal of Fluid Mechanics

Parallel shear flows come with continuous symmetries of translation in the downstream and spanwise direction. As a consequence, flow states that differ in their spanwise or downstream location but are otherwise identical are dynamically equivalent. In the case of travelling waves, this trivial degree of freedom can be removed by going to a frame of reference that moves with the state, thereby turning the travelling wave in the laboratory frame to a fixed point in the comoving frame of reference. We here discuss a general method by which the translational displacements can be removed also for more complicated and dynamically active states and demonstrate its application for several examples. For flows states in the asymptotic suction boundary layer we show that in the case of the long-period oscillatory edge state we can find local phase speeds which remove the fast oscillations and reveal the slow vortex dynamics underlying the burst phenomenon. For spanwise translating states we show that the method removes the drift but not the dynamical events that cause the big spanwise displacement. For a turbulent case we apply the method to the spanwise shifts and find slow components that are correlated over very long times. Calculations for plane Poiseuille flow show that the long correlations in the transverse motions are not special to the asymptotic suction boundary layer.

5.5.1. Introduction

Parallel shear flows like plane Couette flow or the asymptotic suction boundary layer, have continuous translational symmetries in the wall-parallel directions: flow states that differ only by a shift in these directions are dynamically equivalent. Different geometries can bring in other or additional symmetries. For instance, convection in cylindrical containers is invariant under rotations around the cylinder axis, and flow down a cylindrical pipe is invariant under rotations around the axis as well. The time evolution of these flow fields does not always preserve these symmetries, in the sense

that deformations of the velocity fields and translations along the symmetric directions are mixed. The implications of these continuous symmetries have been discussed in the context of exact coherent structures and dynamical systems approaches to the transition to turbulence in shear flows (Willis et al., 2013; Cvitanović et al., 2012b; Mellibovsky and Eckhardt, 2012), but they are also related to the applications and analyses using Taylors frozen flow approximations (Taylor, 1938; Townsend, 1980; Zaman and Hussain, 1981; Del Álamo and Jiménez, 2009). In both cases the issue is whether and how one can remove the motion along the symmetry axis.

As a specific example for the connection to exact coherent structures, consider the case of plane Couette flow in small domains that are periodic in the downstream and spanwise direction (Nagata, 1990; Clever and Busse, 1997; Waleffe, 2003; Wang et al., 2007; Schneider et al., 2008). The exact coherent states described by Nagata (1990); Clever and Busse (1997) are stationary solutions to the incompressible Navier-Stokes equation. They are fully 3-d with all velocity components active and variations in all three spatial directions, and they are invariant under translation in the downstream and spanwise direction (because of the periodic boundary conditions). Accordingly, they can be shifted anywhere within the domain. A second class of states are travelling waves, i.e. states that move downstream without change of shape, so that they can be described by velocity fields of the form $\mathbf{u}_{TW}(x-ct, y, z)$ (Nagata, 1997; Gibson et al., 2008). They become stationary in a frame of reference moving with the phase speed c. The third class of states are periodic solutions where the velocity field returns to its original shape after some period T. More generally, the velocity field can reappear in shape but at a location displaced along the symmetry axis (Viswanath, 2007; Gibson et al., 2009).

In the following we will outline calculations by which the advection along a symmetry axis can be extracted and removed from the time evolution, so that the nontrivial parts of the dynamics are highlighted. We will demonstrate the method for flow states in the asymptotic suction boundary layer (Schlichting, 1982), where rich dynamical structures exist (Kreilos et al., 2013; Khapko et al., 2013, 2014), and in plane Poiseuille flow. Further examples and applications are forthcoming.

In §2 we describe the method and its relation to other expressions in the literature. In §3 we describe its application to states in the asymptotic suction boundary layer: the long-period edge state with its conspicuous bursts (Kreilos et al., 2013), the sideways traveling localized states (Khapko et al., 2013) and a turbulent state, where slow spanwise drifts that are correlated over very long times are identified. In §4 briefly discuss an application to plane Poiseuille flow, and show that the spanwise drifts are also present in that case. We conclude with general remarks and an outlook in §5.

5.5.2. Symmetry related motions

We consider the time evolution of a velocity field in the form

$$\partial_t \mathbf{u}(x,y,z,t) = \mathbf{f}(\mathbf{u}(x,y,z,t),t) \tag{5.5.1}$$

in a situation where the right hand side is invariant under a translation along the x-axis. The velocity field $\mathbf{u}(x,y,z,t)$ at time t is one point in the state space of the system, the velocity fields $\mathbf{u}(x,y,z,t+\Delta t)$ at time $t+\Delta t$ and $\mathbf{u}(x-\Delta x,y,z,t)$ displaced by Δx in space are two other points. The difference vectors in the direction of time evolution and spatial shifts will be referred to as the time-evolution and displacement vectors, respectively. Using a first order Taylor-expansion, one finds that the time-evolution vector points along the right hand side of the evolution equation,

$$\mathbf{u}(x,y,z,t+\Delta t) - \mathbf{u}(x,y,z,t) \approx \Delta t\, \mathbf{f}(\mathbf{u}(x,y,z,t),t) \tag{5.5.2}$$

and the displacement vector points along the derivative of the velocity field,

$$\mathbf{u}(x-\Delta x,y,z,t) - \mathbf{u}(x,y,z,t) \approx -\Delta x\, \partial_x \mathbf{u}(x,y,z,t) \tag{5.5.3}$$

Usually, $\mathbf{f}$ has components parallel to the displacement vector, so that the time evolution mixes a change in the velocity field with a translation. Removing the displacement from $\mathbf{f}$ then leaves the non-trivial components of the time-evolution. In order to relate Δx and Δt, we introduce a phase velocity c such that $\Delta x = c\Delta t$, and then consider the time evolved and displaced field $\mathbf{u}(x-c\Delta t,y,z,t+\Delta t)$, which in a Taylor expansion to first order in time, becomes

$$\mathbf{u}(x-c\Delta t,y,z,t+\Delta t) \approx \mathbf{u}(x,y,z,t)+(-c\partial_x \mathbf{u}(x,y,z,t)+\mathbf{f}(\mathbf{u}(x,y,z,t),t))\Delta t \tag{5.5.4}$$

Projecting with $\partial_x \mathbf{u}(x,y,z,t)$ one finds that the parallel components are removed by the choice

$$c = \frac{\langle \partial_x \mathbf{u}(x,y,z,t) \cdot \mathbf{f}(\mathbf{u}(x,y,z,t),t)\rangle}{||\partial_x \mathbf{u}(x,y,z,t)||^2} \tag{5.5.5}$$

where

$$\langle \mathbf{u}(x,y,z,t) \cdot \mathbf{f}(x,y,z,t)\rangle = \int (\mathbf{u}\cdot\mathbf{f})(x,y,z,t)\, dxdydz \tag{5.5.6}$$

is the usual Euclidean scalar product and $||\mathbf{u}||^2 = \langle \mathbf{u}\cdot\mathbf{u}\rangle$ the associated norm. Since the velocity fields and the right hand side of the evolution equation vary in time, the phase speed calculated from (5.5.5) is usually also a function of time, $c(t)$. This expression is the infinitesimal version of the shifts described in equation (2.13) of Mellibovsky and Eckhardt (2012) and has been discussed under various names by various authors, see e.g. Smale (1970); Rowley et al. (2003); Cvitanović et al. (2012b). We will use the term *method of comoving frames*, since it reflects the underlying idea most directly: we introduce a frame of reference that moves with the flow so that the advection is subtracted and only the active part of the dynamics remains.

For travelling waves of the form $\mathbf{u}_{TW}(x-ct, y, z)$ the time evolution vector $\mathbf{f}$ and the displacement vector $\partial_x \mathbf{u}$ are strictly parallel, so that the advection speed determined by (5.5.5) agrees exactly with the phase speed of the wave, i.e. $\mathbf{f}(\mathbf{u}(x, y, z, t)) = c\partial_x \mathbf{u}(x, y, z, t)$. We therefore checked our implementation of the method of comoving frames by computing the the advection speed of a travelling wave (publicly available as TW2 in the database on `www.channelflow.org`). and find that the result from the Newton algorithm agrees with our implementation using finite differences to within a relative accuracy of 10^{-5}.

5.5.3. Flow states in the asymptotic suction boundary layer

The asymptotic suction boundary layer (ASBL) is the flow of an incompressible fluid over a flat plate into which the fluid is sucked with a constant homogeneous suction velocity V_S (Schlichting, 1982; Fransson and Alfredsson, 2003). We choose our coordinate system such that x points downstream, y normal to the plate, and z in the spanwise direction. The free stream velocity scale is denoted U_∞. Far away from any leading edge, the laminar flow profile is an exact solution to the incompressible Navier-Stokes equations,

$$\mathbf{u}(y) = (U_\infty(1 - \mathrm{e}^{-y/\delta}), -V_S, 0), \tag{5.5.7}$$

where $\delta = V_S/\nu$ is the displacement thickness. The laminar profile $\mathbf{u}(y)$ is translationally invariant in directions parallel to the wall. The Reynolds number is defined as $Re = U_\infty \delta/\nu = U_\infty/V_S$. Velocity, length and time are measured in units of U_∞, δ and $t_0 = \delta/U_\infty$, respectively, with t_0 also referred to as advective time unit.

We study the application of the method of comoving frames in the ASBL and in plane Poiseuille flow by direct numerical simulations, using channelflow (Gibson, 2012), as in our previous studies (Kreilos et al., 2013; Zammert and Eckhardt, 2013). Channelflow is a pseudo-spectral code developed and maintained by John F. Gibson, which expands the velocity field with Fourier-modes in the periodic directions and Chebyshev-Polynomials in the wall-normal direction. In this section, we study the flow in the ASBL at Reynolds number $Re = 500$ in numerical domains of size $L_x \times h \times L_z = 6\pi \times 25 \times 3\pi$ in units of δ with a resolution of $96 \times 193 \times 96$ modes, using periodic boundary conditions in the parallel to the walls and no-slip conditions at the walls. We have confirmed that a height of 25 is sufficient by verifying that our results do not change if a height of 50 is used instead. The Reynolds number of 500 in our calculations together with our chosen domain size is just large enough to make spontaneous decay from the turbulent state very unlikely and allows us to compute long turbulent trajectories.

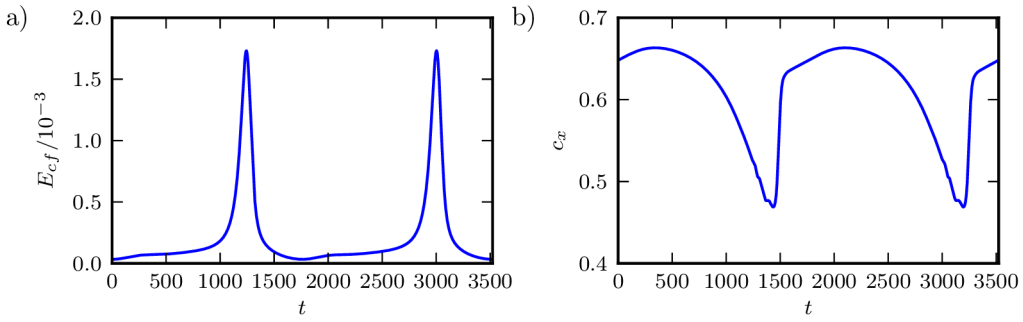

Figure 5.5.1.: Energy and advection velocity of the edge state in ASBL at $Re = 500$. The left frame shows the clear increase in energy when the edge state goes through the bursting phase. Studies of the flow field then show that afterwards it is displaced by half a box width, so that the full period are two bursting events in energy. The left frame shows the advection speed extracted by symmetry projection. It shows that as the energy goes up the structures slow down noticeably.

Downstream advection of the edge state

The edge state in the asymptotic suction boundary layer is a periodic orbit with two different time scales (Kreilos et al., 2013). On a short time scale of about 15 advective time units, the dynamics is similar to that of a travelling wave. On longer time scales of about 1500 advective time units one finds energetic bursts that are clearly visible in the cross-flow energy[1] in figure 5.5.1(a). The flow is composed of two counter-rotating downstream-oriented vortices and a pair of low- and high-speed streaks. During the bursts, the streaks break up, and reappear shifted by half a box width with respect to their original position.

Observation of the dynamics during a burst is complicated by the advection of the structures which happens on a much faster time scale than the bursts. Using (5.5.5) one can calculate an instantaneous advection speed c_x in the downstream direction and go to a comoving frame of reference that removes the fast oscillations and reveals the slow dynamics underlying the bursts. Figure 5.5.1(b) shows the instantaneous advection velocity which is almost constant during the low-energy phase of the state and drops noticeably as the energy increases and the state becomes more complicated.

The full power of the method of comoving frames and the different dynamics in the laboratory and the comoving frame of reference is most prominently visible in the movie provided with the online material. To give some indication of the differences, we have extracted the spanwise velocity component at one point in the flow. The

[1] The cross flow energy is a measure that has proven useful in the characterization of the dynamics of shear flows. It contains only the energy in the wall-parallel directions and is hence not dominated by the high energy content of the downstream components. It is defined by $E_{cf} = \int_V \left(v^2 + w^2\right) \mathrm{d}^3x/V$ where the integration is over a box of volume V.

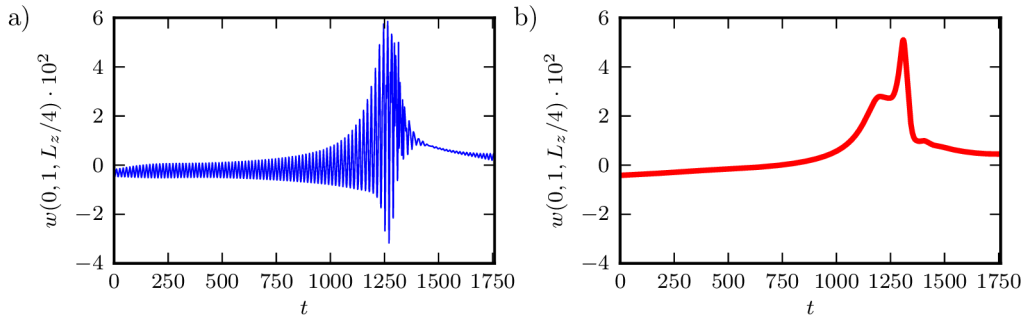

Figure 5.5.2.: Comparison of the edge state dynamics in the laboratory frame and the comoving frame of reference. Shown is the time evolution of a single spanwise velocity component, $w(0, 1, L_z/4)$, as a function of time for one burst. In the laboratory frame of reference (left panel), the signal shows rapid oscillations, corresponding to the travelling-wave like behaviour of the edge state on short time scales, with the energetic burst visible as regions of larger amplitude oscillations. In the comoving frame of reference (right panel), the rapid oscillations are gone and the evolution of the component is rather smooth with an increase during the burst: the short-term dynamics has been completely eliminated and only the long-term dynamics are visible. A movie of the time evolution that shows the differences much more clearly is provided as supplementary material.

time trace in the labframe is shown in figure 5.5.2(a) and in the comoving frame of reference in figure 5.5.2(b). The high-frequency jitter on the signal in the labframe is due to the rapid advection in the downstream direction. In the comoving frame this is removed entirely, so that the gradual built up of a strong spanwise velocity and its rapid break down stands out clearly. The movie then shows that the velocity field during the low energy phase is dominated by down stream streaks with a weak sinusoidal modulation in the spanwise direction. As time goes on, the modulation amplitude increases, until the streaks break up. After the burst, the streaks and vortices form again, but displaced by half a box width in the spanwise direction.

The calculations are in a domain with periodic boundary conditions in the downstream and the spanwise directions. The flow naturally attains a discrete symmetry, a shift in the downstream direction by half a box length and a reflection on the midplane in the spanwise direction (Kreilos et al., 2013). With this discrete symmetry, the symmetry related advection velocities in the spanwise direction as calculated from (5.5.5) vanish exactly. For turbulent velocity fields this symmetry is broken and spanwise components do appear, as we discuss in §5.5.3.

Spanwise advection of localized edge states

The discrete symmetry involving a spanwise reflection is broken if the domain is extended wide enough in the spanwise direction so that the state localizes. Edge states

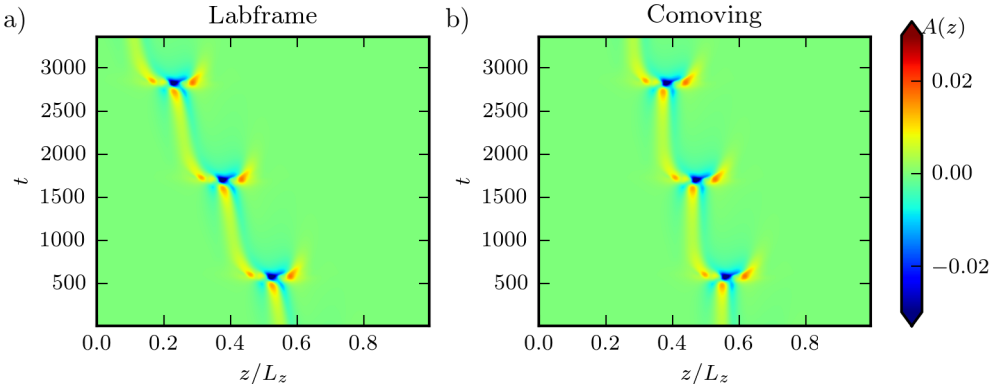

Figure 5.5.3.: Space-time plot of the x-averaged wall-normal velocity $A(z,t)$, eq (5.5.8), for the left jumping edge state in a wide domain (Khapko et al., 2013). The edge state is localized and during the calm phases between two bursts it consists of a pair of downstream-oriented counter-rotating vortices, visible by the alternating pattern of fluid moving up (red) and down (blue). At the bursts the structures break up and reform at a different spanwise location. a) In the laboratory frame, in the calm phases the red and blue lines are tilted, reflecting a spanwise drift. b) In the comoving frame of reference, the red and blue regions are aligned along the time-axis during the calm phases, indicating that the drift has been removed. However, the spanwise displacement at the bursts remains, indicating that it is not caused by advection but by internal dynamics of the flow.

in this setting have been calculated in (Khapko et al., 2013, 2014); their dynamics is similar to the one in periodic domains, and shows long calm phases that are interrupted by violent bursts, during which the structures break up and reform at a position that is shifted in the spanwise direction. These studies also show that different patterns in the spanwise displacement are possible: states may always be shifted to the right or the left, they may alternate between left and right shifts or they may even follow irregular patterns of left and right shifts. We here focus on a state that always shifts to the left.

In order to obtain a 2-d representation of the four-dimensional space-time evolution of the flow state we pick the wall-normal velocity at the height δ as a good indicator of up- and downwelling motion that can be connected to vortices. Since the domains are relatively short, we average this quantity in the downstream direction. The resulting observable

$$A(z,t) = \langle v(x, y=\delta, z, t)\rangle_x \tag{5.5.8}$$

depends on the spanwise coordinate z and time t and can be represented in 2-d color plots. For three periods of the left-shifting state we find the representation shown in figure 5.5.3. In the laboratory frame of reference (left panel), we see that there is an alternating pattern of fluid moving up and down (red and blue), corresponding to alternating streamwise vortices. At the bursts, the structures break up and are reformed almost symmetrically left and right, of which only the left one survives. In

between the bursts the structures slowly and constantly drift to the left, as indicated by the finite slope of the lines. In the right panel, in the comoving frame of reference, the drift is completely removed and the structures are stationary in the calm phase, while they are still displaced at the bursts. This clearly shows that the method of comoving frames is able to separate the advective part of the time evolution (i.e. the drift) from the dynamically active and relevant part, in this case the break-up and displacement of the structures.

Spanwise drift of turbulent states

We now turn to turbulent flows and an analysis of spanwise shifts within the same computational domain as in §5.5.3. The general expression (5.5.5) for the phase speed with $\partial_x \mathbf{u}$ replaced by $\partial_z \mathbf{u}$ will not vanish in general (unless there are discrete symmetries as mentioned before). However, one would expect this contribution to be small and more or less uncorrelated. Indeed, the time traces in figure 5.5.4(a) show a strongly fluctuating signal with a small amplitude and a probability density function (pdf) that is well approximated by a Gaussian (figure 5.5.4(b)).

The correlation function of the advection speeds is shown in figure 5.5.5(a). It is based on data from 14 turbulent trajectories, each integrated for 200 000 time units. Initially, the correlation function falls of rather quickly, but then develops a wide background. As the inset shows, this background can be well approximated by an exponential form with a characteristic time of more than 4000 advective time units. Armed with the information that this correlation time is so long, one can begin to see evidence for it in figure 5.5.4(a), where the average of the fluctuations over the first 3000 time units is slightly above 0, whereas it is below zero for the remaining 7000 time units. The consequences of this are that the integrated advection speed, i.e. the distance over which the velocity field are displaced,

$$z_0(t) = \int_0^t c_z(\tau) d\tau, \tag{5.5.9}$$

first increases and then decreases. This is shown in figure 5.5.5(b).

The effect of the transverse drift and its removal on the flow patterns is shown in figure 5.5.6, in the reduced representation (5.5.8) of the velocity fields. Regions with strongly positive or negative components in the normal direction show up as ridges that meander in space and time. This is particularly noticeable in the labframe (left frame). The black line on top of the figure is the integrated spanwise drift (5.5.9): it is perfectly aligned with the ridges in $A(z,t)$ and underlines the drift to the right. In the comoving frame of reference (right panel), the structures are then shifted by this amount in the spanwise direction, and the structures are more parallel to the vertical axis.

In view of the long time correlations found in the spanwise direction, we also checked the downstream advection velocity. The downstream component fluctuates around

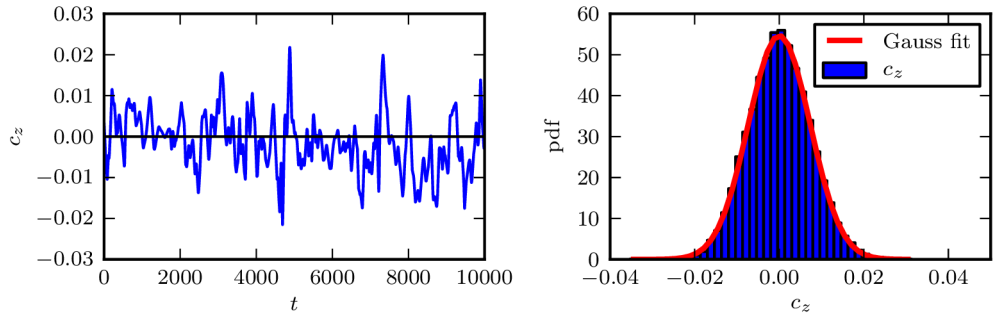

Figure 5.5.4.: Transverse advection velocity for a turbulent trajectory in the ASBL. a) The spanwise advection velocities c_z are small and fluctuate randomly. b) The distribution of the advection velocities is almost perfectly Gaussian, indicating that it mainly consists of random noise.

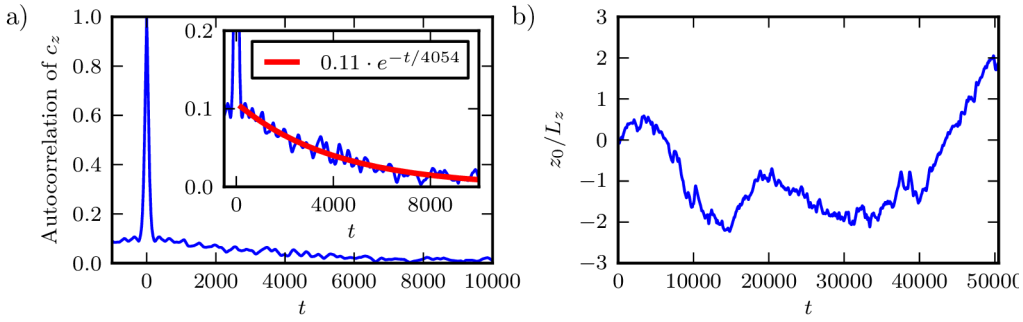

Figure 5.5.5.: Correlation function and integrated displacements in spanwise direction in the ASBL. The correlation function of the spanwise advection speed (left frame) shows a strong central peak, indicative of weak correlations, and a broad background reaching out to very long times. The inset shows that this tail is well captured by an exponential distribution with a characteristic time of more than 4000 natural units. The frame on the right shows the integrated advection speed, or displacement, in the spanwise direction. The long correlations show up as modulations over very long periods. Note that the time scale covered is five times that shown in figure 5.5.4(a).

a mean advection velocity $\overline{c}_x \approx 0.667$. The pdf is close to Gaussian with a weak but noticeable asymmetry to larger speeds, see igure 5.5.7(a). The autocorrelation function of the fluctuations around the mean, figure 5.5.7(b), falls off rapidly, but is significantly wider than the one for the spanwise shifts. The background is broader but less well characterized by a single exponential than in the case of the spanwise shift.

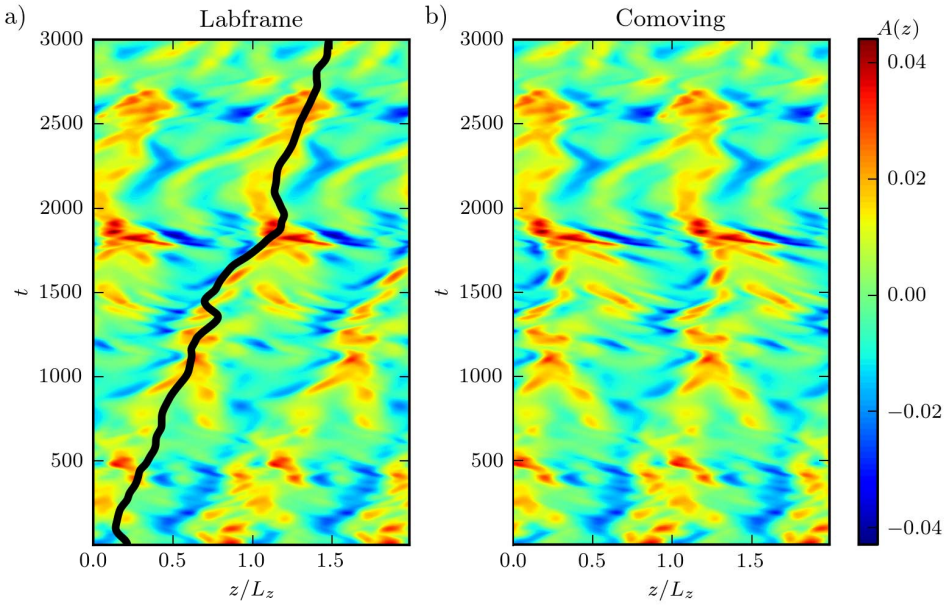

Figure 5.5.6.: Space-time plot of the x-averaged wall-normal velocity $A(z,t)$, eq (5.5.8), demonstrating the effect of the method of comoving frames on a turbulent trajectory in the ASBL. The width of the box is twice the computation domain in order to highlight advection across the spanwise boundaries. For most times, there are two regions, predominantly blue and red, respectively, corresponding to one pair of large-scale downstream vortices. a) In the laboratory frame, the blue and red regions are tilted, reflecting a gradual spanwise drift. The thick black line is the integrated advection velocity, and it falls along a prominent ridge in the structures. b) In the comoving frame of reference, where the drift is subtracted, the two colored regions are essentially stationary and aligned along the time-axis.

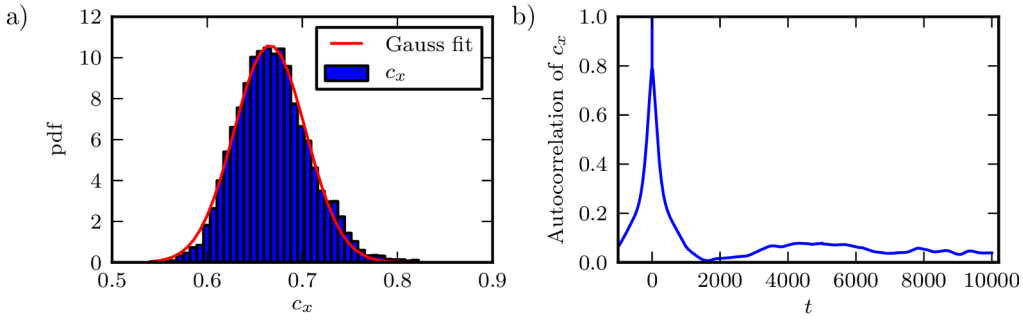

Figure 5.5.7.: Pdf and autocorrelation function for the downstream advection velocity in the ASBL. In contrast to the spanwise advection, figure 5.5.5, it drops rather quickly to zero and does not show the long tails noted above.

5.5.4. Turbulent flow states in plane Poiseuille flow

In this section we apply the method of comoving frames to plane Poiseuille flow. As shown in (Toh and Itano, 2003; Zammert and Eckhardt, 2013), plane Poiseuille flow has exact coherent structures that are remarkably similar to the ones found in the ASBL, and their phase speeds in the streamwise and spanwise directions can be determined as in the case of the ASBL. We here focus on a turbulent state and its transverse drift.

We perform direct numerical simulations of plane Poiseuille flow with constant bulk velocity at $Re = 3000$, based on the laminar center-line velocity U_0 and the channel half-width. The laminar flow profile is given by $\mathbf{u}(y) = (1 - y^2, 0, 0)$, so that the bulk velocity becomes $U_{bulk} = (2/3)U_0$. For the computations we use a domain of size $L_x \times L_y \times L_z = \pi \times 2 \times 0.4\pi$, a resolution of $32 \times 65 \times 32$ modes, and Gibson's code channelflow (Gibson, 2012).

As in §5.5.3 we study the spanwise and streamwise drifts. To calculate the correlation function of the advection speeds data from 20 turbulent trajectories, each integrated for 50 000 time units d/U_0 is used. The average of the downstream advection velocity c_x is 0.675 and therefore slightly larger than the bulk velocity. As in the ASBL, the probability density function of c_x in figure 5.5.8(a) is well approximated by a Gaussian and the correlation function of the downstream advection velocities, shown in figure 5.5.8(b), quickly drops to zero.

The spanwise advection velocities are also Gaussian distributed with a mean value of zero (not shown). The correlation function for the spanwise velocities in figure 5.5.8(c) also shows a wide background as in the case of the ASBL. An exponential fit yields a characteristic time of about 300 time units. This weak long-ranged correlation can be seen in the integrated advection speeds z_0 (5.5.9) in figure 5.5.8(d). The plot reveals several segments in which the flow drifts in the same direction. They are a few hundred time units long, consistent with the correlation time of about 300.

The different transverse correlation times are unusual. Compared to the ASBL the characteristic times of the background correlation differ by a factor of 13. Yet the coherent structures studied by Toh and Itano (2003) and Zammert and Eckhardt (2013) show bursts on time scales that are similar. The difference presumably comes about because the coherent structures in plane Poiseuille flow are localized near one wall, whereas the determination of the advection speed involves an integration over the entire domain. Uncorrelated motions close to the upper and lower walls will thus reduce the correlation time.

5.5.5. Concluding remarks

The examples show that one of the appealing features of the transformation (5.5.5) is the local and instantaneous removal of a downstream advective component in the time evolution. The speed by which this component is removed depends on the state

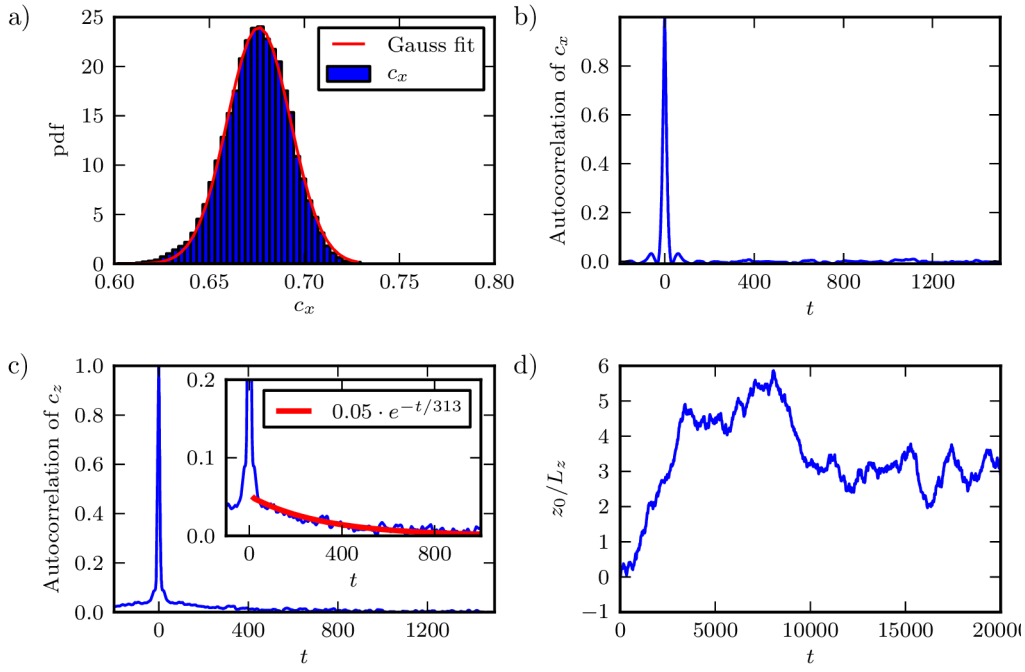

Figure 5.5.8.: Application of the method of comoving frames to plane Poiseuille flow at $Re = 3000$. (a) The streamwise advection velocity fluctuates around a mean value of 0.675 what is close to the bulk velocity. The distribution of the velocities is almost gaussian. (b) The correlation function of the downstream advection velocity quickly drops to zero. (c) The correlation function of the spanwise advection speed shows a strong central peak, indicative of weak correlations, and a broad background reaching out to long times. The inset shows that this tail is well captured by an exponential distribution with a characteristic time of about 300 time units. In (d) the the integrated advection speed, or displacement, in the spanwise direction is shown.

and hence varies in time. However, once this component is removed, the changes in vortices and streaks stand out much more clearly and become accessible to further analysis.

It is possible to extend this analysis from local in time also to local in space, and to find advection speeds that focus on particular features of the flow. The key to this is the scalar product that enters the projection to obtain eq. (5.5.5). In the calculations shown here we use the usual Euclidian scalar product with the scalar product of all components integrated over all of space, eq. (5.5.5). For other situations and applications, suitable adaptations of the method are possible. For instance, if not all velocity components are available, one could base the projection on a subset of components. Also, if the velocity fields are only known in a subset of the space, the integration may be limited to that subset. Extensions in this direction are currently being explored.

Another extension of the method uses different representations of the velocity field, e.g. expansions in spectral modes and restrictions in the scalar product to subsets of the modes. For instance, if the velocity fields are given in a Fourier representation, one can extract phase speeds for individual Fourier components. Del Álamo and Jiménez (2009) used such an idea in their intriguing discussion of the effects of Taylors frozen flow hypothesis (Taylor, 1938; Townsend, 1980; Zaman and Hussain, 1981) on turbulent spectra: they defined a wavenumber dependent phase speed (their equation (2.4)) that is equivalent to (5.5.5) when applied to a single spanwise Fourier mode.

The method for the extraction of symmetry related motions and the expression for the advection speed given in equation (5.5.5) are easy to calculate and to extract from both numerical and experimental data. For the use with experimental data, the time-evolution vector is replaced by finite differences between velocity fields at different times, and the spatial derivative can be approximated by finite differences in space. With a sufficiently good spatial and temporal resolution, the results are indistinguishable from full analytical approximations. If the time steps are longer it may be advisable to turn to the optimization methods described in Mellibovsky and Eckhardt (2012), where the velocity field $\mathbf{u}(x, y, z, t)$ is used as a template and a suitable shift is determined by minimizing $||(\mathbf{u}(x, y, z, t + \Delta T) - \mathbf{u}(x - \Delta x, y, z, t)||^2$. The shift and advection speed determined by this method and the one from eq. (5.5.5) become equivalent in the limit of small Δt where Taylor expansions are possible.

Continuous symmetries appear in many fields, and various methods for separating shifts along the symmetry axis from dynamical changes have been developed (see Cvitanović et al. (2012a); Froehlich and Cvitanović (2012); Cvitanović et al. (2012b)). In the fluid mechanical context they have appeared in connection with derivations of low-dimensional models using proper orthogonal decomposition (Rowley and Marsden, 2000; Rowley et al., 2003). Their relevance for the detection of relative periodic orbits, including a successul application of the method of slices, which allows an exact symmetry reduction, has been emphasized in Willis et al. (2013).

The method of comoving frames described in §5.5.2 helps in removing some of the advective and dynamically less relevant components, but it does not solve all problems related to finding relative periodic orbits, since it is not a general symmetry reduction scheme. For instance, the state shown in the first example in §5.5.3 passes through an intermediate state where the flow fields are shifted by half a box width in the spanwise direction. This shift is a dynamic one, not related to advection, and hence not removed. Therefore, for a periodic orbit calculation, one would still have to take the initial state and its images under discrete symmetries and check whether the flow returns to the symmetry related copy. The situation gets even more complicated for the states in the wider domains as discussed in Khapko et al. (2013, 2014): For instance, the states that steadily move to the left do repeat after a suitable shift in the spanwise direction, but as shown in §5.5.3 this translation is again not removed by the continuous shifts since it is a result of the changes in the flow fields.

Nevertheless, judging by the examples we have analyzed so far, the removal in

particular of the downstream advection reveals underlying coherent structures, or candidates for coherent structures, more clearly than the laboratory frame dynamics.

Acknowledgements

We thank John F Gibson for providing and maintaining the open source Channelflow.org code, Marc Avila for discussions that motivated this investigation, Predrag Cvitanović for extensive exchanges on continuous symmetries, Hannes Brauckmann and Matthew Salewski for comments and Francesco Fedele for encouragement. This work has been supported in part by the Deutsche Forschungsgemeinschaft within Forschergruppe FOR1182.

5.6. Bypass transition in boundary layers as an activated process

Tobias Kreilos[1,2], Taras Khapko[3], Philipp Schlatter[3], Yohann Duguet[4], Dan S. Henningson[3] and Bruno Eckhardt[1,5]

[1]Fachbereich Physik, Philipps-Universität Marburg, D-35032 Marburg, Germany
[2]Max Planck Institute for Dynamics and Self-Organization, D-37077 Göttingen, Germany
[3]Linné FLOW Centre, KTH Mechanics, Royal Institute of Technology, SE-100 44 Stockholm, Sweden
[4]LIMSI-CNRS, Université Paris-Sud, UPR 3251, F-91403, Orsay, France
[5]J.M. Burgerscentrum, Delft University of Technology, NL-2628 CD Delft, The Netherlands

Manuscript in preparation

Many shear flows, like pipe flow or plane Couette flow, show transition to turbulence while the laminar profile is linearly stable. This is also observed in the Blasius boundary layer (BBL) in the presence of disturbances, e.g. finite roughness on the plate, sound or disturbances in the free-stream, so that in numerous cases relevant for engineering purposes the classical route to turbulence via the exponential growth of Tollmien-Schlichting waves is bypassed (Schmid and Henningson, 2001; Saric et al., 2002). In this paper, we investigate the bypass transition in the BBL subject to free-stream turbulence, inspired from recent developments in the study of internal shear flows, and we model it using a probabilistic cellular automaton (PCA) describing the spatio-temporal aspects of the transition.

In internal shear flows a framework to describe the transition to turbulence from a dynamical systems perspective has been developed in the last two decades. Unstable flow states that are invariant solutions to the governing Navier-Stokes equations appear in saddle-node bifurcations with growing Reynolds number (Re), forming a dense network which supports turbulence. The boundary in state space separating the basin of attraction of the turbulent state from the laminar one, is called the edge of chaos (Skufca et al., 2006; Eckhardt et al., 2007). To trigger transition, a perturbation must be on the turbulent side of this edge. The boundary comes closer to the laminar state as Re increases, leading to a double-threshold in Re and amplitude that must be crossed in order to trigger transition (Grossmann, 2000). There are indications that the situation is analogous in the BBL, with the additional complication that the Reynolds number grows with increasing distance from the leading edge and that all perturbations are advected downstream towards higher Re. The calculation of a critical trajectory, neither laminar nor fully turbulent, has been documented in (Duguet et al., 2012).

The transition to turbulence in the boundary layer occurs via the generation of isolated turbulent spots, which are advected downstream and grow in size. Similarly, turbulence in pipe flow at moderate Re occurs in localized patches, termed puffs and

slugs (Wygnanski and Champagne, 1973), so that (in spatially extended systems) the spatio-temporal aspects of the transition process are of importance. At low Re in pipe flow turbulence is transient and transition from turbulent to laminar motion is frequently observed (Hof et al., 2006). The localized puffs can split and slugs can grow, leading to an expansion of turbulence and once the probability to split surpasses the probability to decay, turbulence is sustained (Moxey and Barkley, 2010; Avila et al., 2011).

Several models have been developed to understand this behavior (Barkley, 2011a,b). Among the most intriguing ones are simple probabilistic cellular automata (PCA) (Chaté and Manneville, 1987, 1988b), where space and time are discretized and the possible states of the flow in each cell at each instant in time are reduced to being laminar or turbulent. The time evolution is then governed by given probabilities with which turbulence can spread, persist or decay (Bottin et al., 1998; Daviaud et al., 1990; Sipos and Goldenfeld, 2011).

In this paper we develop a data-driven PCA model for bypass transition in boundary layers. The main difference with pipe flow is that the model must be inherently 2+1 dimensional (since spreading in the streamwise and spanwise direction are possible) and that at least one parameter of the model must depend on the streamwise position to reflect the growing Reynolds number. The model topology and its parameters are deduced from numerical simulations of a boundary layer subject to different levels of free-stream turbulence, thus allowing for a direct comparison of the model with the simulations.

The numerical set-up is similar to the one used by Brandt et al. (2004). The flat plate boundary-layer flow is simulated with a fully spectral code (Chevalier et al., 2007), which solves the incompressible Navier–Stokes equations on a orthogonal parallelepiped. The free-stream turbulence at the inlet is generated by a superposition of modes from the continuous spectrum of the Orr-Sommerfeld and Squire operators (Brandt et al., 2004). Our approach is based on long-time statistics, the smallest scales of turbulence are modeled by a subgrid-scale model, which in turn reduces the computational cost considerably. We checked that using this large eddy simulation (LES) model the transition location is not affected significantly. We performed simulations for different intensities of the free-stream turbulence, ranging from Tu = 3.0% to 4.0% of the free-stream velocity U_∞, while keeping the integral length scale constant in all cases. More details on the solver, the free-stream turbulence generation technique, as well as the simulation set-up are given in the appendix. There are two common definitions of the Reynolds number, based on either the distance to the leading edge $\mathrm{Re}_x = U_\infty x/\nu$ or the local laminar displacement thickness $\mathrm{Re}_\delta = U_\infty \delta/\nu$ with δ given by $1.72\sqrt{\nu x/U_\infty}$; we mainly use Re_x in this work since plots look nicer, but for theoretical considerations we prefer Re_δ. The beginning of the numerical domain is at $\mathrm{Re}_\delta = 300$ and we measure all quantities in units of δ at this position and U_∞.

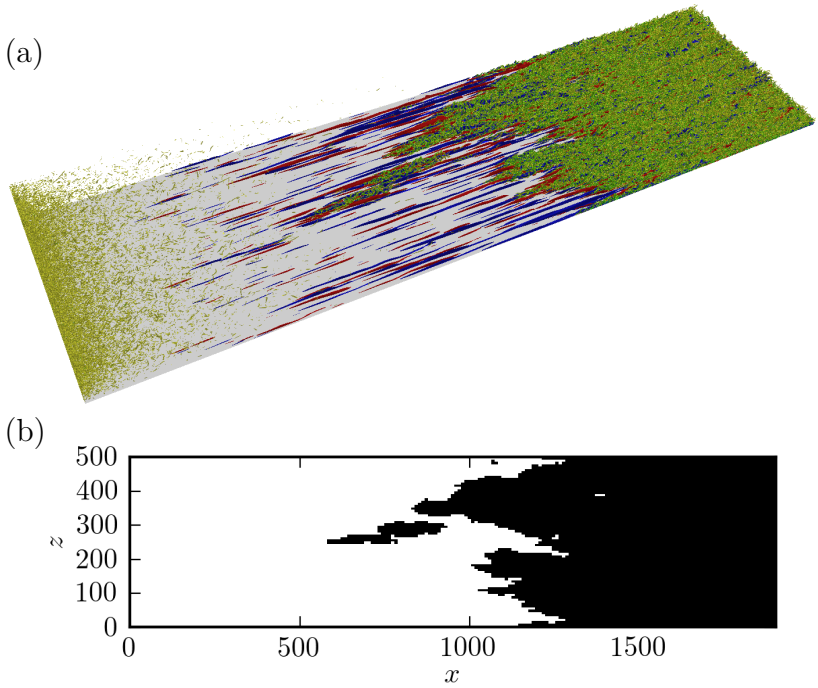

Figure 5.6.1.: A three-dimensional snapshot of the simulation and its reduction to two-dimensional a binary representation. (a) A snapshot from the LES simulations, with streaks visualized by negative (blue) and positive (red) isocontours of downstream velocity and vortices by by isocontours (green) of the λ_2 vortex detection criterion. The flow is from left to right, we see the free-stream turbulence entering the domain on the left and decaying further downstream. Streaks are induced close to the wall by the free stream turbulence, which subsequently break down, giving rise to turbulent spots. The distinction between turbulence and non-turbulent streaky flow is evident by the presence of vortical motion. (b) The binary representation of the above snapshot. The correspondence between the (green) turbulent patches and the black regions is evident, confirming that our reduction faithfully discriminates between turbulent and non-turbulent motion.

In the presence of free-stream turbulence above a laminar boundary layer, regions of alternating low and high streamwise velocity emerge as a direct effect of receptivity. Those low- and high-speed streaks can be clearly seen near the beginning of the domain in figure 5.6.1(a). The streaks exhibit non-normal linear transient growth (Hœpffner et al., 2005) and develop a waviness, before breaking down into turbulent spots (Henningson et al., 1987), visible as the green patches in figure 5.6.1(a). As the spots propagate downstream, they spread in both the streamwise and spanwise direction, merge and eventually lead to a fully turbulent boundary-layer flow.

To allow for a match with the desired PCA we transfer the LES data to a coarser grid, with the new grid spacing defining one independent cell in the PCA, and assign a binary value of laminar or turbulent to each cell. The procedure is briefly outlined

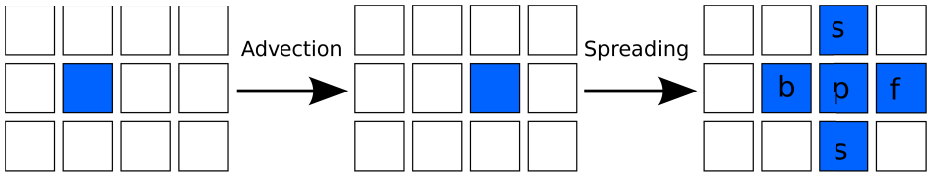

Figure 5.6.2.: A sketch of the probabilistic model. On the 2D grid, with downstream direction on the horizontal axis and spanwise on the vertical one, a turbulent cell (blue) is first advected one cell per timestep to the right. Subsequently, it may induce turbulence in the neighbouring cells according to given probabilities.

below, further details can be found in the appendix. As an indicator for turbulent motion the local spanwise shear stress at the wall $\tau_s = \partial w/\partial y|_{y=0}$ is used. This choice has the advantage that it is a wall-based quantity which is independent of the wall-normal position where it is measured. τ_s is high in the presence of downstream vortices, which are weak in the streaky flow before the turbulence transition and strong beyond it. Inspection of the spanwise and downstream-temporal autocorrelation functions of τ_s suggests a cell size of $dx \times dz = 9.9 \times 6.5$, together with a timestep $dt = 22$, corresponding to an advection velocity of structures of $dx/dt = 0.45$. The data is reduced to the coarser grid using spatial averaging and a Gaussian filter with kernel size of half a cell applied afterwards to remove spurious events. Finally, a threshold is introduced, based on the probability density distribution of the unfiltered data, with the threshold set in the minimum of the PDF, with $\tau_s = 0.3$. In figure 5.6.1(b) we show the binary representation of the above snapshot, the black regions capture well the turbulent regions seen in figure 5.6.1(a).

Our PCA model describes the evolution of turbulent spots by probabilistic spreading of turbulence on the 2D grid; it is schematically depicted in figure 5.6.2. The first step is deterministic and models the advection, translating all cells by one gridpoint in the downstream direction. In a second step, a turbulent cell can persist with probability p_p and infect neighbouring cells, spreading turbulence forward, backward or sideways (left and right) with probabilities p_f, p_b and p_s, respectively; diagonal interaction on the 2D-grid is not allowed. In addition, we allow for a spontaneous nucleation of turbulence with probability p_c. The model is simulated on the grid corresponding to the coarse grid of the numerical simulation, with $N_x \times N_z = 204 \times 76$ gridpoints using periodic boundary conditions in the spanwise direction and an empty inflow. Our model is more general than the deterministic model of (Vinod and Govindarajan, 2004, 2007), where the probabilities to persist and spread sideways and forward were identically one.

Estimates for the four probabilities can be obtained from the numerical data in the following way: there are five cells that determine whether a given cell is laminar or turbulent. The probability that after one timestep a cell is laminar is the product of the probability that turbulence does not persist in the cell times all probabilities

that no surrounding cell spreads turbulence into it, leading to a product of up to five terms of the form $(1-p)$, one term for each neighbouring turbulent cell. Since each of the five surrounding cells can be laminar or turbulent, there are $2^5 = 32$ possible initial configurations. They can be identified in the simulation data, and by counting the states that follow we can determine the associated probability that a configuration leads to turbulence. Since we can express this probability as a product of the four spreading probabilities, we obtain 32 equations for the four unknowns, a system which we solve with a least squares method.

Figure 5.6.3(a–d) shows the resulting probabilities for all free-stream turbulence intensities. The probabilities are very similar for all Tu-levels, with a sharp increase near the onset of transition and a quick settling to an almost constant value afterwards, with p_f and p_b showing a slight overshoot near the onset. Neglecting the laminar region before any turbulence is encountered and the onset of transition, where almost no events are detected during the simulations and the statistics is extremely poor, all probabilities appear to be independent of both Re_δ and Tu. We hence choose constant probabilities for the PCA, the values are indicated by the black lines in figure 5.6.3(a-d). Note that p_p, the probability for turbulence to persist, is one, indicating that Reynolds numbers are so high that no decay event occurs in practice.

The last information needed for the full description of the PCA is the nucleation rate p_c with which turbulence is spontaneously created. The FST induces perturbations in the boundary layer whose average amplitudes are proportional to the FST intensity. The perturbations exhibit linear non-normal growth as they are advected downstream until they cross a Re-dependent threshold and nucleate a spot. Starting with an initial perturbation of a given amplitude, the location where a spot is nucleated can be computed as follows: the non-normal growth is described by $A(\mathrm{Re}_\delta) = A_0(\mathrm{Re}_\delta - k/\mathrm{Tu})$ (see figure 5.6.13 in the appendix or Fransson et al. (2005)), with k a constant. We make an ansatz for the threshold function to be given by $f(\mathrm{Re}_\delta) = a/(\mathrm{Re}_\delta - \mathrm{Re}_{\delta,c})$, and by demanding that $A(\mathrm{Re}_\delta) = f(\mathrm{Re}_\delta)$, we obtain the relation between the initial amplitude and the nucleation Reynolds number

$$A_0 = \frac{a}{\mathrm{Re}_\delta - \mathrm{Re}_{\delta,c}} \frac{1}{\mathrm{Re}_\delta - k/\mathrm{Tu}}. \tag{5.6.1}$$

We assume that the initial amplitudes of the perturbations are not always the same but distributed according to a Gaussian like

$$p_{A_0}(A_0)\mathrm{d}A_0 = \frac{c}{\mathrm{Tu}} \mathrm{e}^{-(A/\mathrm{Tu})^2} \cdot \mathrm{e}^{-b/\mathrm{Tu}} \mathrm{d}A_0, \tag{5.6.2}$$

where the factor $\mathrm{e}^{-b/\mathrm{Tu}}$ captures the observation that a higher Tu leads to a higher spot nucleation rate (Narasimha, 1957; Fransson et al., 2005). Using equation (5.6.1) we can map equation (5.6.2) to a distribution of Reynolds numbers, where spots are created, via

$$p_{\mathrm{Re}_\delta}(\mathrm{Re}_\delta)\mathrm{d}\mathrm{Re}_\delta = p_{A_0}(A_0(\mathrm{Re}_\delta)) \left| \frac{\mathrm{d}A_0}{\mathrm{d}\mathrm{Re}_\delta} \right| \mathrm{d}\mathrm{Re}_\delta, \tag{5.6.3}$$

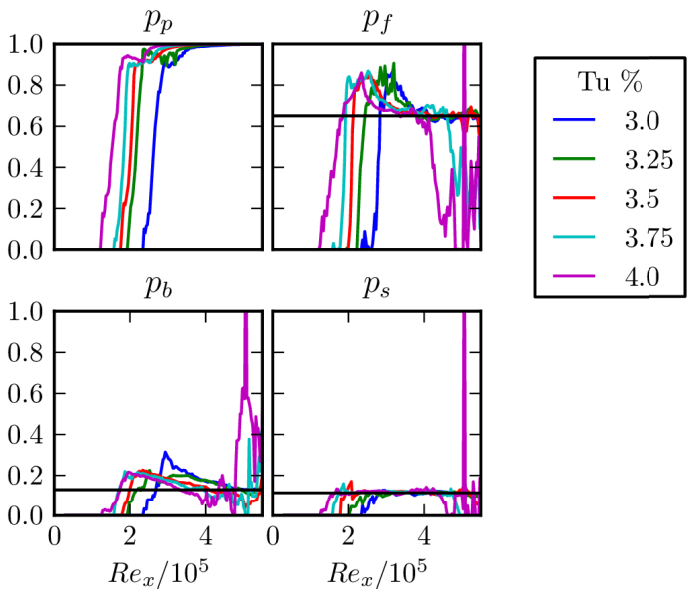

Figure 5.6.3.: Probabilities to persist (p_p), spread forward (p_f), sideways (p_s) or backwards (p_b) estimated from the numerical data for different FST intensities. While there is some variation in the earliest phase of transition, where very few events happen and the statistics are poor, there is afterwards almost no variation with downstream position. Furthermore, there is no dependence of the probabilities on the level of FST disturbances – once a turbulent spot is created, its time evolution is intrinsic and independent of position and what happens in the free stream. The black lines indicate the constant values of the probabilities that are chosen for the PCA, p_p is equal to one.

which is finally mapped to a distribution of locations that can be used in the simulations of the PCA. The constants a, b, c, k and $\mathrm{Re}_{\delta,c}$ are obtained by demanding that the simulation of the PCA with this $p_c(x)$ reproduces the measured intermittency curves and performing a least squares fit on the constants. The mechanisms underlying our model are illustrated in figure 5.6.4 and the obtained nucleation rates are shown in figure 5.6.5.

Note that a delta-distribution for the nucleation rate, as suggested by the concentrated breakdown hypothesis of Narasimha (Dhawan and Narasimha, 1957; Narasimha, 1985), does not lead to a good agreement with the numerical data.

The comparison of intermittency between the numerical data and the PCA is shown in figure 5.6.6, where the intermittency curves for all values of Tu are shown with the corresponding curve from the PCA plotted on top with black dashes. The agreement between the two curves is excellent in all cases, validating a posteriori our approach of determining the nucleation rate. A more detailed comparison for Tu = 3.5%, taking spatio-temporal properties into account, is shown in figure 5.6.7, where in addition to the intermittency the average width of spots $w(x)$ and the average number of

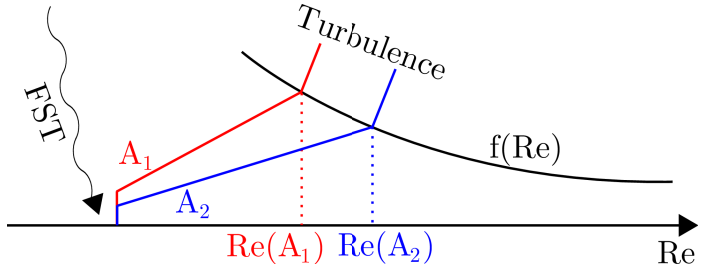

Figure 5.6.4.: Sketch of the mechanism underlying the spot nucleation model. Free-stream turbulence disturbances penetrate into the boundary layer and induce perturbations. These perturbations exhibit non-normal linear growth until crossing a Re-dependent threshold, where they give rise to the nucleation of a turbulent spot. As illustrated in the figure, the initial amplitude of the perturbation is not unique for one level of Tu, leading to different locations where spots appear. Assuming a distribution of initial amplitudes, we hence obtain a distribution of locations, which is used as the probability p_c to nucleate a spot in the PCA.

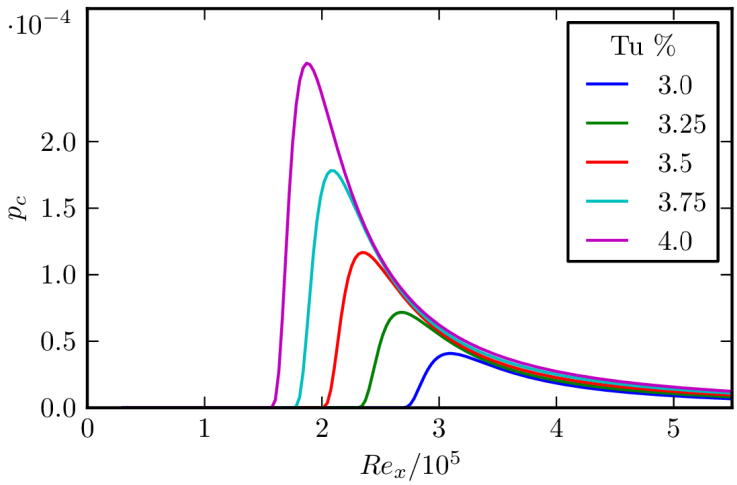

Figure 5.6.5.: The nucleation rate $p_c(x)$ for all values of Tu. The curves show a sudden strong increase with a pronounced maximum, after which the probability drops. At each timestep in the PCA a cell at position x becomes turbulent with probability $p_c(x)$ irrespective of the surrounding cells.

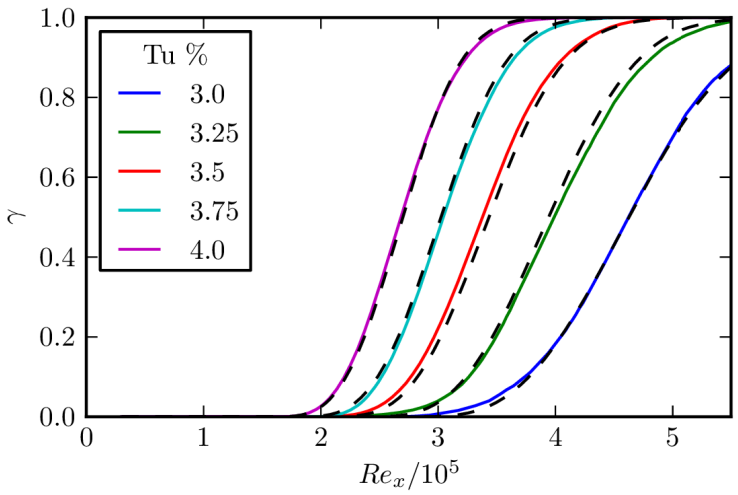

Figure 5.6.6.: The intermittency curves shift to the left and get steeper for higher Tu. The colored lines correspond to the numerical data, the intermittency curves obtained from the PCA are plotted on top with black dashes. They agree very well, showing that our model faithfully describes the transitional boundary layer.

independent spots $n(x)$ is shown, each quantity plotted together with its standard deviation (the curves for the remaining values of Tu are found in the appendix). The agreement is very good – our PCA is able to reproduce the spatio-temporal aspects of bypass transition in boundary layers. Note that for the smallest values of Tu, our model seems to slightly underestimate the number of spots, which upon inspection of movies is related to flickering not completely removed after thresholding. A movie showing a run of the model together with the numerical simulation is available as online material and further confirms the agreement.

Statistics for bypass transition in the BBL is extremely well reproduced with a simplistic PCA model, where all spreading probabilities are independent of the ambient FST level and Reynolds number (at least over the transition region) and only the rate at which new turbulent spots are created varies. Expressed differently, the transition is an *activated process*: once turbulence is triggered, the evolution of a spot is independent of the environment. This is in good agreement with the existence of an edge of chaos in the BBL: free-stream turbulence perturbations trigger a crossing of the edge, but once the edge is crossed the spreading of turbulence does not depend on the original perturbation anymore.

For higher free-stream turbulence intensities, the transition region is moved upstream and the transition happens faster. This can be seen for our simulations in figure 5.6.6, where the intermittency γ is plotted for all five Tu values. This is in line with the observations from linearly stable shear flows, where the threshold in amplitude needed to trigger transition decreases with increasing Re (Grossmann, 2000),

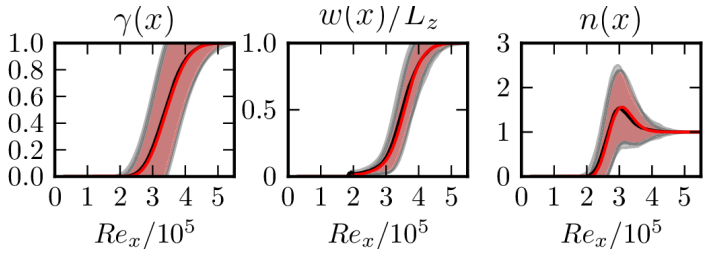

Figure 5.6.7.: Comparison of spot statistics between the LES (black) and the model (red) for Tu = 3.5% for different quantities. The shaded colored area indicates the value ± one standard deviation. (a) the intermittency $\gamma(x)$, measuring the fraction of turbulent sites. (b) the number of independent spots $w(x)$ at each downstream location. (c) the average width of independent spots $n(x)$. The agreement between the numerical data and the model is excellent, not only in the actual values but also in their standard deviation, showing that not only the intermittency is captured by the model but also spatio-temporal quantities as size and distribution of spots are well described by the model.

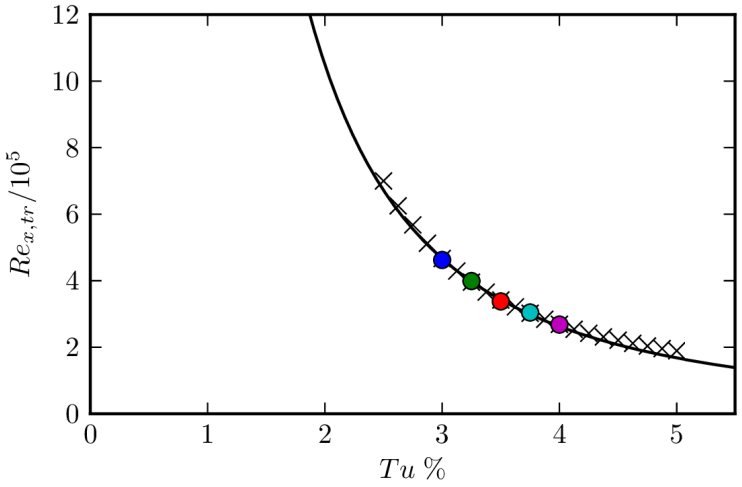

Figure 5.6.8.: Transition position $\mathrm{Re}_{x,tr}$ as a function of turbulence intensity. Circles correspond to the LES data, the straight line shows a fit of the expected Tu^{-2} scaling to the data points. Black crosses are obtained from a parameter-extrapolation of the PCA. The current model accurately predicts the transition position for higher Tu, while the estimation for Tu < 3.0% is somewhat too far downstream.

with the edge of chaos coming closer to the laminar state. For higher Tu the perturbations in the flow have a higher amplitude and can cross the edge earlier, triggering a larger number of spots further upstream, leading to an intermittency curve shifted upstream and steeper. This is quantitatively captured in the variation of the transition position $\mathrm{Re}_{x,tr}$, where $\gamma(\mathrm{Re}_{x,tr}) = 0.5$. In numerous studies (e.g. Matsubara and Alfredsson, 2001; Fransson et al., 2005) a dependence of $\mathrm{Re}_{x,tr} \propto 1/\mathrm{Tu}^2$ has been found. The transition position is plotted as a function of Tu in figure 5.6.8, the agreement between the model and the expected scaling is excellent for all Tu from $2.5 - 4.5$, with some deviation at higher Tu. This might be a hint that at such high Tu the form of the threshold function that we assumed in the derivation of the nucleation rate is no longer valid as the saddle-node bifurcation creating the edge state is approached. We would expect a square-root divergence close to the bifurcation instead of the $1/\mathrm{Re}_\delta$ scaling.

In conclusion, we have successfully developed a PCA that models the spatio-temporal properties of the bypass transition to turbulence in the BBL. Only the rate at which turbulence is nucleated in the model depends on Re and the free-stream turbulence intensity, all other model parameters are constant. Bypass transition in boundary layers is hence an activated process where, once a turbulent spot is created, its development is independent of the environmental noise. This fits the picture developed for transition in linearly stable shear flows, where invariant solutions created in saddle-node bifurcations form the scaffold of turbulence, and suggests that the situation in the BBL is similar. What an exact solution is remains a challenging question for future studies.

Appendix

In the following, we describe the numerical setup for the LES simulations, motivate our parameter choices and describe in detail how the probabilistic model is deduced from the data.

Numerical setup

The time evolution of the boundary-layer flow is simulated using a fully spectral code (Chevalier et al., 2007), which solves the incompressible Navier-Stokes equations in a channel geometry. For spatial discretization of the flow field a Fourier basis is used in the streamwise and spanwise directions and a Chebyshev expansion in the wall-normal one. Second-order Crank-Nicolson and third-order Runge-Kutta methods are used for time advancement of linear and nonlinear terms, respectively.

The no-slip (homogeneous Dirichlet) boundary conditions are imposed at the lower wall, whereas the free-stream is represented using Neumann boundary conditions. As a consequence of Fourier discretization periodic boundary conditions are imposed in the streamwise and spanwise directions. Thus in order to simulate the spatially

growing boundary layer a fringe region is included at the end of the numerical domain. In the fringe region a volume forcing is added, damping all fluctuations and returning the flow to the required inflow state.

We perform large-eddy simulations (LES) in a box of size $L_x \times L_y \times L_z = 2000\delta_0^* \times 130\delta_0^* \times 500\delta_0^*$ with a resolution of $N_x \times N_y \times N_z = 1024 \times 201 \times 768$. Here δ_0^* is the displacement thickness at the beginning of the domain. The subgrid scales are modeled with a relaxation-term model (ADM-RT) (Schlatter et al., 2004).

Free-stream turbulence generation

The free-stream turbulence at the inlet is formed by a superposition of the continuous spectrum of the Orr-Sommerfeld and Squire operators (Brandt et al., 2004). The modes are chosen in the specific way in order to ensure isotropy of the resulting turbulence. An energy spectrum characteristic for isotropic homogeneous turbulence is obtained by rescaling the coefficients of the superposition. The integral length scale of turbulence, which corresponds to the peak in the energy spectrum, is set to $L_I = 10$. This value is somewhat higher than the ones used in Brandt et al. (2004) and motivates the use of a higher numerical domain in our study.

A measure for turbulent activity

In the model we develop for the spatial development of turbulent spots, we neglect variations in the wall-normal direction and reduce the boundary layer to two dimensions, an approach that is justified from many experimental and numerical studies. As a criterion to decide whether a cell is turbulent we choose the spanwise wall-shear stress $\tau_s = \partial w/\partial y|_{y=0}$. Before transition to turbulence, the flow consists mainly of streamwise oriented streaks, which have high energy in the downstream velocity fluctuations but only very little in the spanwise ones. After breakdown of the streaks, the flow exhibits strong vortical motion. Strong downstream vortices lead to a higher spanwise wall-shear stress, so that τ_s is high if the flow is turbulent. Furthermore, τ_s is a wall-based quantity, showing no ambiguity in the position where it is measured and readily available from the numerical simulations.

Determining a good cell size

The grid spacing of the performed simulation is $D_x = 1.95$ and $D_z = 0.65$. In order to reduce the data to the PCA model, we need to determine the size of one "independent" cell and the length of a time-step.

To get an estimate of an appropriate discretization, we look at the autocorrelation-function of τ_s. Since we expect the structures to be advected fast downstream but only slowly in the spanwise direction, we calculate the purely spatial autocorrelation in the spanwise direction (figure 5.6.9) and the space-time autocorrelation in the downstream direction (figure 5.6.10).

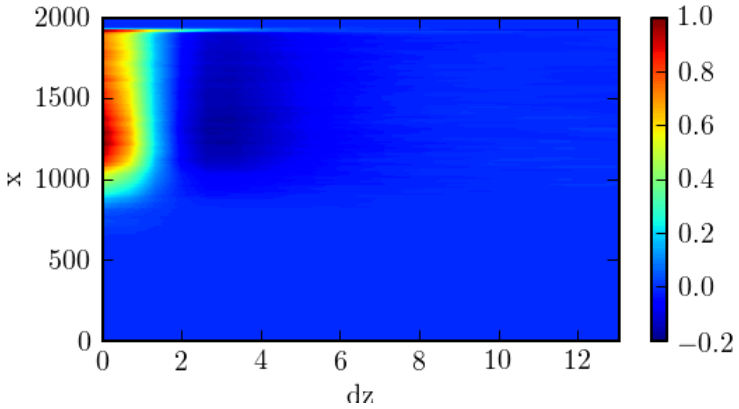

Figure 5.6.9.: Autocorrelation in the spanwise direction for every downstream location x. Before the transition region τ_s vanishes, afterwards the autocorrelation function is almost independent of x. There is a strong positive correlation for $z \lesssim 2$ and a somewhat weaker, but clear, anticorrelation for $2 \lesssim z \lesssim 5$, corresponding to a vortex and a counter-rotating neighbor, respectively.

The autocorrelation in the spanwise direction is computed independently for all downstream positions, $C_z(x, dz) = \langle \int \tau_s(x, z, t)\tau_s(x, z + dz, t)\mathrm{d}z \rangle_t$, with $\langle\rangle_t$ indicating temporal averaging. Figure 5.6.9 shows that it is extremely small before transition to turbulence occurs. Afterwards, it is almost independent of x, indicating that the size of the structures does not depend on the downstream location. There is a strong positive correlation for $z \lesssim 1.5$, corresponding to the width of a single vortex, and a somewhat weaker but still clear negative correlation for $2 \lesssim z \lesssim 5$, corresponding to the counter-rotating vortex. We want our cell size to average over one vortex pair, which ranges from -2 to 5. A good estimate of dz is hence given by $dz \simeq$ 6-7 and we choose $dz = 10D_z = 6.5$.

Looking at the space-time autocorrelation

$$C_{xt}(dx, dt) = \left\langle \int \tau_s(x, z, t)\tau_s(x + dx, z, t + dt)\mathrm{d}x\mathrm{d}t \right\rangle_z$$

in figure 5.6.10, we see a very strong positive finger pointing into the plane, corresponding to the speed at which the structures are advected. The finger is rather thin, indicating that the advection speed is constant everywhere for all structures. The finger has a slope of $dx/dt = 0.45$, which is depicted by the black line in figure 5.6.10 and we naturally choose this measure to define dt once dx is chosen. The autocorrelation function does, however, not give a good estimate for dx and we deliberately choose $dx = 5D_x = 9.5$ as a compromise between averaging over enough gridpoints and keeping the time-step low (which means more statistics from a simulated trajectory). The time-step that follows is $dt = dx/0.45 = 22$. We have tried different values for dx during the fitting procedure outlined below and verified a posteriori that the

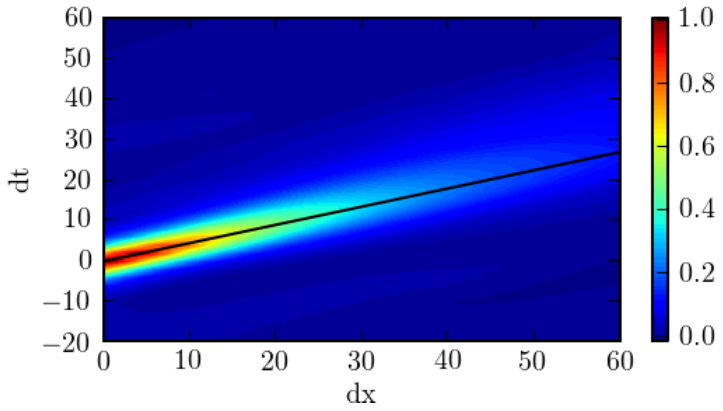

Figure 5.6.10.: The autocorrelation function of τ_s in time and downstream direction shows a strong positive correlation in the direction $dx/dt = 0.45$, indicated by the black line and corresponding the the average advection speed in the boundary layer.

exact choice of dx does not influence our qualitative results, as long as dx is not too large. Note, however, that the choice of dx of course changes the quantitative results, namely the probabilities to spread or persist.

The box size of the simulations $L_x \times L_z = 2000 \times 500$ translates to a 2D grid of size $N_x \times N_z = 204 \times 76$ for the model.

Thresholding

In order to distinguish between laminar and turbulent cells we choose a threshold for τ_s and define everything below the threshold as laminar and everything above it as turbulent. The threshold is estimated from the probability density function of τ_s, shown in figure 5.6.11 for all five turbulence intensity levels. The PDF is high near 0, drops as τ_s increases and shows a peak, whose height increases with free-stream turbulence intensity as larger parts of the box are turbulent. Associating the high values near 0 with patches of purely laminar flow and the peak around $\tau_s = 0.9$ with turbulent patches, we place the threshold in the gap separating the two at $\tau_s = 0.3$. The effect of the thresholding is illustrated in figure 5.6.12(a,b) for the snapshot of the simulation with Tu = 3.5% already shown in figure 5.6.1, before (a) and after (b) applying the threshold.

Filtering

After applying the threshold some undesired effects remain, detecting a single laminar cell in a turbulent region or showing a flickering of isolated turbulent cells in a laminar region, only existent for a single timestep. To prevent those spurious events from contaminating our statistics, we apply a Gaussian filter with kernel size 0.5 cells in both spatial directions before applying the threshold. The effect is shown in

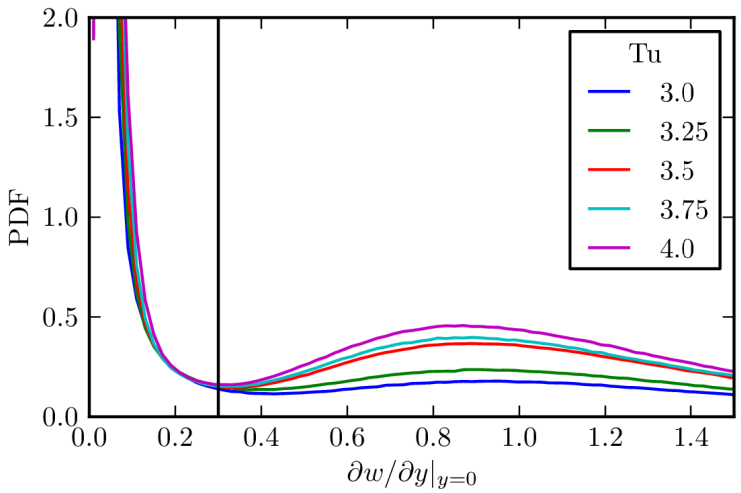

Figure 5.6.11.: The probability density function of τ_s for different free-stream turbulence intensities is used to determine a threshold defining laminar and turbulent. The PDF is high around 0, drops afterwards and shows a peak around 0.9. The chosen threshold is indicated by the black vertical line at 0.3.

figure 5.6.12(c) and the comparison with panel (b) confirms that the filter has the desired effect without distorting the snapshot.

Fitting parameters

The model is sketched in figure 5.6.2. The first step, the advection, is deterministic and just moves every cell one step to the right. In a second step, the cell can spread or decay. The probabilities are p_f to spread forward, p_p to persist, p_s to spread right or left and p_b to spread backwards. The probability that a cell C is laminar after one time step, $p(C(x+1,z,t+1) \equiv 0)$, depends on the state of the surrounding cells. It is given by the product of the probabilities that the surrounding cells do not spread turbulence in this cell and reads:

$$\begin{aligned}(1-p_p)C(x,z,t)\cdot(1-p_b)C(x+1,z,t)\\ \cdot(1-p_f)C(x-1,z,t)\cdot(1-p_s)C(x,z-1,t)\\ \cdot(1-p_s)C(x,z+1,t)\end{aligned}$$

This consideration leads to a system of equations from the numerical data from which the probabilities can be calculated. For example, consider the case where only the cells at $C(x,z,t)$ and $C(x,z-1,t)$ are turbulent, all others are laminar. Let us call this configuration A_{pl} since the two probabilities involved are persisting and spreading left. Precisely, the probability that $C(x+t,z,t+1)$ is laminar in the next

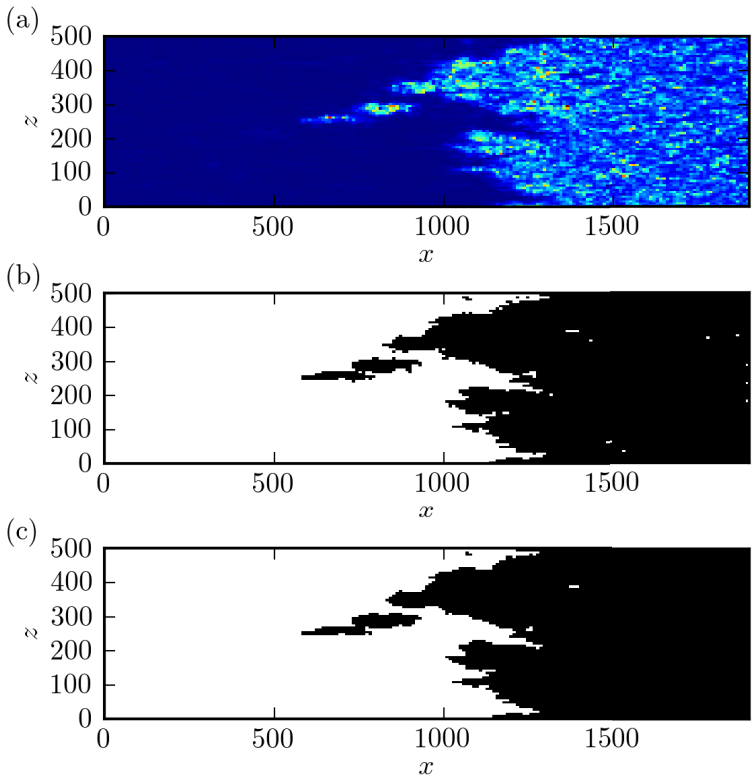

Figure 5.6.12.: The effect of thresholding and Gaussian filter for a snapshot taken from the simulation with Tu = 3.5%. Panel (a) shows τ_s for this snapshot on the coarse grid. In panel (b) the threshold $\tau_s = 0.3$ is applied to the data from panel (a). We see some flickering in the turbulent region, isolated white cells that are gone in the next timestep. In panel (c), a Gaussian filter with kernel size 0.5 cells is used before applying the threshold. As desired, the isolated white and black cells are removed without distorting the LES data.

time step is given by

$$p(C(x+t,z,t+1) \equiv 0) = (1-p_p)(1-p_s). \tag{5.6.4}$$

We now scan through the numerical data and count all situations where only those two cells are turbulent, N_{pl}, and how often this leads to the cell $C(x+1,z,t+1)$ to be laminar, L_{pl}. Then, L_{pl}/N_{pl} gives us a numerical value for the left hand side of eq. (5.6.4). There are $2^5 = 32$ possible configurations and for each configuration we get one equation for our four parameters, a system that is solved with a least-squares algorithm.

Note that the probability to nucleate a turbulent cell is neglected in this analysis, since it is small compared to the spreading probabilities. It however needs to be modeled in order to perform simulations of the PCA.

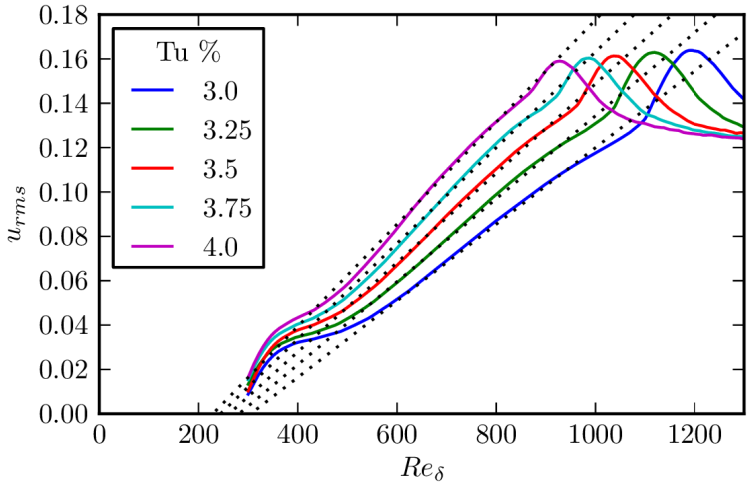

Figure 5.6.13.: Streamwise velocity fluctuations u_{rms} at y where u_{rms} is maximal for all values of Tu, obtained from the LES data. Close to the inflow there is an initial phase of receptivity, after which the streak amplitude (that are associated with u_{rms}) grows linearly with Re_δ. The slope is proportional to Tu, indicating a linear receptivity mechanism. The dotted lines are from a fit $u_{rms} = m\mathrm{Tu}(\mathrm{Re}_\delta - k/\mathrm{Tu})$ with m and k independent of Tu.

The nucleation rate

In the derivation of the nucleation rate, we introduced the non-normal linear growth of the perturbation amplitudes as $A(\mathrm{Re}_\delta) = A_0(\mathrm{Re}_\delta - \mathrm{Re}_{\delta,0})$ and claimed that $\mathrm{Re}_{\delta,0} = k/\mathrm{Tu}$. To back up this claim, we present the variation of the streamwise velocity fluctuations u_{rms} with Re_δ in figure 5.6.13, assuming that the perturbation amplitude of our discussion is related to u_{rms}. The dotted lines in the figure correspond to a fit $u_{rms} = m(\mathrm{Re}_\delta - k/\mathrm{Tu})$ with m and k independent of Tu; they agree very well with the measured curves in the linear part, confirming the relation we used.

The constants a, b, c, k and $\mathrm{Re}_{\delta,c}$ appearing in the functional dependence of p_c are determined via comparison with the LES data. We define an error-function as the difference between the measured intermittency value at every gridpoint and the one obtained from a simulation of the model with a given set of constants. The five constants are then determined with a least squares fit minimizing the difference in the intermittency. Note that only the intermittency is used in this process, the other quantities used in the comparison follow automatically.

The values of the parameters obtained this way are: $a = 2.7 \cdot 10^5, b = 19, R_c = 500, c = 5.4 \cdot 10^9, k = 2.6 \cdot 10^3$. The nucleation rates p_c have been given in figure 5.6.5.

It should be noted that the interpretation of the multiplicative parameters is ambiguous and only their relative values have a physical meaning – for example we do not know absolute values for streak amplitudes or threshold function, but the combination chosen uniquely determines them. Furthermore, the interdependence of the

parameters is quite large, so that a calculation with e.g. $\mathrm{Re}_{\delta,c} = 400$ and appropriately adjusted values of the other constants also gives results which agree well with the five measured gamma curves; we hence do not want to claim that we have computed the exact form of the threshold curve for example.

Comparison between simulation and model

In order to compare between the simulation and the model, we use three statistical quantities. The first one is the intermittency $\gamma(x)$, defined as the fraction of cells that is turbulent. An instantaneous value of γ is obtained for every time step and in addition to the average value we consider the standard deviation.

The comparison of the intermittency between model and simulations was shown in figure 5.6.6, the standard deviation can be seen in the left panel of figure 5.6.14 for all values of Tu. We see that not only the intermittency but also the fluctuations thereof are extremely well reproduced by the model.

The middle and right panels of figure 5.6.14 show the width of independent spots $w(x)$ and the number of independent spots $n(x)$ as a function of downstream position for all Tu. The accordance is very good in general, but we note a small underestimation of the number of spots for the smaller two values of Tu.

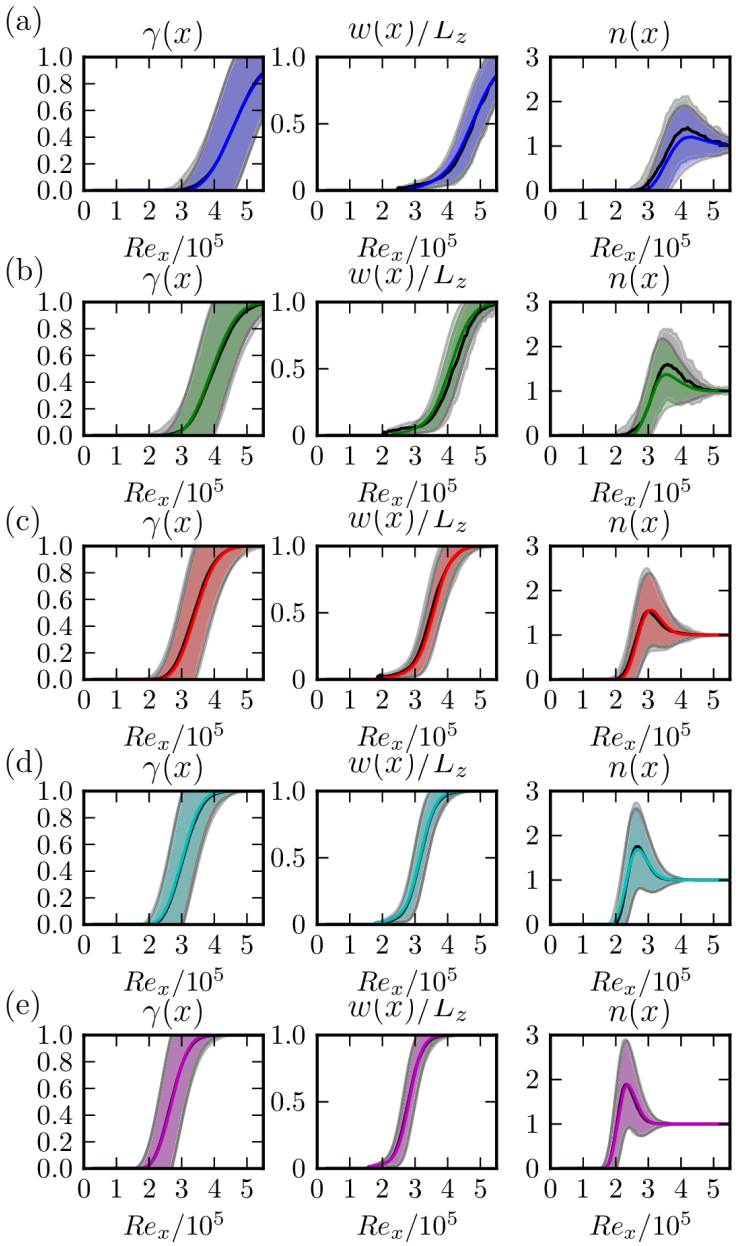

Figure 5.6.14.: Comparison of spot statistics between the numerical data and the PCA for all five values of Tu, with color coding the same as in other figures. For each quantity, the value from the LES simulations is shown in black with the gray shaded area indicating ± one standard deviation and the value obtained from the PCA is plotted in color. In most cases, the agreement is so good in all quantities, intermittency, spot width and number of independent spots, that no difference between the two curves is visible. Only for the smallest two values of Tu, there is a very small underestimation of the number of spots in the model.

5.7. Author contributions to the publications

1. Tobias Kreilos and Bruno Eckhardt
   Periodic orbits near onset of chaos in plane Couette flow
   Published in: Chaos, 22(4), 047505 (2012)

   The computations were performed by TK following an adjointly designed study protocol. The data analysis was done by TK with input from BE. The paper was jointly written based on a first draft prepared by TK.

2. Tobias Kreilos, Bruno Eckhardt, and Tobias M. Schneider
   Increasing Lifetimes and the Growing Saddles of Shear Flow Turbulence
   Published in: Physical Review Letters 112, 044503 (2014)

   The idea was developed by TK in discussions TS and BE. TK performed the computations and analyzed the data with input from BE and TS. The paper was written by TK and TS with feedback from BE.

3. Tobias Kreilos, Gregor Veble, Tobias M. Schneider and Bruno Eckhardt
   Edge states for the turbulence transition in the asymptotic suction boundary layer
   Published in: Journal of Fluid Mechanics 726, 100-122 (2013)

   The particular edge state was first found by GV. The implementation of the edge state tracking algorithm in channelflow and some studies and documentations of the properties of the state were already part of the diploma thesis of TK. The significant new contribution here is the identification of the SNIPER bifurcation as the origin of the oscillating state. The major part of the paper was written by TK with input from BE and feedback from TS and GV.

4. Taras Khapko, Tobias Kreilos, Philipp Schlatter, Yohann Duguet, Bruno Eckhardt and Dan S. Henningson
   Localized edge states in the asymptotic suction boundary layer
   Published in: Journal of Fluid Mechanics 717, R6 (2013)

   The edge tracking simulations were done independently by TKr and TKh using two different codes. TKr used channelflow, for which he parallelized the timestepper, TKh used the SIMSON code. The periodic states were first found by TKr. The paper was written by TKh with input from the other authors.

5. Tobias Kreilos, Stefan Zammert and Bruno Eckhardt
   Symmetry related slow processes in the asymptotic suction boundary layer
   Accepted for publication in: Journal of Fluid Mechanics

   The key idea and implementation were developed in joint discussion between TK and BE. TK performed simulations and data analysis for the ASBL, SZ

contributed the parallel studies in plane Poiseuille flow. BE, TK and SZ wrote the paper.

6. Tobias Kreilos, Taras Khapko, Philipp Schlatter, Yohann Duguet, Dan S. Henningson and Bruno Eckhardt
Bypass transition in boundary layers as an activated process
Manuscript in preparation

   The idea was conceived in discussions between BE and YD and refined in exchanges between all authors. Simulations have been performed by TKh with help of PS. The data analysis and parameter determination for the cellular automaton was done by TKr with input from the other authors. TKr wrote the major part of the manuscript with feedback from the other authors and TKh contributed the parts on the numerical simulations.

A. Parallelizing the channelflow library

In recent years a paradigm shift happened in high performance computing, as single processors have barely become faster and the gain in computational power stems mainly from the efficient, parallel use of large numbers of processors. In order to perform direct numerical simulations of extended velocity fields, the open-source DNS code channelflow (Gibson, 2012) has been parallelized as part of this work.

The parallelization is implemented with the message passing interface (MPI), which defines communication operations between processors, making heavy use of the efficient routines provided by the FFTW library. The velocity field data, all spectral or physical coefficients of the numerical representation of a velocity field, is distributed among all processors in two dimensions, allowing to use very large numbers of processors. Apart from this distribution of the data and the necessary redistribution operations nothing is changed from the serial channelflow code. Our implementation has a parallel efficiency of roughly 40% on a cluster at the MPI-DS in Göttingen with 768 processors and the performance scales almost linearly as shown in strong-scaling studies on the same machine.

A.1. Description of the parallelization

Conceptual setup

Channelflow uses a semi-implicit method to solve the Navier-Stokes equations, where the nonlinear part is calculated explicitly and the linear part, in the form of the τ equations, is solved implicitly with the influence matrix method (see Canuto et al., 1988, for details). The τ-equations are a set of independent equations for each tuple of (k_x, k_z) Fourier-modes and their solution is efficient in parallel if the necessary information is available on a single processors, so that no communication is needed in this step. We hence adopt the distribution of the velocity data along x and z suggested by this consideration, with all Chebyshev-coefficients belonging to a (k_x, k_z)-tuple locally available.

The nonlinear term involves vector-products of the velocity field and its derivatives and is computed in physical space. The transformation from spectral to physical representation requires a Chebyshev-transformation in the wall-normal direction, which

can be computed locally, and a two-dimensional Fourier transformation in the xz-plane, requiring large amounts of inter-process communication.

Computation of the nonlinear term

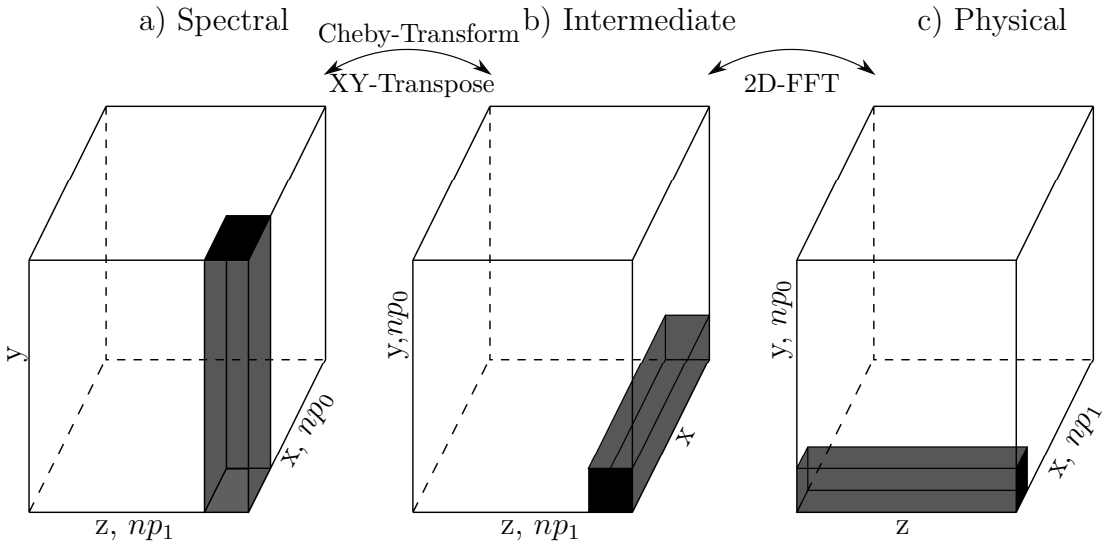

Figure A.1.1.: Illustration of the data distribution in spectral and physical space. The shaded area shows the data that is locally available on process 0. The downstream, wall-normal and spanwise directions point towards the back, the right and the top, respectively. a) In spectral state, the data is distributed along x and z and each process has access to all Chebyshev coefficients on a small patch of (x,z) Fourier modes. A Chebyshev transform can hence be readily executed, as all necessary information is locally available. b) Following the Chebyshev transform, a transpose operation is performed in the x-y-plane, redistributing the data between the processes. c) To complete the transform, FFTW is called to do a distributed 2D-transform, where all processors holding data on a slice in y are combined. The operation involves yet another transpose operation, so that in physical space the data is distributed along x and y.

The transformation to the physical representation requires a discrete Chebyshev transformation in the y-direction and two fast Fourier transformations (FFT) along x and z. All operations are done by first making all necessary information locally available on a single processor and then performing the transform without further inter-process communication.

As explained above, in spectral state the velocity field data is distributed such that each process has access to all Chebyshev components on a small patch of (x,z) Fourier modes. The distribution in spectral state is illustrated in figure A.1.1(a), the shaded

area represents the information that is locally available on process 0. The Chebyshev transformation can hence be readily executed.

To perform the first FFT a redistribution of the data among the processes is necessary, in our implementation performed in the x-y plane (figure A.1.1b), requiring an all-to-all communication between all processors that possess data of the same k_z; the data is now distributed along y and z and all processes execute the FFT for their share of the data. Afterwards, a second redistribution of the data takes place, this time in the x-z plane, so that the data is distributed along x and y, before all processes execute the FFT in the z-direction. The final distribution is illustrated in figure A.1.1(c).

Having calculated the nonlinear term in physical space, all operations need to be performed in reverse order to arrive at a spectral representation of the nonlinear term that can be added to the linear part.

Non-parallel parts of the code

The parallelization that is currently implemented and that we described above covers the time integration of a given velocity field. There is currently no parallel i/o available, instead for saving or loading flowfields the field is transferred to process 0 and then only process 0 does the i/o. The advantage of this approach is, however, that there are no changes in the file format and velocity field data can be transferred between either the serial or the parallel code.

Interfacing the parallel timestepper with the routines used for dynamical systems analysis, in particular the Newton solver, required substantial changes in the original code. This part is currently under active development in collaboration with Hecke Schrobsdorff and Tobias M. Schneider.

A.2. Technical details

All transpose operations are implemented with FFTW, the fastest Fourier transform in the west (Frigo and Johnson, 2005), which provides routines for 1D-parallelized 2D-FFTs and transpose operations that are at least as efficient as MPI all-to-all.

We divide the total number of processes np in two directions, $np = np_0 \times np_1$. In spectral state, np_0 and np_1 correspond to the number of processes used for the distribution along x and z, respectively. We require np_0 to divide the number of gridpoints in the downstream direction M_x, i.e. $M_x \% np_0 \equiv 0$. In the wall normal direction, we apply padding to the next multiple of np_0 to facilitate the implementation of the transpose operation in x-y and the total number of gridpoints becomes $M_{y,pad} \geq M_y$. Note that is is preferable to keep the difference $M_{y,pad} - M_y$, i.e. the number of padded y-slices, small, since the FFTs are done in packages of np_0 and in the last round hence $M_{y,pad} - M_y$ processors are idle. The distribution in the spanwise direction is left to

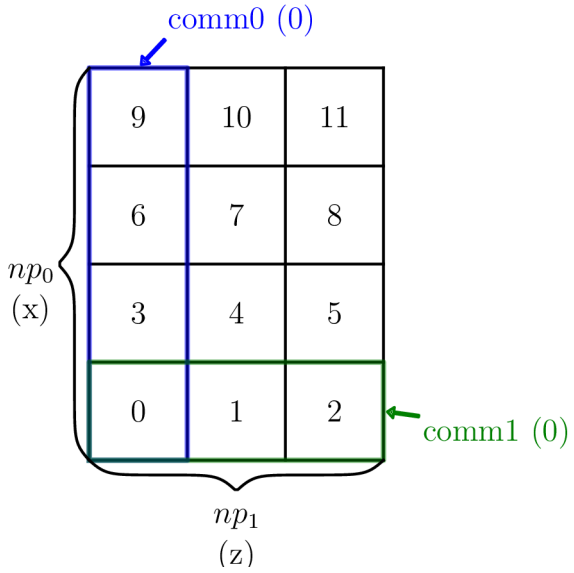

Figure A.2.1.: Grouping of processors into communicators. The figure illustrates the data distribution with 12 processors with $np_0 = 4$ and $np_1 = 3$, the number of the process is written in the middle of the patch of data which is locally available. In spectral state, the expansion in z is along the horizontal axis and the expansion in x along the vertical axis, as indicated in the figure. If for example the flowfield has 32 modes in x, this would correspond to process 0 having the data from $m_x = 0$ to 7. In physical state np_1 corresponds to distribution in x and np_0 to y. The colored frames indicate the communicators comm0 and comm1 into which process 0 belongs.

FFTW and no requirements exist that restrict np_1. In physical space, np_0 and np_1 are the distribution of processes in y and x, respectively.

The two different transpose operations require two overlapping groups of communicators. The first group (comm0) consists of np_1 communicators with np_0 processes each and the communicators are used for the x-y transpose. The second group of communicators (comm1) contains np_0 communicators with np_1 processes; each of these np_0 communicators performs individual distributed 2D FFTs in one x-z plane. The distribution is illustrated in figure A.2.1.

We make heavy use of routines from FFTW (Frigo and Johnson, 2005), based on FFTW version 3.3 and the efficiency of our implementation is largely due to the efficiency of FFTW. While the x-y transpose in each communicator in comm0 could also be done with MPI all-to-all, we implemented it with FFTW, which on initialization tries different algorithms including all-to-all and chooses the fastest one. FFTW implements parallel Fourier transforms with a 1D parallelization, which is exactly what is needed for the 2D FFT in one x-z-plane, and we consequently make again use of the parallel capabilities of FFTW, so that the second transpose operation is only implicitly implemented.

The alignement of the arrays in memory is dictated by the requirements of the transpose operations. In spectral state, the alignment is z^*x^*yi in row-major order, where * indicates that this direction is distributed (the index i enumerates the components of the velocity). The first transpose changes the distribution from x to y, resulting in z^*xy^*i and after the 2D FFT the alignment in the physical representation is x^*zy^*i.

A.3. Verification

We have performed several tests to verify that the parallelization does not change the results obtained with the code. In all tests, we assume that the serial code works correctly and check the parallel version against the serial one.

As a first test, the transformations of a velocity field from spectral to physical state and back are verified by comparing every single expansion coefficient with a transformation performed with the serial code. The difference is always smaller than the numerical accuracy of the double-precision floating point numbers used in channelflow.

As a second test, we compare the full time-integration of a velocity field. An initial field is first integrated for ten time units with the serial code and stored to disk, with the initial field taken from a turbulent trajectory so that we can be sure to have positive Lyapunov exponents. Afterwards, the same initial field is integrated with the parallel version and the difference to the stored field is computed. This distance is on the order of 10^{-16}, i.e. the numerical precision, and we conclude that the parallel code works correctly.

A.4. Usage: How to write parallel programs

Using MPI with channelflow

Inside the channelflow library all information connected to the distribution $np = np_0 \times np_1$ is encapsulated in the class `CfMPI`. To make use of the parallel capabilities of the integrator, a CfMPI-object needs to be created and a pointer to that object must be passed to all FlowField constructors. The creation of DNS-objects, time integration etc. works as before.

The CfMPI constructor takes two arguments, namely the number of processors np_0 and np_1, which are optional if np is a square number in which case $np_0 = np_1 = \sqrt{np}$ is the default value. The only limitation is that np_0 must divide M_x, the number of gridpoints in the downstream direction.[1]

[1] It is currently not possible to create CfMPI objects that do not use all processes from 0 to $np_0 \times np_1$, as might be useful if one wants to integrate several FlowFields simultaneously.

MPI will complain if `MPI_Finalize()` is called before all flowfields are destructed, because the FFTW plans belonging to each flowfield create MPI communicators. The easiest way to circumvent associated MPI warnings is to enclose everything between `MPI_Init` and `MPI_Finalize` in a bracketed block `{}`.

Necessary elements of a parallel program

The first line in the main function of a program using channelflow with MPI is usually

```
MPI_INIT(&argc, &argv); {
```

(note the curly bracket opening a block at the end of the line) and the last one before return

```
} MPI_FINALIZE();
```

Before creating the first flowfield, create a (global) CfMPI object, specifying the desired distribution

```
CfMPI* cfmpi = new CfMPI(nproc0, nproc1);
```

and pass the pointer to each new flowfield, e.g.

```
FlowField u ("filename", cfmpi);
```

Passing the CfMPI pointer is not necessary when copying flowfields

```
FlowField u1 = u0;
```

Do not forget to delete all cfmpi objects at the end, before calling finalize:

```
delete cfmpi;
```

Locally available information

To keep track of which data is available on the current process, there are a couple of additional functions in the flowfield class.

1. `Nloc()` gives the total number of local gridpoints
2. `nxlocmin()` gives the global index of the first locally available gridpoint in x in physical state
3. `Nxloc()` gives the local number of gridpoints in x in physical state.
   `Nxloc() + nxlocmin()` can be used as the upper boundary of a loop.
4. `Nyloc()` and `nylocmin()` give the corresponding information in y.
5. To account for the padding, there is also a function `nylocmax()` to give an upper boundary for loops, to avoid accessing the padded values.
6. `Nypad()` gives the global padded number of gridpoints (`Ny()` is the unpadded number).

7. For spectral state, there are the functions `Mxloc()`, `mxlocmin()`, `Mzloc()` and `mzlocmin()`, respectively.

The locally available data in spectral representation is in the range `mxlocmin <= mx < mxlocmin+Mxloc` and `mzlocmin <= mz < mzlocmin+Mzloc` and in in the physical state it is `nxlocmin <= nx < nxlocmin+Nxloc` and `nylocmin <= ny < nylocmax`. All these functions are of type `lint`, which is a typedef to `ptrdiff_t`, an integer that is guaranteed to have 64 bits on a 64 bit machine (which is important for large flowfields) and also required by the parallel FFTW.

Deadlocks – and how to avoid them

The parallelization is done so that (almost) all calls are collective calls. A program can hence be written almost as if it was serial. Deadlocks will occur if a function that expects to be called by all processes is only called by one. For example, the following will never return:

```
if (taskid == 0) cout << L2Norm(u) << endl;
```

because the function L2Norm gets called only by process 0. This deadlock is for example avoided in the following way:

```
Real l2 = L2Norm(u);
if (taskid == 0) cout << l2 << endl;
```

which will calculate the L2Norm with all processes and then output only on process 0.

For convencience, there's also a function called printout, which takes a string and prints it on process 0. So the following code also works:

```
printout(r2s(L2Norm(u)));
```

A.5. Benchmarks

We have benchmarked the parallel code with strong scaling tests on the Thor cluster at the Max Planck institute for dynamics and self-organization in Göttingen. The cluster consists of 48 nodes, each of which contains 2 8-core Intel Xeon E5-2670 CPUs with 2.60GHz. The individual nodes are interconnected with Infiniband network and the maximum number of cores is hence 768.

The benchmark setup is rather simple: we use a velocity field of size $N_x \times N_y \times N_z = 1024 \times 121 \times 1024$ gridpoints and integrate it for ten time units, measuring the wall-clock time elapsed for each time unit, excluding the first one where the multistep integrator is initialized. The benchmark result is then simply the elapsed wall-clock time per time unit. The distribution of processors plays an important role and for the velocity field we used, the distribution with $np_0 = 32$ is optimal since it reduces the amount of inter-node communications during the transpose operations.

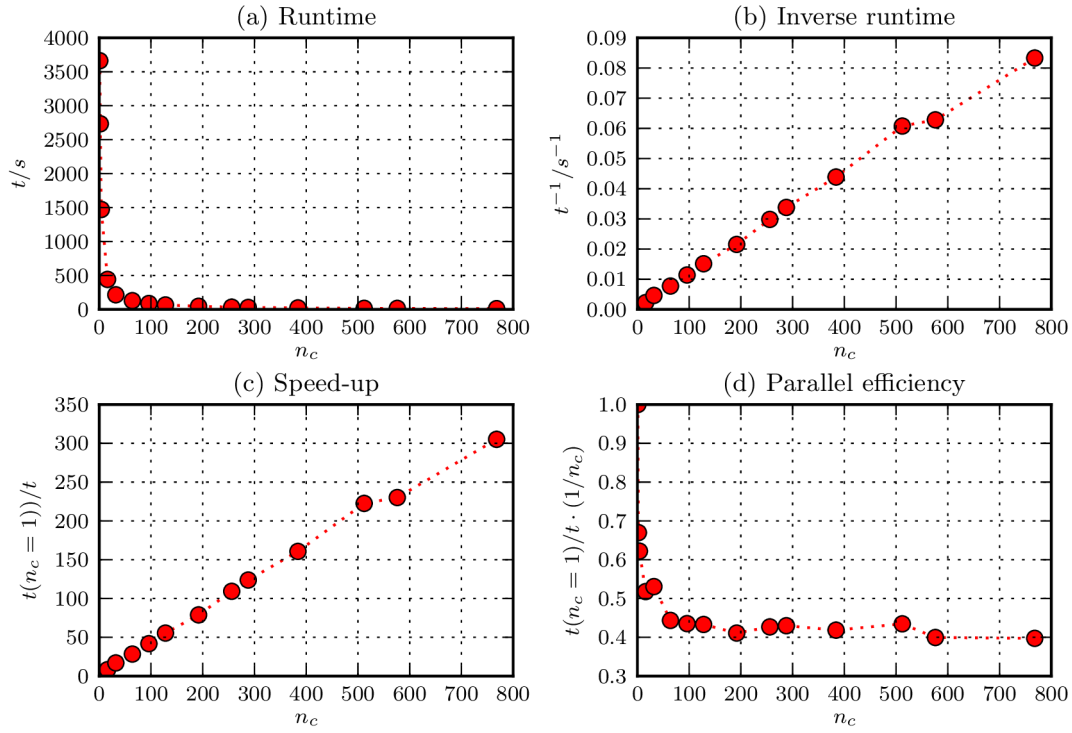

Figure A.5.1.: Benchmark of the parallel code in a strong scaling study. The benchmark is performed by measuring the average wall-clock time elapsed for a time-step with a field of size $N_x \times N_y \times N_z = 1024 \times 121 \times 1024$. (a) The total wall-clock time for one time step as a function of the number of cores. (b) The inverse of the elapsed time scales almost linearly with the number of cores. (c) The speed-up, the time on one process divided by the time on n_c processes, also scales almost linearly for a greater number of processes. (d) The parallel efficiency is the speed-up divided by the number of cores n_c. It drops to about 50% for 16 cores, the maximum number on one node. From 32 to 768 cores, it is almost constant at about 40%, validating an almost linear scaling.

The results in this strong scaling study are plotted in figure A.5.1. Panel (a) shows the time elapsed for each time unit, which drops from 3663 seconds with one process (the serial code, i.e. no communication at all) to 12 seconds on 768 processors. We see that for many processors the speed-up (panel c), the runtime on one processor divided by the runtime, scales almost linearly with the number of processors. This is further confirmed by the parallel efficiency, the speed-up divided by the number of processors, panel d. The efficiency drops to roughly 50% for 16 processors, which is the largest number available within one node. Given the extensive amount of communications necessary during the transpose operations, this is not too surprising.

With 32 cores, Infiniband communication is necessary and the efficiency drops to

slightly more than 40%. As the number of processes is increased further, the efficiency stays almost constant at 40%, up to the maximum number of 768 cores. The overall efficiency of the parallelization is satisfying and the linear scaling an excellent result.

Acknowledgements

All credits go to Philipp Schlatter from KTH Stockholm, who explained the ideas of parallelizing this type of code, and to FFTW, which provides the efficient transpose and 2D-FFT operations needed. The implementation was simplified by the great work of John F. Gibson, who wrote easily readable and highly organized code. We thank Hecke Schrobsdorff and Tobias M. Schneider for great work on parallelizing the remaining parts of the code.

Bibliography

Abshagen, J., Lopez, J., Marques, F., and Pfister, G. Symmetry Breaking Via Global Bifurcations of Modulated Rotating Waves in Hydrodynamics. *Physical Review Letters*, 94(7):074501, 2005.

Adrian, R. J. Hairpin vortex organization in wall turbulence. *Physics of Fluids*, 19 (4):041301, 2007.

Adrian, R. J., Meinhart, C. D., and Tomkins, C. D. Vortex organization in the outer region of the turbulent boundary layer. *Journal of Fluid Mechanics*, 422:1–54, 2000.

Alfredsson, P. and Matsubara, M. Free-stream turbulence, streaky structures and transition in boundary layer flows. In *Fluids 2000 Conference and Exhibit*, Reston, Virigina, 2000. American Institute of Aeronautics and Astronautics.

Allhoff, K. T. and Eckhardt, B. Directed percolation model for turbulence transition in shear flows. *Fluid Dynamics Research*, 44(3):031201, 2012.

Andereck, C. D., Liu, S. S., and Swinney, H. L. Flow regimes in a circular Couette system with independently rotating cylinders. *Journal of Fluid Mechanics*, 164: 155–183, 1986.

Andersson, P., Berggren, M., and Henningson, D. S. Optimal disturbances and bypass transition in boundary layers. *Physics of Fluids*, 11:134–150, 1999.

Andersson, P., Brandt, L., Bottaro, A., and Henningson, D. S. On the breakdown of boundary layer streaks. *Journal of Fluid Mechanics*, 428:29–60, 2001.

Antonia, R. A., Fulachier, L., Krishnamoorthy, L. V., Benabid, T., and Anselmet, F. Influence of wall suction on the organized motion in a turbulent boundary layer. *Journal of Fluid Mechanics*, 190:217–240, 1988.

Armbruster, D., Guckenheimer, J., and Holmes, P. Heteroclinic cycles and modulated travelling waves in systems with O(2) symmetry. *Physica D*, 29(3):257–282, 1988.

Aubry, N., Holmes, P., Lumley, J. L., and Stone, E. The dynamics of coherent structures in the wall region of a turbulent boundary layer. *Journal of Fluid Mechanics*, 192:115–173, 1988.

Avila, K., Moxey, D., de Lozar, A., Avila, M., Barkley, D., and Hof, B. The onset of turbulence in pipe flow. *Science*, 333(6039):192–196, 2011.

Avila, M., Willis, A. P., and Hof, B. On the transient nature of localized pipe flow turbulence. *Journal of Fluid Mechanics*, 646:127–136, 2010.

Avila, M., Mellibovsky, F., Roland, N., and Hof, B. Streamwise-Localized Solutions at the Onset of Turbulence in Pipe Flow. *Physical Review Letters*, 110(22):224502, 2013.

Barkley, D. Simplifying the complexity of pipe flow. *Physical Review E*, 84(1):016309, 2011a.

Barkley, D. Modeling the transition to turbulence in shear flows. *Journal of Physics: Conference Series*, 318:032001, 2011b.

Barkley, D. and Tuckerman, L. S. Computational Study of Turbulent Laminar Patterns in Couette Flow. *Physical Review Letters*, 94(1):014502, 2005.

Bayly, B. J., Orszag, S. A., and Herbert, T. Instability mechanisms in shear-flow transition. *Annual Review of Fluid Mechanics*, 20:359–391, 1988.

Biau, D. Laminar-turbulent separatrix in a boundary layer flow. *Physics of Fluids*, 24:034107, 2012.

Blackwelder, R. F. and Eckelmann, H. Streamwise vortices associated with the bursting phenomenon. *Journal of Fluid Mechanics*, 94(03):577–594, 1979.

Blasius, H. *Grenzschichten in Flüssigkeiten mit kleiner Reibung*. PhD thesis, Göttingen, 1907.

Bottin, S. and Chaté, H. Statistical analysis of the transition to turbulence in plane Couette flow. *The European Physical Journal B - Condensed Matter and Complex Systems*, 6(1):143–155, 1998.

Bottin, S., Daviaud, F., Manneville, P., and Dauchot, O. Discontinuous transition to spatiotemporal intermittency in plane Couette flow. *Europhysics Letters*, 43(2): 171–176, 1998.

Brand, E. and Gibson, J. F. A doubly-localized equilibrium solution of plane Couette flow. *arXiv:1404.2887*, 2014.

Brandt, L., Schlatter, P., and Henningson, D. S. Transition in boundary layers subject to free-stream turbulence. *Journal of Fluid Mechanics*, 517:167–198, 2004.

Brosa, U. Turbulence without Strange Attractor. *Journal of Statistical Physics*, 55 (5/6):1303–1312, 1989.

Busse, F. H. Non-linear properties of thermal convection. *Reports on Progress in Physics*, 41(12):1929, 1978.

Canuto, C., Hussaini, M. Y., Quarteroni, A., and Zang, T. A. *Spectral Methods in Fluid Dynamics*. Springer Berlin Heidelberg, Berlin, Heidelberg, 1988. ISBN 978-3-540-52205-8.

Chantry, M., Willis, A. P., and Kerswell, R. R. The genesis of streamwise-localized solutions from globally periodic travelling waves in pipe flow. 2013.

Chaté, H. and Manneville, P. Transition to turbulence via spatio-temporal intermittency. *Physical Review Letters*, 58(2):112–115, 1987.

Chaté, H. and Manneville, P. Continuous and Discontinuous Transition to Spatio-Temporal Intermittency in Two-Dimensional Coupled Map Lattices. *Europhysics Letters (EPL)*, 6(7):591–595, 1988a.

Chaté, H. and Manneville, P. Spatio-temporal intermittency in coupled map lattices. *Physica D: Nonlinear Phenomena*, 32(3):409–422, 1988b.

Cherubini, S., De Palma, P., Robinet, J.-C., and Bottaro, A. Edge states in a boundary layer. *Physics of Fluids*, 23:051705, 2011.

Chevalier, M., Schlatter, P., Lundbladh, A., and Henningson, D. S. A pseudo-spectral solver for incompressible boundary layer flows. Technical report, KTH Mechanics, Stockholm, Sweden, 2007.

Christiansen, F., Cvitanović, P., and Putkaradze, V. Spatiotemporal chaos in terms of unstable recurrent patterns. *Nonlinearity*, 10:55, 1997.

Clever, R. M. and Busse, F. H. Tertiary and quaternary solutions for plane Couette flow. *Journal of Fluid Mechanics*, 344:137–153, 1997.

Cross, M. C. and Hohenberg, P. C. Pattern formation outside of equilibrium. *Reviews of Modern Physics*, 65:851–1112, 1993.

Crutchfield, J. P. and Kaneko, K. Are Attractors Relevant to Turbulence? *Physical Review Letters*, 60(26):2715–2719, 1988.

Cvitanović, P. Invariant measurement of strange sets in terms of cycles. *Physical Review Letters*, 61:2729–2732, 1988.

Cvitanović, P. Recurrent flows : the clockwork behind turbulence. *Journal of Fluid Mechanics*, 726:1–4, 2013.

Cvitanović, P. and Eckhardt, B. Periodic-orbit quantization of chaotic systems. *Physical Review Letters*, 63(8):823–826, 1989.

Cvitanović, P. and Eckhardt, B. Periodic orbit expansions for classical smooth flows. *Journal of Physics A: Mathematical and General*, 24(5):L237–L241, 1991.

Cvitanović, P. and Gibson, J. F. Geometry of the turbulence in wall-bounded shear flows: periodic orbits. *Physica Scripta*, T142:014007, 2010.

Cvitanović, P., Artuso, R., Mainieri, G., Tanner, G., and Vattay, G. *Chaos: Classical and quantum*. `ChaosBook.org` Niels Bohr Institute Copenhagen, 14 edition, 2012a.

Cvitanović, P., Borrero-Echeverry, D., Carroll, K. M., Robbins, B., and Siminos, E. Cartography of high-dimensional flows: a visual guide to sections and slices. *Chaos*, 22:047506, 2012b.

Danforth, C. M. "Chaos in an Atmosphere Hanging on a Wall", 2013. URL `http://mpe2013.org/2013/03/17/chaos-in-an-atmosphere-hanging-on-a-wall/`, Accessed 04.04.2014.

Darbyshire, A. G. and Mullin, T. Transition to turbulence in constant-mass-flux pipe flow. *Journal of Fluid Mechanics*, 289:83–114, 1995.

Dauchot, O. and Bertin, E. The glass transition in a nutshell: a source of inspiration to describe the subcritical transition to turbulence. *arXiv:1310.6967*, 2014.

Daviaud, F., Bonetti, M., and Dubois, M. Transition to turbulence via spatiotemporal intermittency in one-dimensional Rayleigh-Bénard convection. *Physical Review A*, 42(6):3388–3399, 1990.

de Lozar, A., Mellibovsky, F., Avila, M., and Hof, B. Edge State in Pipe Flow Experiments. *Physical Review Letters*, 108(21):214502, 2012.

Del Álamo, J. C. and Jiménez, J. Estimation of turbulent convection velocities and corrections to Taylor's approximation. *Journal of Fluid Mechanics*, 640:5–26, 2009.

Dhawan, S. and Narasimha, R. Some properties of boundary layer flow during the transition from laminar to turbulent motion. *Journal of Fluid Mechanics*, 3(04): 418–436, 1957.

Drazin, P. G. and Reid, W. H. *Hydrodynamic stability*. Cambridge Mathematical Library, 2. edition, 2004.

Duguet, Y., Willis, A. P., and Kerswell, R. R. Transition in pipe flow: the saddle structure on the boundary of turbulence. *Journal of Fluid Mechanics*, 613:255–274, 2008.

Duguet, Y., Schlatter, P., and Henningson, D. S. Localized edge states in plane Couette flow. *Physics of Fluids*, 21:111701, 2009.

Duguet, Y., Schlatter, P., and Henningson, D. S. Formation of turbulent patterns near the onset of transition in plane Couette flow. *Journal of Fluid Mechanics*, 650:119–129, 2010a.

Duguet, Y., Willis, A. P., and Kerswell, R. R. Slug genesis in cylindrical pipe flow. *Journal of Fluid Mechanics*, 663:180–208, 2010b.

Duguet, Y., Schlatter, P., Henningson, D. S., and Eckhardt, B. Self-sustained localized structures in a boundary-layer flow. *Physical Review Letters*, 108:044501, 2012.

Duguet, Y., Monokrousos, A., Brandt, L., and Henningson, D. S. Minimal transition thresholds in plane Couette flow. *Physics of Fluids*, 25(8):084103, 2013.

Duriez, T., Aider, J.-L., and Wesfreid, J. Self-Sustaining Process through Streak Generation in a Flat-Plate Boundary Layer. *Physical Review Letters*, 103(14): 144502, 2009.

Eckhardt, B. Periodic Orbit Theory. *arXiv:chao-dyn/9303015*, 1991.

Eckhardt, B. Turbulence transition in pipe flow: some open questions. *Nonlinearity*, 21:T1, 2008.

Eckhardt, B. and Ott, G. Periodic orbit analysis of the Lorenz attractor. *Zeitschrift für Physik B*, 93:259–266, 1994.

Eckhardt, B., Schneider, T. M., Hof, B., and Westerweel, J. Turbulence transition in pipe flow. *Annual Review of Fluid Mechanics*, 39:447–468, 2007.

Eckhardt, B., Faisst, H., Schmiegel, A., and Schneider, T. M. Dynamical systems and the transition to turbulence in linearly stable shear flows. *Philosophical transactions. Series A, Mathematical, physical, and engineering sciences*, 366:1297–1315, 2008.

Eckmann, J. Roads to turbulence in dissipative dynamical systems. *Reviews of Modern Physics*, 53:643–654, 1981.

Emanuel, K. in "Edward Lorenz, father of chaos theory and butterfly effect, dies at 90", 2008. URL `http://newsoffice.mit.edu/2008/obit-lorenz-0416`, Accessed 16.04.2014.

Emmons, H. W. The Laminar-Turbulent Transition in a Boundary Layer-Part I. *Journal of the Aeronautical Sciences*, 18(7):490–498, 1951.

Faisst, H. and Eckhardt, B. Transition from the Couette-Taylor system to the plane Couette system. *Physical Review E*, 61:7227–7230, 2000.

Faisst, H. and Eckhardt, B. Traveling waves in pipe flow. *Physical Review Letters*, 91:224502, 2003.

Faisst, H. and Eckhardt, B. Sensitive dependence on initial conditions in transition to turbulence in pipe flow. *Journal of Fluid Mechanics*, 504:343–352, 2004.

Feigenbaum, M. J. The onset spectrum of turbulence. *Physics Letters A*, 74(6): 375–378, 1979.

Fransson, J. H. M. *Investigations of the asymptotic suction boundary layer*. PhD thesis, KTH, Stockholm, 2001.

Fransson, J. H. M. and Alfredsson, P. H. On the disturbance growth in an asymptotic suction boundary layer. *Journal of Fluid Mechanics*, 482:51–90, 2003.

Fransson, J. H. M., Matsubara, M., and Alfredsson, P. H. Transition induced by free-stream turbulence. *Journal of Fluid Mechanics*, 527:1–25, 2005.

Frigo, M. and Johnson, S. The Design and Implementation of FFTW3. *Proceedings of the IEEE*, 93(2):216–231, 2005.

Froehlich, S. and Cvitanović, P. Reduction of continuous symmetries of chaotic flows by the method of slices. *Communications in Nonlinear Science and Numerical Simulation*, 17(5):2074–2084, 2012.

Gebhardt, T. and Grossmann, S. Chaos transition despite linear stability. *Physical Review E*, 50(5):3705–3711, 1994.

Gibson, J. F. Channelflow Website. www.channelflow.org, 2011.

Gibson, J. F. Channelflow: A spectral Navier-Stokes simulator in C++. Technical report, U. New Hampshire, 2012. URL `Channelflow.org`.

Gibson, J. F. and Brand, E. Spatially localized solutions of shear flows. 2013.

Gibson, J. F., Halcrow, J., and Cvitanović, P. Visualizing the geometry of state space in plane Couette flow. *Journal of Fluid Mechanics*, 611:107–130, 2008.

Gibson, J. F., Halcrow, J., and Cvitanović, P. Equilibrium and traveling-wave solutions of plane Couette flow. *Journal of Fluid Mechanics*, 638:243–266, 2009.

Gollub, J. P. and Swinney, H. L. Onset of Turbulence in a Rotating Fluid. *Physical Review Letters*, 35(14):927–930, 1975.

Grebogi, C., Ott, E., and Yorke, J. A. Crises, sudden changes in chaotic attractors, and transient chaos. *Physica D: Nonlinear Phenomena*, 7(1-3):181–200, 1983.

Grebogi, C., Ott, E., and Yorke, J. A. Critical exponent of chaotic transients in nonlinear dynamical systems. *Physical Review Letters*, 57:1284–1287, 1986.

Grossmann, S. The onset of shear flow turbulence. *Reviews of Modern Physics*, 72: 603–618, 2000.

Guckenheimer, J. and Holmes, P. *Nonlinear oscillations, dynamical systems and bifurcations of vector fields*, volume 42 of *Applied Mathematical Sciences*. Springer-Verlag, 1983.

Gutzwiller, M. C. Periodic orbits and classical quantization conditions. *Journal of Mathematical Physics*, 12(3):343, 1971.

Gutzwiller, M. C. Chaos in classical and quantum mechanics. *Journal of Physics A: Mathematical and Theoretical*, 43:285302, 1990.

Halcrow, J. *Charting the state space of plane Couette flow: Equilibria, relative equilibria, and heteroclinic connections*. PhD thesis, Georgia Institute of Technology, 2008.

Halcrow, J., Gibson, J. F., Cvitanović, P., and Viswanath, D. Heteroclinic connections in plane Couette flow. *Journal of Fluid Mechanics*, 621:365–376, 2009.

Hamilton, J. M., Kim, J., and Waleffe, F. Regeneration mechanisms of near-wall turbulence structures. *Journal of Fluid Mechanics*, 287:317–348, 1995.

Hanson, J. D., Cary, J. R., and Meiss, J. D. Algebraic decay in self-similar Markov chains. *Journal of Statistical Physics*, 39(3-4):327–345, 1985.

Head, M. R. and Bandyopadhyay, P. New aspects of turbulent boundary-layer structure. *Journal of Fluid Mechanics*, 107:297–338, 1981.

Henningson, D. S., Spalart, P., and Kim, J. Numerical simulations of turbulent spots in plane Poiseuille and boundary-layer flow. *Physics of Fluids*, 30(10):2914, 1987.

Hocking, L. M. Non-linear instability of the asymptotic suction velocity profile. *Quarterly Journal of Mechanics and Applied Mathematics*, 28(3):341, 1975.

Hœpffner, J., Brandt, L., and Henningson, D. S. Transient growth on boundary layer streaks. *Journal of Fluid Mechanics*, 537:91–100, 2005.

Hof, B., Juel, A., and Mullin, T. Scaling of the Turbulence Transition Threshold in a Pipe. *Physical Review Letters*, 91(24):244502, 2003.

Hof, B., van Doorne, C. W. H., Westerweel, J., Nieuwstadt, F. T. M., Faisst, H., Eckhardt, B., Wedin, H., Kerswell, R. R., and Waleffe, F. Experimental observation of nonlinear traveling waves in turbulent pipe flow. *Science*, 305:1594–1598, 2004.

Hof, B., Westerweel, J., Schneider, T. M., and Eckhardt, B. Finite lifetime of turbulence in shear flows. *Nature*, 443:59–62, 2006.

Hof, B., de Lozar, A., Kuik, D. J., and Westerweel, J. Repeller or Attractor? Selecting the Dynamical Model for the Onset of Turbulence in Pipe Flow. *Physical Review Letters*, 101:214501, 2008.

Hopf, E. A mathematical example displaying features of turbulence. *Communications on Pure and Applied Mathematics*, 1(4):303–322, 1948.

Itano, T. and Toh, S. The dynamics of bursting process in wall turbulence. *Journal of the Physics Society of Japan*, 8502(3):703–716, 2001.

Itano, T., Akinaga, T., Generalis, S. C., and Sugihara-Seki, M. Transition of Planar Couette Flow at infinite Reynolds numbers. *arXiv:1306.2702*, 2014.

Jeong, J. and Hussain, F. On the identification of a vortex. *Journal of Fluid Mechanics*, 285:69–94, 1995.

Jeong, J., Hussain, F., Schoppa, W., and Kim, J. Coherent structures near the wall in a turbulent channel flow. *Journal of Fluid Mechanics*, 332:185–214, 1997.

Jiménez, J. and Moin, P. The minimal flow unit in near-wall turbulence. *Journal of Fluid Mechanics*, 225:213–240, 1991.

Jiménez, J. and Moser, R. D. What are we learning from simulating wall turbulence? *Philosophical transactions. Series A, Mathematical, physical, and engineering sciences*, 365:715–732, 2007.

Jiménez, J., Kawahara, G., Simens, M. P., Nagata, M., and Shiba, M. Characterization of near-wall turbulence in terms of equilibrium and "bursting" solutions. *Physics of Fluids*, 17:15105, 2005.

Joslin, R. D. Aircraft laminar flow control. *Annual Review of Fluid Mechanics*, 30: 1–29, 1998.

Kadanoff, L. P. and Tang, C. Escape from strange repellers. *Proceedings of the National Academy of Sciences of the United States of America*, 81(4):1276–1279, 1984.

Kawahara, G. Laminarization of minimal plane Couette flow: Going beyond the basin of attraction of turbulence. *Physics of Fluids*, 17(4):041702, 2005.

Kawahara, G. and Kida, S. Periodic motion embedded in plane Couette turbulence: regeneration cycle and burst. *Journal of Fluid Mechanics*, 449:291–300, 2001.

Kawahara, G., Uhlmann, M., and van Veen, L. The significance of simple invariant solutions in turbulent flows. *Annual Review of Fluid Mechanics*, 44(1):203–225, 2012.

Kerswell, R. R. Recent progress in understanding the transition to turbulence in a pipe. *Nonlinearity*, 18(6):R17–R44, 2005.

Kerswell, R. R. and Tutty, O. R. Recurrence of travelling waves in transitional pipe flow. *Journal of Fluid Mechanics*, 584:69–102, 2007.

Khapko, T. Transition to turbulence in the asymptotic suction boundary layer. Technical report, Royal Institute of Technology, Department of Mechanics, Stockholm, Sweden, 2014.

Khapko, T., Kreilos, T., Schlatter, P., Duguet, Y., Eckhardt, B., and Henningson, D. S. Localized edge states in the asymptotic suction boundary layer. *Journal of Fluid Mechanics*, 717:R6, 2013.

Khapko, T., Duguet, Y., Kreilos, T., Schlatter, P., Eckhardt, B., and Henningson, D. S. Complexity of localised coherent structures in a boundary-layer flow. *The European Physical Journal E*, 37(4):32, 2014.

Klebanoff, P. S., Tidstrom, K. D., and Sargent, L. M. The three-dimensional nature of boundary-layer instability. *Journal of Fluid Mechanics*, 12(01):1–34, 1962.

Kline, S. J., Reynolds, W. C., Schraub, F. A., and Runstadler, P. W. The structure of turbulent boundary layers. *Journal of Fluid Mechanics*, 30(04):741–773, 1967.

Koschmieder, E. L. *Bénard Cells and Taylor vortices*. Cambridge Monographs on Mechanics and Applied Mathematics. Cambridge University Press, 1993. ISBN 9780521402040.

Kreilos, T. and Eckhardt, B. Periodic orbits near onset of chaos in plane Couette flow. *Chaos: An Interdisciplinary Journal of Nonlinear Science*, 22(4):047505, 2012.

Kreilos, T., Veble, G., Schneider, T. M., and Eckhardt, B. Edge states for the turbulence transition in the asymptotic suction boundary layer. *Journal of Fluid Mechanics*, 726:100–122, 2013.

Kreilos, T., Eckhardt, B., and Schneider, T. M. Increasing Lifetimes and the Growing Saddles of Shear Flow Turbulence. *Physical Review Letters*, 112(4):044503, 2014a.

Kreilos, T., Khapko, T., Schlatter, P., Duguet, Y., Henningson, D. S., and Eckhardt, B. Bypass transition in boundary layers as an activated process. *Manuscript in preparation*, 2014b.

Kreilos, T., Zammert, S., and Eckhardt, B. Comoving frames and symmetry-related dynamics in parallel shear flows. *arXiv:1309.4590*, 2014c.

Lagha, M. and Manneville, P. Modeling transitional plane Couette flow. *The European Physical Journal B*, 58:433–447, 2007.

Lai, Y.-C. and Grebogi, C. Converting transient chaos into sustained chaos by feedback control. *Physical Review E*, 49(2):1094–1098, 1994.

Lai, Y.-C. and Tél, T. *Transient Chaos: Complex Dynamics on Finite Time Scales*. Springer, 2011. ISBN 9781441969873.

Lan, Y. and Cvitanović, P. Unstable recurrent patterns in Kuramoto-Sivashinsky dynamics. *Physical Review E*, 78(2):026208, 2008.

Lebovitz, N. R. Shear-flow transition: the basin boundary. *Nonlinearity*, 22:2645, 2009.

Lebovitz, N. R. Boundary collapse in models of shear-flow transition. *Communications in Nonlinear Science and Numerical Simulation*, 17:2095–2100, 2012.

Levin, O. and Henningson, D. S. Turbulent spots in the asymptotic suction boundary layer. *Journal of Fluid Mechanics*, 584:397–413, 2007.

Levin, O., Davidsson, E. N., and Henningson, D. S. Transition thresholds in the asymptotic suction boundary layer. *Physics of Fluids*, 17:114104, 2005.

Li, Y.-T. and Yorke, J. A. Period Three Implies Chaos. *The American Mathematical Monthly1*, 82(10):985–992, 1975.

Lorenz, E. N. Deterministic Nonperiodic Flow. *Journal of the Atmospheric Sciences*, 20:130–141, 1963.

Lundbladh, A. and Johansson, A. V. Direct simulation of turbulent spots in plane Couette flow. *Journal of Fluid Mechanics*, 229:499–516, 1991.

Madré, T. Turbulence Transition in the Asymptotic Suction Boundary Layer, Diplomarbeit, Philipps Universität Marburg, 2011, Philipps Universität Marburg.

Manneville, P. Spatiotemporal perspective on the decay of turbulence in wall-bounded flows. *Physical Review E*, 79(2):025301, 2009.

Mariani, P., Spalart, P., and Kollmann, W. Direct simulation of a turbulent boundary layer with suction. *Near-wall turbulent flows*, pages 347–356, 1993.

Marinc, D. Localised edge-states in plane Couette flow, Diplomarbeit, Philipps Universität Marburg, 2008, Philipps Universität Marburg.

Matsubara, M. and Alfredsson, P. H. Disturbance growth in boundary layers subjected to free-stream turbulence. *Journal of Fluid Mechanics*, 430:149–168, 2001.

Maurer, J. and Libchaber, A. Rayleigh-Bénard experiment in liquid helium ; frequency locking and the onset of turbulence. *Journal de Physique Lettres*, 40(16): 419–423, 1979.

Mellibovsky, F. and Eckhardt, B. Takens-Bogdanov bifurcation of travelling-wave solutions in pipe flow. *Journal of Fluid Mechanics*, 670:96–129, 2011.

Mellibovsky, F. and Eckhardt, B. From travelling waves to mild chaos: a supercritical bifurcation cascade in pipe flow. *Journal of Fluid Mechanics*, 709:149–190, 2012.

Mellibovsky, F. and Meseguer, A. Critical threshold in pipe flow transition. *Philosophical transactions. Series A, Mathematical, physical, and engineering sciences*, 367(1888):545–560, 2009.

Mellibovsky, F., Meseguer, A., Schneider, T. M., and Eckhardt, B. Transition in Localized Pipe Flow Turbulence. *Physical Review Letters*, 103(5):054502, 2009.

Melnikov, K., Kreilos, T., and Eckhardt, B. Long-wavelength instability of coherent structures in plane Couette flow. *Physical Review E*, 89(4):043008, 2014.

Meseguer, A. and Trefethen, L. N. Linearized pipe flow to Reynolds number 10^7. *Journal of Computational Physics*, 186(1):178–197, 2003.

Metropolis, N., Stein, M. L., and Stein, P. R. On finite limit sets for transformations on the unit interval. *Journal of Combinatorial Theory, Series A*, 44:25–44, 1973.

Moehlis, J., Eckhardt, B., and Faisst, H. Fractal lifetimes in the transition to turbulence. *Chaos: An Interdisciplinary Journal of Nonlinear Science*, 14:S11, 2004a.

Moehlis, J., Faisst, H., and Eckhardt, B. A low-dimensional model for turbulent shear flows. *New Journal of Physics*, 6:56, 2004b.

Moffatt, H. K. Fixed points of turbulent dynamical systems and suppression of nonlinearity. *Whither Turbulence? Turbulence at the Crossroads*, 357:250–257, 1990.

Moin, P. and Kim, J. Tackling Turbulence with Supercomputers. *Scientific American*, 276:62–68, 1997.

Morkovin, M. V. On the many faces of transition. In Wells, C., editor, *Viscous drag reduction*, pages 1–31. Springer US, 1969. ISBN 978-1-4899-5581-4.

Moxey, D. and Barkley, D. Distinct large-scale turbulent-laminar states in transitional pipe flow. *Proceedings of the National Academy of Sciences of the United States of America*, 107(18):8091–8096, 2010.

Mullin, T. Experimental studies of transition to turbulence in a pipe. *Annual Review of Fluid Mechanics*, 43(1):1–24, 2011.

Nagata, M. Three-dimensional finite-amplitude solutions in plane Couette flow: bifurcation from infinity. *Journal of Fluid Mechanics*, 217:519–527, 1990.

Nagata, M. Three-dimensional traveling-wave solutions in plane Couette flow. *Physical Review E*, 55:2023–2025, 1997.

Narasimha, R. On the distribution of intermittency in the transition region of a boundary layer. *Journal of the Aeronautical Sciences*, 24(9):711–712, 1957.

Narasimha, R. The laminar-turbulent transition zone in the boundary layer. *Progress in Aerospace Sciences*, 22(1):29–80, 1985.

Navier, C. L. M. H. Mémoire sur les lois du mouvement des fluides. *Mémoires de l'Académie Royale des Sciences de l'Institut de France*, 6:389–440, 1823.

Newhouse, S., Ruelle, D., and Takens, F. Occurrence of strange Axiom A attractors near quasi periodic flows on T^m, $m \geq 3$. *Communications in Mathematical Physics*, 64:35–40, 1978.

Orszag, S. A. Accurate solution of the Orr–Sommerfeld stability equation. *Journal of Fluid Mechanics*, 50(04):689–703, 1971.

Orszag, S. A. and Kells, L. C. Transition to turbulence in plane Poiseuille and plane Couette flow. *Journal of Fluid Mechanics*, 96(01):159–205, 1980.

Ott, E. Strange attractors and chaotic motions of dynamical systems. *Reviews of Modern Physics*, 53:655–671, 1981.

Ott, E. *Chaos in Dynamical Systems*. Cambridge University Press, 1993. ISBN 9780521010849.

Peixinho, J. and Mullin, T. Decay of Turbulence in Pipe Flow. *Physical Review Letters*, 96:094501, 2006.

Peixinho, J. and Mullin, T. Finite-amplitude thresholds for transition in pipe flow. *Journal of Fluid Mechanics*, 582:169–178, 2007.

Poincaré, H. *Les méthodes nouvelles de la mécanique céleste*, volume 10. Gauthier-Villars, Paris, 1892.

Pomeau, Y. and Manneville, P. Intermittent Transition to Turbulence in Dissipative Dynamical Systems. *Communications in Mathematical Physics*, 74:189–197, 1980.

Prigent, A., Grégoire, G., Chaté, H., Dauchot, O., and van Saarloos, W. Large-Scale Finite-Wavelength Modulation within Turbulent Shear Flows. *Physical Review Letters*, 89(1):014501, 2002.

Pringle, C. C. T. and Kerswell, R. R. Asymmetric, Helical, and Mirror-Symmetric Traveling Waves in Pipe Flow. *Physical Review Letters*, 99(7):074502, 2007.

Pringle, C. C. T., Duguet, Y., and Kerswell, R. R. Highly symmetric travelling waves in pipe flow. *Philosophical transactions. Series A, Mathematical, physical, and engineering sciences*, 367(1888):457–472, 2009.

Reshotko, E. Boundary-Layer Stability and Transition. *Annual Review of Fluid Mechanics*, 8:311–349, 1976.

Reynolds, O. An experimental investigation of the circumstances which determine whether the motion of water shall be direct or sinous and the law of resistance in parallel channels. *Philosophical Transactions of the Royal Society*, 174:935–982, 1883.

Riols, A., Rincon, F., Cossu, C., Lesur, G., Longaretti, P.-Y., Ogilvie, G. I., and Herault, J. Global bifurcations to subcritical magnetorotational dynamo action in Keplerian shear flow. *Journal of Fluid Mechanics*, 731:1–45, 2013.

Robinson, S. K. Coherent motions in the turbulent boundary layer. *Annual Review of Fluid Mechanics*, 23(1):601–639, 1991.

Romanov, V. A. Stability of plane-parallel Couette flow. *Functional Analysis and Its Applications*, 7(2):137–146, 1973.

Rowley, C. W. and Marsden, J. E. Reconstruction equations and the Karhunen–Loève expansion for systems with symmetry. *Physica D: Nonlinear Phenomena*, 142(1-2): 1–19, 2000.

Rowley, C. W., Kevrekidis, I. G., Marsden, J. E., and Lust, K. Reduction and reconstruction for self-similar dynamical systems. *Nonlinearity*, 16:1257–1275, 2003.

Ruelle, D. and Takens, F. On the Nature of Turbulence. *Communications in Mathematical Physics*, 20(3):167–192, 1971.

Salwen, H., Cotton, F. W., and Grosch, C. E. Linear stability of Poiseuille flow in a circular pipe. *Journal of Fluid Mechanics*, 98(2):273–284, 1980.

Saric, W. S., Reed, H. L., and Kerschen, E. J. Boundary-Layer Receptivity to Freestream Disturbances. *Annual Review of Fluid Mechanics*, 34:291–319, 2002.

Schlatter, P. and Örlü, R. Turbulent asymptotic suction boundary layers studied by simulation. *Journal of Physics: Conference Series*, 318(2):022020, 2011.

Schlatter, P., Stolz, S., and Kleiser, L. LES of transitional flows using the approximate deconvolution model. *International Journal of Heat and Fluid Flow*, 25(3):549–558, 2004.

Schlatter, P., Brandt, L., de Lange, H. C., and Henningson, D. S. On streak breakdown in bypass transition. *Physics of Fluids*, 20:101505, 2008.

Schlichting, H. *Grenzschicht Theorie*. Verlag G. Braun, 8. edition, 1982. ISBN 9783540230045.

Schlichting, H. *Boundary-layer theory*. Springer, 2004. ISBN 9783540662709.

Schmid, P. J. and Henningson, D. S. *Stability and Transition in Shear Flows*. Number Bd. 142 in Applied mathematical sciences. Springer, 2001. ISBN 9780387989853.

Schmiegel, A. *Transition to turbulence in linearly stable shear flows*. PhD thesis, Philipps-Universität Marburg, 1999.

Schmiegel, A. and Eckhardt, B. Fractal stability border in plane Couette Flow. *Physical Review Letters*, 79:5250–5253, 1997.

Schneider, T. M. *State space properties of transitional pipe flow*. PhD thesis, Philipps-Universität Marburg, 2007.

Schneider, T. M. and Eckhardt, B. Lifetime statistics in transitional pipe flow. *Physical Review E*, 78:46310, 2008.

Schneider, T. M. and Eckhardt, B. Edge states intermediate between laminar and turbulent dynamics in pipe flow. *Philosophical transactions. Series A, Mathematical, physical, and engineering sciences*, 367(1888):577–587, 2009.

Schneider, T. M., Eckhardt, B., and Vollmer, J. Statistical analysis of coherent structures in transitional pipe flow. *Physical Review E*, 75:66313, 2007a.

Schneider, T. M., Eckhardt, B., and Yorke, J. A. Turbulence transition and the edge of chaos in pipe flow. *Physical Review Letters*, 99:34502, 2007b.

Schneider, T. M., Gibson, J. F., Lagha, M., De Lillo, F., and Eckhardt, B. Laminar-turbulent boundary in plane Couette flow. *Physical Review E*, 78:37301, 2008.

Schneider, T. M., De Lillo, F., Buehrle, J., Eckhardt, B., Dörnemann, T., Dörnemann, K., and Freisleben, B. Transient turbulence in plane Couette flow. *Physical Review E*, 81:015301(R), 2010a.

Schneider, T. M., Gibson, J. F., and Burke, J. Snakes and Ladders: Localized Solutions of Plane Couette Flow. *Physical Review Letters*, 104(10):104501, 2010b.

Schneider, T. M., Marinc, D., and Eckhardt, B. Localized edge states nucleate turbulence in extended plane Couette cells. *Journal of Fluid Mechanics*, 646:441–451, 2010c.

Schoppa, W. and Hussain, F. Coherent structure generation in near-wall turbulence. *Journal of Fluid Mechanics*, 453:57–108, 2002.

Sipos, M. and Goldenfeld, N. Directed percolation describes lifetime and growth of turbulent puffs and slugs. *Physical Review E*, 84(3):035304, 2011.

Sivashinsky, G. I. Nonlinear analysis of hydrodynamic instability in laminar flames—I. Derivation of basic equations. *Acta Astronautica*, 4(11-12):1177–1206, 1977.

Skufca, J. D., Yorke, J. A., and Eckhardt, B. Edge of chaos in a parallel shear flow. *Physical Review Letters*, 96:174101, 2006.

Smale, S. Topology and mechanics. I. *Inventiones Mathematicae*, 10(4):305–331, 1970.

Smith, T. R., Moehlis, J., and Holmes, P. Heteroclinic cycles and periodic orbits for the O(2)-equivariant 0:1:2 mode interaction. *Physica D*, 211(3-4):347–376, 2005.

Spalart, P. R. Direct simulation of a turbulent boundary layer up to $R_\Theta = 1410$. *Journal of Fluid Mechanics*, 187:61–98, 1988.

Spalart, P. R. and Yang, K.-S. Numerical study of ribbon-induced transition in Blasius flow. *Journal of Fluid Mechanics*, 178:345–365, 1987.

Stavans, J., Heslot, F., and Libchaber, A. Fixed Winding Number and the Quasiperiodic Route to Chaos in a Convective Fluid. *Physical Review Letters*, 55(11):1239, 1985.

Stokes, G. G. On the theories of the internal friction of fluids in motion, and of the equilibrium and motion of elastic solids. *Transactions of the Cambridge Philosophical Society*, 8:287–305, 1845.

Strogatz, S. H. *Nonlinear dynamics and chaos: With applications to physics, biology, chemistry, and engineering.* 1994. ISBN 9780738204536.

Tasaka, Y., Schneider, T. M., and Mullin, T. Folded Edge of Turbulence in a Pipe. *Physical Review Letters*, 105(17):174502, 2010.

Taylor, G. I. The Spectrum of Turbulence. *Proceedings of the Royal Society A: Mathematical, Physical and Engineering Sciences*, 164(919):476–490, 1938.

Theodorsen, T. Mechanism of turbulence. In *Proceedings of the Second Midwestern Conference on Fluid Mechanics*, pages 1–18. Ohio State University, 1952.

Thibert, J. J., Reneaux, J., and Schmitt, V. ONERA activities on drag reduction. In *17th ICAS Congress, Stockolm (Sweden), September 9-14*, 1990.

Toh, S. and Itano, T. A periodic-like solution in channel flow. *Journal of Fluid Mechanics*, 481:67–76, 2003.

Townsend, A. A. *The structure of turbulent shear flow*. Cambridge University Press, 1980. ISBN 9780521298193.

Tsukahara, T., Seki, Y., Kawamura, H., and Tochio, D. DNS of Turbulent Channel Flow with Very Low Reynolds Numbers. In *Proceedings of the 4th International Symposium on Turbulence and Shear Flow Phenomena*, pages 935–940, 2005.

Tuckerman, L. S. and Barkley, D. Global Bifurcations to Traveling Waves in Axisymmetric Convection. *Physical Review Letters*, 61(4):408–411, 1988.

Tuckerman, L. S., Kreilos, T., Schrobsdorff, H., Schneider, T. M., and Gibson, J. F. Turbulent-laminar patterns in plane Poiseuille flow. *arXiv:1404.1502*, 2014.

van Veen, L. and Kawahara, G. Homoclinic tangle on the edge of shear turbulence. *Physical Review Letters*, 107:114501, 2011.

van Veen, L., Kida, S., and Kawahara, G. Periodic motion representing isotropic turbulence. *Fluid Dynamics Research*, 38(1):19–46, 2006.

Vinod, N. and Govindarajan, R. Pattern of Breakdown of Laminar Flow into Turbulent Spots. *Physical Review Letters*, 93(11):114501, 2004.

Vinod, N. and Govindarajan, R. The signature of laminar instabilities in the zone of transition to turbulence. *Journal of Turbulence*, 8:N2, 2007.

Viswanath, D. Recurrent motions within plane Couette turbulence. *Journal of Fluid Mechanics*, 580:339–358, 2007.

Viswanath, P. R. Aircraft viscous drag reduction using riblets. *Progress in Aerospace Sciences*, 38(6-7):571–600, 2002.

Vollmer, J., Schneider, T. M., and Eckhardt, B. Basin boundary, edge of chaos and edge state in a two-dimensional model. *New Journal of Physics*, 11:013040, 2009.

Waleffe, F. Hydrodynamic stability and turbulence: beyond transients to a self-sustaining process. *Studies in applied mathematics*, 95(3):319–343, 1995.

Waleffe, F. On a self-sustaining process in shear flows. *Physics of Fluids*, 9:883–900, 1997.

Waleffe, F. Three-dimensional coherent states in plane shear flows. *Physical Review Letters*, 81:4140–4143, 1998.

Waleffe, F. Exact coherent structures in channel flow. *Journal of Fluid Mechanics*, 435:93–102, 2001.

Waleffe, F. Homotopy of exact coherent structures in plane shear flows. *Physics of Fluids*, 15:1517–1534, 2003.

Wang, J., Gibson, J. F., and Waleffe, F. Lower Branch Coherent States in Shear Flows: Transition and Control. *Physical Review Letters*, 98(20):204501, 2007.

Wedin, H. and Kerswell, R. R. Exact coherent structures in pipe flow: travelling wave solutions. *Journal of Fluid Mechanics*, 508:333–371, 2004.

Willis, A. P. and Kerswell, R. R. Critical Behavior in the Relaminarization of Localized Turbulence in Pipe Flow. *Physical Review Letters*, 98:014501, 2007.

Willis, A. P. and Kerswell, R. R. Coherent Structures in Localized and Global Pipe Turbulence. *Physical Review Letters*, 100(12):124501, 2008.

Willis, A. P., Cvitanović, P., and Avila, M. Revealing the state space of turbulent pipe flow by symmetry reduction. *Journal of Fluid Mechanics*, 721:514–540, 2013.

Wygnanski, I. J. and Champagne, F. H. On transition in a pipe. Part 1. The origin of puffs and slugs and the flow in a turbulent slug. *Journal of Fluid Mechanics*, 59 (2):281–335, 1973.

Wygnanski, I. J., Sokolov, M., and Friedman, D. On a turbulent 'spot' in a laminar boundary layer. *Journal of Fluid Mechanics*, 78(04):785–819, 1976.

Zaman, K. B. M. Q. and Hussain, A. K. M. F. Taylor hypothesis and large-scale coherent structures. *Journal of Fluid Mechanics*, 112:379–396, 1981.

Zammert, S. and Eckhardt, B. Periodically bursting edge states in plane Poiseuille flow. *arXiv:1312.6783*, 2013.

Zammert, S. and Eckhardt, B. A Fully Localised Periodic Orbit In Plane Poiseuille Flow. *arXiv:1404.2582*, 2014.

Curriculum Vitae

since 05/2011	PhD student under supervision of Prof. Dr. Bruno Eckhardt University of Marburg, Germany
08/2013 – 01/2014	Doctoral researcher in the group of Dr. Tobias M. Schneider at the Max-Planck-Institute for Dynamics and Selforganization, Göttingen
05/2013	4-week research stay Nordita program *Stability and Transition*, Stockholm, Sweden
31/03/2011	Degree: Diplom Physik from the University of Marburg, Germany
10/2009 – 03/2011	Diploma thesis under supervision of Prof. Dr. Bruno Eckhardt Title of the work: *Turbulence Transition in the Asymptotic Suction Boundary Layer*
09/2008 – 08/2009	Exchange student in the Erasmus programme of the EU Université Joseph Fourier, Grenoble, France
09/2007 – 03/2011	Study of physics at the University of Marburg, Germany
09/2005 – 08/2007	Study of physics until pre-diploma at the University of Freiburg, Germany

Wissenschaftlicher Werdegang

seit 05/2011	Doktorand bei Prof. Dr. Bruno Eckhardt Philipps-Universität Marburg
08/2013 – 01/2014	Wissenschaftlicher Mitarbeiter bei Dr. Tobias M. Schneider Max-Planck-Institut für Dynamik und Selbstorganisation Göttingen
05/2013	4-wöchiger Forschungsaufenthalt Nordita-Programm *Stability and Transition* Stockholm, Schweden
31/03/2011	Abschluss: Diplom Physik, Philipps-Universtiät Marburg
10/2009 – 03/2011	Diplomarbeit bei Prof. Dr. Bruno Eckhardt Titel der Arbeit: *Turbulence Transition in the Asymptotic Suction Boundary Layer*
09/2008 – 08/2009	Studium, Erasmus-Programm der Europäischen Union Université Joseph Fourier, Grenoble, Frankreich
09/2007 – 03/2011	Studium Physik (Diplom), Philipps-Universität Marburg
09/2005 – 08/2007	Studium Physik (Diplom) bis einschl. Vordiplom, Albert-Ludwigs-Universität Freiburg

Acknowledgements

There are many people who made this work possible and to whom I am deeply thankful.

First of all I would like to thank my supervisor Bruno Eckhardt. His excitement about new findings and his never ending curiosity have been a constant source of motivation, not to forget his deep knowledge in so many areas. I do not know how often we had talked for five minutes and I had not only solved a problem I had been working on for weeks but also got new ideas and projects for months. Nevertheless I was always free to pursue own ideas, guided by his sound advice.

I would like to express my thanks to Tobias Schneider for his inspiring enthusiasm, our good discussions and the great support, scientifically, computationally and personally, he gave me throughout this work and during my time in Göttingen. Thanks to Priya Subramanian, Hecke Schrobsdorff, Denny Fliegner and the rest of the MPIDS group. I felt always welcome in Göttingen, appreciate working together and am grateful for the computing support. Special thanks to Tobias and Hecke for the great joint effort in finishing the parallelization of channelflow.

I want to express my thanks to my collaborators from Stockholm and Paris, Taras Khapko, Philipp Schlatter, Yohann Duguet and Dan Henningson. It was a great pleasure to be in this collaboration and I very much enjoyed the great time I had during my visits to Stockholm and the stimulating discussions during our meetings. Special thanks to Philipp for sharing his knowledge about the parallelization of spectral codes. I am particularly grateful to Dan for the opportunity to come to KTH in 2012 and to participate in the Nordita program *Stability and Transition* in 2013.

This work would not have been possible without the channelflow code and I would like to thank John Gibson for providing and maintaining the code as well as for his advice during the parallelization. Thanks to Thomas Gebhardt for his support regarding the use of the MaRC and MaRC2 clusters and to Andreas Oppermann and Andreas Schrimpf, who were of great help in all problems we had with the administration of our group's computers.

Life at work was rarely boring, for which I have to thank Annika, Felix, Florian, Hannes, Jan, Jens, Konstantin, Konstanze, Kristof, Lars, Lisa, Marina, Michael, Michael, Patrick, Shuxin and Stefan. I enjoyed the amicable and cooperative atmosphere in our group, the willingness to help each other and our numerous discussions about life, the universe and everything. And I will certainly miss our after-lunch stops at the Bohne! I was glad to share an office with Hannes, enjoying the nice atmosphere and our short-distance chats about computer problems, fluid mechanics,

science in general and the small and big problems of life. Special thanks to Michael and Stefan for proofreading this work.

Life would be sad if it weren't for good friends. Thank you for being there, Bianca, Cornelia, Martin, Nicole and Philipp as well as Benni, Gioia, Martin, Nine, Robert and Svenja. Not to forget my flat-mates, Claudia and Steven, who not only endured me while I was working on this thesis but were always willing to share a beer after a long day.

Ganz besonderer Dank gebührt meinen Eltern und meinem Bruder, die immer an mich geglaubt und mich in so vielen Dingen unterstützt haben. Ohne euch wäre ich diesen Weg niemals gegangen. Und nicht zuletzt danke ich Nicola, schon alleine dafür dass es dich gibt. Dein Lächeln hat mich durch alle Schwierigkeiten getragen.